Cardiff University

School of Chemistry

Development of Luminescent Iridium(III) and Rhenium(I) Complexes for Optoelectronic Applications

Thesis submitted for the degree of Doctor of Philosophy by:

Kaitlin Alexandra Phillips

August 2019

CARDIFF UNIVERSITY

SCHOOL OF CHEMISTRY

ABSTRACT

DOCTOR OF PHILOSOPHY

Synthesis and Characterisation of Novel Long-Wavelength Phosphorescent Metal Complexes of Iridium(III) and Rhenium(I)

By Kaitlin Alexandra Phillips

The purpose of the work reported in this thesis was to develop novel phosphorescent transition metal complexes. These species are of importance due to the wide range of applications which will be discussed in further detail throughout this work. There is a clear need for the development of new red-emitting species which are of particular interest in the fields of OLEDs and bioimaging.

Chapter 2 describes the effect of cyclometallating ligand substitution upon the photophysical properties of cationic iridium(III) complexes with an ancillary 2,2'-bipyridine ligand. A series of cyclometallating ligands based upon quinoxaline were synthesised and functionalised with electron withdrawing and donating groups. It was found that substitution was an effective method for the fine-tuning of emission wavelength and that the methylated species synthesised were excellent triplet-triplet annihilation upconversion donors.

Chapter 3 utilises the same cyclometallating ligands from chapter two and describes the effect of ancillary ligand upon the overall photophysical properties. Picolinic acid and pyrazinoic acid were used as ancillary ligands to give a series of eleven novel complexes which all showed red emission and increased the total tuning range of emission wavelength.

Chapter 4 describes the effect of conjugation upon the emission of cationic iridium(III) complexes. Four novel bis-cyclometallated iridium(III) complexes were synthesised with a series of benzo[*g*]quinoxaline ligands. Results showed near-infrared emission comparable to previous reports in literature but also showed visible green emission which previous reports has not observed.

Chapter 5 describes the synthesis of four novel organic lumophores based upon a dicyanodibenzodioxin structure. It was shown that emission from these species is dominated by a charge transfer transition arising from the dicyanodibenzodioxin core of the compounds. Coordination of these compounds to rhenium(I) gave four novel neutral complexes that exhibited dual red and green emission. It was also noted that exchange of the axial halide ligand in the neutral species with acetonitrile gave a cationic species that showed green emission only.

Contents

1. Introduction 1
1.1. Introduction 2
1.2. Luminescence 2
1.2.1. The Jablonski Diagram 2
1.2.2. The Stokes Shift 3
1.2.3. Kasha's Rule 4
1.2.4. Quantum Yield and Luminescence Lifetime 4
1.2.5. Luminescence Quenching 6
1.2.5.1. Collisional Quenching 6
1.2.5.2. Static Quenching 7
1.2.6. Solvent Relaxation 7
1.2.7. Resonance Energy Transfer 8
1.3. Luminescence Measurements 8
1.3.1. Steady State Measurements 8
1.3.2. Time Resolved Measurements 9
1.4. Recording Spectra 9
1.4.1. Emission Spectra 10
1.4.2. Excitation Spectra 10
1.5. Types of Lumophores 11
1.5.1. Organic Lumophores 11
1.6. Transition Metal Complexes 12
1.7. Phosphorescent Transition Metal Complexes 12
1.7.1. First Row Transition Metal Complexes 12
1.7.2. Second and Third Row Transition Metal Complexes 14
1.7.2.1. d^6 Configuration 14
1.7.2.2. d^8 Configuration 16
1.7.2.3. d^{10} Configuration 17
1.7.3. Fluorescent Transition Metal Complexes 19
1.8. Summary 19
1.9. References 20
2. Ligand-Tuneable, Red-Emitting Iridium(III) Complexes for Efficient Triplet–Triplet Annihilation Upconversion Performance 23
2.1. Introduction 24
2.1.1. Applications of Iridium(III) Complexes 24

2.1.2. Photocatalysts 24
2.1.3. Photovoltaics 25
2.1.4. Bioimaging 25
2.1.5. Triplet-Triplet Annihilation Upconversion 26
2.2. Aims 29
2.3. Results and Discussion 30
2.3.1. Synthesis and Characterisation 30
2.3.2. X-Ray Crystallography 35
2.3.3. Cyclic Voltammetry 39
2.3.4. Photophysical Properties 40
2.3.5. Density Functional Theory 43
2.3.6. Transient Absorption Spectroscopy 47
2.3.7. Triplet-Triplet Annihilation Upconversion Measurements 49
2.4. Conclusion 52
2.5. Experimental 53
2.6. References 62
3. Neutral Iridium(III) Complexes Incorporating Cyclometallated Quinoxaline Ligands: Synthesis, Characterisation and Luminescence Properties 65
3.1. Introduction 66
3.1.1. OLEDs 66
3.1.2. Iridium Complexes 69
3.1.3. Picolinic Acid 71
3.2. Aims 72
3.3. Results and Discussion 73
3.3.1. Synthesis 73
3.3.2. Characterisation 75
3.3.2.1. NMR Spectroscopy 75
3.3.2.2. Mass Spectrometry 78
3.3.3. Electrochemistry 80
3.3.4. Photophysical Studies 81
3.3.4.1. UV-vis Absorption Spectra 81
3.3.4.2. Emission Data 84
3.3.4.3. Luminescence Lifetime 88
3.3.4.4. Quantum Yield 89
3.3.4.5. Solvent Studies 91
3.3.5. Computational Studies 94

3.3.6. Transient Absorption Studies 96
3.4. Conclusion 98
3.5. Experimental 99
3.6. References 105
4. Dual Visible/ Near-IR Emission from Organometallic Iridium(III) Complexes 107
4.1. Introduction 108
4.1.1. Near Infrared 108
4.2. Aims 111
4.3. Results and Discussion 112
4.3.1. Synthesis of Ligands 112
4.3.2. Synthesis of Complexes 116
4.3.3. UV-Vis and Luminescence Spectroscopy 119
4.3.4. Density Functional Theory Calculations 125
4.4. Conclusion 128
4.5. Experimental 129
4.6. References 134
5. Exploratory Synthesis: Toward the synthesis of dicyanodibenzodioxin ligands and their rhenium(I) coordination chemistry 135
5.1. Introduction 136
5.1.1. Dicyanodibenzodioxin Derivatives 136
5.1.2. Rhenium(I) 140
5.1.3. Rhenium Complexes in OLED Devices 141
5.1.4. Rhenium Complexes in Photocatalysis 141
5.1.5. Rhenium Complexes in Bioimaging 143
5.2. Aims 146
5.3. Results and Discussion 147
5.3.1. Synthesis and characterisation of dicyanobenzodioxins 147
5.3.2. Coordination chemistry with rhenium(I) 155
5.3.3. Photophysical Data 163
5.4. Conclusion 174
5.5. Experimental 175
5.6. References 179
6. Summary and Further Work 181
6.1. Summary 182
6.2. Future Work 182
7. Appendix 185

Acknowledgements

Firstly, I would like to thank my supervisor, Professor Simon Pope, for giving me the opportunity to pursue my PhD studies. Your endless encouragement and support have made all the difference. I would also like to extend my thanks to my industrial supervisors Dr Andy Hallett and Dr Sean O'Kell from STG Aerospace; thank you for finding time for me to visit! I would also like to thank KESS 2 for providing the funding for this project.

A big thank you to all the staff in the inorganic department for creating a great atmosphere to work in. Thanks especially to Woody and Angelo for being my review panel and never being too mean in a viva. Thanks to all the people who keep the school running every day, especially Rob, Simon, Robin and Tom, without whom, the school would probably fall apart.

Furthermore, I am grateful to Dr Joe Beames and Thomas Stonelake, whose work has contributed hugely to the publication of the two papers at the end of this thesis.

My time studying wouldn't have been the same without all the amazing people that I've been able to share it with. Thank you to Adam, Lara, Sam and Stokes for helping me settle into PhD life, and to all the members who have joined since who have kept the lab a happy place to be. Plus a special thanks to Ella who helped keep girl power alive! A huge thanks also goes to all of my friends in the inorganic department, especially Corey and Alex who never fail to cheer me up!

Outside of university, I owe a huge thank you to Sam who has stood by me and encouraged me every day over the last three years. I also need to thank my parents and grandparents who, while they may not always be sure what it is I'm doing, have always believed I'd do it in the end.

Diolch yn fawr iawn i chi i gyd!

Table to Figures

Figure 1.1: Jablonski diagram..... 2
Figure 1.2: Diagram showing the Stokes shift..... 4
Figure 1.3: The structures and quantum yields of fluorophores rhodamine 101,[9] 9,10-diphenylanthracene,[10] and fluorescein.[11] 5
Figure 1.4: Jablonski diagram illustrating the radiative and non-radiative processes involved in collisional quenching. Where FRET is fluorescence energy transfer to an acceptor molecule, A, and Σk_i is the sum of all non-radiative processes except for quenching, k_q. 6
Figure 1.5: The copper(II) complex on the left was found to quench the fluorescence of the dansyl(DNS)-amino acid by static quenching.[21] 7
Figure 1.6: Simplified diagram of luminescence spectrometer set-up. 10
Figure 1.7: Organic fluorophores with a polyaromatic structure. 11
Figure 1.8: Examples of new organic fluorophores. 12
Figure 1.9: Examples of phosphorescent chromium(III) and copper(I) complexes. 13
Figure 1.10: Left) Phosphorescent complex of Fe(II) reported by Vogler.[51] Right) Phosphorescent complex of Fe(III) reported by Chábera et al.[52] 14
Figure 1.11: Complexes of ruthenium(II) and osmium(II) with their photophysical properties.[57,58] 15
Figure 1.12: Structures and emission wavelengths of rhodium(III) complexes. Left and centre complexes recorded as ethanol: methanol glasses, right complex recorded in acetonitrile solution.[61,62] 16
Figure 1.13: Phosphorescent complexes of platinum(II) along with photophysical properties.[63–65] 16
Figure 1.14: Phosphorescent palladium(II) metalloporphyrins. 17
Figure 1.15: Examples of phosphorescent silver(I) complexes. 18
Figure 1.16: Examples of phosphorescent gold(I) complexes. 18
Figure 1.17: Examples of fluorescent transition metal complexes.[80–82] 19
Figure 2.1:Examples of iridium(III) complexes developed as photocatalysts. 25
Figure 2.2: Complexes developed for photovoltaic applications. 25
Figure 2.3: Iridium complexes synthesised as bioimaging agents. 26
Figure 2.4: Schematic of triplet-triplet annihilation. Where D = donor molecule and A = acceptor molecule..... 26
Figure 2.5: Examples of common triplet-triplet annihilation acceptor compounds. 27
Figure 2.6: Examples of transition metal complexes developed as triplet-triplet annihilation donors. 28
Figure 2.7: Examples of upconversion donor species based on iridium complexes..... 28
Figure 2.8: Assignment of proton NMR spectrum of ligand HL3. (300 MHz, $CDCl_3$) 31
Figure 2.9: Overlaid NMR spectra of HL3 (red) and HL6 (black). (300 MHz, $CDCl_3$) 32
Figure 2.10: Structures of seven cationic bis-cyclometallated iridium(III) complexes. 33
Figure 2.11: Proton NMR data for complex C4. (400 MHz, acetone-d_6)..... 34
Figure 2.12: High-resolution mass spectrum of complex C2a with molecular ion peak. 35
Figure 2.13: X-ray structures of the cation in the complexes a) **$[Ir(L2)_2(bpy)]PF_6$;** b) **$[Ir(L5)_2(bpy)]PF_6$** and c) **$[Ir(L7)_2(bpy)]PF_6$**. 36
Figure 2.14: Packing diagram of complex C2a 38
Figure 2.15: Packing diagram of complex C5a 38
Figure 2.16: Overlay of the crystal structure (blue) and DF-DFT//B3LYP/6-31G*(SDD) optimised structures (brown) for **$[Ir(L5)_2(bpy)]PF_6$**. The structures exhibit an RMSD of 0.427 Å. 39

Figure 2.17: Cyclic voltammograms recorded for complex C4a [(Ir(L4)$_2$(bpy))(MeCN)][PF$_6$]$_2$ under argon. Voltammogram recorded in 0.25 M [NH$_4$][PF$_6$], scan rate υ = 200 mV/s with Fc/Fc$^+$ couple at +0.46 for reference.....40
Figure 2.18: UV-vis absorption spectra of ligands HL1-7 recorded in chloroform (1x10^{-5} M) 40
Figure 2.19: Steady state emission spectra of ligands HL1-7. Spectra recorded in chloroform, λ_{ex} = 350 nm.....41
Figure 2.20: UV-vis absorption spectra of complexes C1a-7a. Recorded in CHCl$_3$, 1x10^{-5} M.....42
Figure 2.21: Comparison between absorption spectra of HL1 and C1a.....43
Figure 2.22: Isosurfaces of the Kohn-Sham **[Ir(L1)$_2$(bpy)]PF$_6$** frontier molecular orbitals (DFT//B3LYP/6-31G*).....44
Figure 2.23: Bottom) Experimental absorption spectrum of complex C1a. Top) TD-DFT//CAM-B3LYP/6-31 G*(SDD) convoluted absorption spectrum.....45
Figure 2.24: Overlaid steady state emission spectra for complexes C1a-7a. λ_{ex} = 450 nm.....46
Figure 2.25: Left) Transient absorption spectrum of complex C1a shown in black, overlaid with the emission spectrum of the same complex shown in red. Right) Transient absorption lifetime measurements made at selected wavelengths, highlighted as grey bars in the left hand figure. The red traces indicate mono-exponential fits to these measurements with corresponding lifetimes displayed in each panel. Recorded in chloroform, λ_{ex} = 355 nm.....48
Figure 2.26: Transient absorption spectra of complexes C1a, C5a and C6a. The spectra show qualitatively similar features. Recorded in chloroform; λ_{ex} = 355 nm. 49
Figure 2.27: Clockwise from top left: The upconversion fluorescence of C1a, C2a, C7a and C5a as photosensitisers in toluene. DPA was used as the acceptor. excitation was achieved with a continuous laser at l = 510 nm and power density of 5.2 mW under a deaerated atmosphere. c(sensitiser) = 1.0x10^{-5} M; c(DPA) = 1.6x10^{-3}, 1.6x10^{-3}, 2.6x10^{-4} and 2.0x10^{-4} M, respectively; 20 ˚C.....50
Figure 2.28: Photographs of the emission of selected triplet sensitisers C1a, C2a and C5a alone and the upconversion with DPA in toluene. Excitation was achieved with a continuous laser of λ = 510 nm and power density of 5.2 mW under a deaerated atmosphere. c(sensitisers) = 1x10^{-5} M; c(DPA) = a) 1.6x10^{-3}, b) 1.6x10^{-3} and c) 2.0x10^{-4} M; 20 ˚C.....51
Figure 3.1: Typical structure of an OLED device.[13] 67
Figure 3.2: Jablonksi diagram illustrating the transition from a ^{3}MLCT state to the ground state.[14] 68
Figure 3.3: Examples of transition metal complexes used as dopants in OLED devices.[19–21].....68
Figure 3.4: Structure and emission properties of fac-[Ir(ppy)$_3$] 69
Figure 3.5: Ancillary ligands used in bis-cyclometallated iridium complexes.[30] Top) L-R) Acetylacetone, picolinic acid and N-methylsalicylimine. Bottom) Substituted acetylacetone ligands.[29] 70
Figure 3.6: Recent neutral iridium(III) complexes synthesised for OLED applications.....70
Figure 3.7: Transition metal complexes with a picolinic acid ligand. 71
Figure 3.8: From left to right) Blue-, green- and red-emitting complexes of iridium(III) with a picolinic acid ligand.[36–38] 72
Figure 3.9: Structures of neutral bis-cyclometallated iridium(III) complexes of formula [Ir(L)$_2$(pic)] 74
Figure 3.10:Structures of neutral bis-cyclometallated iridium(III) complexes of formula [Ir(L)$_2$(pyz)].....74
Figure 3.11: Comparison of the proton NMR spectra of C1b (black) and a cationic complex from chapter 2 bearing the same C^N ligand. 76

Figure 3.12: Inequivalency of protons ortho- to cyclometallating site. Circled signals correspond to proton highlighted in red. 77
Figure 3.13: High-resolution mass spectrum recorded for C4c. Spectrum shows molecular ion peak, fragments and a sodium adduct. 79
Figure 3.14: Cyclic voltammogram recorded for complex C1b in DCM with NH_4PF_6 as electrolyte. Potential reported relative to Ag/Ag^+ electrode. Fc/Fc^+ used as internal reference at +0.46 V. Scanning rate of 200 mV s^{-1}. 81
Figure 3.15: Left) UV-vis absorption spectra recorded for complexes C1b-7b. All samples recorded in chloroform at 10^{-5} M. 82
Figure 3.16: UV-vis absorption spectra recorded for complexes C2c, C4c, C5c and C7c. All samples recorded in chloroform at 10^{-5}M. 83
Figure 3.17: UV-vis spectra showing the effect of ancillary ligand. Black) Neutral complex with L2 and picolinic acid ligand. Red) Neutral complex with L2 and pyrazinoic acid ligand. Blue) Cationic complex with L2 and 2,2'-bipyridine ligand. 84
Figure 3.18: Normalised emission spectra recorded for complexes C1b-7b in aerated $CHCl_3$, λ_{ex} = 495 nm. 85
Figure 3.19: Normalised emission spectra recorded for complexes C2c, C4c, C5c and C7c in aerated $CHCl_3$, λ_{ex} = 495 nm. 85
Figure 3.20: Overlaid absorption spectra of complexes bearing L2 with different ancillary ligands. 86
Figure 3.21: Absorption and emission spectra for complex C1b illustrating the Stokes shift. ... 87
Figure 3.22: Overlaid emission spectra of all complexesin this chapter, combined with the emission spectra of cationic complexes C1a-7a from chapter 2. 88
Figure 3.23: UV-vis absorption spectra recorded for complex C2c in different solvents. All spectra recorded at a concentration of 10^{-5} M. 92
Figure 3.24: Emission spectra recorded for complex C2c in different solvents, showing positive solvatochromism. λ_{ex} = 495 nm. 93
Figure 3.25: Comparison of experimental emission spectrum (red) and simulated emission spectrum (black) of complex C1b. 95
Figure 3.26: Left) TA spectra recorded for picolinate complexes C1b-7b. Right) TA spectra recorded for pyrazinoate complexes C2c, C5c and C7c 97
Figure 4.1: Illustration of electromagnetic spectrum from ultraviolet to infrared region. 108
Figure 4.2: Examples of NIR-emitting iridium(III) complexes with OLED applications.[10–12] 109
Figure 4.3: Conjugation and addition of heteroatoms results in a bathochromic shift in emission wavelength.[8] 109
Figure 4.4: Near-IR emitting complexes with simpler cyclometallating ligands.[16,18,19] 110
Figure 4.5: Proton NMR spectrum recorded for ligand HL4 in $CDCl_3$. Selected proton assignments are shown in circles. 113
Figure 4.6: Packing diagram for ligand HL3 obtained from crystal data. Ellipsoids are drawn at 50 % probability. 114
Figure 4.7: X-ray structure of ligand HL3. Ellipsoids drawn at 50 % probability. Crystal data: $C_{24}H_{14}Br_2N_2$, Mr = 490.19, monoclinic, P21/n (No. 14), a - 5.7963(2) Å, b = 21.8021(9) Å, c = 15.1661(6) Å, β = 91.211(3)˚, α = γ = 90 ˚, V = 1916.15(13) Å3, T = 100(2) K, Z = 4, Z' = 1, μ(MoKα) = 4.243 mm-1, 19907 reflections measured, 4396 unique (Rint = 0.0501) which were used in all calculations. The final wR2 was 0.1219 (all data) and R1 was 0.0491 (I>2(I)). 114
Figure 4.8: Structures and yields of complexes synthesised in this study. 116
Figure 4.9: High-resolution mass spectrum recorded for complex C3. 117

Figure 4.10: Observed mass spectromegtry data for complex C3 compared with theoretical data for the same complex. 118
Figure 4.11: Proton NMR spectrum recorded for complex C1 showing the signal arising from proton adjacent to cyclometallating site. Recorded in $CDCl_3$, 400 MHz. 118
Figure 4.12: UV-Vis absorption spectra recorded for ligands HL1-4. Recorded in $CHCl_3$ at $1x10^{-5}$ M 119
Figure 4.13: Emission spectra recorded for ligands HL1-4. Recorded as chloroform solutions, λ_{ex} = 400 nm. 120
Figure 4.14: UV-vis absorption spectra recorded for complexes C1-4. Recorded as solutions in chloroform at $1x10^{-5}$ M 121
Figure 4.15: Overlaid absorption spectra of complex C1 (black) and ligand HL1 (red) showing additional bands observed in complex. 122
Figure 4.16: Visible emission spectra for complexes C1-4. Recorded in aerated $CHCl_3$, λ_{ex} = 470 nm. 123
Figure 4.17: Steady state near-IR emission spectra pf the complexes. The peak at 1274 nm is due to the photogeneration of, and subsequent emission from, $^1O_2$. (Aerated $CHCl_3$, λ_{ex} = 505 nm) 124
Figure 4.18: A comparison of the calculated geometries of the singlet and triplet excited states for complex C3 (left, RMSD = 0.185 Å) and C4 (right, RMSD = 0.149 Å). 125
Figure 4.19: Franck - Condon simulation of the L1 A-X transition (blue), overlaid against the experimental emission spectra of the free ligand HL1 (red) and the complex C1 (black). The spectra are offset by their respective vibronic origin, and are displayed as emission energy (cm^{-1}) relative to zero. The grey bars show different vibronic features. 127
Figure 5.1: Left) Dibenzodioxin structure. Right) Cytotoxic derivative of dibenzodioxin.[5] 136
Figure 5.2: Examples of dicyanodibenzodioxin based compounds.[3] 137
Figure 5.3: Structures of chelating ligands dppz and tatpp alongside the hypothetical structures of dicyanodibenzodioxin ligands. 138
Figure 5.4: Examples of ruthenium(II) complexes with dppz and tatpp ligands.[12] 139
Figure 5.5: Rhenium(I) tricarbonyl complexes bearing dppz and hypothetical tatpp based structures 139
Figure 5.6: Structures and photophysical properties of simple tricarbonylrhenium(I) complexes. From left to right: $[Re(bpy)(CO)_3Cl]$,[22] $[Re(phen)(CO)_3Cl]$,[23] and $[Re(dppz)(CO)_3Cl]$[24,25]. 140
Figure 5.7: Examples of rhenium(I) complexes designed as OLED dopants 141
Figure 5.8: Structures of complexes used as photocatalysts for the reduction of CO_2 to CO. From left to right: $[Re(bpy)(CO)_3Cl]$,[29] $[Re(bpy)(CO)_3\{P(OEt)_3\}]$,[30] and $[Re(PyNHC\text{-}PhCF_3)(CO)_3Br]$.[31] 142
Figure 5.9: Recently published complexes for photocatalytic applications. Left) Nanographene-complexes reported by Qiao et al.[32] Right) Diatomic Ru(II)-Re(I) complex used as part of a supramolecular photocatalyst by Kamata et al.[33] 142
Figure 5.10: Some of the first examples of tricarbonylrhenium(I) complexes studied as biological imaging agents reported.[34] 143
Figure 5.11: Biological imaging agents of Re(I) incorporating biological substrates 144
Figure 5.12: Rhenium(I) complexes developed as bioimaging agents.[37,38] 145
Figure 5.13: Proton NMR spectrum recorded for ligand L1 in deuterated DMSO with assignments for each proton. 148
Figure 5.14: Fluorine NMR spectrum recorded for ligand L1 in deuterated DMSO 149
Figure 5.15: Carbon NMR spectrum recorded for ligand L1 in deuterated DMSO. 149
Figure 5.16: FTIR ATR spectrum recorded for ligand L1. Inset) HRMS data for L1 showing the molecular ion peak at 337.1096 amu. 150

Figure 5.17: Proton NMR spectrum recorded for ligand L2 in deuterated DMSO. 152
Figure 5.18: High resolution mass spectrum recorded for ligand L2 showing [M + H] peak. Peak for starting material is absent. 153
Figure 5.19: Structures and yields of tricarbonylrhenium complexes synthesised. 155
Figure 5.20: Proton NMR spectrum recorded for $[Re(CO)_3(L3)Br]$. 156
Figure 5.21: High-resolution mass spectrum of complex $[Re(CO)_3(L1)Br]$ showing sodium adduct, [M + Na]. 157
Figure 5.22: Structures and yields of cationic complexes with ligands L1 – L4. 159
Figure 5.23: Proton NMR data for cationic complex $[Re(CO)_3(L4)(MeCN)][BF_4]$. 159
Figure 5.24: Carbon NMR spectrum recorded for complex $[Re(CO)_3(L3)(MeCN)][BF_4]$ in deuterated DMSO. 160
Figure 5.25: Crystal structure of complex $[Re(CO)_3(L3)(MeCN)][BF_4]$. 160
Figure 5.26: Examples of similar dioxin compounds from literature along with relevant photophysical data.[3,43,44] 163
Figure 5.27: UV-vis absorption spectra recorded for ligands L1-4. Measured in $CHCl_3$ at a concentration of $1x10^{-5}$ M. 164
Figure 5.28: Normalised emission spectra recorded for ligands L1-4. Spectra recorded on $CHCl_3$ at room temperature. 165
Figure 5.29: UV-vis absorption spectra recorded for neutral complexes fac-$[Re(CO)_3(L)Br]$. Samples recorded in $CHCl_3$ at concentration of $1x10^{-5}$ M. 166
Figure 5.30: Left) UV/vis absorption data recorded for complex $[Re(CO)_3(L1)Br]$. Right) UV-vis data from literature for complex $[Re(CO)_3(dppz\text{-}F_2)Cl]$.[16] 167
Figure 5.31: Steady state emission spectra recorded for complexes fac-$[Re(CO)_3(L)Br]$ in $CHCl_3$. 168
Figure 5.32: UV-vis absorption spectra recorded for cationic complexes fac-$[Re(CO)_3(L)(MeCN)][BF_4]$. Recorded in MeCN at concentration $1x10^{-5}$ M. 169
Figure 5.33: Steady state emission spectra recorded for complexes fac-$[Re(CO)_3(L)(MeCN)][BF_4]$. Measured in MeCN at room temperature. 170
Figure 5.34: Steady state emission spectra recorded for complex fac-$[Re(CO)_3(L3)(MeCN)][BF_4]$ in MeCN using different excitation wavelengths. 171
Figure 5.35: Steady state emission sprectrum of complex fac-$[Re(CO)_3(L3)(MeCN)][BF_4]$ recorded in different solvents using an excitation wavelength of 420 nm. 172
Figure 6.1: Crystal structure obtained by single crystal x-ray diffraction. 184

Table of Schemes

Scheme 2.1: Synthesis scheme of ligands HL1-7 30
Scheme 2.2: General scheme for synthesis of cationic iridium(III) complexes. 32
Scheme 3.1: Synthesis of cyclometallating ligands used in this study. 73
Scheme 3.2: Synthesis of neutral bis-cyclometallated complexes from chloro-bridged iridium(III) dimer species. 73
Scheme 3.3:Alternative synthetic route to complex C2c 75
Scheme 4.1: Synthesis scheme for ligands HL1-4. 112
Scheme 4.2: Synthesis of bis-cyclometallated irdidium(III) complexes. 116
Scheme 5.1: Synthesis of dicyanodibenzodioxins.[1] 137
Scheme 5.2: Proposed route to formation of second dioxin bridge. Where **A** is an aromatic diol and **B** is tetrafluoroterephthalonitrile. 137

Scheme 5.3: Synthesis of 1,10-phenanthroline-5,6-diol from 1,10-phenanthroline. 147
Scheme 5.4: Synthesis of ligand L1 from 1,10-phenanthroline-5,6-diol. 147
Scheme 5.5: Synthesis of ligands L2, L3 and L4. 151
Scheme 5.6: Proposed synthetic route to tattp dicyanodibenzodioxin analogue. 154
Scheme 5.7: Alternative route to bridging dicyanodibenzodioxin ligand. 154
Scheme 5.8: Synthesis of rhenium complex from dioxin ligand. 155
Scheme 5.9: Ligand exchange to give cationic complexes. 158
Scheme 6.1: Proposed synthesis of bis-cyclometallated iridium(III) complexes with dioxin-based ligands. 183

Table of Tables

Table 2.1: Fluorine NMR data including chemical shift values and coupling constants. 34
Table 2.2: Selected bonds lengths for complexes C2a, C5a and C7a. 36
Table 2.3: Selected bond angles for complexes C2a, C5a and C7a. 36
Table 2.4: Excitation contributions to the lowest lying singlet excited states of complex C1. Only single electron excitation contributions greater than 10 % are shown. Q1 and Q2 pertain to the two quinoxaline ligands. 44
Table 2.5: Computed spectral properties for all complexes; experimentally observed band positions are given in parentheses. Values in italic are those calculated for an adiabatic system. The experimental spin-allowed absorption band positions are taken from the band onsets, whereas the spin-forbidden parameters are λmax value. (a) Recorded in chloroform. (b) Recorded in chloroform; λ_{ex} = 355 nm. 45
Table 2.6: Photophysical data for complexes C1a-C7a. 47
Table 2.7: Emission and upconversion data of the complexes recorded in toluene. 50
Table 3.1: Tabulated fluorine NMR data for fluorinated complexes C4b, C7b, C4c and C7c compared with free ligand and cationic counterparts. 77
Table 3.2: Redox potentials for all complexes in this chapter. Cyclic voltammogramms recorded in DCM with NH_4PF_6 as an electrolyte. Scanning rate of 200 mV s^{-1} used. Values reported relative to Ag/Ag+ electrode with ferrocene as a reference. 80
Table 3.3: UV-vis absorption data collected for all complexes in $CHCl_3$ at $1x10^{-5}$ M. 81
Table 3.4: Luminescent lifetimes recorded for neutral iridium(III) complexes. λ_{ex} = 295 nm, recorded in aerated $CHCl_3$ 88
Table 3.5: A table listing the effect of ancillary ligand upon the luminescence lifetime of complexes with the same cyclometallating ligands. λ_{ex} = 295 nm, all samples recorded in $CHCl_3$ 89
Table 3.6: Quantum yield values for all complexes with $[Ru(bpy)_3][PF_6]_2$ as a standard. (Φ_Δ = 0.018 in acetonitrile.[47] 89
Table 3.7: Photophysical data collected for all neutral complexes. 90
Table 3.8: Emission and lifetime data recorded for complex C8 in different solvents along with their dielectric constants. [a] - l_{ex} = 495 nm, [b] - l_{ex} = 295 nm. 94
Table 3.9: A summary of the calculated percentage contributions to each MO from each part of the complex. Q1 and Q2 refer to the inequivalent quinoxaline ligands 94
Table 3.10: Absorption and emission values calculated for each complex. Experimental values for $T_1 \rightarrow S_0$ are written in parentheses. 96
Table 4.1: Selected bond length data for compound HL3. 115
Table 4.2: Selected bond angles for compound HL3. 115

Table 4.3: Comparison of literature UV-vis absorption spectra with data recorded in this study for complex C1. 121
Table 4.4: Photophysical data recorded for ligands HL1-4 and complexes C1-4. [a] Recorded in aerated CHCl3; [b] λex = 405 nm; [c] λex = 295 nm; [d] λex = 505 nm; [e] λex = 355 nm 124
Table 4.5: Comparison of data recorded for complex C1 with data previously recorded for the same complex. * Lifetime stated is intrinsic lifetime, τ_0 125
Table 4.6: Calculated HOMO and LUMO contributions for each complex. 126
Table 4.7: Calculated vertical transitions for complexes C1-4 126
Table 5.1: Positions of nitrile stretch in infrared spectrum for ligands L1 - L4. 154
Table 5.2: Position of metal carbonyl stretches in the neutral rhenium complexes with dicyanodibenzodioxin ligands. 157
Table 5.3: Data collection parameters for complex $[Re(CO)_3(L3)(MeCN)][BF_4]$. 161
Table 5.4: Selected bond lengths for the coordination sphere or complex $[Re(CO)_3(L3)(MeCN)][BF_4]$ 161
Table 5.5: Selected bond angles in the coordination sphere of $[Re(CO)_3(L3)(MeCN)][BF_4]$ 162
Table 5.6: Carbonyl infrared stretches for cationic rhenium complexes 163
Table 5.7: Photophysical data for ligands L1-4. 165
Table 5.8: Photophysical data for fac-$[Re(CO)_3(L)Br]$ complexes. 168
Table 5.9: Luminescence lifetimes recorded for complexes fac-$[Re(CO)_3(L)(MeCN)][BF_4]$.Measurements recorded in MeCN at room temperature, λ_{ex} = 295 nm. 171
Table 5.10: Luminescence lifetimes recorded for complex fac-$[Re(CO)_3(L3)(MeCN)][PF_6]$ in different solvents. Measurements ecorded at room temperature, $\lambda_{ex} = 295$ nm. 173
Table 6.1: Crystal data collection parameters for iridium complex with dicyanodibenzodioxin ligand 184

Table of Equations

Equation 1.1 5
Equation 1.2 5
Equation 1.3 5
Equation 1.4 6
Equation 1.5 7
Equation 1.6 8
Equation 1.7 8
Equation 1.8 9

Abbreviations

Spectroscopy and Techniques

ATR – Attenuated Total Reflectance

FT – Fourier Transform

IR – Infrared

UV-vis – Ultraviolet – Visible

UV – Ultraviolet

NMR – Nuclear Magnetic Resonance

MS – Mass Spectrometry

LR – Low Resolution

HR – High Resolution

TLC – Thin Layer Chromatography

CV – Cyclic Voltammetry

TD – Time Dependent

DFT – Density Functional Theory

TA – Transient Absorption

2D – Two Dimensional

3D – Three Dimensional

m/z – Mass/Charge Ratio

δ – Chemical Shift

ppm – Parts Per Million

s – Singlet

d – Doublet

t – Triplet

q – Quartet

m – Multiplet

$\{^1H\}$ – Proton Decoupled

λ – Wavelength

nm – nanometre

s – Seconds

ms – milliseconds

μs – Microseconds

ns - Nanoseconds

Photophysical and Chemical Properties

IC – Internal Conversion

ISC – Intersystem Crossing

SOC – Spin Orbit Coupling

LED – Light Emitting Diode

OLED – Organic Light Emitting Diode

MC – Metal Centred

IL – Intra Ligand

CT – Charge Transfer

ILCT – Intraligand Charge Transfer

MLCT – Metal-to-Ligand Charge Transfer

^{3}MLCT – Triplet Metal-to-Ligand Charge Transfer

LLCT – Ligand-to-Ligand Charge Transfer

HOMO – Highest Occupied Molecular Orbital

LUMO – Lowest Unoccupied Molecular Orbital

abs – Absorption

em – Emission

exc – Excitation

τ – Lifetime

Φ – Quantum Yield

S_0 – Singlet Ground State

S_1 – First Singlet Excited State

T_1 – First Triplet Excited State

RET – Resonance Energy Transfer

FRET – Förster Resonance Energy Transfer

Solvents and Chemicals

DCM – Dichloromethane

DMF – Dimethylformamide

DMSO – Dimethylsulfoxide

THF – Tetrahydrofuran

MeCN – Acetonitrile

EtOH – Ethanol

$CHCl_3$ – Chloroform

^{t}Bu – Tert-butyl

bpy – 2,2'-bipyridine

phen – 1,10-phenanthroline

Me – Methyl

Et – Ethyl

Ph - Phenyl

pic – Picolinate

pyz – Pyrazinoate

acac – Acetylacetone

L – Ligand

DNA – Deoxyribosenucleic acid

H_2SO_4 – Sulfuric Acid

HCl – Hydrochloric Acid

HNO_3 – Nitric Acid

MeOH – Methanol

$MgSO_4$ – Magnesium Sulfate

K_2CO_3 – Potassium Carbonate

$AgBF_4$ – Silver Tetrafluoroborate

NH_4PF_6 – Ammonium Hexafluorophosphate

NaOH – Sodium Hydroxide

NaBr – Sodium Bromide

1. Introduction

1.1. Introduction

The work in this thesis focuses upon the synthesis and characterisation of novel luminescent transition metal complexes. A large part of the analysis of these complexes is centred upon the photophysical properties that they exhibit. Therefore, this chapter provides an introduction to the phenomena of luminescence and phosphorescence as well as properties such as lifetime and quantum yield which are discussed in detail in later chapters. Furthermore, examples of well-known and more recent luminescent transition metal complexes will be discussed as well as their potential applications.

1.2. Luminescence

1.2.1. The Jablonski Diagram

The phenomenon of luminescence is described as the spontaneous emission of light from a substance and was first described in 1888.[1] Luminescence can be split into two different categories – fluorescence and phosphorescence – depending upon the emitting state of the compound. The differences between these processes can be more clearly understood by use of a Jablonski diagram such as that shown in Figure 1.1. The Jablonski diagram was first proposed by Prof. Alexander Jablonski in 1935 and describes the absorption and emission processes that can occur in a luminescent species.[2]

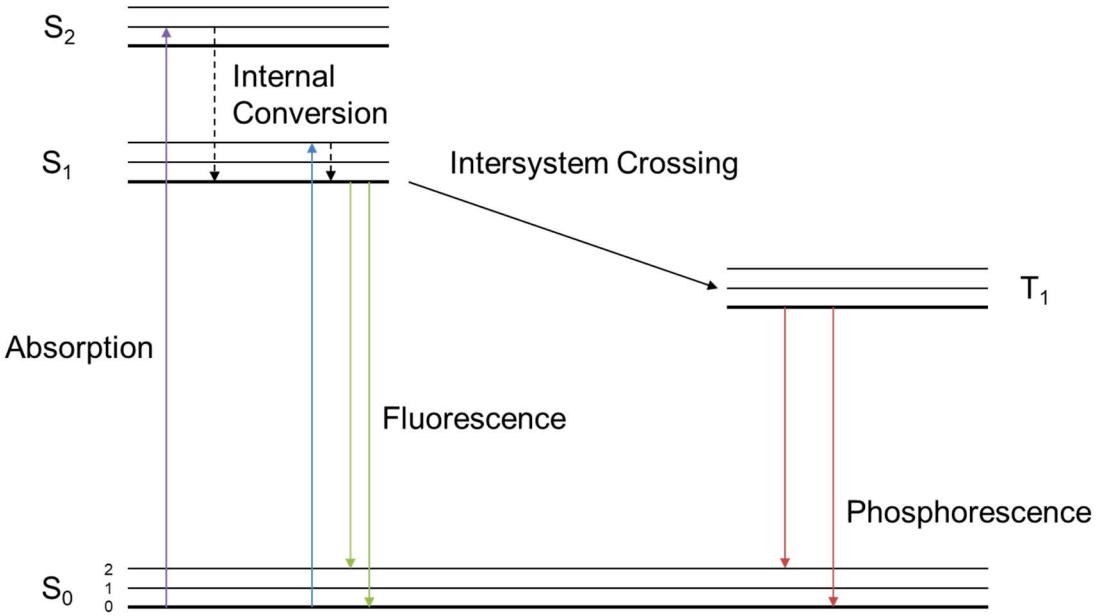

Figure 1.1: Jablonski diagram

The processes shown in the diagram include:

- **Absorption** – The absorption of light excites an electron from the ground state, S_0, into a higher energy excited state, S_1 or S_2.
- **Internal Conversion** – A non-radiative process that involves the fast relaxation to the lowest energy vibrational level of S_1.
- **Fluorescence** – The emission of light from a singlet excited state, S_1.
- **Intersystem Crossing** – This is a spin conversion process from singlet state S_1 to triplet state T_1.
- **Phosphorescence** – The emission of light from an excited triplet state, T_1.

In addition to these processes, it is also worth noting that there are additional non-radiative pathways in which an electron can relax back to the ground state S_0.

Fluorescence is a very fast process with lifetimes of typically 10^{-9} – 10^{-6} s. These short lifetimes are a consequence of the spin selection rule; as there is no change in quantum spin number from S_1 to S_0, fluorescence is formally spin-allowed and relaxation occurs rapidly.[3] Conversely, phosphorescence lifetimes are relatively much longer and can extend to >100 s. This is because the spin selection rule is broken in phosphorescence as the spin quantum number must change between T_1 and S_0.

1.2.2. The Stokes Shift

The energy of luminescent emission from a species is lower than the energy of absorption. This is due to energy being lost through non-radiative processes such as internal conversion and intersystem crossing before the fluorescence or phosphorescence emission. The difference in energy between the absorption and emission is known as the Stokes shift and was first reported by G. G. Stokes in the mid nineteenth century.[4]

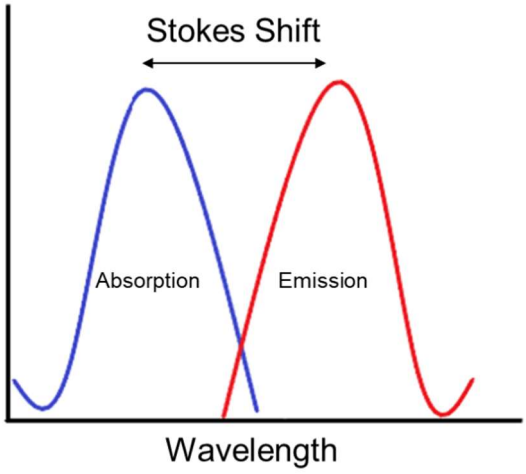

Figure 1.2: Diagram showing the Stokes shift.

1.2.3. Kasha's Rule

The processes of internal conversion and, where applicable, intersystem crossing cause emission only to occur from the lowest energy excited state of a luminescent molecule. As a result of this, emission profiles are usually independent of the wavelength of light used to excite the species,

meaning that the emission spectrum will look identical regardless of the energy of the incident light. This is known as Kasha's rule, named for Michael Kasha who first reported the phenomenon in 1950.[5]

Many exceptions to this rule have been reported through the years, however a recent study reassessed a number of these anomalies and found all but one of their studied compounds, azulene, do obey Kasha's rule. The majority of the previously reported exceptions to the rule were found to be either impure samples or molecular systems in the gas phase with insufficiently coupled vibrational relaxation.[6]

1.2.4. Quantum Yield and Luminescence Lifetime

The photoluminescence quantum yield, Φ, is a measurement of how efficiently a luminescent molecule converts absorbed light into emitted light and is essentially the ratio of photons emitted to photons absorbed. The quantum yield is described in Equation 1.1. The equation shows that the quantum yield, Φ, is equal to the rate of emission, Γ, divided by the sum of emissive and non-emissive processes, k_{nr}.[7]

$$\Phi = \frac{\Gamma}{\Gamma + k_{nr}}$$

Equation 1.1

Examples of compounds that exhibit very high quantum yield values include rhodamine dyes,[8,9] 9,10-diphenylanthracene,[10] and fluorescein.[11] The structures of these compounds along with their quantum yield values are shown in Figure 1.3.

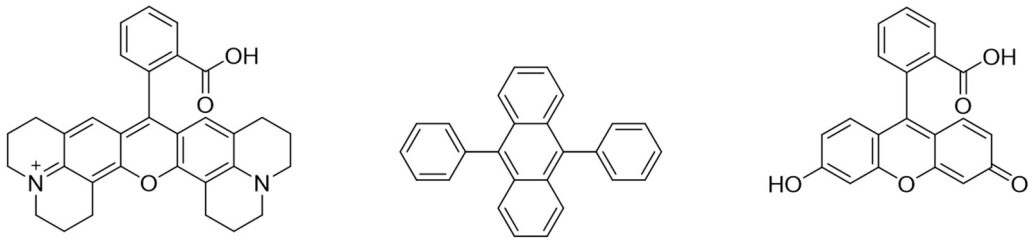

Rhodamine 101 Φ = 1.00 | 9,10-diphenylanthracene Φ = 0.90 | Fluorescein Φ = 0.95

Figure 1.3: The structures and quantum yields of fluorophores rhodamine 101,[9] 9,10-diphenylanthracene,[10] and fluorescein.[11]

Another important property of a luminescent molecule is the luminescence lifetime, τ. This is the average amount of time that the compound spends in the excited state before relaxing back into the ground state.[7] As fluorescence is a random process, not every molecule will spend the same amount of time in the excited state. The lifetime is related to the rate of fluorescence by the following equation:

$$\tau = \frac{1}{\Gamma + k_{nr}}$$

Equation 1.2

Once the rate of fluorescence, Γ, has been calculated or measured, it is possible to calculate the natural lifetime, τ_n, of the lumophore. The natural lifetime is the average amount of time spent in the excited state in the absence of any non-radiative processes, k_{nr}.

$$\tau_n = \frac{1}{\Gamma}$$

Equation 1.3

The natural lifetime can also be calculated from the quantum yield value and the measured lifetime. This relationship is shown in Equation 1.4.

$$\tau_n = \frac{\tau}{\Phi}$$

Equation 1.4

A high rate of internal conversion can lower the quantum yield of a luminescent molecule as it contributes to the non-radiative processes. In particular, aromatic compounds containing nitro groups typically have large k_{nr} values, and as a result, are weakly emissive. Also, heavy atoms, such as chlorine, can facilitate intersystem system crossing which also leads to lower rates of emission.[7]

1.2.5. Luminescence Quenching

Quenching is described as any process that decreases the intensity of luminescent emission from a species.[7] The different forms of luminescence quenching are discussed below.

1.2.5.1. Collisional Quenching

Collisional quenching occurs when a luminescent molecule collides with another molecule, known as a quencher, in solution. The collisional quenching pathway is illustrated in the Jablonski diagram in Figure 1.4.

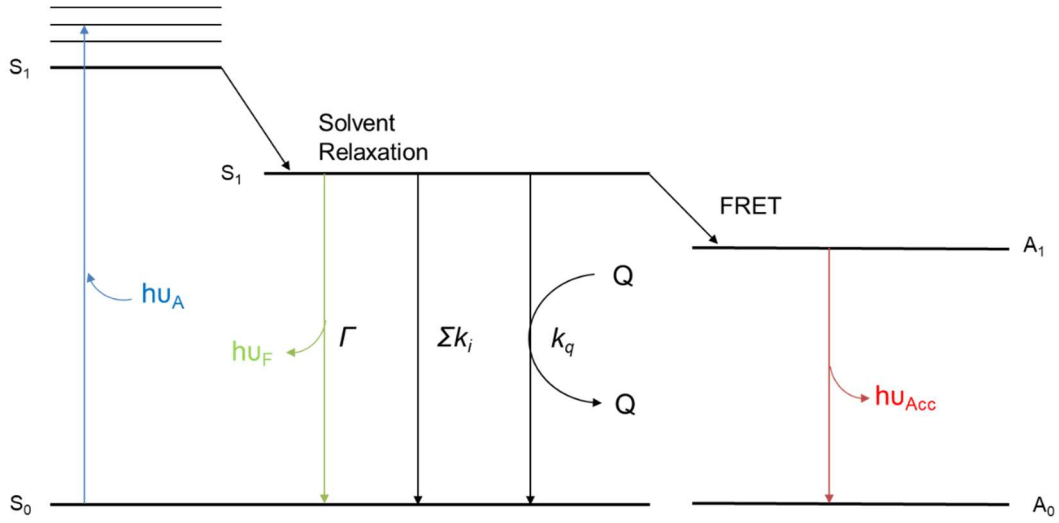

Figure 1.4: Jablonski diagram illustrating the radiative and non-radiative processes involved in collisional quenching. Where FRET is fluorescence energy transfer to an acceptor molecule, A, and Σk_i is the sum of all non-radiative processes except for quenching, k_q.

The process of collisional quenching is described in the Stern-Volmer equation, shown below (Equation 1.5). The terms F_0 and F refer to the fluorescence intensity in the absence and in the presence of a quencher respectively, and [Q] is the concentration of the quencher species. The lifetime in the absence of quencher species is termed τ_0 and k_q is the rate of quenching. Together, these terms make up the Stern-Volmer quenching constant, *K,* and represent the sensitivity of a species towards a quencher.

$$\frac{F_0}{F} = 1 + K[Q] = 1 + \ k_q \tau_0 [Q]$$

Equation 1.5

Molecules that can act as collisional quenchers include oxygen,[12–14] halogens,[15,16] and amines.[17–19] The mechanisms of quenching differ between species, for example, heavy atoms such as halogens are good quencher species due to spin-orbit coupling.[7]

1.2.5.2. Static Quenching

Static quenching is a form of quenching that occurs in the ground state independently of diffusion or collisions. One such type of quenching occurs when the lumophore forms a non-fluorescent complex with another compound.[7,20] An example of this is observed in the interaction between the copper complex and the amino acid shown in Figure 1.5. The fluorescence from the dansyl(DNS)-amino acid on the right of the figure was found to be quenched upon binding to the copper complex on the left. This was reported by Corradini *et al.* in 1992.[21]

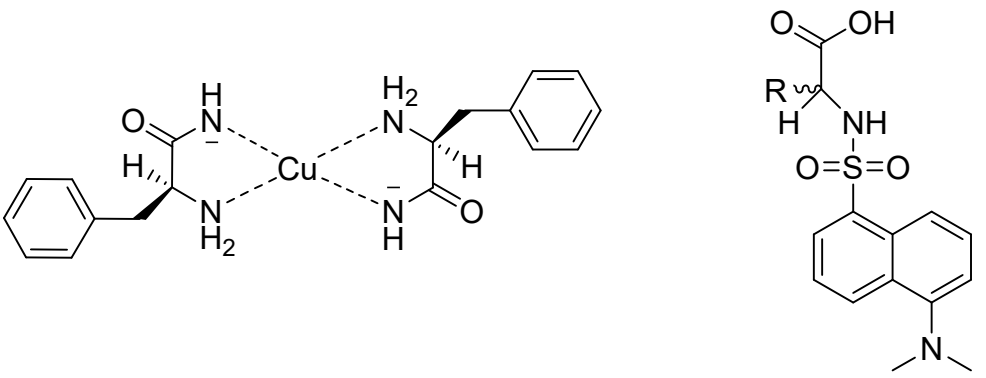

Figure 1.5: The copper(II) complex on the left was found to quench the fluorescence of the dansyl(DNS)-amino acid by static quenching.[21]

1.2.6. Solvent Relaxation

Molecules of solvent can also have an effect upon the wavelength of emission. Solvent molecules can arrange themselves around the excited state dipole of the lumophore (which is often larger than that in the ground state). This can stabilise the excited state, lowering the energy and causing a bathochromic shift in emission. [22]

1.2.7. Resonance Energy Transfer

Resonance energy transfer, RET, is another non-radiative process that can occur. This happens when there is an overlap between the emission spectrum of the lumophore, known as the

donor, and the absorption spectrum of another molecule, known as the acceptor.[23] The acceptor molecule does not need to be luminescent itself and the process does not involve the emission of light from the donor. Instead, a dipole-dipole interaction couples the donor and acceptor molecules. As a result of this, it is the distance between the donor and acceptor molecules that determines the extent of energy transfer. The rate of energy transfer, $k_T(r)$, is calculated using Equation 1.6 where R_0 describes the spectral overlap between donor and acceptor, τ_D is the lifetime of the donor in the absence of the acceptor and r is the distance between the donor and acceptor molecules.

$$k_T(r) = \frac{1}{\tau_D}\left(\frac{R_0}{r}\right)^6$$

Equation 1.6

The efficiency of this process between a donor and acceptor molecule at a fixed distance apart is described in Equation 1.7. These equations clearly show that this process is highly dependent upon the factor r.

$$E = \frac{{R_0}^6}{{R_0}^6 + r^6}$$

Equation 1.7

This sort of energy transfer has been made use of in the field of analytical biochemistry. It allows for the measurement of distances between 10 - 100 Å and as such has been implemented as a "spectroscopic ruler" in determining the distance between important sites in proteins.[24,25]

1.3. Luminescence Measurements

Luminescent properties are measured using a luminescence spectrometer. There are two types of luminescent measurement that can be obtained from a fluorescence spectrometer, steady state and time-dependent measurements.

1.3.1. Steady State Measurements

Steady state measurements are the most common sort of measurements taken. They involve the constant illumination of the sample by light and the emission intensity is measured. Steady state of the sample is achieved almost instantaneously due the extremely short lifetimes associated with fluorescence.[7]

1.3.2. Time Resolved Measurements

During a time resolved measurement, the sample is exposed to a short pulse of light and the intensity decay of fluorescence is measured. Typically, the pulse width of the excitation light used is shorter than the time taken for fluorescence to decay. This means that a high-speed detector is required for the measurement of fluorescence on a nanosecond timescale. The fluorescence intensity of a molecule can be described using Equation 1.8 where I_0 is the intensity at time $t = 0$ and τ is the lifetime of the lumophore.[7]

$$I(t) = I_0\, e^{-t/\tau}$$

Equation 1.8

It is also important to note that the steady state and time resolved measurements are linked as the steady state measurement is simply an average of the time resolved events. However, time resolved measurements can provide information that is lost in the averaging process of steady state. Through time resolved measurements it is possible to obtain information on quenching pathways, resonance energy transfer and molecular conformations.

1.4. Recording Spectra

Luminescence spectra are recorded using a luminescence spectrometer. Figure 1.6 shows the typical set up for a luminescence spectrometer. Common light sources that are available include arc xenon lamps, photodiodes and lasers. The optical filters and monochromators process the path of the light and the photomultiplier tube, PMT, detects the output light.

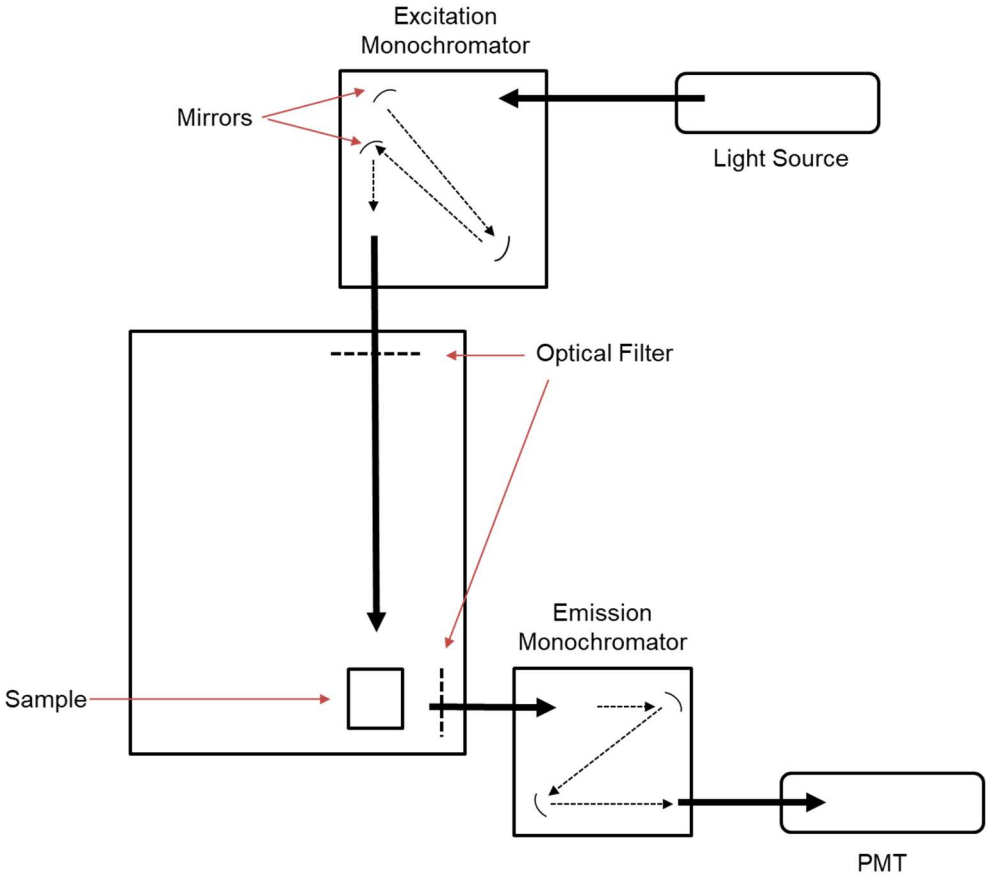

Figure 1.6: Simplified diagram of luminescence spectrometer set-up.

1.4.1. Emission Spectra

To record an emission spectrum an appropriate excitation wavelength, λ_{ex}, must first be chosen. Typically, the wavelength chosen matches the wavelength at which the molecule absorbs light, this can be observed in the UV-vis absorption spectrum which is usually recorded prior to luminescence measurements. Next, a scanning range is chosen using the emission monochromator. It is important to begin the scanning range at a higher wavelength than that used for excitation to avoid damaging the instrument. The spectra are produced as a plot of emission intensity vs. wavelength.

1.4.2. Excitation Spectra

To record an excitation spectrum, the emission monochromator is set to the emission maximum, λ_{em}, which is determined from the emission spectrum. The excitation monochromator scans through wavelengths from around 250 nm up to around 15 nm λ_{em}. The peaks observed in the excitation spectrum are those wavelengths of light that are responsible for the emission peak observed. In general, the excitation spectrum will closely resemble the absorption spectrum of the lumophore.

1.5. Types of Lumophores

1.5.1. Organic Lumophores

The majority of organic fluorophores are aromatic compounds. These compounds are good chromophores and their emission wavelengths can be altered with varying the functional groups and the amount of conjugation in the species. Examples of some polyaromatic lumophores are shown in Figure 1.7.

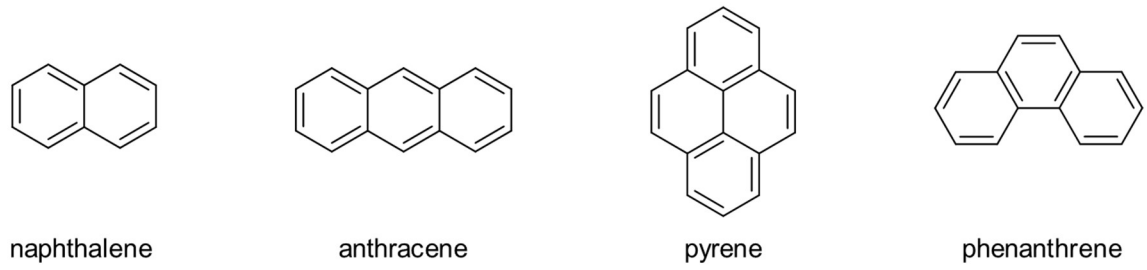

Figure 1.7: Organic fluorophores with a polyaromatic structure.

Due to the aromatic nature of these compounds, the absorption bands arise from a π-π^* transition.[26] The emission arises from a low-lying singlet π^* state and is formally fluorescence. It is known that extending the conjugation of these molecules can bathochromically shift the emission.

The compounds in Figure 1.7 show fluorescence in the UV to blue region of the visible spectrum. But it is known that extending the conjugation of organic fluorophores can cause a bathochromic shift in the emission wavelength. As such, new compounds have been developed to create organic fluorophores that emit at different wavelengths across the whole spectrum from UV to near infra-red wavelengths.

The field of organic fluorophores is still expanding today, and some newer compounds are shown in Figure 1.8. The compound on the left of the image is an example from 2019 which showed emission at around 675 nm in the solid state. In addition to this, when the compound was incorporated into a polyethylene film and heated to different temperatures, the emission wavelength was found to decrease to around 550 nm at temperatures of 80 ˚C and higher.[27] The compound on the right of the image was also reported in 2019. The dye was developed for use as a dopant in organic light emitting diodes, OLEDs, and showed an emission wavelength of around 600 nm in toluene, and a quantum yield value of 57%.[28]

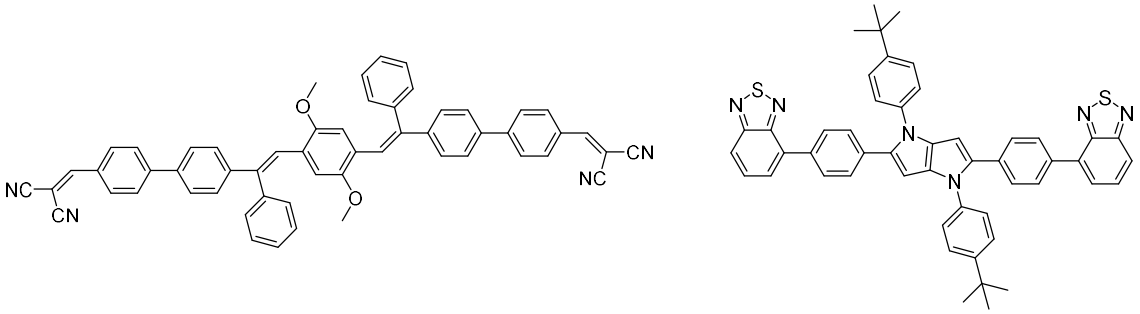

Figure 1.8: Examples of new organic fluorophores.

1.6. Transition Metal Complexes

Transition metal complexes are attractive lumophores as it is possible to tune the electronic properties of these species by carefully choosing the ligand system and the metal to be used. This allows the emitting state of the complex to be pre-determined. The transitions typically expected for a transition metal complex are as follows:

- **Metal Centred (MC)**: These are transitions that occur between the d orbitals of the metal centre, also known as dd transitions.
- **Metal-to-Ligand-Charge-Transfer (MLCT):** Transitions that involve the excitation of a metal centred electron to an anti-bonding (π^*) orbital of the ligand.
- **Intra-Ligand (IL):** The promotion of an electron in a π-bonding or non-bonding orbital of the ligand to an anti-bonding orbital of the same ligand.
- **Ligand-to-Metal-Charge-Transfer (LMCT):** These transitions involve the movement of an electron from the ligand system to the metal centre.[29]

Which of these states is the lowest-lying, and therefore the emitting state, can depend upon the metal centre, the ligand system and the geometry of the complex, making metal complexes ideal starting points for the design of new luminescent compounds for many applications.[30] Some of these applications include chemosensing,[31] biological imaging,[32–34] organic light emitting diodes,[35–37] and as dyes in solar cells.[38–40] Some prominent examples are discussed below along with some newer developments.

1.7. Phosphorescent Transition Metal Complexes

1.7.1. First Row Transition Metal Complexes

First row transition metals have weaker spin-orbit coupling effects and as such, phosphorescence is not commonly observed. While there have been reports of manganese(I) and manganese(II) complexes exhibiting phosphorescence in solid glasses at low temperatures,[41,42] and weak phosphorescence from some nickel(0) complexes in solution,[43,44] the main examples of room temperature phosphorescence have been from complexes of chromium(III) and copper(I).

The emission wavelengths of chromium(III) complexes are typically restricted to the red region of the spectrum due to the small energy gaps between ground and excited states in first row transition metals.[45,46] In the case of copper(I) complexes, the emission is often weak and short-lived. However, multi-nuclear complexes have shown significant room temperature phosphorescence.[47]

Shown in Figure 1.9 are some examples of phosphorescent chromium (III) and copper(I) complexes. The chromium complex on the left of the figure was reported in 2017 by Barbour *et al.* and showed near infra-red emission at 796 nm. In addition to this, the complex also showed a long lifetime of 600 ns.[48] The complex in the centre of Figure 1.9 is a dinuclear copper(I) complex which showed emission at 663 nm, with a lifetime of 16 ns. The authors also reported a low quantum yield value of $1x10^{-4}$.[49] The final copper complex shown is a more recent example and was reported in 2018 by Liu *et al.* The mononuclear complex showed emission at 691 nm, with a lifetime of 750 ns.[50]

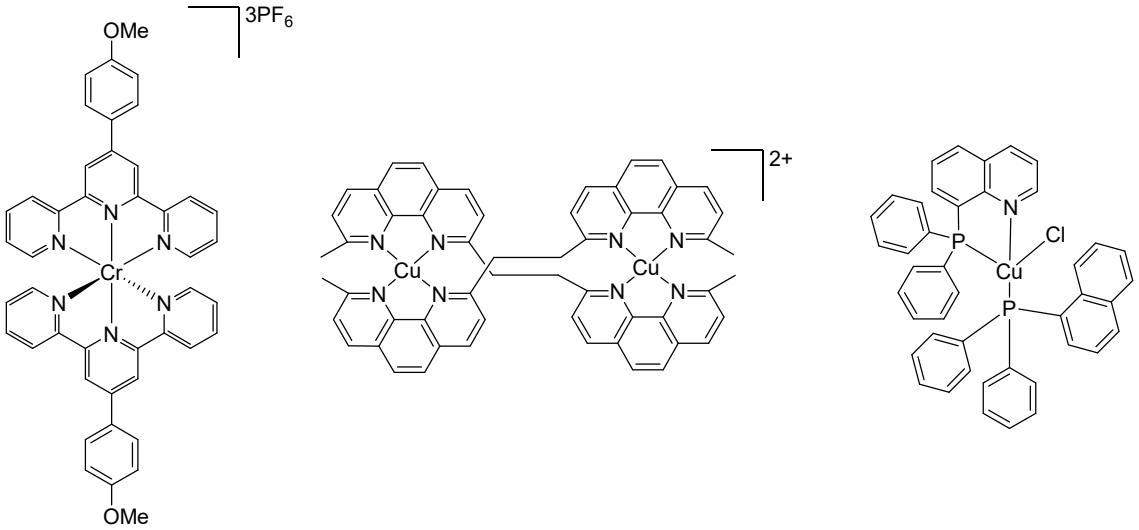

Figure 1.9: Examples of phosphorescent chromium(III) and copper(I) complexes.

More recently, an example of a phosphorescent iron(II) complex was reported by Vogler in 2016.[51] The tetrahedral Fe(II) complex with a binap (2,2'-bis(diphenylphosphino)-1,1'-binaphthyl) ligand showed intraligand phosphorescent emission in the solid state at 505 nm. The structure of this complex is shown in Figure 1.10. Another example of a photoluminescent iron complex was reported by Chábera *et al.* in 2017.[52] The octahedral low-spin d^5 complex was synthesised using the carbene ligand btz (3,3'-dimethyl-1,1'-bis(*p*-tolyl)-4,4'-bis(1,2,3-triazol-5-ylidene)) and showed emission at 600 nm with an emission lifetime of 100 ps. The emission was found to arise from an excited ^{3}LMCT state.

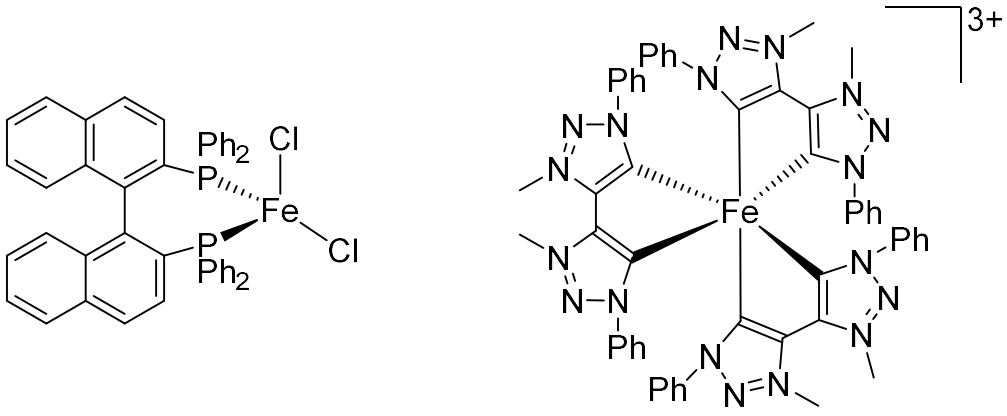

Figure 1.10: Left) Phosphorescent complex of Fe(II) reported by Vogler.[51] Right) Phosphorescent complex of Fe(III) reported by Chábera et al.[52]

1.7.2. Second and Third Row Transition Metal Complexes

The atoms in the second and third rows of the transition metals are heavier than those in the first row and, as a result, cause a stronger spin-orbit coupling effect. This helps to increase the rate of intersystem crossing from a singlet excited state to a triplet excited state. The consequence of this is that room temperature phosphorescence in solution and in the solid state is much more common for complexes of these metals than those of the first row. Furthermore, high quantum yields can be observed as the mixing of singlet and triplet states via spin-orbit coupling eliminates the spin-forbidden nature of the transition from $T_1 \rightarrow S_0$.[29] Phosphorescent complexes of the 2nd and 3rd row transition metals can be characterised by the d electron configuration of the metal.

1.7.2.1. d^6 Configuration

The metals that fall into this category include rhenium(I), ruthenium(II), osmium(II), rhodium(III) and iridium(III). Examples of rhenium(I) and iridium(III) complexes are discussed in detail in later chapters, and as such this introduction will focus only on ruthenium(II), osmium(II) and rhodium(III) complexes.

Complexes of ruthenium(II) with simple polypyridine ligands, such as 2,2'-bipyridine and 1,10-phenanthroline, have been well studied over the last few decades for their photophysical properties.[53,54] It is known that phosphorescence from these complexes arises from a low-lying ^{3}MLCT state and that quantum yields for these complexes typically range between 10^{-1} – 10^{-3} and lifetimes in the microsecond range. In addition to this, it has been noted that ligand tuning is largely inefficient and that the emission from these complexes is almost always in the orange-red region of the spectrum.[54]

Osmium(II) complexes with polypyridine ligands have also been extensively studied. Due to strong back-bonding to the ligands from the osmium centre, the emission lifetimes observed from these complexes are much shorter than from ruthenium(II) complexes and are generally in the order of 10^{-2} μs.[55,56] However, the use of π-acid ligands such as phosphine or arsine alongside polypyridine ligands can extend the lifetime of phosphorescence up to tens of microseconds.[57] Ligand tuning has also been found to be more effective in changing the emission wavelength of Os(II) complexes than in Ru(II) complexes. While complexes such as $[Os(bpy)_3]^{2+}$ and $[Os(phen)_3]^{2+}$ emit in the red to near infra-red region,[58,59] emission can be shifted into the green region of the spectrum by the use of phosphine ligands.[57]

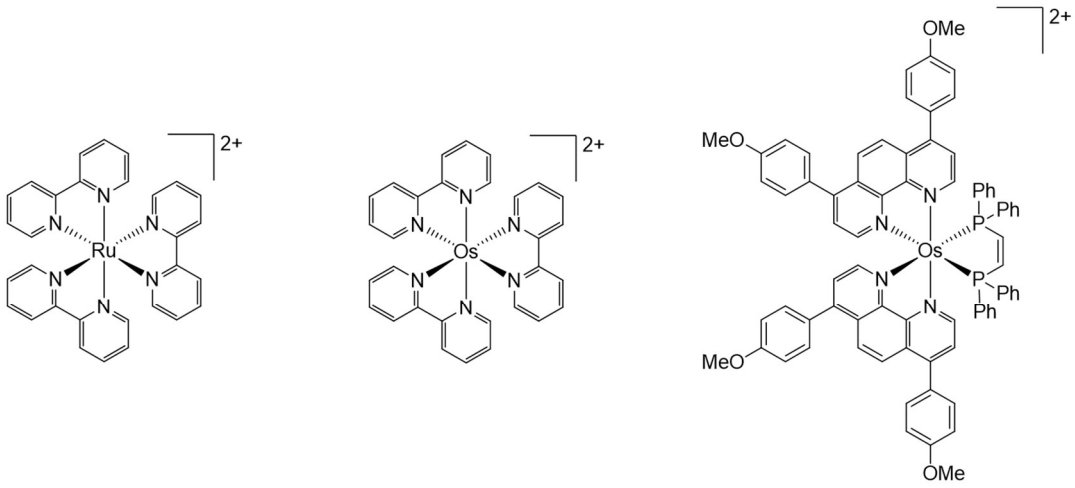

Figure 1.11: Complexes of ruthenium(II) and osmium(II) with their photophysical properties.[57,58]

Rhodium(III) and iridium(III) also have d^6 electron configurations. Room temperature phosphorescence in solution is commonly observed in complexes of Ir(III), but phosphorescence from complexes of Rh(III) is often only observed in low temperature glasses.[60,61] This is due to rhodium(III) having weaker spin-orbit coupling than iridium(III). Exceptions to this are observed in cyclometallated complexes of rhodium(III) with diimine ligands. An example of such a complex is shown on the right of Figure 1.12; this complex was reported by Mandal *et al.* in 2014 and showed emission in solution at room temperature with a quantum yield value of 0.035 and a two-component lifetime, τ = 2.3 ns (83 %), 4.5 ns (17 %).[62]

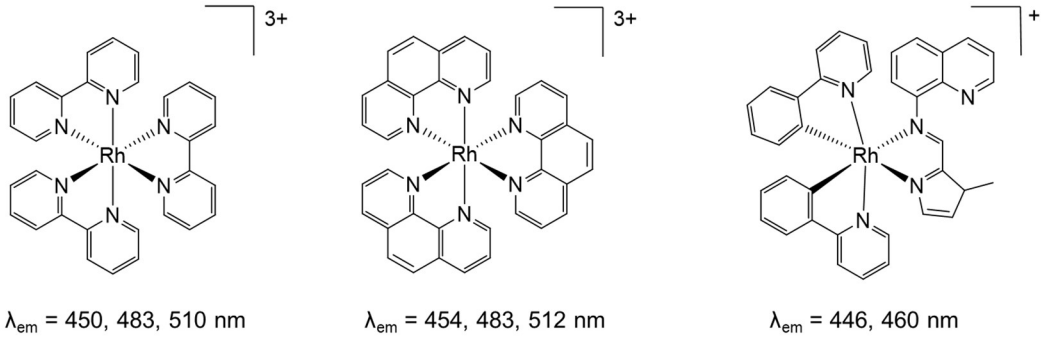

Figure 1.12: Structures and emission wavelengths of rhodium(III) complexes. Left and centre complexes recorded as ethanol: methanol glasses, right complex recorded in acetonitrile solution.[61,62]

1.7.2.2. d^8 Configuration

There are fewer examples of phosphorescent d^8 metal complexes than those with a d^6 configuration. There have been many reports of room temperature phosphorescence in solution from complexes of platinum(II). This is because the heavy platinum centre increases the rate of intersystem crossing which enhances phosphorescence. Three examples of such complexes are shown in Figure 1.13 along with some of their photophysical properties.

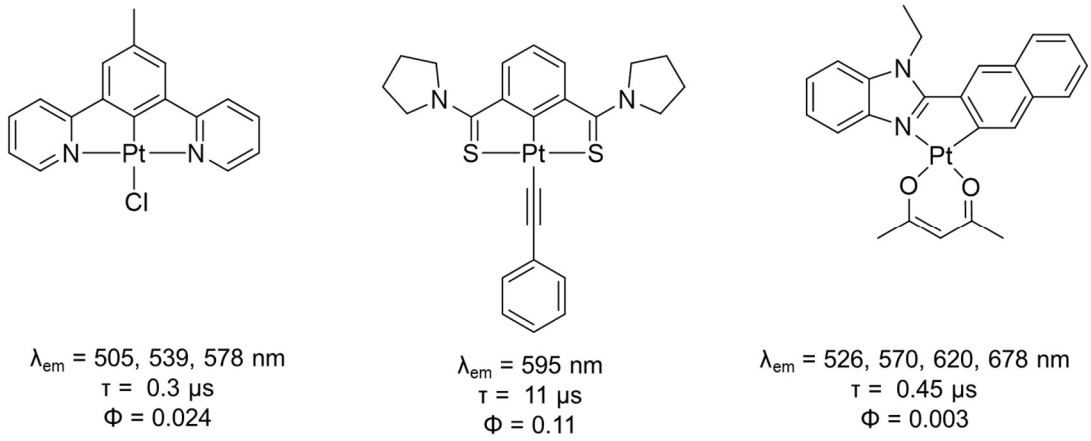

Figure 1.13: Phosphorescent complexes of platinum(II) along with photophysical properties.[63–65]

The complex on the left was reported in 2003 by Williams *et al.* and at the time was only the second report of luminescence from a platinum(II) complex with an N^C^N cyclometallating ligand.[63] The complex in the centre of the figure was reported in 2004 and is one of the earliest examples of a luminescent platinum(II) complex with an S^C^S pincer ligand. The complex showed long-lived phosphorescence at 595 nm and is air stable. These properties make the complex a good candidate for use in optoelectronic devices.[64] The final complex shown is a much more recent example of a luminescent platinum complex. This species was reported as part of a series of eight cyclometallated complexes. While the lifetime and quantum yield of this complex in air are much lower than those reported for the other complexes in Figure 1.13, the emission wavelengths observed are much longer. The authors intend to incorporate these particular ligands into solid state lighting devices.[65]

Phosphorescence from palladium(II) complexes is much rarer due to the weaker heavy atom effect when compared to platinum(II).[29] The room temperature emission of many Pd(II) complexes has been due to fluorescence,[66,67] with phosphorescence only observed at low temperatures.[68,69] The most common ligand system in palladium(II) complexes is porphyrin. Metalloporphyrins of platinum and palladium typically show red phosphorescence. Two examples of palladium(II) metalloporphyrins are shown in Figure 1.14. The complex on the left of the figure, meso-tetra (carbonyl phenyl) porphyrin palladium, is a well reported luminescent complex that shows near infra-red emission at 695 nm. In 2019, the complex was incorporated into a new hydrogel and used as an imaging agent.[70] The complex on the right of the figure was reported by Łapok *et al*. in 2016 in addition to a platinum(II) complex with the same porphyrin ligand. The palladium complex exhibited emission at 1007 nm in air at room temperature with a lifetime of 15 μs.[71]

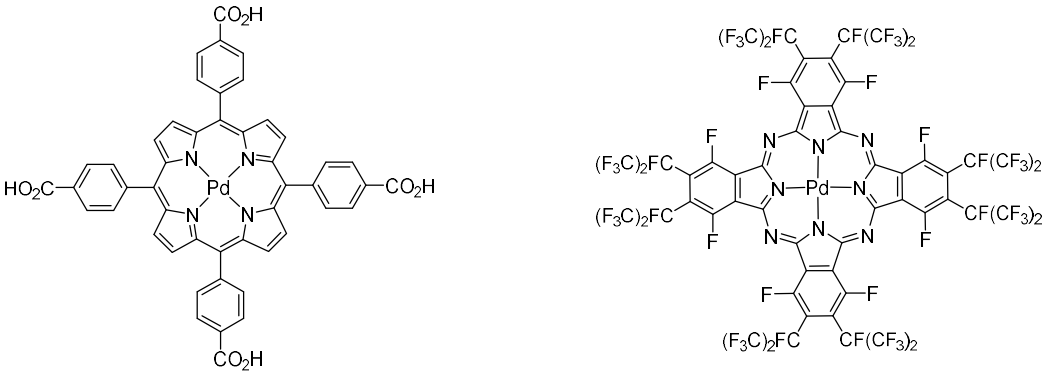

Figure 1.14: Phosphorescent palladium(II) metalloporphyrins.

1.7.2.3. d^{10} Configuration

Both silver(I) and gold(I) have d^{10} electron configurations. The photophysical properties of silver(I) complexes have been much less well studied than other metal systems due to the light-sensitivity of silver(I). Of the complexes that have shown phosphorescence, many exhibit similar structures to copper(I) complexes due to the similar bonding modes of these two metals. An example of this is the hexanuclear complex shown on the left of Figure 1.15. In a study where both the silver(I) and copper(I) analogues were synthesised; the silver complex showed room temperature phosphorescence in solution and in the solid state at 515nm. This was a substantial blue-shift from the copper(I) species which showed emission at 595 nm.[72] The complex on the right of the figure is a silver metallocycle reported in 2018 that exhibits phosphorescence at low temperatures with an emission wavelength of 448 nm and a lifetime of 138 µs.[73]

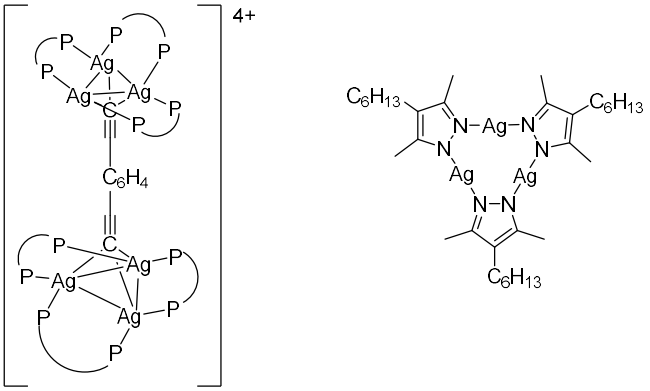

Figure 1.15: Examples of phosphorescent silver(I) complexes.

In contrast, phosphorescent complexes of gold(I) are much more common. The geometry of gold(I) complexes is typically either two- or three-coordinate with the most common ligand systems being carbene, phosphine, thiolate and acetylide ligands. Gold(I) complexes have shown phosphorescence across the whole visible spectrum. Two recent examples of these complexes are shown in Figure 1.16. The complex shown on the left of the figure was reported in 2018 by Chen *et al.* and showed phosphorescence in the solid state. The complex showed emission at around 570 nm with a second, less intense emission at around 450 nm.[74] The second complex is a dinuclear example of a gold(I) complex with carbene ligands that was reported in 2019. This complex also showed emission in the solid state, with an emission wavelength of 430 nm and a lifetime of 0.23 µs.[75]

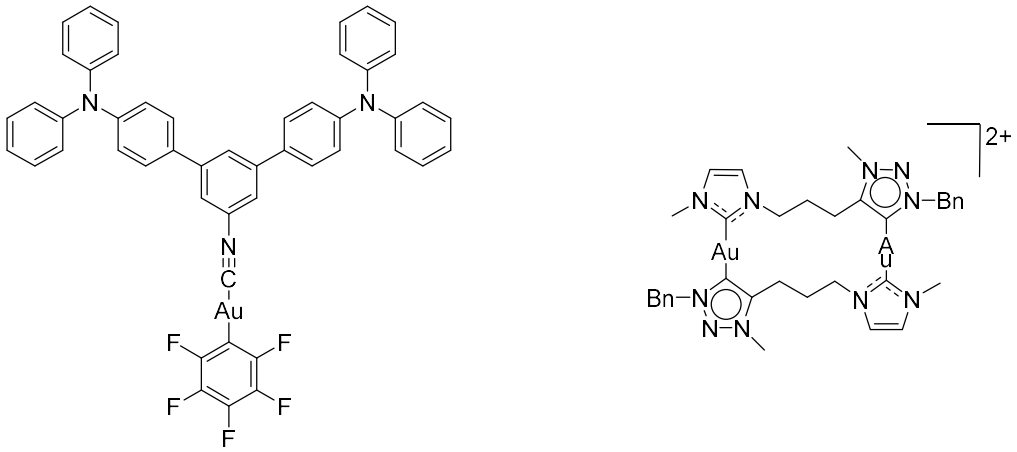

Figure 1.16: Examples of phosphorescent gold(I) complexes.

1.7.3. Fluorescent Transition Metal Complexes

It is known that the singlet excited state lifetimes for transition metal complexes are extremely short. For example, the fluorescence lifetime of $[Ir(ppy)_3]$ has been reported at around 100 fs,[76,77] and that of $[Ru(bpy)_3]^{2+}$ has been recorded at 15 ± 10 fs.[78] This is because the heavy metal atom in such complexes facilitates intersystem crossing which can have rates of around 10^{12} s^{-1}, the result of this is that fluorescence is often very difficult to observe and the fluorescence quantum yields are very low, with that of $[Ru(bpy)_3]^{2+}$ reported at $9x10^{-5}$. [79] Despite this, there have been reports of transition metal complexes that exhibit fluorescence from a singlet excited state with lifetimes on the nanosecond timescale. Some examples of these complexes are shown in Figure 1.17.

The rhodium complex on the left of the figure was reported in 2010 by Malder *et al.* The complex shown below was found to exhibit a long lived singlet excited state, this was found to be due to an unusually slow rate of intersystem crossing.[80] The complex in the centre of the figure is an example of a fluorescent platinum complex first reported in 2010 as part of a series of platinum complexes with perylene-type ligands. The complex shown exhibited a fluorescence lifetime of 1.9 ns and a quantum yield value of 0.43.[81] The final complex in the figure is a fluorescent copper(I) complex. The complex shows fluorescence emission from a ^{1}MLCT excited state, with a lifetime of 15 ps and an quantum yield value of $2.1x10^{-5}$. [82]

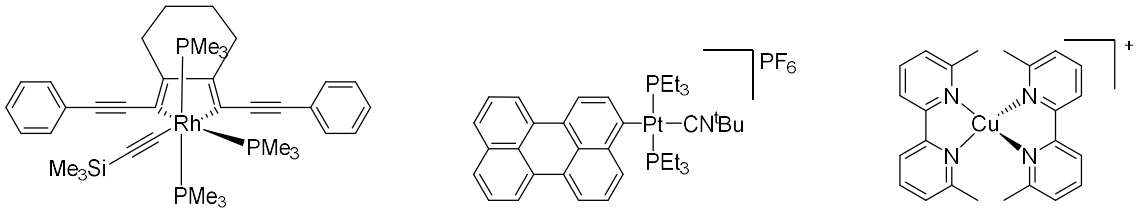

Figure 1.17: Examples of fluorescent transition metal complexes.[80–82]

1.8. Summary

As the above examples illustrate, transition metal complexes with conjugated organic ligands are a versatile group of compounds. The photophysical properties of these species can be manipulated with relative ease to give emission wavelengths across the whole of the visible

spectrum and even into the near infra-red. In addition to this, it is possible to adapt the quantum efficiency and lifetime to best serve individual applications.

1.9. References

1. *Annalen der Physik*, J.A. Barth, 1888.
2. A. Jabłoński, *Z. Für Phys.*, 1935, **94**, 38–46.
3. D. C. Harris and M. D. Bertolucci, *Symmetry and Spectroscopy: An Introduction to Vibrational and Electronic Spectroscopy*, Courier Corporation, 1989.
4. Stokes George Gabriel, *Philos. Trans. R. Soc. Lond.*, 1852, **142**, 463–562.
5. M. Kasha, *Discuss. Faraday Soc.*, 1950, **9**, 14–19.
6. J. C. del Valle and J. Catalán, *Phys. Chem. Chem. Phys.*, 2019, **21**, 10061–10069.
7. J. R. Lakowicz, *Principles of Fluorescence Spectroscopy*, Springer Science & Business Media, 2007.
8. R. Kubin and A. Fletcher, *J. Lumin.*, 1982, **27**, 455–462.
9. T. Karstens and K. Kobs, *J. Phys. Chem.*, 1980, **84**, 1871–1872.
10. 10. S. Hamai and F. Hirayama, *J. Phys. Chem.*, 1983, **87**, 83–89.
11. J. H. Brannon and D. Magde, *J. Phys. Chem.*, 1978, **82**, 705–709.
12. H. Weil-Malherbe and J. Weiss, *Nature*, 1942, **149**, 471.
13. A. Weinreb, *J. Chem. Phys.*, 1962, **36**, 890–894.
14. M. N. Möller and A. Denicola, *Free Radic. Biol. Med.*, 2018, **128**, 137–143.
15. A. Chmyrov, T. Sandén and J. Widengren, *J. Phys. Chem. B*, 2010, **114**, 11282–11291.
16. R. Giri, *Spectrochim. Acta. A. Mol. Biomol. Spectrosc.*, 2004, **60**, 757–763.
17. A. Nakajima and H. Akamatu, *Bull. Chem. Soc. Jpn.*, 1969, **42**, 3030-+.
18. M. M. Martin and W. R. Ware, *J. Phys. Chem.*, 1978, **82**, 2770–2776.
19. B. E. Colenda, H.-S. Lee, J. H. Reibenspies and R. D. Hancock, *Inorganica Chim. Acta*, 2018, **482**, 478–490.
20. G. Weber, *Trans. Faraday Soc.*, 1948, **44**, 185–189.
21. R. Corradini, G. Sartor, R. Marchelli, A. Dossena and A. Spisni, *J. Chem. Soc. Perkin Trans. 2*, 1992, 1979–1983.
22. Y. T. Mazurenko and N. Bakhshiev, *Opt Spectrosc*, 1970, **21**, 490–494.
23. T. Förster, *Ann. Phys.*, 1948, **437**, 55–75.
24. P. G. Wu and L. Brand, *Anal. Biochem.*, 1994, **218**, 1–13.
25. L. Stryer, *Annu. Rev. Biochem.*, 1978, **47**, 819–846.
26. R. M. Silverstein, F. X. Webster, D. J. Kiemle and D. L. Bryce, *Spectrometric Identification of Organic Compounds*, John Wiley & Sons, 2014.
27. B. Yu, D. Liu, Y. Wang, T. Zhang, Y.-M. Zhang, M. Li and S. X.-A. Zhang, *Dyes Pigments*, 2019, **163**, 412–419.
28. Y. Zhou, M. Zhang, J. Ye, H. Liu, K. Wang, Y. Yuan, Y.-Q. Du, C. Zhang, C.-J. Zheng and X.-H. Zhang, *Org. Electron.*, 2019, **65**, 110–115.
29. R. C. Evans, P. Douglas and C. J. Winscom, *Coord. Chem. Rev.*, 2006, **250**, 2093–2126.
30. G. A. Crosby, *Acc. Chem. Res.*, 1975, **8**, 231–238.
31. J. N. Demas and B. A. DeGraff, *Coord. Chem. Rev.*, 2001, **211**, 317–351.
32. H. J. Youn, E. Terpetschnig, H. Szmacinski and J. R. Lakowicz, *Anal. Biochem.*, 1995, **232**, 24–30.
33. X.-Q. Guo, F. N. Castellano, Li and J. R. Lakowicz, *Anal. Chem.*, 1998, **70**, 632–637.
34. K. K.-W. Lo, M.-W. Louie and K. Y. Zhang, *Coord. Chem. Rev.*, 2010, **254**, 2603–2622.
35. M. A. Baldo, S. Lamansky, P. E. Burrows, M. E. Thompson and S. R. Forrest, *Appl. Phys. Lett.*, 1999, **75**, 4–6.

36. V. Adamovich, J. Brooks, A. Tamayo, A. M. Alexander, P. I. Djurovich, B. W. D'Andrade, C. Adachi, S. R. Forrest and M. E. Thompson, *New J. Chem.*, 2002, **26**, 1171–1178.
37. S. Welter, K. Brunner, J. W. Hofstraat and L. D. Cola, *Nature*, 2003, **421**, 54.
38. . O'Regan and M. Grätzel, *Nature*, 1991, **353**, 737.
39. Sauvé Geneviève, M. E. Cass, G. Coia, S. J. Doig, I. Lauermann, K. E. Pomykal and N. S. Lewis, *J. Phys. Chem. B*, 2000, **104**, 6821–6836.
40. E. I. Mayo, K. Kilså, T. Tirrell, P. I. Djurovich, A. Tamayo, M. E. Thompson, N. S. Lewis and H. B. Gray, *Photochem. Photobiol. Sci.*, 2006, **5**, 871–873.
41. R. M. Carlos and M. G. Neumann, *J. Photochem. Photobiol. Chem.*, 2000, **131**, 67–73.
42. B. D. Rossenaar, E. Lindsay, D. J. Stufkens and A. Vlček, *Inorganica Chim. Acta*, 1996, **250**, 5–14.
43. R. C. G. Frem, A. C. Massabni, A. M. G. Massabni and A. E. Mauro, *Inorganica Chim. Acta*, 1997, **255**, 53–58.
44. H. Kunkely and A. Vogler, *Inorg. Chem. Commun.*, 2000, **3**, 143–144.
45. M. A. Jamieson, N. Serpone and M. Z. Hoffman, *Coord. Chem. Rev.*, 1981, **39**, 121–179.
46. A. D. Kirk and G. B. Porter, *J. Phys. Chem.*, 1980, **84**, 887–891.
47. V. W.-W. Yam and K. K.-W. Lo, *Chem. Soc. Rev.*, 1999, **28**, 323–334.
48. J. C. Barbour, A. J. I. Kim, E. deVries, S. E. Shaner and B. M. Lovaasen, *Inorg. Chem.*, 2017, **56**, 8212–8222.
49. A. Juris and R. Ziessel, *Inorganica Chim. Acta*, 1994, **225**, 251–254.
50. L.-P. Liu, Q. Li, S.-P. Xiang, L. Liu, X.-X. Zhong, C. Liang, G. H. Li, T. Hayat, N. S. Alharbi, F.-B. Li, N.-Y. Zhu, W.-Y. Wong, H.-M. Qin and L. Wang, *Dalton Trans.*, 2018, **47**, 9294–9302.
51. A. Vogler, *Inorg. Chem. Commun.*, 2016, **67**, 32–34.
52. P. Chábera, Y. Liu, O. Prakash, E. Thyrhaug, A. E. Nahhas, A. Honarfar, S. Essén, L. A. Fredin, T. C. B. Harlang, K. S. Kjær, K. Handrup, F. Ericson, H. Tatsuno, K. Morgan, J. Schnadt, L. Häggström, T. Ericsson, A. Sobkowiak, S. Lidin, P. Huang, S. Styring, J. Uhlig, J. Bendix, R. Lomoth, V. Sundström, P. Persson and K. Wärnmark, *Nature*, 2017, **543**, 695–699.
53. A. Juris, V. Balzani, F. Barigelletti, S. Campagna, P. Belser and A. von Zelewsky, *Coord. Chem. Rev.*, 1988, **84**, 85–277.
54. B.-Z. Shan, Q. Zhao, N. Goswami, D. M. Eichhorn* and D. P. Rillema*, *Coord. Chem. Rev.*, 2001, **211**, 117–144.
55. M. Frank, M. Nieger, F. Vögtle, P. Belser, A. von Zelewsky, L. De Cola, V. Balzani, F. Barigelletti and L. Flamigni, *Inorganica Chim. Acta*, 1996, **242**, 281–291.
56. M. L. Fetterolf and H. W. Offen, *J. Phys. Chem.*, 1985, **89**, 3320–3323.
57. B. Carlson, G. D. Phelan, W. Kaminsky, L. Dalton, X. Jiang, S. Liu and A. K.-Y. Jen, *J. Am. Chem. Soc.*, 2002, **124**, 14162–14172.
58. S. D. Bergman, I. Goldberg, A. Barbieri, F. Barigelletti and M. Kol, *Inorg. Chem.*, 2004, **43**, 2355–2367.
59. E. M. Kober, B. P. Sullivan, W. J. Dressick, J. V. Caspar and T. J. Meyer, *J. Am. Chem. Soc.*, 1980, **102**, 7383–7385.
60. W. L. Huang, J. R. Lee, S. Y. Shi and C. Y. Tsai, *Transit. Met. Chem.*, 2003, **28**, 381–387.
61. H. M. Burke, J. F. Gallagher, M. T. Indelli and J. G. Vos, *Inorganica Chim. Acta*, 2004, **357**, 2989–3000.
62. S. Mandal, D. K. Poria, D. K. Seth, P. S. Ray and P. Gupta, *Polyhedron*, 2014, **73**, 12–21.
63. J. A. G. Williams, A. Beeby, E. S. Davies, J. A. Weinstein and C. Wilson, *Inorg. Chem.*, 2003, **42**, 8609–8611.

64. T. Kanbara, K. Okada, T. Yamamoto, H. Ogawa and T. Inoue, *J. Organomet. Chem.*, 2004, **689**, 1860–1864.
65. P.-H. Lanoë, A. Moreno-Betancourt, L. Wilson, C. Philouze, C. Monnereau, H. Jamet, D. Jouvenot and F. Loiseau, *Dyes Pigments*, 2019, **162**, 967–977.
66. D. Song, Q. Wu, A. Hook, I. Kozin and S. Wang, *Organometallics*, 2001, **20**, 4683–4689.
67. M. Kandaz, A. R. Özkaya and A. Cihan, *Transit. Met. Chem.*, 2003, **28**, 650–657.
68. F. Neve, A. Crispini, C. Di Pietro and S. Campagna, *Organometallics*, 2002, **21**, 3511–3518.
69. P. D. Harvey and H. B. Gray, *J. Am. Chem. Soc.*, 1988, **110**, 2145–2147.
70. R. Xue, S. Wei, X. Dong, T. Zhu, J. Yuan, L. Feng, Q. Wang, Y. Yang and H. Wang, *Appl. Organomet. Chem.*, 2019, **33**, e4845.
71. Ł. Łapok, M. Obłoza, A. Gorski, V. Knyukshto, T. Raichyonok, J. Waluk and M. Nowakowska, *ChemPhysChem*, 2016, **17**, 1123–1135.
72. V. W.-W. Yam, W. K.-M. Fung and K.-K. Cheung, *Chem. Commun.*, 1997, 963–964.
73. J. Cored, O. Crespo, J. L. Serrano, A. Elduque and R. Giménez, *Inorg. Chem.*, 2018, **57**, 12632–12640.
74. Z. Chen, G. Liu, S. Pu and S. H. Liu, *Dyes Pigments*, 2018, **159**, 499–505.
75. M. Monticelli, M. Baron, C. Tubaro, S. Bellemin-Laponnaz, C. Graiff, G. Bottaro, L. Armelao and L. Orian, *ACS Omega*, 2019, **4**, 4192–4205.
76. G. J. Hedley, A. Ruseckas and I. D. W. Samuel, *Chem. Phys. Lett.*, 2008, **450**, 292–296.
77. K.-C. Tang, K. L. Liu and I.-C. Chen, *Chem. Phys. Lett.*, 2004, **386**, 437–441.
78. A. Cannizzo, F. van Mourik, W. Gawelda, G. Zgrablic, C. Bressler and M. Chergui, *Angew. Chem. Int. Ed.*, 2006, **45**, 3174–3176.
79. A. C. Bhasikuttan, M. Suzuki, S. Nakashima and T. Okada, *J. Am. Chem. Soc.*, 2002, **124**, 8398–8405.
80. A. Steffen, M. G. Tay, A. S. Batsanov, J. A. K. Howard, A. Beeby, K. Q. Vuong, X.-Z. Sun, M. W. George and T. B. Marder, *Angew. Chem. Int. Ed.*, 2010, **49**, 2349–2353.
81. S. Lentijo, J. A. Miguel and P. Espinet, *Inorg. Chem.*, 2010, **49**, 9169–9177.
82. Z. A. Siddique, Y. Yamamoto, T. Ohno and K. Nozaki, *Inorg. Chem.*, 2003, **42**, 6366–6378.

2. Ligand-Tuneable, Red-Emitting Iridium(III) Complexes for Efficient Triplet–Triplet Annihilation Upconversion Performance

2.1. Introduction

This chapter focuses on the design, synthesis and characterisation of cationic bis-cyclometallated iridium(III) complexes. These types of complexes have been well studied over the past few decades for their photophysical properties and, as a result, their applications have become more and more diverse. The main applications of these species are discussed in detail below.

2.1.1. Applications of Iridium(III) Complexes

Cyclometallated octahedral complexes of iridium(III) have a large Δ_o value, and due to the strong σ character of the Ir-C cyclometallating bond, metal-to-ligand charge-transfer (MLCT) and ligand-to-ligand charge transfer (LLCT) are energetically more favourable than metal-centred (MC) transitions.[1–3] As both the metal centre and the ligand are involved in emission, the emission wavelength can be tuned by making changes to the cyclometallating ligand. A property that is often exploited in iridium chemistry.

2.1.2. Photocatalysts

Transition metal complexes undergo an MLCT transition when excited by visible light and as a consequence, they can go through reductive and oxidative quenching pathways easily.[1,4] In the case of ruthenium complexes, this has been utilised in the catalysis of organic transformations.[5,6] More recently, focus has moved to complexes of rhenium and iridium. Examples of some iridium complexes used as photocatalysts are shown in Figure 2.1. The complex on the left of the figure was first used as a catalyst by Stephenson *et al.* to break down lignin biomass substrates in a photoflow reactor.[7] The same catalyst has since been used to catalyse a [4+2] ring-opening reaction in cyclobutylanilines with alkynes,[8] and in a separate study was found to aid asymmetric azapinacol cyclization.[9] The complex in the centre of the figure was found to perform selective C-H vinylation utilising vinyl sulfones. The reaction resulted in good yields and the methodology also extended to *N*-Boc α-amino acids.[10] The final complex in the figure was reported in 2013 and was found to be a highly efficient photocatalyst for CO_2 reduction.[11]

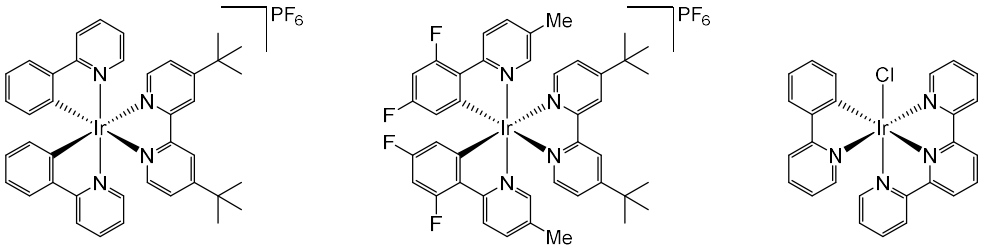

Figure 2.1:Examples of iridium(III) complexes developed as photocatalysts.

2.1.3. Photovoltaics

Iridium complexes have also found use as light-harvesting molecules in photovoltaics; examples of these complexes are shown in Figure 2.2. The first complex in the figure was reported in 2015 and was used to fabricate a bulk heterojunction solar cell. The device exhibited a power conversion efficiency of 0.25 %, which although low, showed that the complex was a good starting point for the design of complexes for photovoltaic applications.[12] The central complex in the figure was reported in 2018 as part of an artificial FRET antenna with the complex used as the donor, and a BODIPY-type dye as an acceptor.[13] The complex on the right side of the figure shows the general structure of a series of complexes reported in 2017 where an efficiency of up to 0.62 % was recorded when these species were incorporated into TiO_2-based *n*-type dye-sensitised solar cells.[14]

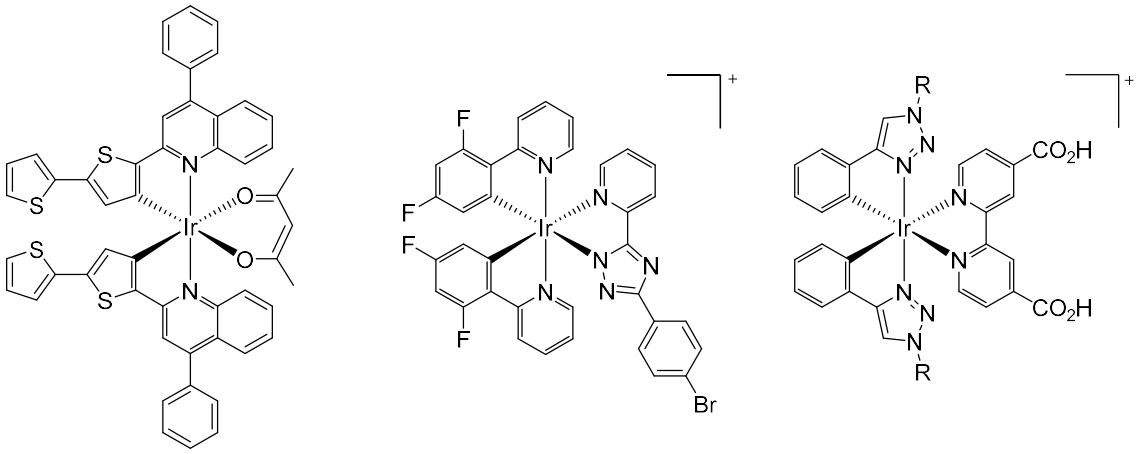

Figure 2.2: Complexes developed for photovoltaic applications.

2.1.4. Bioimaging

One field where cationic iridium complexes have found particular use is bioimaging. Some of the most important requirements for cell imaging agents are low toxicity and preference for concentrating in a particular organelle.[15,16] Metal complexes can be made to meet these requirements by the use of non-toxic, non-labile ligands with substituents that target specific organelles. In addition to this, metal complexes are particularly attractive due to their long-lived phosphorescence and large Stokes shifts.[17–19]

The first report of cationic iridium(III) complexes used as stains in living cells came in 2008, these complexes are shown in the left and centre of Figure 2.3. The complex on the left of the image

is a green emitting species while the complex in the centre showed red emission, however both complexes selectively stained the cytoplasm of cells.[20] The complex on the right of the figure is one of the most recent examples of an iridium based imaging agent. This complex was reported in 2019 as a detector for Cu^{2+} ions in cells. The complex shows green phosphorescence which is rapidly turned off in the presence of Cu^{2+} ions.[21]

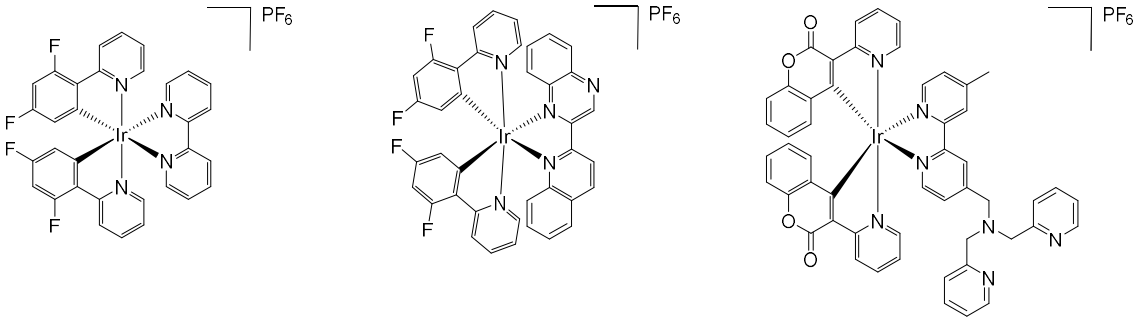

Figure 2.3: Iridium complexes synthesised as bioimaging agents.

2.1.5. Triplet-Triplet Annihilation Upconversion

Triplet-triplet annihilation upconversion (TTA UC) is a process whereby high energy light is produced from a low energy light input. One of the most promising applications of this phenomenon is to increase the efficiency of solar cells.[22] The process involves the excitation of a donor molecule into a triplet excited state followed by triplet-triplet energy transfer to an appropriate acceptor molecule. Collision of two such acceptor molecules results in the population of a higher energy singlet level and produces upconverted delayed fluorescence exhibiting an anti-Stokes shift.[23]

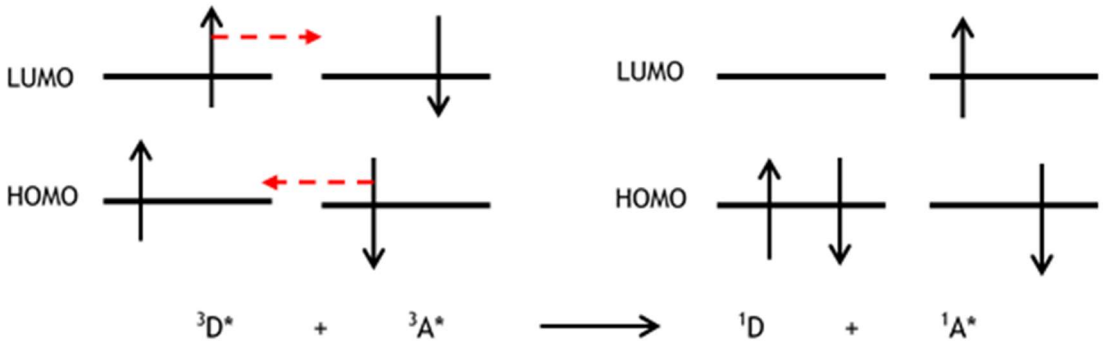

Figure 2.4: Schematic of triplet-triplet annihilation. Where D = donor molecule and A = acceptor molecule.

Typically, the triplet acceptor molecules are commercial compounds used without further modification, but the criteria for a good acceptor is as follows: 1) The energy of the excited singlet state should be less than twice the energy of the excited triplet state ($2 \times E_{T1} > E_{S1}$) to allow population of the singlet state upon annihilation. 2) The compound should possess a high fluorescence quantum yield. 3) The T_1 energy level should be tuneable, and 4) the acceptor must have good photochemical stability. Examples of common acceptor molecules include anthracene, 9,10-diphenylanthracene (DPA), perylene and boron-dipyrromethene (BODIPY). The structures of these compounds are shown in Figure 2.5.[24]

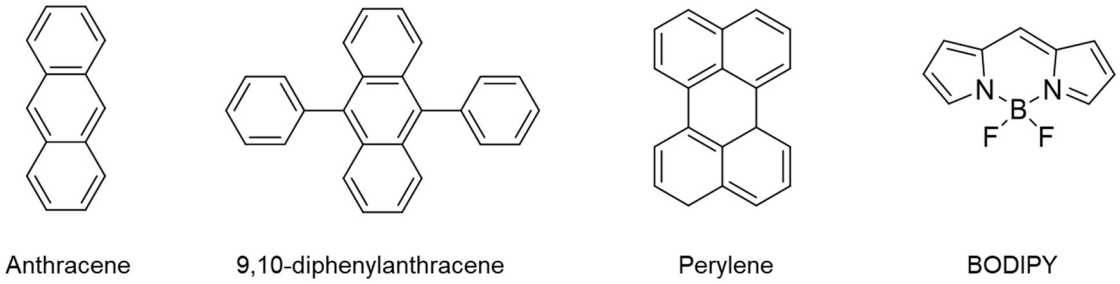

Figure 2.5: Examples of common triplet-triplet annihilation acceptor compounds.

For efficient TTA UC, the donor molecule must exhibit efficient intersystem crossing, strong absorption in the visible region and long phosphorescent lifetimes.[25] Late transition metal complexes have become well studied in this field because, in addition to the properties mentioned above, they also have large spin-orbit coupling constants and efficient intersystem crossing to the triplet state.[24]

Ruthenium polyimine complexes have been studied for a long time for their upconversion efficiency. Figure 2.6 shows a ruthenium complex with a phenanthroline ligand that has a pyrene substituent. This complex was reported by Ji *et al.* in 2011 with an upconversion efficiency of 9.8 %.[26] Platinum and palladium porphyrin complexes have also been of interest. The complex in the centre of Figure 2.6 is a platinum porphyrin complex with a reported Φ_{UC} value of 0.65 %.[27] One potential explanation for this relatively low value is the large size of the sensitiser molecule which may slow diffusion rate of the triplet state.[28] The complex on the far right of the figure is a palladium complex which has a Φ_{UC} = 4.00%.[29]

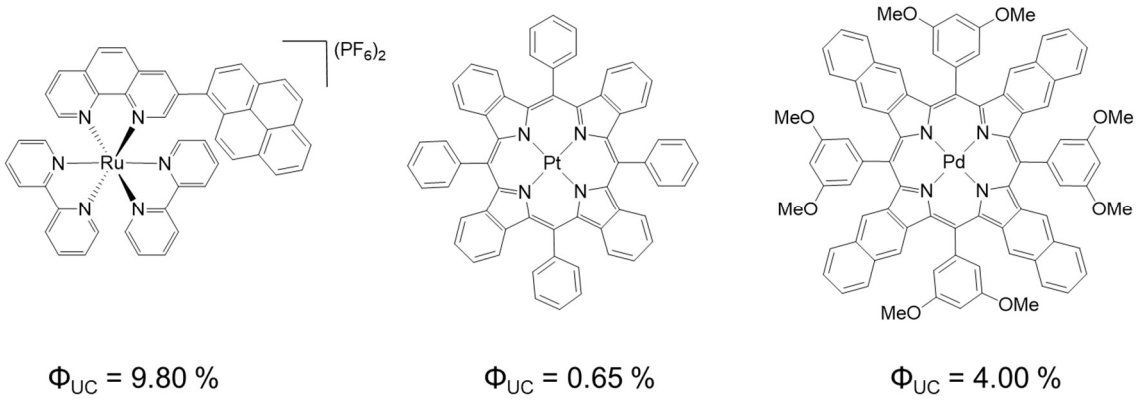

Figure 2.6: Examples of transition metal complexes developed as triplet-triplet annihilation donors.

Iridium(III) complexes are of particular interest in producing new sensitiser species for upconversion as they can have much higher Φ_{UC} values. Some recent examples are shown in Figure 2.7. The tris-cyclometallated complex in the left of the image was reported by Peng *et al* in 2014 who found that when R_2 was an alkyl chain, Φ_{UC} = 0.26 %, but replacement of this group with a pyrene derivative caused this value to increase to 4.1 % .[30] The complex in the middle of the figure is a bis-cyclometallated complex which uses a diimine ligand with a coumarin substituent to achieve a Φ_{UC} value of 23.4 %. [31] The complex on the right of the figure was reported in 2016 and had the highest reported Φ_{UC} value, at the time of this current work, for a triplet sensitiser species at 31.6 %.[32]

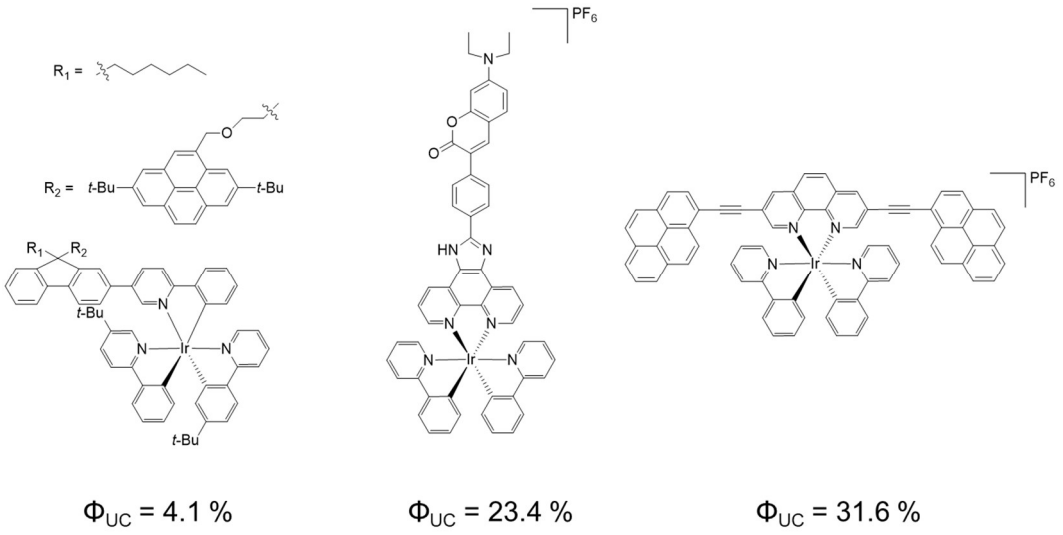

Φ_{UC} = 4.1 % Φ_{UC} = 23.4 % Φ_{UC} = 31.6 %

Figure 2.7: Examples of upconversion donor species based on iridium complexes.

2.2. Aims

The aim of this chapter was to investigate the effects of cyclometallating ligand substituents upon the photophysical properties of their complexes. In this study, a series of seven cyclometallating complexes based upon quinoxaline derivatives have been synthesised that bear electron withdrawing and electron donating groups.

These ligands were then coordinated to iridium along with a 2,2'-bipyridine ancillary ligand to give a series of cationic bis-cyclometallated iridium(III) complexes. The photophysical properties of these ligands were then fully investigated in an attempt to understand how ligand substituents can change the emission properties of organometallic complexes. In addition to this, DFT computational studies were performed in an effort to explain the experimental results observed. Also, the complexes were investigated for their potential use as upconversion sensitisers.

2.3. Results and Discussion

2.3.1. Synthesis and Characterisation

In this chapter of work, seven cyclometallating ligands were synthesised. These compounds were based upon quinoxaline and were differently functionalised to contain either electron withdrawing or electron donating groups. The substituents used were fluoro- and chloro- groups to induce an electron withdrawing effect, and methyl groups which have a weak electron donating effect. The general scheme for the synthesis of these ligands is shown in Scheme 2.1.

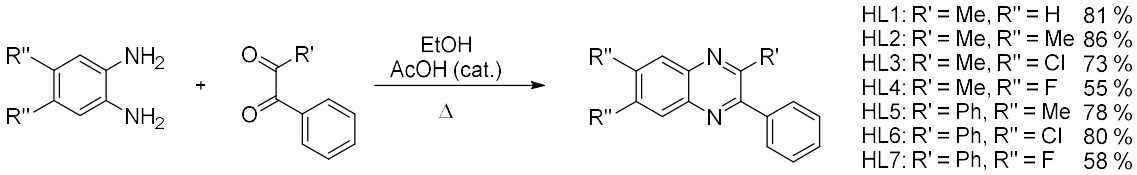

Scheme 2.1: Synthesis scheme of ligands HL1-7

The synthesis involves dissolving a phenyldiamine with benzil or 1-phenyl-1,2-propanedione in ethanol and heating to reflux in the presence of a catalytic amount of acetic acid. The ligands HL3-7 precipitated from the reaction mixture as solids after several hours and, after filtration and washing, required no further purification. However, the ligands HL1 and HL2 did not precipitate from the reaction mixture as solids. Instead, for these ligands, the solvent was removed under reduced pressure and the crude product taken up in dichloromethane and washed with dilute hydrochloric acid. The organic phase was then dried under reduced pressure to give the pure ligands as waxy solids.

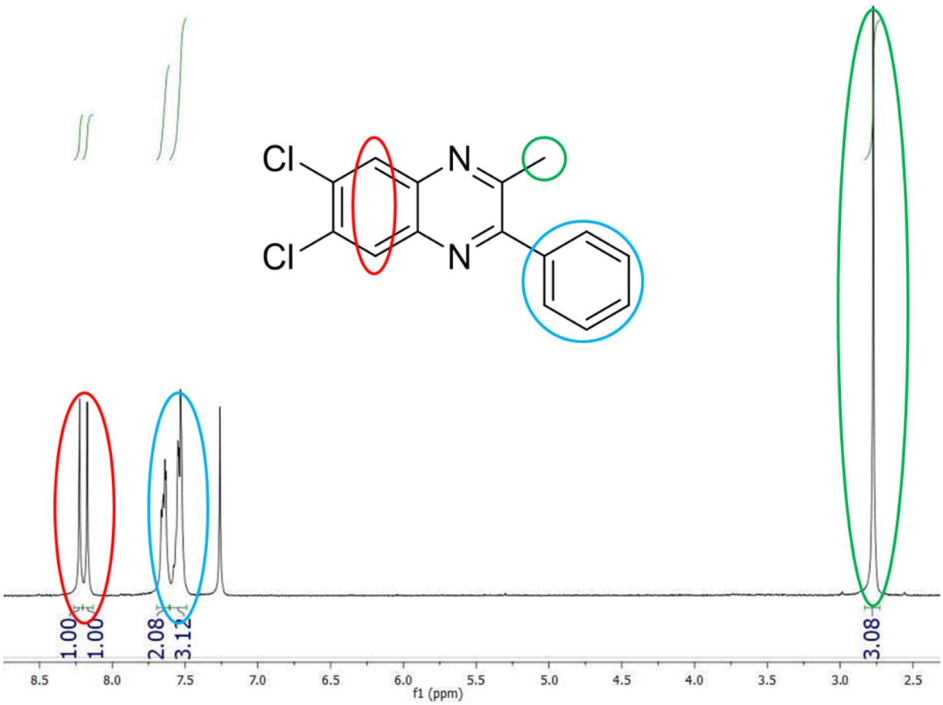

Figure 2.8: Assignment of proton NMR spectrum of ligand HL3. (300 MHz, $CDCl_3$)

Figure 2.8 shows the proton NMR spectrum of ligand HL3. The two singlets at 8.23 and 8.18 ppm are assigned to the aromatic protons nearest to the chloro-substituents, and the singlet at the higher ppm value is that on the same side of the molecule as the phenyl substituent. They appear as two singlets due to the asymmetry of the molecule. The phenyl substituent is electron withdrawing and as a result this proton is slightly more de-shielded than the other. The multiplets at 7.64 and 7.53 ppm arise from the phenyl substituent and the singlet at 2.77 ppm corresponds to the methyl substituent.

The electron withdrawing effect of the phenyl moiety can be seen more clearly in Figure 2.9, where the proton NMR spectra of the di-phenyl substituted ligand is overlaid with the corresponding phenyl-, methyl-substituted ligand. The protons corresponding to the two singlets seen at 8.23 and 8.18 ppm in the spectrum of HL3, are equivalent in HL6. Because of this, the two protons cause one singlet in the proton NMR at 8.29 ppm. The chemical shift of this singlet is higher than those seen in HL3 due to the extra electron withdrawing effect that occurs when there are two phenyl moieties in the molecule.

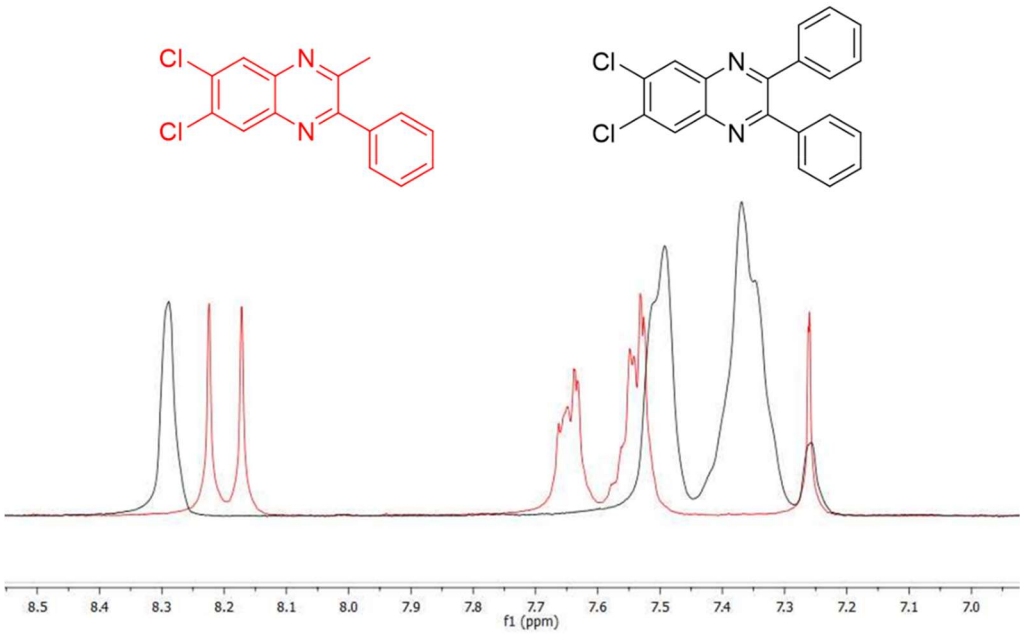

Figure 2.9: Overlaid proton NMR sub-spectra of HL3 (red) and HL6 (black). (300 MHz, $CDCl_3$)

The ligands were also characterised by carbon NMR spectroscopy, high resolution mass spectrometry and, where applicable, fluorine NMR spectroscopy.

The ligands were reacted with iridium trichloride, $IrCl_3.xH_2O$, to form the dimeric species $[\{Ir(L)_2\text{-}\mu\text{-}Cl\}_2]$ as reported in literature.[33] These reaction conditions have been shown to result in the *cis*-C,C and *trans*-N,N coordination mode of the cyclometallating ligand.[34–36] This species was then used in the next step without further characterisation. The dimer was dissolved in 2-ethoxyethanol with 2,2'-bipyridine and heated at reflux for 24 hours to give a series of cationic bis-cyclometallated iridium(III) complexes as chloride salts.

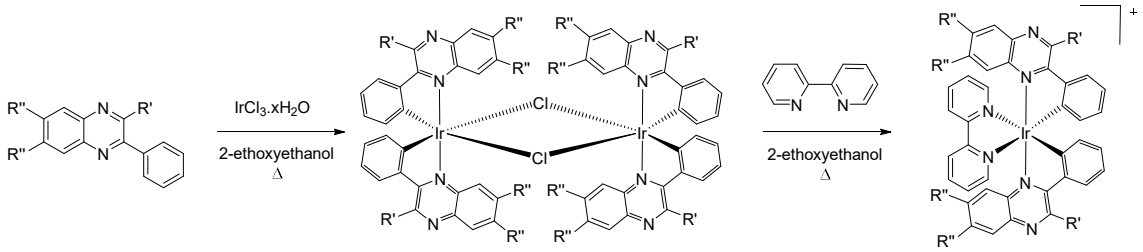

Scheme 2.2: General scheme for synthesis of cationic iridium(III) complexes.

A saturated aqueous solution of ammonium hexafluorophosphate (NH_4PF_6) was added to the reaction flask to form the PF_6 salt of the complex which precipitated from solution as a red solid. Where purification was required, this was carried out by column chromatography in DCM:MeOH (95:5). A pale-yellow band eluted first which was found to be free cyclometallating ligand, which was then followed by a red band. The red band was dried under reduced pressure and re-precipitated from DCM and diethyl ether to give the pure cationic complex.

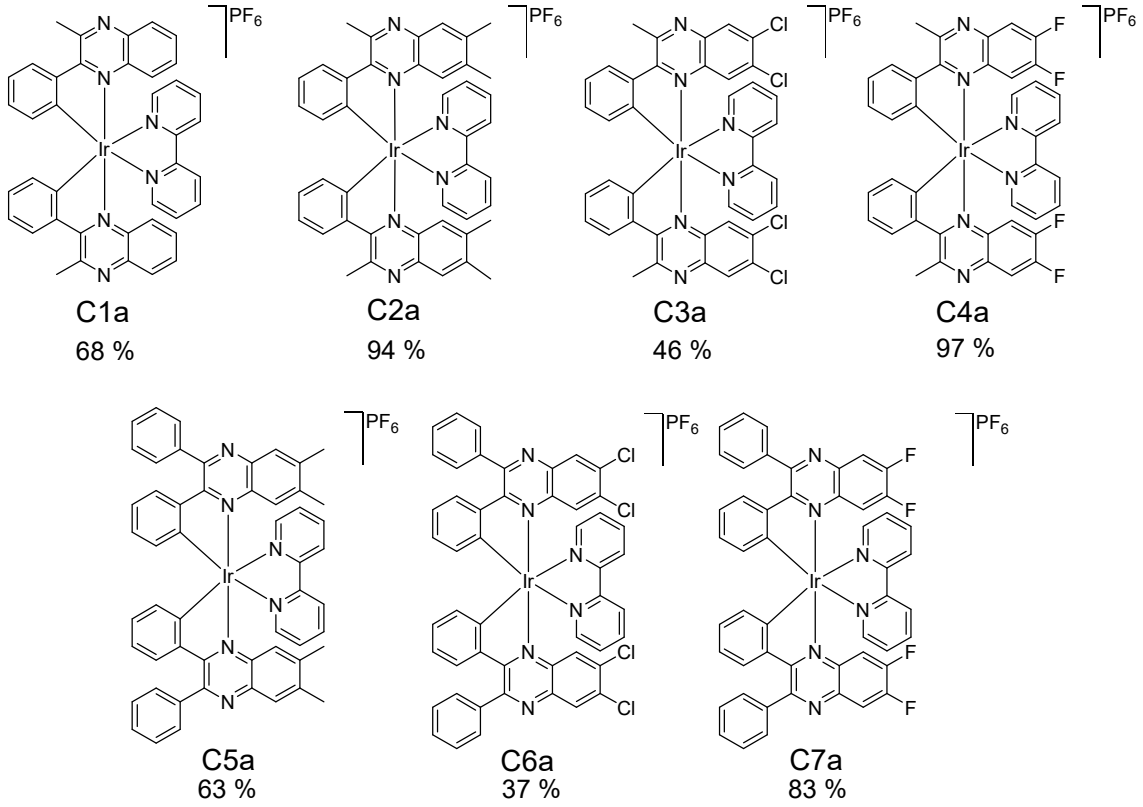

Figure 2.10: Structures of seven cationic bis-cyclometallated iridium(III) complexes.

The complexes were characterised by proton, carbon and where applicable, fluorine NMR spectroscopy. In addition to this, all complexes were also analysed by high resolution mass spectrometry, IR, UV-vis, transient absorption (TA) and luminescence spectroscopy.

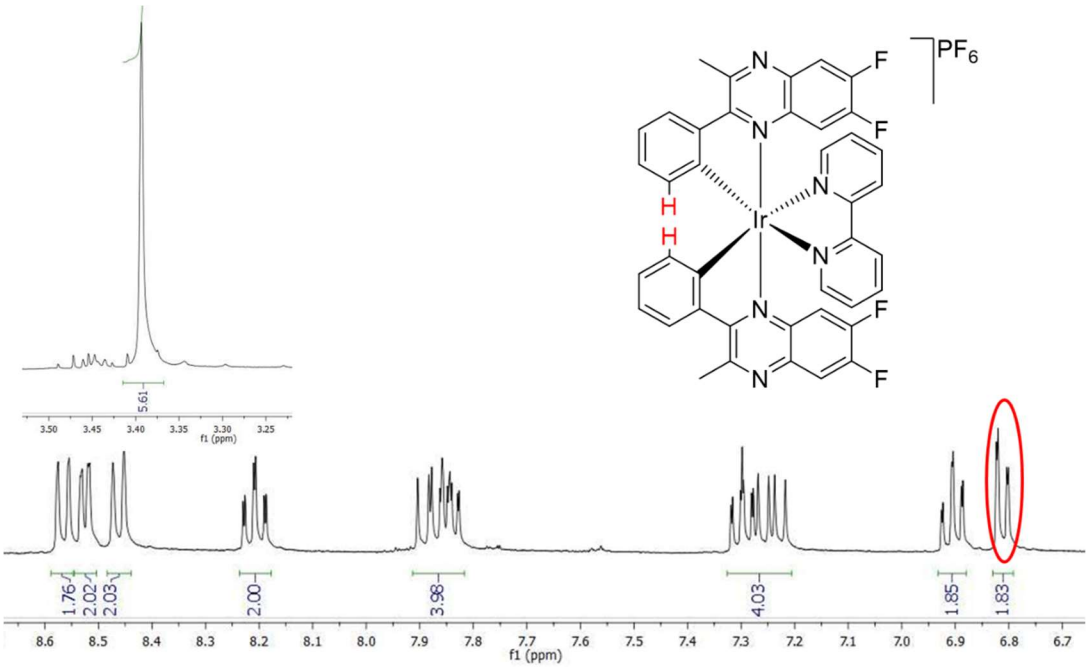

Figure 2.11: Proton NMR spectrum of complex C4a. (400 MHz, acetone-d_6)

Figure 2.11 shows the proton NMR spectrum recorded for C4a. The circled signal at 6.81 ppm is a doublet which corresponds to the protons highlighted in red in the structure above. An upfield shift of the proton *ortho*- to the cyclometallating site on the phenyl moiety of the ligand is observed due to shielding by the ring currents of the aromatic moieties of adjacent ligands.

The two fluoro- containing ligands, HL4 and HL7, and their corresponding complexes, C4a and C7a, were analysed by fluorine NMR spectroscopy and the data has been tabulated in Table 2.1. The chemical shifts of the fluorine atoms in the complexes shift upfield compared to those in the related free ligand. In the case of HL7, in addition to the upfield shift, the fluorine environments of the cyclometallating ligand become inequivalent upon coordination to the metal centre and two separate signals are observed. In both complexes, a signal is observed at -72.6 ppm which is not seen in the free ligand, due to the hexafluorophosphate anion.

Table 2.1: Fluorine NMR data including chemical shift values and coupling constants.

Compound	Ligand δ (^3J(F,F)) [ppm]	PF_6^- δ (^1J(F,P)) [ppm]
HL4	-130.4 (d, 21 Hz), -131.2 (d, 21 Hz)	
$[Ir(L4)_2(bpy)]PF_6$	-131.7 (d, 22 Hz), -133.7 (d, 22 Hz)	-72.6 (d, 712 Hz)
HL7	-129.9 (s)	
$[Ir(L7)_2(bpy)]PF_6$	-130.3 (d, 22 Hz), -132.7 (d, 22 Hz)	-72.6 (d, 700 Hz)

The data obtained from proton, carbon and fluorine NMR data confirm that each complex isolated was pure and only one isomer was present in each case.

All of the complexes in this study were also characterised by high-resolution mass spectrometry. In all cases the molecular ion peak was present, and in some cases, a peak corresponding to a fragment containing both cyclometallating ligands but not the 2,2'-bipyridine ancillary ligand was also present. The isotope pattern was also consistent with an iridium-containing species.

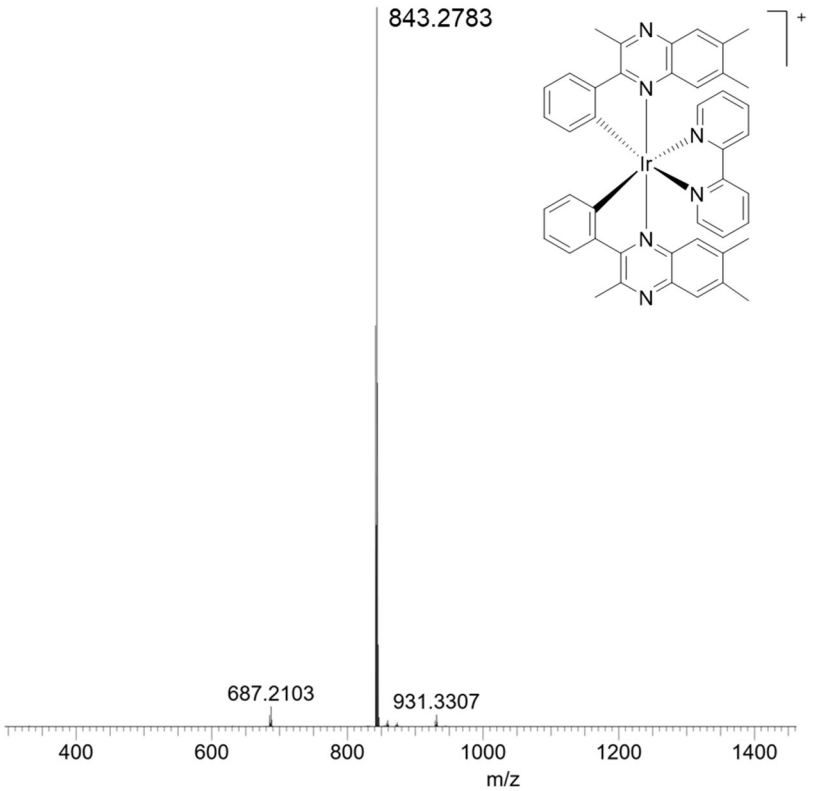

Figure 2.12: High-resolution mass spectrum of complex C2a with molecular ion peak.

2.3.2. X-Ray Crystallography

Single crystal X-ray data were obtained for complexes C2a, C5a and C7a. The crystals were grown *via* vapour diffusion of diethyl ether into saturated solutions of the complexes in acetonitrile. The crystal data was collected by the UK National Crystallography Service with the collection

parameters are reported in the experimental section of this chapter. The data show that the complexes have a distorted octahedral geometries around the iridium(III) centre and also confirms that the cyclometallating ligands chelate in a *cis*-C,C and *trans*-N,N manner. This also supports the theory that the *trans* influence of the phenyl group is stronger than that of the N-heterocycle donors as .[37–39]

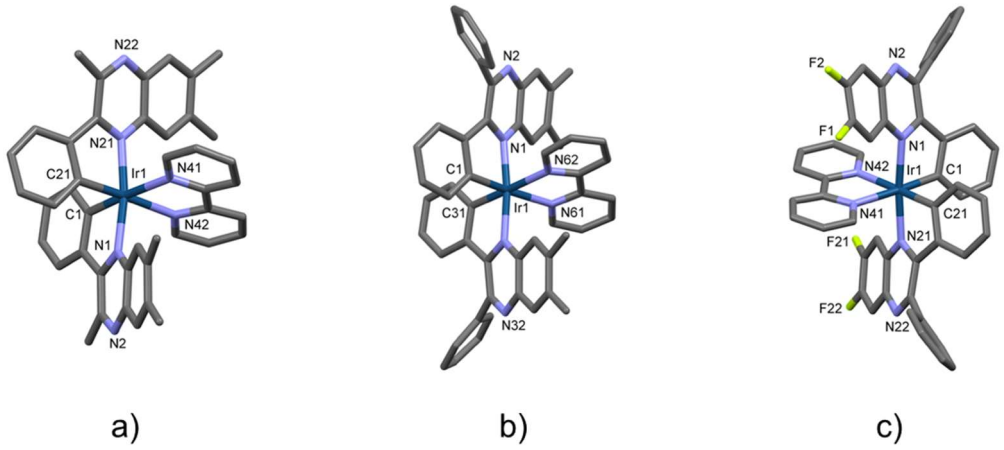

Figure 2.13: X-ray structures of the cation in the complexes a) ***[Ir(L2)$_2$(bpy)]PF$_6$;*** *b)* ***[Ir(L5)$_2$(bpy)]PF$_6$*** *and c)* ***[Ir(L7)$_2$(bpy)]PF$_6$.***

The structures also reveal that the ligand-Ir bond lengths match those expected for iridium(III) species. Additionally, it can be seen in the packing diagrams that there are intermolecular π-π interactions between the phenyl rings of quinoxaline ligands on neighbouring complexes. These rings are highlighted in blue in Figure 2.14.

Table 2.2: Selected bonds lengths for complexes C2a, C5a and C7a.

C2a			**C5a**			**C7a**		
Atom	**Atom**	**Length/Å**	**Atom**	**Atom**	**Length/Å**	**Atom**	**Atom**	**Length/Å**
Ir1	N1	2.067(3)	Ir1	N1	2.050(7)	Ir1	N1	2.090(6)
Ir1	N21	2.090(3)	Ir1	N31	2.071(8)	Ir1	N21	2.081(6)
Ir1	N41	2.167(3)	Ir1	N61	2.149(7)	Ir1	N41	2.161(6)
Ir1	N42	2.176(3)	Ir1	N62	2.179(7)	Ir1	N42	2.168(6)
Ir1	C1	1.992(4)	Ir1	C1	1.999(9)	Ir1	C1	1.987(7)
Ir1	C21	2.014(4)	Ir1	C31	2.004(9)	Ir1	C21	2.004(7)
						Ir2	N51	2.083(7)
						Ir2	N71	2.101(7)
						Ir2	N91	2.143(6)
						Ir2	N92	2.174(6)
						Ir2	C51	1.984(8)

						Ir2	C71	1.985(7)

Table 2.3: Selected bond angles for complexes C2, C5 and C7.

C2a				C5a				C7a			
Atom	**Atom**	**Atom**	**Angle/°**	**Atom**	**Atom**	**Atom**	**Angle/°**	**Atom**	**Atom**	**Atom**	**Angle/°**
N1	Ir1	N21	170.94 (13)	N1	Ir1	N31	173.2(3)	N1	Ir1	N41	100.1(2)
N1	Ir1	N41	102.78 (13)	N1	Ir1	N61	100.3(3)	N1	Ir1	N42	82.9(2)
N1	Ir1	N42	84.10(13)	N1	Ir1	N62	81.5(3)	N21	Ir1	N1	174.3(2)
N21	Ir1	N41	82.80(13)	N31	Ir1	N61	84.6(3)	N21	Ir1	N41	84.1(2)
N21	Ir1	N42	104.35 (13)	N31	Ir1	N62	104.3(3)	N21	Ir1	N42	102.0(2)
N41	Ir1	N42	75.46(13)	N61	Ir1	N62	75.8(3)	N41	Ir1	N42	75.7(2)
C1	Ir1	N1	79.48(15)	C1	Ir1	N1	80.1(3)	C1	Ir1	N1	79.9(3)
C1	Ir1	N21	96.25(15)	C1	Ir1	N31	95.7(3)	C1	Ir1	N21	96.2(3)
C1	Ir1	N41	170.06 (14)	C1	Ir1	N61	172.2(3)	C1	Ir1	N41	174.8(3)
C1	Ir1	N42	95.29(14)	C1	Ir1	N62	96.7(3)	C1	Ir1	N42	99.1(3)
C1	Ir1	C21	87.66(16)	C1	Ir1	C31	88.2(3)	C1	Ir1	C21	85.8(3)
C21	Ir1	N1	92.62(15)	C31	Ir1	N1	95.2(3)	C21	Ir1	N1	96.2(3)
C21	Ir1	N21	79.15(16)	C31	Ir1	N31	79.4(4)	C21	Ir1	N21	79.2(3)
C21	Ir1	N41	101.82 (14)	C31	Ir1	N61	99.5(3)	C21	Ir1	N41	99.4(3)
C21	Ir1	N42	175.10 (15)	C31	Ir1	N62	173.5(3)	C21	Ir1	N42	174.8(3)
								N51	Ir2	N71	173.8(2)
								N51	Ir2	N91	100.3(2)
								N51	Ir2	N92	81.9(2)
								N71	Ir2	N91	83.8(2)
								N71	Ir2	N92	103.8(3)
								N91	Ir2	N92	75.6(2)
								C51	Ir2	N51	79.7(3)

C2a				C5a				C7a			
Atom	**Atom**	**Atom**	**Angle/°**	**Atom**	**Atom**	**Atom**	**Angle/°**	**Atom**	**Atom**	**Atom**	**Angle/°**
								C51	Ir2	N71	96.8(3)
								C51	Ir2	N91	173.2(3)
								C51	Ir2	N92	97.7(3)
								C51	Ir2	C71	87.9(3)
								C71	Ir2	N51	95.4(3)
								C71	Ir2	N71	79.2(3)
								C71	Ir2	N91	98.9(3)
								C71	Ir2	N92	173.2(3)
								N51	Ir2	N71	173.8(2)
								N51	Ir2	N91	100.3(2)

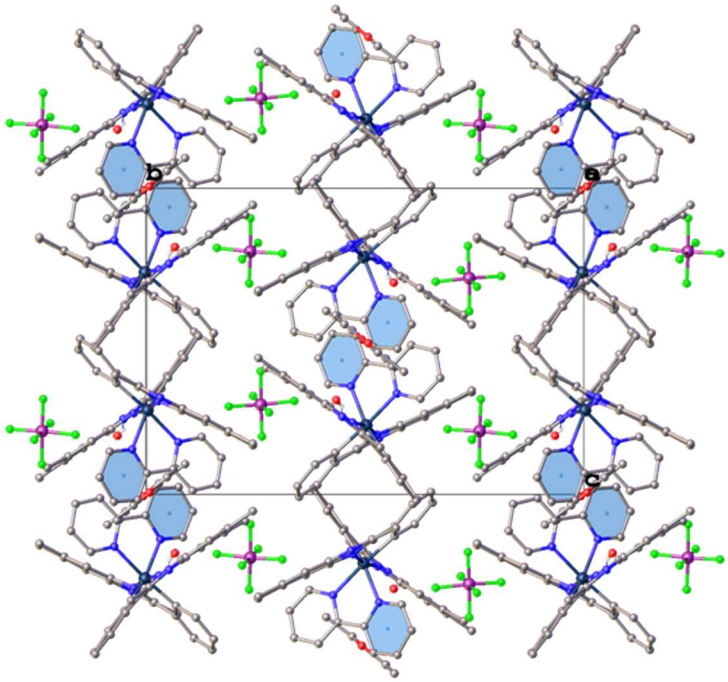

Figure 2.14: Packing diagram of complex C2a showing intermolecular π-π interactions of aromatic rings highlighted in blue.

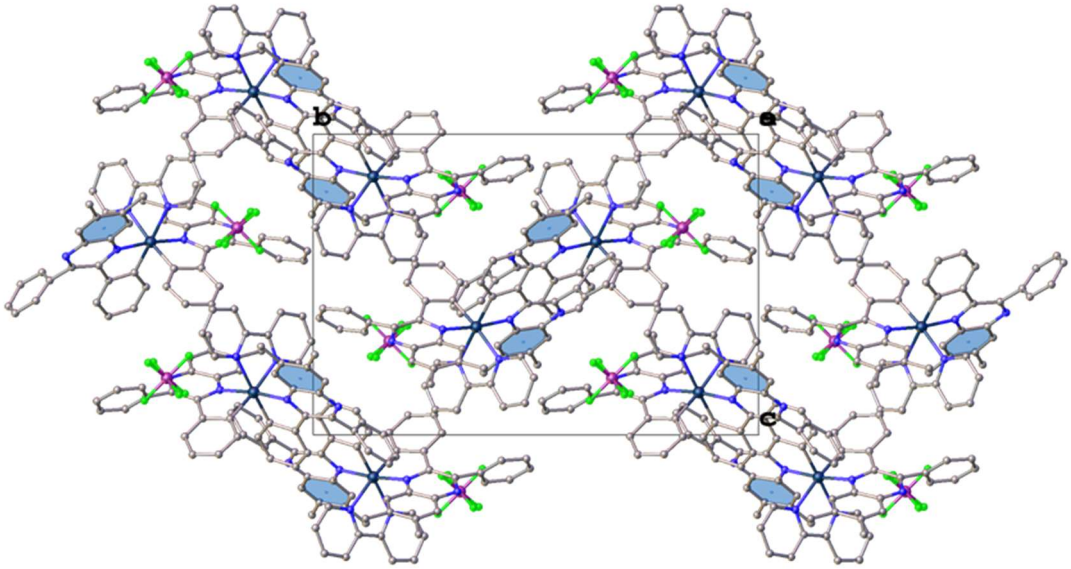

Figure 2.15: Packing diagram of complex C5a

Figure 2.16 shows the crystal structure of complex C5a overlaid with the computationally optimised structure. The computational work in this study was carried out by Thomas Stonelake and Dr Joseph Beames (Cardiff University). From the figure, it can be observed that the computational method used is able to adequately reproduce the crystal structure (RMSD < 0.5 Å), with the position of the methyl substituents introducing the major source of discrepancy which is likely from a combination of errors in both crystallography and DFT. The methyl groups have low frequency vibrational motions associated with flexing and torsional motions which can account for this discrepancy.

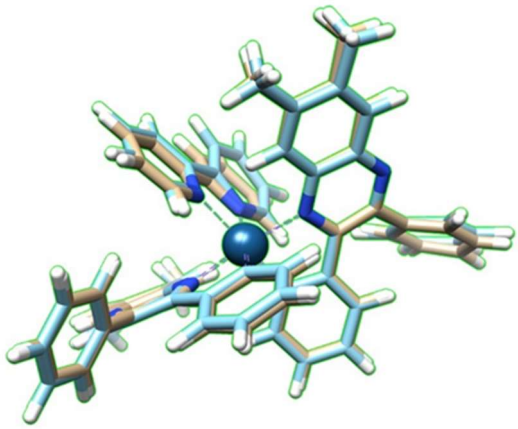

Figure 2.16: Overlay of the crystal structure (blue) and DF-DFT//B3LYP/6-31G(SDD) optimised structures (brown) for* ***[Ir(L5)$_2$(bpy)]PF$_6$****. The structures exhibit an RMSD of 0.427 Å.*

There is also some discrepancy at the bipyridine position where the computationally optimised structure is closer to C_2 symmetry. The RMSD value for complex C2a is < 0.2 Å between the crystallography and computational geometry which also illustrates this effect.

2.3.3. Cyclic Voltammetry

Cyclic voltammetry measurements were carried out upon the complexes in de-oxygenated dichloromethane. The cyclic voltammograms were measured by using a platinum disc electrode (scan rate υ = 200 mVs^{-1}, $1x10^{-3}$ M solutions, 0.1 M $[NBu_4][PF_6]$ as a supporting electrolyte). Each complex showed an irreversible oxidation process between + 1.4 and +1.6 V, which was assigned to a $Ir^{3+/4+}$ process. The lowest E_{ox} values were observed for the methylated species C1, C2 and C5 which is consistent with the electron-donating ability of the quinoxaline ligands. The signal at around -0.9 V is irreversible and was assigned to a ligand centred reduction. An example voltammogram recorded for complex C4 is shown in Figure 2.17.

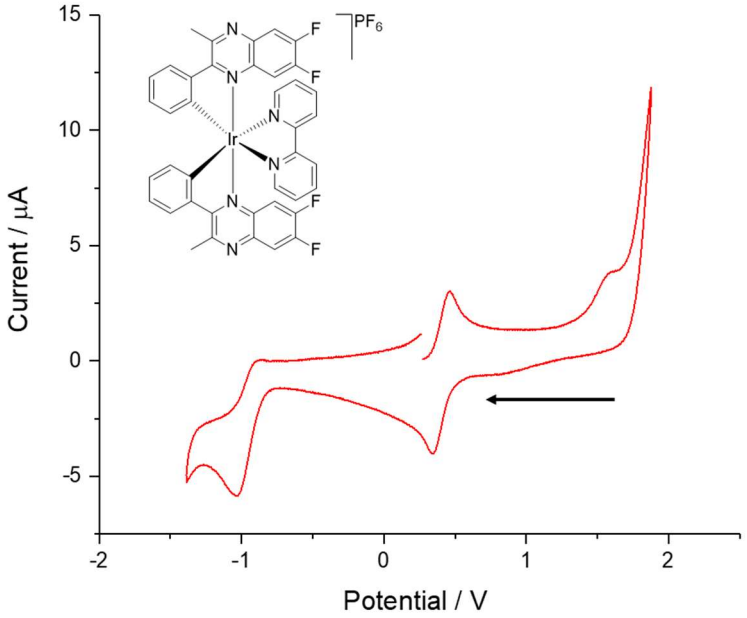

Figure 2.17: Cyclic voltammograms recorded for complex C4 $[(Ir(L4)_2(bpy))(MeCN)][PF_6]_2$ under argon. Voltammogram recorded in 0.25 M $[NH_4][PF_6]$, scan rate υ = 200 mV/s with Fc/Fc^+ couple at +0.46 for reference.

2.3.4. Photophysical Properties

The UV-vis absorption spectra of ligands HL1-7 are shown in Figure 2.18. All of the ligands absorb light in the UV region of the spectrum. The transitions shown arise from π-π* transitions in addition to n-π* transitions due to the heteroatom in the aromatic ring.

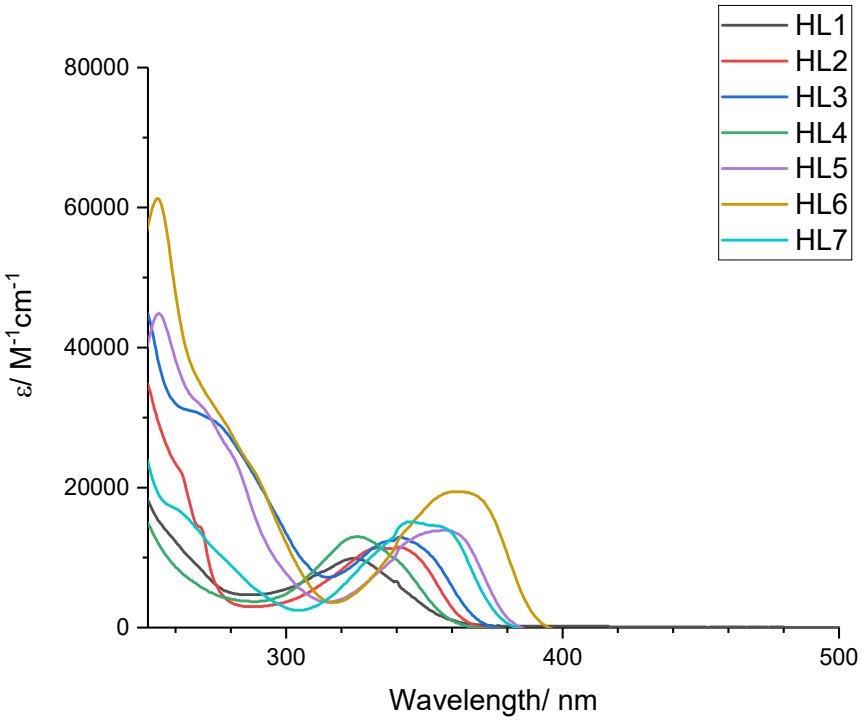

Figure 2.18: UV-vis absorption spectra of ligands HL1-7 recorded in chloroform ($1x10^{-5}$ M)

The spectra also show that the substituents on the ligands have an influence on the wavelength of light absorbed by the molecule. The unsubstituted ligand, HL1, has the lowest λ_{max} value at 325 nm, whilst the chloro-substituted ligand, HL6, has the highest value at 362 nm. It is also worth noting that the ligands with two phenyl substituents have longer absorption wavelengths than their counterparts with one phenyl and one methyl group.

The steady state emission spectra of the free ligands were also recorded and the results are shown in Figure 2.19. All of the ligands emit light in the UV region of the spectrum and the emission profiles of the ligands match what would be expected from their absorption spectra, in that the ligand with the longest λ_{max} value, HL6, has the longest emission wavelength at 408 nm. Overall, there is an emission range of 45 nm across the series.

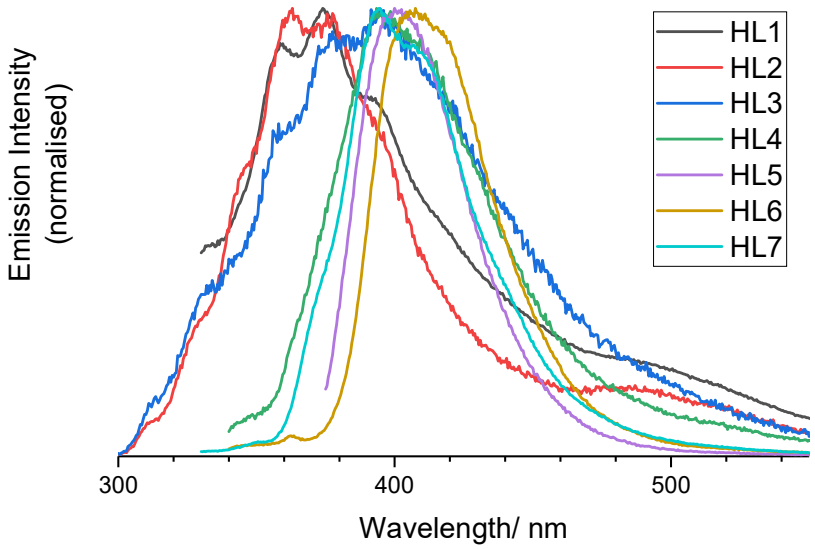

Figure 2.19: Steady state emission spectra of ligands HL1-HL7. Spectra recoded in chloroform, λ_{ex} = 350 nm.

All of the complexes in this study were also characterised by UV-vis absorption spectroscopy and luminescence spectroscopy.

The UV-vis absorption spectra of complexes C1a-7a were recorded in chloroform at a concentration of $1x10^{-5}$ M. The overlaid spectra of the complexes are shown in Figure 2.20 and show that each possesses three distinct features. The bands with high molar extinction coefficients between 260 and 400 nm are associated with ligand-centred transitions from the quinoxaline and bipyridine ligands. These are assigned as π-π* transitions; it is also likely that there are some n-π* transitions arising from the heteroatoms in the quinoxaline backbone. There is a weak, broad signal at between 474-498 nm with ε ~ 5000 $M^{-1}cm^{-1}$, that along with a stronger feature at 400-450 nm possess some metal-to-ligand charge transfer (MLCT) character. The exact position of these bands is dependent upon the substituents on the quinoxaline ligand with the halogenated species showing longer absorption wavelengths, and the methylated species having the shortest values. All complexes also showed a much weaker feature that extended to around 600 nm, which has typically been attributed to the spin-forbidden ^{3}MLCT transition in iridium(III) species.

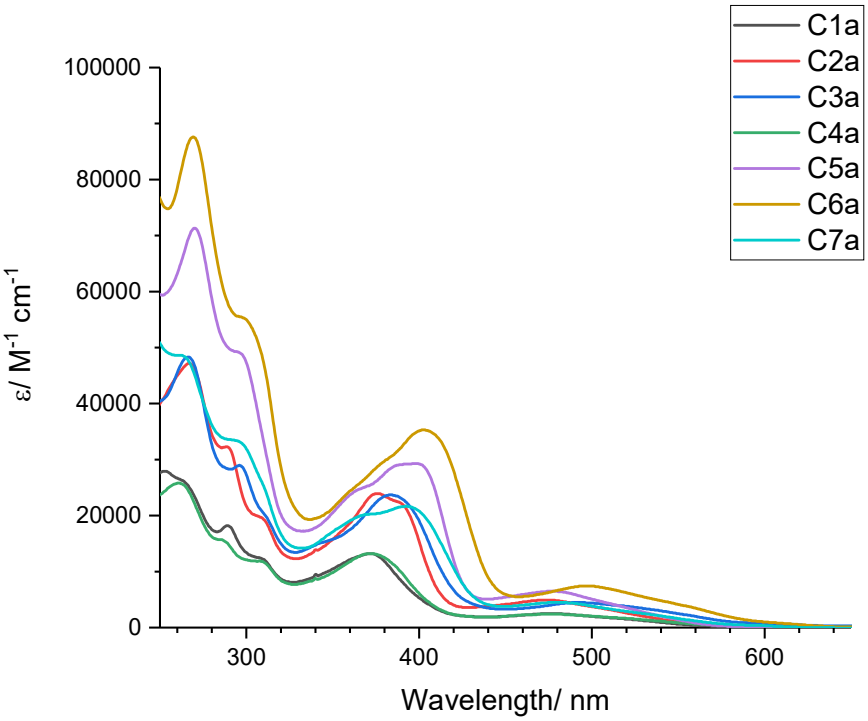

Figure 2.20: UV-vis absorption spectra of complexes C1a-7a. Recorded in $CHCl_3$, $1x10^{-5}$ M

A comparison of the absorption spectrum of HL1 and the absorption spectrum of C1a is shown in Figure 2.21. The feature at around 400-450 nm in the spectrum of the complex is not seen in the spectrum of the ligand, confirming that this transition does have some MLCT character. In addition to this, the absorption at 325 nm in the ligand, has red-shifted to 372 nm in the complex.

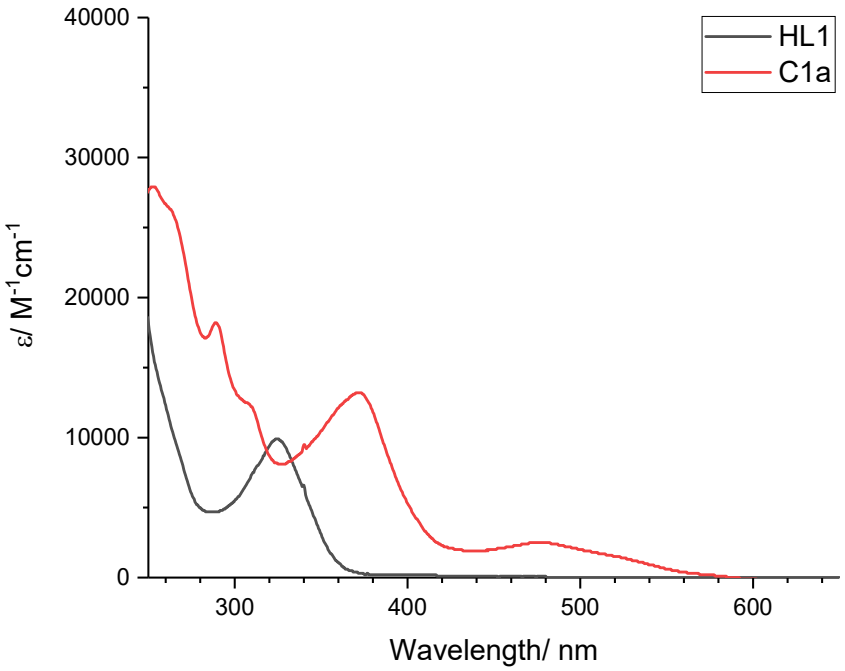

Figure 2.21: Comparison between absorption spectra of HL1 and C1a.

2.3.5. Density Functional Theory

All computational studies in this piece of work were carried out by Thomas Stonelake and Joseph Beames (Cardiff University). A more in-depth discussion of this work can be found in the publication in the appendix of this thesis.[40]

The Kohn-Sham frontier orbitals of complex C1a were calculated and are shown in Figure 2.22. These calculations show that the occupied molecular orbitals have strong Ir 5d character while the unoccupied orbitals are more ligand centred. The contributions to the HOMO are equally split between the metal (33 %) and the two quinoxaline ligands (33 and 33 %), with a negligible contribution from the 2,2'-bipyridine ligand (1 %). However, the LUMO is predominantly quinoxaline ligand centred (48 and 47 %). Table 2.4 shows the contributions for each complex in the series.

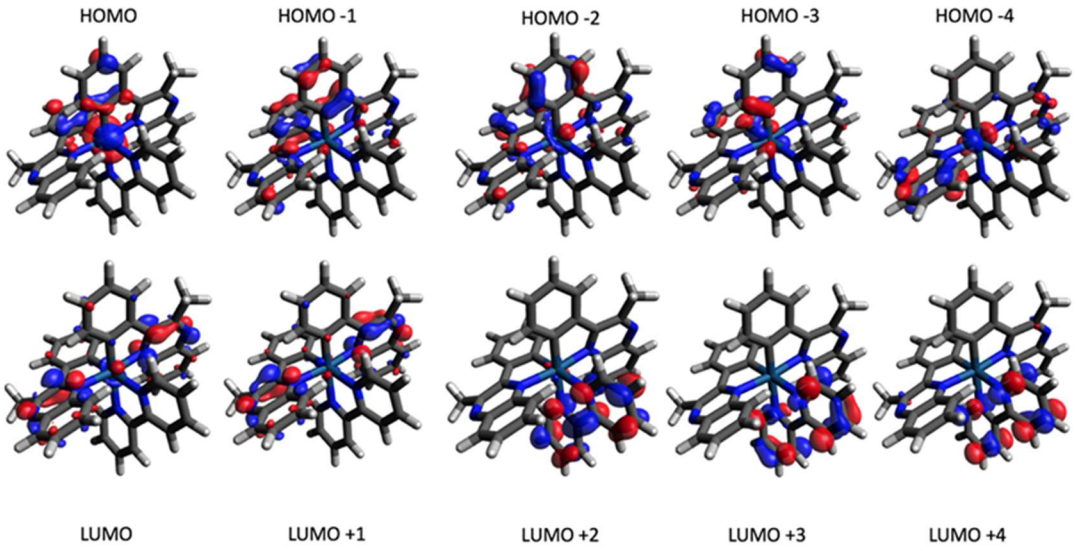

Figure 2.22: Isosurfaces of the Kohn-Sham ***[Ir(L1)$_2$(bpy)]PF$_6$*** *frontier molecular orbitals (DFT//B3LYP/6-31G*)*

Table 2.4: Excitation contributions to the lowest lying singlet excited states of complex C1. Only single electron excitation contributions greater than 10 % are shown. Q1 and Q2 pertain to the two quinoxaline ligands.

	Moiety Contribution to Molecular Orbital (%)			
Orbital	**Ir (5d)**	**Bpy**	**Q1**	**Q2**
LUMO + 4	1	67	16	16
LUMO + 3	2	79	9	9
LUMO + 2	2	97	0	1
LUMO + 1	4	1	47	48
LUMO	3	2	48	47
HOMO	33	2	33	33
HOMO – 1	3	1	48	48
HOMO – 2	10	1	44	45
HOMO – 3	22	3	38	37
HOMO - 4	17	0	43	40

For complex C1a, the longest wavelength singlet excitation was predicted to be at 405 nm and does not account for the broad feature observed at around 475 nm in the absorption spectrum. This feature is typically assigned to the formally spin forbidden $T_1 \leftarrow S_0$ transition but may become weakly allowed due to spin-orbit coupling effects (Table 2.5). This is also in agreement with the energy of the T_1 state which corresponds to a predicted ^{3}MLCT band at 514 nm. Figure 2.23 shows that these values compare qualitatively with the observed UV-vis spectrum of C1a.

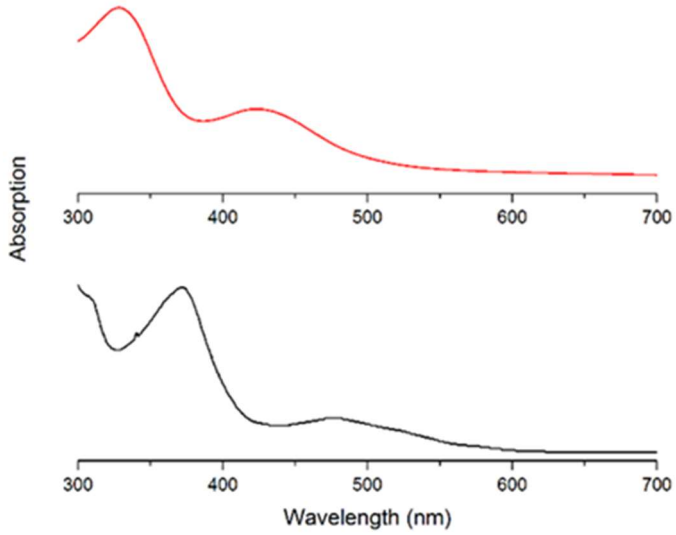

Figure 2.23: Bottom) Experimental absorption spectrum of complex C1a. Top) TD-DFT//CAM-B3LYP/6-31 G(SDD) convoluted absorption spectrum.*

These calculations suggest that the low-energy transition at between 400-450 nm, formerly assigned as having MLCT character, is not purely MLCT. In fact, the major contribution to this transition is ligand centred, which can explain why the energy of this transition depends upon the ligand substituents. This is also supported by the experimental steady state emission data, discussed below.

Due to the favourable correlation between the experimental and computed UV-vis absorption spectra, the relative band positions of all complexes have been calculated and are displayed in Table 2.5.

Table 2.5: Computed spectral properties for all complexes; experimentally observed band positions are given in parentheses. Values in italic are those calculated for an adiabatic system. The experimental spin-allowed absorption band positions are taken from the band onsets, whereas the spin-forbidden parameters are λmax value. (a) Recorded in chloroform. (b) Recorded in chloroform; λ_{ex} = 355 nm.

Compound[a]	**$S_1 \leftarrow S_0$ / nm[a]**	**$T_1 \leftarrow S_0$ / nm[b]**	**$T_1 \rightarrow S_0$ / nm[b]**
C1a	405 (372)	541 (477)	691, *607* (627)
C2a	402 (402)	533 (474)	698, *605* (617)
C3a	419 (406)	565 (500)	708, *630* (634)
C4a	409 (394)	552 (480)	692, *612* (624)
C5a	406 (417)	540 (479)	723, *618* (624)
C6a	423 (428)	572 (501)	730, *642* (645)
C7a	414 (418)	555 (483)	716, *626* (632)

The steady state emission spectra were also recorded for each complex. The species with the longest emission wavelength is the chlorinated complex C6a, with λ_{em} = 642 nm. The shortest

emission wavelength recorded was 616 nm for complex C2a, the trimethylated species. In general, the emission profiles of the complexes follow the same trend seen in the emission spectra of the free ligands, with the halogenated species recording longer wavelengths than the methylated and unsubstituted species. The bathochromic shift observed upon chlorination is a result of changing electronic character of the system, which is clearly shown by the reproducibility of this trend in the $T_1 \leftarrow S_0$ TD-DFT calculations in Table 2.5.

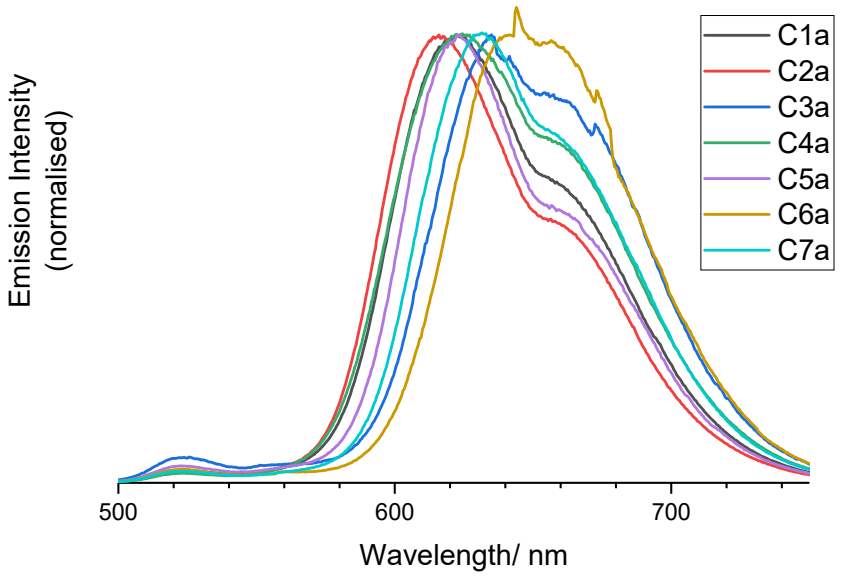

Figure 2.24: Overlaid steady state emission spectra for complexes C1a-7a. λ_{ex} = 450 nm.

Time resolved measurements were also carried out on the complexes. The luminescence lifetime of each complex was measured in chloroform and the results are tabulated below. The lifetimes of the complexes range from 307 - 539 ns with the longest value recorded for the fluorinated complex, C7a, and the shortest value recorded for the chlorinated complex, C6a. The cause of the reduced emission lifetime for the chlorinated species cannot be explained through a mixture of electronic and relativistic effects. It is most likely due to an increase in intersystem crossing rates, which is supported by the particularly high k_r value calculated for the chlorinated complex, C6a. Further computational studies were able to confirm that chlorine substitution of the quinoxaline ligands leads to an increase in S_0/T_1 spin-orbit coupling (SOC), which leads to a shorter T_1 lifetime value.

Table 2.6: Photophysical data for complexes C1a-7a.

Complex	A τ/ ns	B Φ/ %	k_{nr}/ 10^6 s^{-1}	k_r/ 10^5 s^{-1}
C1a	459	5.7	2.05	0.79
C2a	453	5.1	2.09	1.18
C3a	337	1.8	2.91	0.53
C4a	396	6.0	2.37	1.51
C5a	440	6.6	2.12	1.50
C6a	307	6.4	3.05	2.08
C7a	539	7.8	1.71	1.45

The recorded lifetimes showed mono-exponential decay character in each case which is consistent with a single emitting state. The length of the lifetimes also suggest that the nature of the emission is phosphorescent in character for all complexes. The complexes also showed sensitivity to quenching by triplet oxygen ($^3O_2$), as lifetimes extending into the microsecond domain were observed upon degassing the samples. Therefore, all of the photophysical data recorded are consistent with an emitting state that possesses a significant ^{3}MLCT contribution.

2.3.6. Transient Absorption Spectroscopy

Transient absorption spectra of the complexes were measured by Thomas Stonelake and Joseph Beames (Cardiff University). As in the case of the DFT calculations, a more detailed discussion is provided in the appendix of this work.[40]

The TA spectrum of complex C1a is shown in Figure 2.25 and is illustrative of the spectra collected for all complexes. The main features in the spectrum are a ground state bleaching at 355 nm, shown by a negative ΔOD value, two features at around 430 and 560 nm, which correspond to triplet-triplet absorptions, and a long wavelength transition which has been attributed to the spin-forbidden $T_1 \rightarrow S_0$ transition. These features are all consistent with the computational calculations discussed earlier.

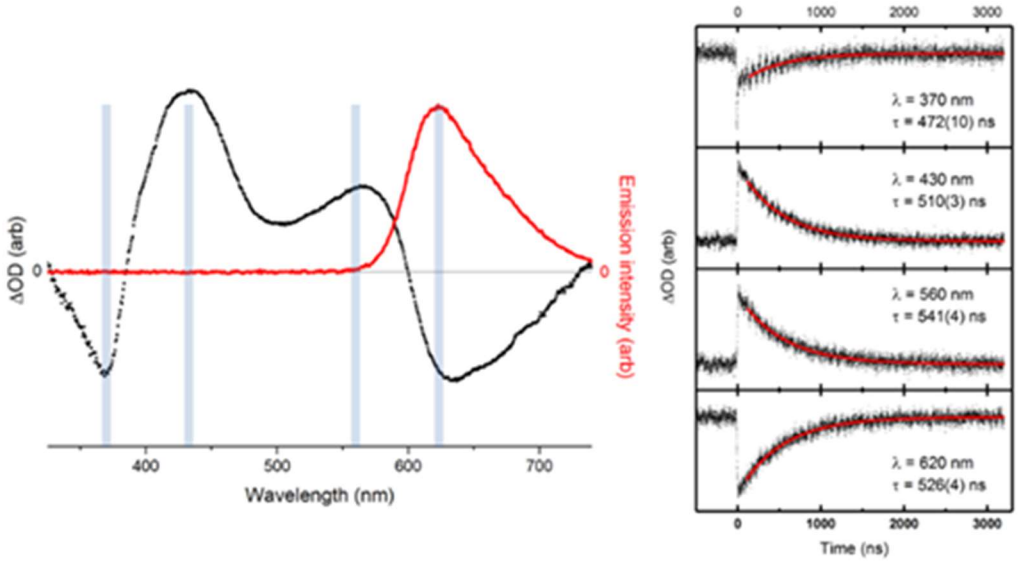

Figure 2.25: Left) Transient absorption spectrum of complex C1a shown in black, overlaid with the emission spectrum of the same complex shown in red. Right) Transient absorption lifetime measurements made at selected wavelengths, highlighted as grey bars in the left hand figure. The red traces indicate mono-exponential fits to these measurements with corresponding lifetimes displayed in each panel. Recorded in chloroform, λ_{ex} = 355 nm.

Each feature in the spectrum exhibits a similar TA lifetime which suggests that they all relate to the same photoexcitation, ISC process and deactivation. This has been attributed to the formation of the lowest triplet state and compares relatively well with the observed lifetime from time-resolved emission measurements.[41] Figure 2.26 shows a comparison of TA spectra for the complexes C1a, C5a and C6a. It can be seen that each spectrum has similar features with the exception of the ground state bleaching which appears as a doublet in the case of C5a and C6a, and does not show the same spectral shape as complex C1a.

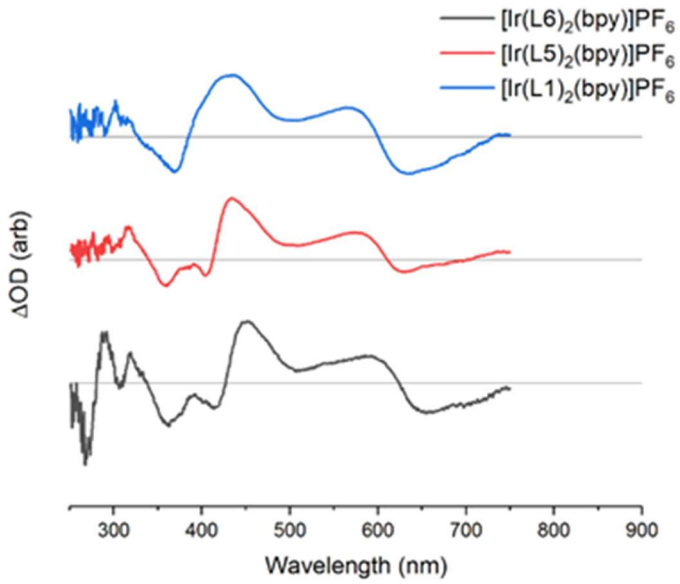

Figure 2.26: Transient absorption spectra of complexes C1a, C5a and C6a. The spectra show qualitatively similar features. Recorded in chloroform; λ_{ex} = 355 nm.

2.3.7. Triplet-Triplet Annihilation Upconversion Measurements

Triplet-triplet annihilation upconversion luminescence experiments were carried out by Kepeng Chen, Yuqi Hou and Prof. Jianzhang Zhao (Dalian University of Technology).

These experiments were carried out in degassed toluene, using the complexes as the donor and 9,10-diphenylanthracene (DPA) as the acceptor. Figure 2.27 shows the emission spectra recorded in degassed toluene. The graphs show overlaid emission spectra of the complex alone in solution and a mixture of the complex and DPA following excitation at 510 nm. The DPA triplet excited state lies below the triplet emitting levels of all the complexes in the series.

When a solution of DPA is irradiated at 510 nm, no emission is observed. In contrast to this, in the majority of cases irradiation of a mixture of complex and DPA at the same wavelength produced an emission at 400-500 nm arising from the DPA. This is indicative of an upconversion process. This was most pronounced in complexes C1a, C2a and C5a which showed significant quenching of the ^{3}MLCT emission band.

These findings were also supported by the measured quantum yields for upconversion shown in Table 2.7. The results varied across the series, but by far the best performing species were the methylated complexes C1a and C2a. These complexes displayed quantum efficiencies of 26 and 39 % respectively, with the latter being the highest recorded value for TTA upconversion with a triplet sensitiser.

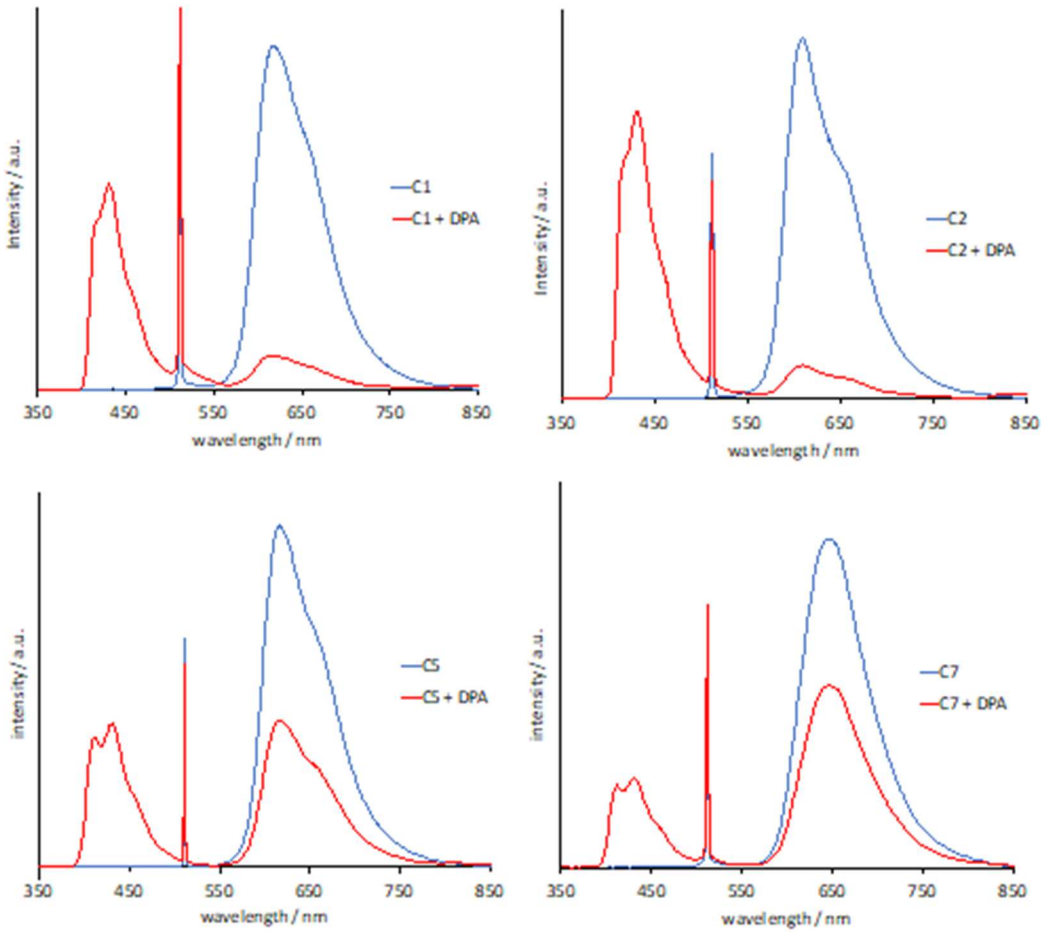

Figure 2.27: Clockwise from top left: The upconversion fluorescence of C1a, C2a, C7a and C5a as photosensitisers in toluene. DPA was used as the acceptor. excitation was achieved with a continuous laser at l = 510 nm and power density of 5.2 mW under a deaerated atmosphere. c(sensitiser) = 1.0x10^{-5} M; c(DPA) = 1.6x10^{-3}, 1.6x10^{-3}, 2.6x10^{-4} and 2.0x10^{-4} M, respectively; 20 ˚C.

The poorest performing complexes were the chlorinated species C3a and C6a. Previous reports have suggested that high molar absorption coefficients in the visible region and long triplet excited-state lifetimes are necessary for efficient triplet sensitisers.[42] As noted earlier, the chlorinated species have some of the shortest lifetimes in the series which goes some way to explaining their low upconversion efficiencies.

Table 2.7: Emission and upconversion data of the complexes recorded in toluene. (a) Recorded in air. (b) Recorded in deaerated toluene. (c) diiodi-BODIPY used as standard (Φ_F = 0.027 in acetonitrile)

Compound	λ_{em} (nm)	τ_{obsd} (µs)[(a)]	τ_{obsd} (µs)[(b)]	Φ_{UC} (%)[(c)]
C1a	618	0.41	2.2	25.9
C2a	609	0.38	2.3	39.3
C3a	656	0.38	0.8	0.1
C4a	638	0.39	1.6	2.0
C5a	617	0.37	2.0	9.6
C6a	660	0.35	1.8	1.0
C7a	646	0.38	1.3	4.0

When recorded in toluene, the luminescence measurements showed a larger range in emission properties. The methylated species display the highest emission energies and longest lifetime values, while the chlorinated complexes show the longest emission wavelength and the shortest lifetimes. Figure 2.28 shows a visual representation of the upconversion process. This photograph shows the best performing complexes, C1a and C2a.

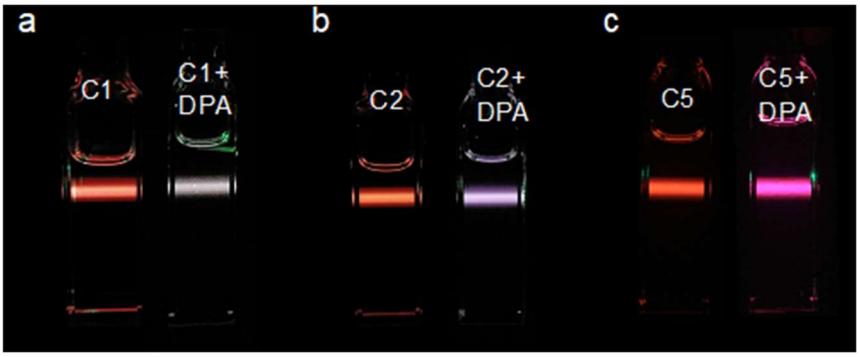

Figure 2.28: Photographs of the emission of selected triplet donors C1a, C2a and C5a alone and the upconversion with DPA in toluene. Excitation was achieved with a continuous laser of λ = 510 nm and power density of 5.2 mW under a deaerated atmosphere. c(sensitisers) = 1x10^{-5} M; c(DPA) = a) 1.6x10^{-3}, b) 1.6x10^{-3} and c) 2.0x10^{-4} M; 20 ˚C.

2.4. Conclusion

In this chapter of work, seven cationic bis-cyclometallated iridium(III) complexes have been successfully synthesised using (poly)substituted quinoxaline ligands. Photophysical studies have shown that the ligand substituents have an effect upon the emission wavelength and lifetimes of these species. This was also confirmed by computational studies which suggest that the emissive state is not purely MLCT in nature but has a significant ligand-centred contribution.

Of the complexes synthesised, the methylated species C1a and C2a have shown particularly high upconversion efficiency when used as sensitisers in triplet-triplet annihilation upconversion. The higher energy and longer-lived excited state triplet emission are two factors that enhance performance. In contrast, the chlorinated complexes show much shorter lifetimes and this is reflected in their poor performance in upconversion experiments. This may be attributed to enhanced ISC which is facilitated by the chlorine substituents, leading to a faster non-radiative deactivation of the ^{3}MLCT state.

2.5. Experimental

All reactions were performed with the use of vacuum line and Schlenk techniques. Reagents were commercial grade and were used without further purification. ^{1}H and $^{13}C\{^{1}H\}$ NMR spectra were measured on NMR-FT Bruker 300 or 400 spectrometers and recorded in CDCl3. Low-resolution mass spectra were obtained by the staff at Cardiff University. High-resolution mass spectra were carried out by at the EPSRC National Mass Spectrometry Service at Swansea University. UV-Vis studies were performed on a Shimadzu UV-1800 as chloroform solutions (10^{-5} M). Photophysical data were obtained on a JobinYvon-Horiba Fluorolog spectrometer fitted with a JY TBX picosecond photodetection module as MeCN solutions. Emission spectra were uncorrected and excitation spectra were instrument corrected. The pulsed source was a Nano-LED configured for 372 nm output operating at 1 MHz. Luminescence lifetime profiles were obtained using the JobinYvon-Horiba FluoroHub single photon counting module and the data fits yielded the lifetime values using the provided DAS6 deconvolution software.

Synthesis of 2-methyl-3-phenylquinoxaline HL1 1-phenyl-1,2-propanedione (2.0 mL, 15 mmol) and 1,2-diaminobenzene (1.60 g, 15 mmol) were dissolved in ethanol (30 mL) with acetic acid (1 mL). The reaction mixture was heated at reflux for 24 hours under a nitrogen atmosphere. The mixture was cooled to room temperature and the solvent removed *in vacuo*. The crude product was taken up in dichloromethane (20 mL) and washed with hydrochloric acid (0.1 M, 2x 20 mL). The organic phase was dried over $MgSO_4$ and dried *in vacuo* to yield a low melting-point, yellow solid (Yield = 3.26 g, 81 %). ^{1}H NMR (400 MHz; $CDCl_3$): δ_H 8.10 (1H, d, J_{HH} = 8.37 Hz, Ar), 8.05 (1H, d, J_{HH} = 8.37 Hz, Ar), 7.67-7.75 (3H, m, Ar), 7.65 (2H, d, J_{HH} = 7.15 Hz, Ar), 7.44-7.54 (3H, m, Ar), 2.77 (3H, s, Me), 2.51 (3H, s, Me) ppm. $^{13}C\{^{1}H\}$ NMR (75 MHz, $CDCl_3$): δ_C 155.7, 153.3, 142.0, 141.7, 139.8, 130.5, 130.0, 129.8, 129.7, 129.3, 129.1, 25.2 ppm. HRMS (ESI) found m/z 220.1072, calcd m/z 220.1073 for $C_{15}H_{12}N_2$; UV vis. ($CHCl_3$) λ_{max} (ε / $dm^3mol^{-1}cm^{-1}$): 325 (9400) nm. IR (solid) υ / cm^{-1} : 3061, 3032, 2961, 1952, 1813, 1686, 1611, 1578, 1557, 1508, 1495, 1483, 1443, 1431, 1395, 1375, 1341, 1248, 1217, 1188, 1132, 1117, 1074, 1030, 1005, 993, 974, 950, 921, 897, 868, 818, 797, 708, 679, 619, 608, 575, 559, 496, 467, 436, 409, 401.

Synthesis of HL2 As L1 but with 1-phenyl-1,2-propanedione (246 mg, 1.7 mmol) and 1,2-diamino-4,5-dimethylbenzene (250 mg, 1.8 mmol). Product collected as a low melting-point, brown solid. (Yield = 361 mg, 86 %). ^{1}H NMR (300 MHz, $CDCl_3$): δ_H 7.85 (s, 1H), 7.80 (s, 1H), 7.64 – 7.62 (m, 2H), 7.53 – 7.44 (m, 3H), 2.74 (s, 3H), 2.50 (s, 3H), 2.48 (s, 3H) ppm. $^{13}C\{^{1}H\}$ NMR (101 MHz, $CDCl_3$): δ_C 153.92, 151.29, 140.27, 139.97, 139.62, 139.32, 128.97, 128.76, 128.49, 128.28, 127.33, 24.20, 20.44, 20.34 ppm. HRMS (ESI) found *m/z* 249.1385, calcd *m/z* 249.1386 for $C_{17}H_{16}N_2$. UV vis. ($CHCl_3$) λ_{max} (ε / $dm^3mol^{-1}cm^{-1}$): 339 (11200), 269 (11400), 262 (21800) nm. IR (solid) υ / cm^{-1} : 3060, 3030, 2961, 1654, 1483, 1445, 1398, 1373, 1337, 1252, 1217, 1204, 1157, 1123, 1076, 1024, 1003, 988, 920, 876, 870, 858, 785, 768, 739, 706, 696, 644, 629, 610, 559, 532, 494, 478, 440, 420, 403.

Synthesis of HL3 As L1 but with 1-phenyl-1,2-propanedione (190 mg, 1.3 mmol) and 1,2-diamino-4,5-dichlorobenzene (250 mg, 1.4 mmol). Upon cooling to room temperature, a white precipitate formed and was collected by filtration. The precipitate was washed with methanol to yield the product as a white solid. (Yield = 283 mg, 73 %). ^{1}H NMR (300 MHz, $CDCl_3$): δ_H 8.22 (s, 1H), 8.17 (s, 1H), 7.66 – 7.62 (m, 2H), 7.58 – 7.52 (m, 3H), 2.77 (s, 3H) ppm. $^{13}C\{^{1}H\}$ NMR (75 MHz, $CDCl_3$): δ_C 155.92, 154.01, 139.97, 139.77, 138.27, 133.69, 129.47, 129.12, 128.91, 128.69, 109.99, 24.54 ppm. HRMS (ESI) found *m/z* 291.0268, calcd *m/z* 291.0264 for $C_{15}H_{10}Cl_2N_2$. UV vis. ($CHCl_3$) λ_{max} (ε / $dm^3mol^{-1}cm^{-1}$): 342 (12800), 268 (30700) nm. IR (solid) υ / cm^{-1} : 3088, 1753,

1697, 1587, 1543, 1491, 1441, 1412, 1389, 1371, 1325, 1246, 1209, 1180, 1169, 1107, 1078, 1022, 1005, 993, 976, 955, 930, 897, 878, 845, 795, 768, 748, 706, 658, 635, 629, 613, 594, 550, 509, 490, 461, 428, 417.

Synthesis of HL4 As for L1 but with 1-phenyl-1,2-propanedione (230 mg, 1.6 mmol) and 1,2-diamino-4,5-difluorobenzene (250 mg, 1.7 mmol). Upon cooling to room temperature, a white precipitate formed and was collected by filtration and washed with methanol. Product collected as a white solid. (Yield = 225 mg, 55 %). ^{1}H NMR (300 MHz, $CDCl_3$): δ_H 7.87 – 7.77 (m, 2H), 7.65 – 7.62 (m, 2H), 7.56 – 7.49 (m, 3H), 2.76 (s, 3H) ppm. $^{13}C\{^{1}H\}$ NMR (101 MHz, $CDCl_3$): δ_C 138.44, 129.29, 128.88, 128.66, 114.78, 114.03, 24.29 ppm. $^{19}F\{^{1}H\}$ NMR (376 MHz, $CDCl_3$): δ_F -130.38 (d, *J* = 21.2 Hz), -131.17 (d, *J* = 21.2 Hz) ppm. HRMS (ESI) found *m/z* 257.0888, calcd *m/z* 257.0885. UV vis. ($CHCl_3$) λ_{max} (ε / $dm^3mol^{-1}cm^{-1}$): 326 (13000) nm. IR (solid) υ / cm^{-1} : 3030, 1630, 1572, 1553, 1497, 1450, 1373, 1356, 1339, 1256, 1227, 1200, 1142, 1078, 1015, 1005, 988, 928, 897, 874, 866, 791, 772, 752, 712, 706, 667, 619, 611, 584, 544, 484, 447, 419, 405.

Synthesis of HL5 Benzil (357 mg, 1.7 mmol) and 1,2-diamino-4,5-dimethylbenzene (250 mg, 1.8 mmol) were dissolved in ethanol (15 mL) and acetic acid (1 mL). The reaction mixture was heated at reflux under a nitrogen atmosphere for 24 hours. The mixture was then cooled to room temperature and a white precipitate was collected by filtration and washed with methanol. (Yield = 413 mg, 78 %). ^{1}H NMR (300 MHz, $CDCl_3$): δ_H 7.92 (s, 2H), 7.51 – 7.48 (m, 4H), 7.35 – 7.31 (m, 6H), 2.49 (s, 6H) ppm. $^{13}C\{^{1}H\}$ NMR (75 MHz, $CDCl_3$): δ_C 152.50, 140.55, 140.21, 139.37, 129.84, 128.53, 128.21, 109.99, 20.50 ppm. HRMS (ESI) found *m/z* 311.1542, calcd *m/z* 311.1543 for $C_{22}H_{18}N_2$. UV vis. ($CHCl_3$) λ_{max} (ε / $dm^3mol^{-1}cm^{-1}$): 356 (13900), 281 (24600), 269 (31800), 254 (44900) nm. IR (solid) υ / cm^{-1} : 2974, 1749, 1549, 1531, 1493, 1474, 1460, 1445, 1416, 1400, 1375, 1346, 1335, 1263, 1211, 1179, 1153, 1074, 1059, 1022, 1003, 966, 932, 870, 849, 814, 783, 773, 762, 741, 725, 691, 633, 608, 598, 556, 530, 519, 492, 476, 436, 413.

Synthesis of HL6 As L5 but with benzil (273 mg, 1.3 mmol) and 1,2-diamino-4,5-dichlorobenzene (250 mg, 1.4 mmol). Product collected as a white solid. (Yield = 367 mg, 80 %). ^{1}H NMR (300 MHz, $CDCl_3$): δ_H 8.29 (s, 2H), 7.52 – 7.49 (m, 4H), 7.37 – 7.35 (m, 6H) ppm. $^{13}C\{^{1}H\}$ NMR (101 MHz, $CDCl_3$): δ_C 154.49, 139.95, 138.39, 134.43, 129.80, 129.29, 128.37 ppm. HRMS (ESI) found *m/z* 351.0450, calcd *m/z* 351.0450 for $C_{20}H_{12}Cl_2N_2$. UV vis. ($CHCl_3$) λ_{max} (ε / $dm^3mol^{-1}cm^{-1}$): 362 (19400), 254 (61300) nm. IR (solid) υ / cm^{-1} : 3067, 3024, 2980, 1589, 1535, 1491, 1452, 1439, 1393, 1337, 1254, 1190, 1109, 1074, 1061, 1020, 999, 964, 920, 883, 874, 831, 814, 766, 733, 719, 692, 640, 621, 606, 598, 546, 511, 488, 480, 444, 426, 419, 409.

Synthesis of HL7 As L5, but with benzil (336 mg, 1.6 mmol) and 1,2-diamino-4,5-difluorobenzene (250 mg, 1.7 mmol). Product collected as an orange solid. (Yield = 296 mg, 58 %). ^{1}H NMR (300 MHz, $CDCl_3$): δ_H 7.91 (td, J_{HH} = 1.37, 9.35 Hz, 2H), 7.51 – 7.48 (m, 4H), 7.41 – 7.31 (m, 6H) ppm. $^{13}C\{^{1}H\}$ NMR (75 MHz, $CDCl_3$): δ_C 154.31, 154.07, 153.69, 150.89, 150.66, 138.51, 138.48, 129.77, 129.13, 128.37, 114.72 ppm. $^{19}F\{^{1}H\}$ NMR (376 MHz, $CDCl_3$): δ_F -129.86 ppm. HRMS (ESI) found *m/z* 319.1044, calcd *m/z* 319.1041 for $C_{20}H_{12}F_2N_2$. UV vis. ($CHCl_3$) λ_{max} (ε / $dm^3mol^{-1}cm^{-1}$): 343 (14900), 261 (16800) nm. IR (solid) υ / cm^{-1} : 3051, 1597, 1568, 1541, 1456, 1435, 1352, 1342, 1246, 1217, 1194, 1175, 1152, 1142, 1082, 1072, 1055, 1022, 1001, 972, 939, 918, 872, 818, 785, 772, 760, 752, 719, 700, 677, 623, 610, 573, 542, 521, 498, 438, 424, 419.

Synthesis of [{Ir(L)$_2$(μ-Cl)}$_2$] $IrCl_3.xH_2O$ (**1 eq.**) and ligand, L (**2 eq.**) were dissolved in 2-ethoxyethanol (10 mL) and the reaction mixture heated at reflux for 48 hours. The reaction was then cooled to room temperature and water (30 mL) was added to form a dark brown

precipitate. The solid was collected by filtration to yield [{Ir(L)$_2$(μ-Cl}$_2$] and was used in subsequent steps without further characterisation or purification.

Synthesis of C1a [{Ir(L1)$_2$(μ-Cl)}$_2$] (100 mg, 0.075 mmol) and 2,2-bipyridyl (0.025 g, 0.16 mmol) were dissolved in 2-ethoxyethanol (10 mL) and heated at reflux for 24 hours under a nitrogen atmosphere. The reaction mixture was then cooled to room temperature and a saturated solution of aqueous ammonium hexafluorophosphate was added. Upon formation of a red precipitate, the mixture was filtered and the precipitate washed with water and diethyl ether to yield the product as a red solid. (Yield = 80 mg, 68 %). ^{1}H NMR (300MHz, $CDCl_3$): δ_H 8.39 (2H, d, J_{HH}= 8.3Hz, Ar), 8.24 (2H, d, J= 8.3Hz, Ar), 8.17 (2H, d, J_{HH}= 5.3Hz, Ar), 8.01 (2H, app.t, J_{HH}= 7.9Hz, Ar), 7.90 (2H, d, J_{HH}= 8.3Hz Ar), 7.45-7.57 (4H, m, Ar), 7.16-7.24 (2H, m, Ar), 7.00 (2H, app.t, J_{HH}= 7.7Hz, Ar), 6.86 (2H, app. t, J_{HH}= 7.7Hz, Ar), 6.61 (2H, d, J_{HH}= 7.6Hz, Ar), 3.36 (6H, s, Me) ppm. ^{13}C{^{1}H} NMR (101MHz; $CDCl_3$): δ_C 163.7, 155.1, 152.6, 152.0, 146.6, 144.0, 140.4, 140.0, 139.7, 135.1, 130.9, 130.5, 130.4, 130.1, 129.2, 127.6, 124.8, 123.6, 123.2, 27.5 ppm. HRMS (ESI) found *m/z* 787.2148, calculated *m/z* 787.2158 for $C_{40}H_{30}IrN_6$. UV vis. ($CHCl_3$): λmax/nm (ε/dm3 mol-1 cm-1) 477 (2500), 372 (13200), 253 (27900) nm. IR (solid) υ / cm^{-1} : 1605, 1578, 1530, 1449, 1427, 1387, 1348, 1261, 1215, 1196, 1165, 1130, 1016, 1001, 897, 837, 770, 750, 731, 704, 660, 627, 592, 557, 459, 420, 415, 405.

Synthesis of C2a As C1a, but with [{Ir(L2)$_2$(μ-Cl)}$_2$] (104 mg, 0.07 mmol) and 2,2-bipyridyl (25 mg, 0.15 mmol). Product collected as a red solid (Yield = 133 mg, 94 %). ^{1}H NMR: (400 MHz, Acetone-d_6): δ_H 8.57 – 8.54 (2 H, m), 8.49 (2 H, dd, J_{HH} = 8.3, 1.2), 8.41 (2 H, dt, J_{HH} = 8.2, 1.0), 8.16 (2 H, ddd, J_{HH} = 8.3, 7.6, 1.6), 7.86 – 7.81 (2 H, m), 7.66 (2 H, s), 7.24 (2 H, ddd, J_{HH} = 8.3, 7.1, 1.3), 7.17 (2 H, s), 6.86 – 6.79 (2 H, m), 6.70 (2 H, dd, J_{HH} = 7.7, 1.3), 3.34 (6 H, s), 2.30 (6 H, s), 1.81 (6 H, s) ppm. ^{13}C {^{1}H} (101 MHz, Acetone): δ_C 164.56, 156.84, 154.00, 153.38, 149.62, 146.39, 142.69, 142.14, 141.53, 140.70, 140.05, 136.48, 132.09, 131.63, 130.00, 129.66, 125.61, 125.24, 124.33, 28.18, 20.36, 20.11 ppm. HRMS (ESI) found *m/z* 843.2783 calculated *m/z* 843.2784 for $C_{44}H_{38}IrN_6$. UV-vis ($CHCl_3$) λ_{max} (ε / dm^{3}mol^{-1}cm^{-1}): 474 (4800), 391 (22100), 376 (23900), 309 (19300), 390 (32300), 268 (47200) nm. IR (solid) υ / cm^{-1} : 1601, 1582, 1560, 1526, 1483, 1445, 1396, 1375, 1342, 1323, 1267, 1219, 1171, 1134, 1063, 993, 835, 795, 768, 737, 702, 660, 627, 556, 474, 434, 420, 403.

Synthesis of C3a As C1a but with [{Ir(L3)$_2$(μ-Cl)}$_2$] (100 mg, 0.06 mmol) and 2,2'-bipyridine (20 mg, 0.1 mmol). Product collected as a red solid. (Yield = 61 mg, 46 %). ^{1}H NMR (400 MHz, Acetone-d_6): δ_H 8.60 (2 H, d, J_{HH} = 8.4), 8.50 (2 H, d, J_{HH} = 8.0), 8.51 (2 H, d, J_{HH} = 8.0), 8.26 – 8.18 (2 H, m), 8.13 (2 H, d, J_{HH} = 1.2), 7.92 – 7.83 (2 H, m), 7.59 (2 H, s), 7.31 (2 H, dd, J_{HH} = 8.3, 6.7), 6.97 – 6.89 (2 H, m), 6.85 (2 H, d, J_{HH} = 8.0), 3.41 (6 H, s) ppm. ^{13}C {^{1}H} NMR (126 MHz, DMSO): δ_C 165.56, 155.14, 154.80, 153.75, 147.29, 143.91, 140.79, 138.80, 138.42, 135.28, 133.16, 132.60, 132.14, 131.53, 129.82, 129.31, 125.05, 124.96, 123.41, 27.34 ppm. HRMS (ESI) found *m/z* 925.0548, calculated *m/z* 925.0558 for $C_{40}H_{26}Cl_4IrN_6$. UV vis. ($CHCl_3$) λ_{max} (ε / dm^{3}mol^{-1}cm^{-1}): 500 (4500), 383 (23700), 298 (28900), 266 (48200) nm. IR (solid) υ / cm^{-1} : 1603, 1576, 1528, 1464, 1447, 1381, 1315, 1265, 1188, 1165, 1132, 1113, 1061, 1026, 1009, 962, 895, 870, 843, 824, 772, 739, 729, 673, 664, 646, 637, 608, 556, 467, 428, 419, 403.

Synthesis of C4a As C1a, but with [{Ir(L4)$_2$(μ-Cl)}$_2$] (101 mg, 0.07 mmol) and 2,2'-bipyridyl (23 mg, 0.15 mmol). Product collected as a red solid. (Yield = 133 mg, 97 %). ^{1}H NMR (400 MHz, Acetone-d_6): δ_H 8.58 (2 H, dd, J_{HH} = 8.3, 1.2), 8.54 (2 H, ddd, J_{HH} = 5.5, 1.6, 0.8), 8.47 (2 H, dt, J_{HH} = 8.2, 1.0), 8.25 – 8.18 (2 H, m), 7.92 – 7.81 (4 H, m), 7.34 – 7.20 (4 H, m), 6.95 – 6.88 (2 H, m), 6.82 – 6.80 (2 H, d, J_{HH} = 8.0), 3.39 (6 H, app. S) ppm. ^{13}C {^{1}H} NMR (101 MHz, Acetone-d_6): δ_C

155.55, 152.77, 147.77, 144.41, 140.52, 135.29, 131.51, 131.13, 128.91, 124.79, 123.34 ppm. ^{19}F NMR (376 MHz, Acetone-d_6): δ_F -72.63 (d, J = 711.7 Hz), -131.73 (d, J = 21.9 Hz), -133.10 (d, J = 21.9 Hz) ppm. HRMS (ESI) found m/z 859.1780, calculated m/z 859.1781 for $C_{40}H_{26}F_4IrN_6$. UV vis. ($CHCl_3$) λ_{max} (ε / $dm^3mol^{-1}cm^{-1}$): 480 (2400), 375 (13200), 311(11800), 288 (15400), 262 (25800) nm. IR (solid) υ / cm^{-1} : 1065, 1578, 1533, 1501, 1447, 1341, 1331, 1252, 1233, 1196, 1128, 1063, 1036, 997, 878, 841, 795, 772, 741, 731, 689, 660, 638, 586, 557, 476, 451, 428, 422, 407.

Synthesis of C5a As C1a but with [{Ir(L5)$_2$(μ-Cl)}$_2$] (150 mg, 0.09 mmol) and 2,2'-bipyridine (29 mg, 0.2 mmol). Product collected as a red solid. (Yield = 124 mg, 63%). ^{1}H NMR (400 MHz, Acetone-d_6): δ_H 9.10 (2 H, dt, J_{HH} = 5.1, 2.2), 8.61 – 8.52 (2 H, m), 8.34 – 8.25 (2 H, m), 8.24 – 8.15 (2 H, m), 7.96 (4 H, dt, J_{HH} = 6.7, 2.7), 7.78 (2 H, s), 7.74 – 7.65 (6 H, m), 7.34 (2 H, s), 7.18 (2 H, ddd, J_{HH} = 8.2, 2.9, 1.5), 6.78 – 6.72 (2 H, m), 6.69 – 6.63 (2 H,m), 6.61 – 6.54 (2 H, m), 2.35 (6 H, s), 1.94 (6 H, s) ppm. ^{13}C {^{1}H} NMR (101 MHz, Acetone-d_6): δ_C 162.58, 156.09, 153.60, 152.81, 149.26, 144.93, 142.80, 141.53, 140.81, 140.42, 139.91, 139.43, 135.23, 131.40, 130.46, 130.06, 129.58, 129.44, 129.21, 124.84, 123.98, 122.37, 19.43, 18.99 ppm. HRMS (ESI) found m/z 967.3086, calcd m/z 967.3099 for $C_{54}H_{42}IrN_6$. UV vis. ($CHCl_3$) λ_{max} (ε / $dm^3mol^{-1}cm^{-1}$): 479 (6500), 400 (29300), 362 (24800), 297 (49000), 269 (71300) nm. IR (solid) υ / cm^{-1} : 1603, 1580, 1479, 1447, 1348, 1321, 1234, 1207, 1159, 1134, 1074, 1024, 1001, 974, 833, 810, 775, 748, 737, 729, 700, 658, 640, 608, 577, 557, 542, 446, 432, 415.

Synthesis of C6a As C1a, but with [{Ir(L6)$_2$(μ-Cl)}$_2$] (100 mg, 0.05 mmol) and 2,2' – bipyridine (19 mg, 0.1 mmol). Product collected as a red solid. (Yield = 48 mg, 37 %). ^{1}H NMR (300 MHz, Acetone-d_6): δ_H 8.98 (2 H, ddd, J_{HH} = 5.5, 1.7, 0.7), 8.60 (2 H, dt, J_{HH} = 8.2, 1.0), 8.30 (2 H, td, J_{HH} = 7.9, 1.6), 8.23 – 8.15 (4 H, m), 7.99 – 7.90 (4 H, m), 7.69 (8 H, q, J_{HH} = 2.2, 1.8), 7.25 – 7.15 (2 H, m), 6.81 – 6.62 (6 H, m) ppm. ^{13}C {^{1}H} NMR (101 MHz, Acetone-d_6): δ_C 166.36, 157.25, 156.93, 155.10, 149.90, 145.27, 142.19, 141.00, 140.74, 140.57, 136.52, 136.16, 133.44, 132.75, 131.91, 131.67, 130.77, 130.55, 126.65, 126.43, 123.84 ppm. HRMS (ESI) found m/z 1049.0839, calculated m/z 1049.0872 for $C_{50}H_{30}Cl_4IrN_6$. UV vis. λ_{max}/ nm ($CHCl_3$) 501(7300), 404 (35300), 299 (54600), 268 (87500) nm. IR (solid) υ / cm^{-1} : 1603, 1576, 1524, 1493, 1445, 1433, 1406, 1383, 1342, 1317, 1258, 1186, 1165, 1132, 1115, 1072, 1045, 1026, 1001, 961, 880, 839, 826, 766, 734, 698, 673, 648, 635, 606, 577, 557, 532, 517, 486, 474, 451, 434, 419.

Synthesis of C7a As C1a but with [{Ir(L7)$_2$(μ-Cl)}$_2$] (100 mg, 0.06 mmol) and 2,2'-bipyridine (19 mg, 0.1 mmol). Product collected as a red solid. (Yield = 108 mg, 83 %). ^{1}H NMR (400 MHz, Acetone-d_6): δ_H 9.10 – 9.06 (2 H, m), 8.63 (2 H, d, J_{HH} = 8.2), 8.35 (2 H, tt, J_{HH} = 8.0, 1.4), 8.22 (2 H, m), 8.01 (6 H, tt, J_{HH} = 8.5, 4.4), 7.79 – 7.68 (6 H, m), 7.46 – 7.37 (2 H, m), 7.28 – 7.20 (2 H, m), 6.87 – 6.79 (2 H, m), 6.77 – 6.72 (2 H, m), 6.69 (2 H, dt, J_{HH} = 7.8, 1.3) ppm. ^{13}C {^{1}H} NMR (101 MHz, Acetone-d_6): δ_C 157.50, 150.05, 142.41, 140.79, 136.71, 133.25, 132.55, 131.76, 130.75, 126.56, 124.00, 117.87 ppm. ^{19}F{^{1}H} NMR (376 MHz, Acetone-d_6): δ_F -72.64 (d, J = 699.9 Hz), -130.30 (d, J = 21.7 Hz), -132.66 (d, J = 22.2 Hz) ppm. HRMS (ESI) found m/z 983.2088, calculated m/z 983.2095 for $C_{50}H_{30}F_4IrN_6$. UV vis. ($CHCl_3$) λ_{max} (ε / $dm^3mol^{-1}cm^{-1}$): 483 (4500), 396 (21600), 367 (20200), 297 (33100), 265 (48600) nm. IR (solid) υ / cm^{-1} : 1603, 1578, 1503, 1447, 1429, 1335, 1275, 1260, 1223, 1204, 1163, 1126, 1072, 1043, 1026, 980, 874, 835, 810, 758, 739, 700, 660, 640, 623, 615, 557, 536, 498.

Crystal data collection parameters

[Ir(L2)$_2$(bpy)][PF$_6$]			
Formula	$C_{46}H_{44}F_6IrN_6OP$	***Z'***	1
***D$_{calc.}$*/ g cm^{-3}**	1.675	**Wavelength/Å**	0.71075
***μ*/mm^{-1}**	3.368	**Radiation type**	MoK_α
Formula Weight	1034.04	***Θ$_{min}$*/°**	1.722
Colour	red	***Θ$_{max}$*/°**	27.483
Shape	block	**Measured Refl.**	44265
Size/mm^3	0.100×0.055×0.035	**Independent Refl.**	9342
***T*/K**	100(2)	**Reflections Used**	7210
Crystal System	monoclinic	***R$_{int}$***	0.0408
Space Group	$P2_1/n$	**Parameters**	588
***a*/Å**	13.7693(2)	**Restraints**	51
***b*/Å**	20.6315(4)	**Largest Peak**	2.313
***c*/Å**	14.5942(3)	**Deepest Hole**	-1.250
***α*/°**	90	**GooF**	1.036
***β*/°**	98.480(2)	***wR$_2$* (all data)**	0.0867
γ/°	90	***wR$_2$***	0.0794
V/Å^3	4100.61(13)	***R$_1$* (all data)**	0.0548
Z	4	***R$_1$***	0.0366

[Ir(L5)$_2$(bpy)][PF$_6$]

Formula	$C_{54}H_{42}F_6IrN_6P$	***Z'***	1
$D_{calc.}$**/ g cm^{-3}**	1.513	**Wavelength/Å**	0.71075
μ**/mm^{-1}**	2.834	**Radiation type**	MoK_α
Formula Weight	1112.10	Θ_{min}**/°**	1.635
Colour	dark red	Θ_{max}**/°**	25.028
Shape	cut block	**Measured Refl.**	38931
Size/mm^3	0.060×0.025×0.010	**Independent Refl.**	8623
***T*/K**	100(2)	**Reflections Used**	5823
Crystal System	monoclinic	R_{int}	0.1029
Space Group	$P2_1/n$	**Parameters**	617
***a*/Å**	14.5802(8)	**Restraints**	639
***b*/Å**	22.2820(11)	**Largest Peak**	2.304
***c*/Å**	16.1754(9)	**Deepest Hole**	-1.142
α/°	90	**GooF**	1.040
β/°	111.734(7)	wR_2 **(all data)**	0.1480
γ/°	90	wR_2	0.1308
V/Å^3	4881.4(5)	R_1 **(all data)**	0.1049
Z	4	R_1	0.0646

$[Ir(L7)_2(bpy)][PF_6]$

Formula	$C_{54}H_{40}F_{10}IrN_6OP$	***Z'***	2
***$D_{calc.}$*/ g cm^{-3}**	1.706	**Wavelength/Å**	0.71075
***μ*/mm^{-1}**	2.975	**Radiation type**	MoK_α
Formula Weight	1202.09	***Θ_{min}*/°**	1.817
Colour	red	***Θ_{max}*/°**	27.486
Shape	cut block	**Measured Refl.**	113221
Size/mm^3	0.060×0.025×0.005	**Independent Refl.**	21466
***T*/K**	100(2)	**Reflections Used**	11036
Crystal System	monoclinic	***R_{int}***	0.1871
Space Group	$P2_1/c$	**Parameters**	1339
***a*/Å**	17.0632(5)	**Restraints**	1349
***b*/Å**	22.3096(6)	**Largest Peak**	3.828
***c*/Å**	24.9163(8)	**Deepest Hole**	-1.303
***α*/°**	90	**GooF**	0.967
***β*/°**	99.205(3)	***wR_2* (all data)**	0.1519
***γ*/°**	90	***wR_2***	0.1223
V/Å^3	9362.8(5)	***R_1* (all data)**	0.1507
Z	8	***R_1***	0.0627

2.6. References

1. L. Flamigni, A. Barbieri, C. Sabatini, B. Ventura and F. Barigelletti, in *Photochemistry and Photophysics of Coordination Compounds II*, eds. V. Balzani and S. Campagna, Springer Berlin Heidelberg, Berlin, Heidelberg, 2007, pp. 143–203.
2. A. Juris, V. Balzani, F. Barigelletti, S. Campagna, P. Belser and A. von Zelewsky, *Coord. Chem. Rev.*, 1988, **84**, 85–277.
3. Y. Ohsawa, S. Sprouse, K. A. King, M. K. DeArmond, K. W. Hanck and R. J. Watts, *J. Phys. Chem.*, 1987, **91**, 1047–1054.
4. C. K. Prier, D. A. Rankic and D. W. C. MacMillan, *Chem. Rev.*, 2013, **113**, 5322–5363.
5. M. A. Ischay, M. E. Anzovino, J. Du and T. P. Yoon, *J. Am. Chem. Soc.*, 2008, **130**, 12886–12887.
6. D. A. Nicewicz and D. W. C. MacMillan, *Science*, 2008, **322**, 77–80.
7. J. D. Nguyen, B. S. Matsuura and C. R. J. Stephenson, *J. Am. Chem. Soc.*, 2014, **136**, 1218–1221.
8. J. Wang and N. Zheng, *Angew. Chem. Int. Ed Engl.*, 2015, **54**, 11424–11427.
9. L. J. Rono, H. G. Yayla, D. Y. Wang, M. F. Armstrong and R. R. Knowles, *J. Am. Chem. Soc.*, 2013, **135**, 17735–17738.
10. A. Noble and D. W. C. MacMillan, *J. Am. Chem. Soc.*, 2014, **136**, 11602–11605.
11. S. Sato, T. Morikawa, T. Kajino and O. Ishitani, *Angew. Chem. Int. Ed.*, 2013, **52**, 988–992.
12. G. Szafraniec-Gorol, A. Słodek, M. Filapek, B. Boharewicz, A. Iwan, M. Jaworska, L. Żur, M. Sołtys, J. Pisarska, I. Grudzka-Flak, S. Czajkowska, M. Sojka, W. Danikiewicz and S. Krompiec, *Mater. Chem. Phys.*, 2015, **162**, 498–508.
13. A. J. Bagnall, M. Santana Vega, J. Martinelli, K. Djanashvili and F. Cucinotta, *Chem. – Eur. J.*, 2018, **24**, 11992–11999.
14. A. Sinopoli, C. J. Wood, E. A. Gibson and P. I. P. Elliott, *Inorganica Chim. Acta*, 2017, **457**, 81–89.
15. R. P. Haugland, *The Handbook: A Guide to Fluorescent Probes and Labeling Technologies*, Molecular Probes, 2005.
16. S. Pandya, J. Yu and D. Parker, *Dalton Trans.*, 2006, **0**, 2757–2766.
17. D.-L. Ma, V. P.-Y. Ma, D. S.-H. Chan, K.-H. Leung, H.-Z. He and C.-H. Leung, *Coord. Chem. Rev.*, 2012, **256**, 3087–3113.
18. D. Parker, *Coord. Chem. Rev.*, 2000, **205**, 109–130.
19. Q. Zhao, F. Li and C. Huang, *Chem. Soc. Rev.*, 2010, **39**, 3007–3030.
20. M. Yu, Q. Zhao, L. Shi, F. Li, Z. Zhou, H. Yang, T. Yi and C. Huang, *Chem. Commun.*, 2008, 2115–2117.
21. T. Yu, Y. Wang, Z. Zhu, Y. Li, Y. Zhao, X. Liu and H. Zhang, Dyes and Pigments, 2019, 161, 252–260.
22. V. Gray, D. Dzebo, M. Abrahamsson, B. Albinsson and K. Moth-Poulsen, *Phys Chem Chem Phys*, 2014, **16**, 10345–10352.
23. P. Duan, N. Yanai and N. Kimizuka, *Chem Commun*, 2014, **50**, 13111–13113.
24. J. Zhao, S. Ji and H. Guo, *RSC Adv.*, 2011, **1**, 937–950.
25. J. Zhao, W. Wu, J. Sun and S. Guo, *Chem. Soc. Rev.*, 2013, **42**, 5323.
26. S. Ji, W. Wu, W. Wu, H. Guo and J. Zhao, *Angew. Chem. Int. Ed.*, 2011, **50**, 1626–1629.
27. T. N. Singh-Rachford and F. N. Castellano, *J. Phys. Chem. Lett.*, 2010, **1**, 195–200.
28. A. Monguzzi, R. Tubino and F. Meinardi, *Phys. Rev. B*, 2008, **77**, 155122.

29. S. Baluschev, V. Yakutkin, T. Miteva, Y. Avlasevich, S. Chernov, S. Aleshchenkov, G. Nelles, A. Cheprakov, A. Yasuda, K. Müllen and G. Wegner, *Angew. Chem. Int. Ed.*, 2007, **46**, 7693–7696.
30. 29 . J. Peng, X. Jiang, X. Guo, D. Zhao and Y. Ma, *Chem. Commun.*, 2014, **50**, 7828.
31. J. Sun, W. Wu, H. Guo and J. Zhao, *Eur. J. Inorg. Chem.*, 2011, **2011**, 3165–3173.
32. Y. Lu, J. Wang, N. McGoldrick, X. Cui, J. Zhao, C. Caverly, B. Twamley, G. M. Ó Máille, B. Irwin, R. Conway-Kenny and S. M. Draper, *Angew. Chem. Int. Ed.*, 2016, **55**, 14688–14692.
33. M. Nonoyama, *Bull. Chem. Soc. Jpn.*, 1974, **47**, 767–768.
34. A. B. Tamayo, B. D. Alleyne, P. I. Djurovich, S. Lamansky, I. Tsyba, N. N. Ho, R. Bau and M. E. Thompson, *J. Am. Chem. Soc.*, 2003, **125**, 7377–7387.
35. S. Lamansky, P. Djurovich, D. Murphy, F. Abdel-Razzaq, R. Kwong, I. Tsyba, M. Bortz, B. Mui, R. Bau and M. E. Thompson, *Inorg. Chem.*, 2001, **40**, 1704–1711.
36. M. G. Colombo, T. C. Brunold, T. Riedener, H. U. Guedel, M. Fortsch and H.-B. Buergi, *Inorg. Chem.*, 1994, **33**, 545–550.
37. M. Polson, S. Fracasso, V. Bertolasi, M. Ravaglia and F. Scandola, *Inorg. Chem.*, 2004, **43**, 1950–1956.
38. M. Albrecht, *Chem. Rev.*, 2010, **110**, 576–623.
39. B. J. Coe and S. J. Glenwright, *Coord. Chem. Rev.*, 2000, **203**, 5–80.
40. K. A. Phillips, T. M. Stonelake, K. Chen, Y. Hou, J. Zhao, S. J. Coles, P. N. Horton, S. J. Keane, E. C. Stokes, I. A. Fallis, A. J. Hallett, S. P. O'Kell, J. M. Beames and S. J. A. Pope, *Chem. – Eur. J.*, 2018, **24**, 8577–8588.
41. L. M. Groves, C. Schotten, J. Beames, J. A. Platts, S. J. Coles, P. N. Horton, D. L. Browne and S. J. A. Pope, *Chem. – Eur. J.*, 2017, **23**, 9407–9418.
42. D. Dzebo, K. Börjesson, V. Gray, K. Moth-Poulsen and B. Albinsson, *J. Phys. Chem. C*, 2016, **120**, 23397–23406.

3. Neutral Iridium(III) Complexes Incorporating Cyclometallated Quinoxaline Ligands: Synthesis, Characterisation and Luminescence Properties

3.1. Introduction

The work presented in this chapter focuses on the photophysical properties of bis-cyclometallated complexes of iridium(III). Unlike the work of the previous chapter, the complexes in this study have an overall neutral charge due to one of the coordination sites of the ancillary ligands bearing a formal negative charge.

The potential applications of neutral iridium(III) complexes are similar to those of cationic iridium complexes in that their uses can include imaging agents,[1,2] and catalysts.[3] But by far, the most widespread application of bis-cyclometallated iridum(III) complexes is in the field of phosphorescent organic light emitting diodes (PhOLEDs). One reason that neutral species are preferred in the manufacturing of OLED devices is that they can be sublimed more easily than cationic species. In this chapter, the background of this field and examples of iridium complexes used as dopants in electroluminescent devices are discussed in detail.

3.1.1. OLEDs

In recent years, organic light emitting diodes (OLEDs) have become increasingly popular as they have high brightness and fast response times.[4–7] OLEDs also open up the possibility of flexible displays and lighting.[8]

An OLED device is typically made up of a series of thin organic layers sandwiched between an anode, such as indium tin oxide, and a metallic cathode. Figure 3.1 illustrates an example of such a device. The organic layers include a hole transport layer, an electron transport layer and, in newer devices, an exciton blocking layer which improves quantum efficiency.[9–11] The organic emitter is either deposited between the conducting layers or doped into the electron transport layer. The first OLED devices used small fluorescent molecules as dopants,[12] but focus has since switched to phosphorescent materials as a means to increase the luminous efficiency of these devices.[13]

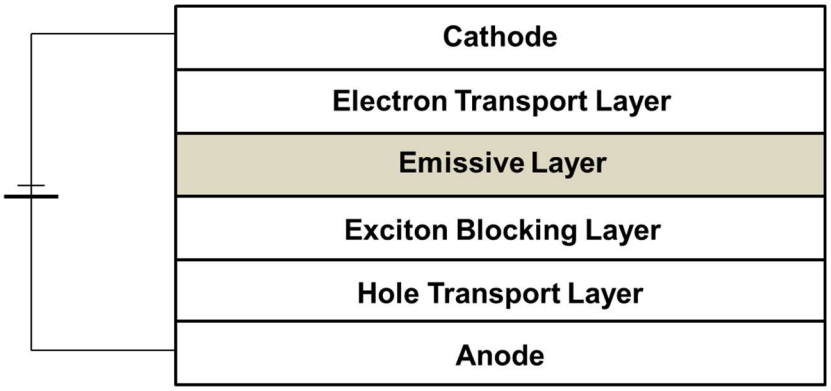

Figure 3.1: Typical structure of an OLED device.[13]

Phosphorescence is emission of light from a triplet excited state, in which the electron in the excited state has the same spin value as that in the ground state. As a result, transitions to the ground state are spin-forbidden and emission rates are slow, meaning that emission lifetimes can reach milliseconds to seconds.[14]

The factors to be considered when designing phosphorescent materials for OLEDs include emission wavelength (λ_{em}), luminescence lifetime (τ) and quantum yield (Φ). Emission wavelength determines the colour output, and in full-colour displays, red, green and blue

emitters are required. A long luminescence lifetime is detrimental to the performance of an OLED device as the length of time a molecule spends in the triplet state is a limiting factor in the conversion of electrical energy to photon energy, therefore an ideal lifetime should fall between 5-50 µs at room temperature. In addition to this, the efficiency of the OLED device is directly linked to the quantum yield of the emitter and as such, the Φ value should be as close to unity as possible. In reality, this is very difficult to achieve, but it is generally accepted that a phosphorescent emitter should have a quantum yield value of at least 0.25 at room temperature.[13]

Organic phosphorescent molecules typically have very long emission lifetimes, meaning they are not ideal for use in OLED devices. Instead, transition metal complexes are often employed as their phosphorescent lifetimes are generally much shorter. This is due in part to the metal-to-ligand charge transfer transition (MLCT) that occurs in these species, which involves an electronic transition from a metal-centred d orbital to a ligand centred π^* orbital.[15] These occur most often in late-transition metal complexes where the metal is in a low oxidation state. Emission from triplet MLCT (^{3}MLCT) states is formally phosphorescence, but as these states are shorter lived than typical phosphorescent states, they have much shorter lifetime values; normally on the scale of microseconds, which are much more applicable to OLED devices.[14]

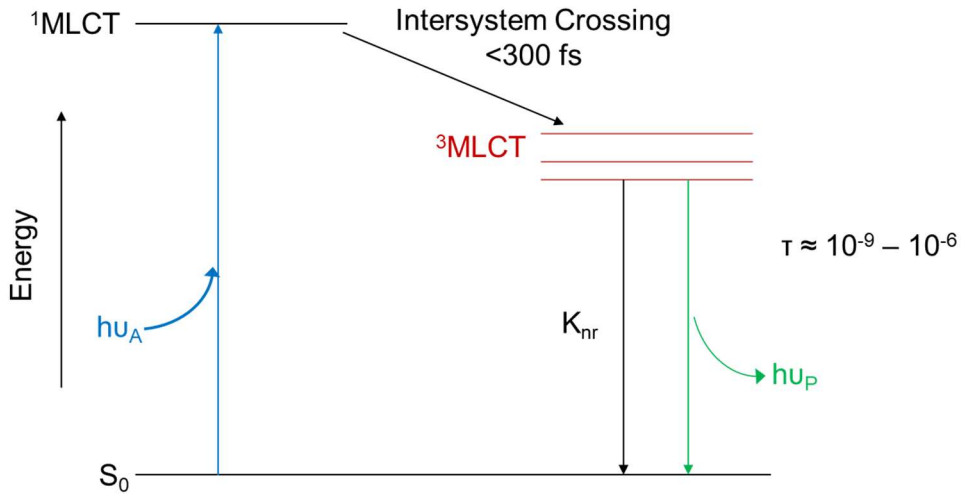

Figure 3.2: Jablonksi diagram illustrating the transition from a ^{3}MLCT state to the ground state.[14]

Organometallic complexes of late-transition metals are most often used as dopants in OLED devices because the heavy metal centre helps to facilitate intersystem crossing to the ^{3}MLCT state through strong spin-orbit coupling.[16,17] Metals such as osmium, iridium, ruthenium and platinum have been most commonly used as phosphorescent emitters.[18] Examples of osmium, ruthenium and platinum complexes developed as phosphors for OLED devices are shown in Figure 3.3.

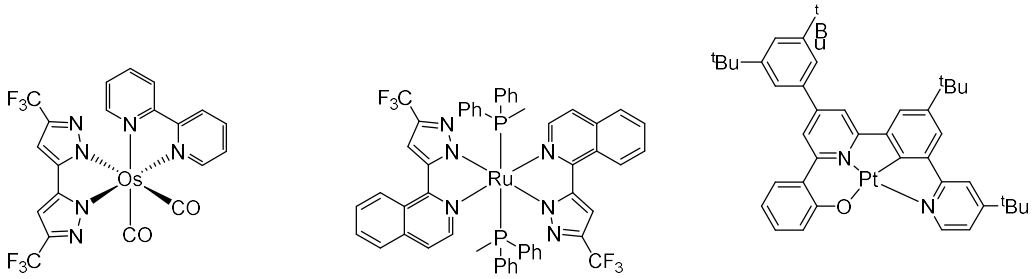

Figure 3.3: Examples of transition metal complexes used as dopants in OLED devices.[19–21]

The complex on the left of the figure is a near-infra red-emitting osmium species reported in 2015 with an emission wavelength of 717 nm and a photoluminescent quantum yield of 8.8 %. [19] The ruthenium complex in the centre was synthesised as part of a series of complexes with differently functionalised ligands. An OLED device was synthesised incorporating this complex and showed strong saturated red emission with excellent efficiency.[20] The platinum species was reported as part of a series of complexes that showed emission between 600-750 nm in the solid state. The complex shown in the figure was used as a co-dopant in an OLED device and showed red emission at a wavelength of 661 nm.[21]

3.1.2. Iridium Complexes

The first tris-cyclometallated iridium complex, *fac*-[Ir(ppy)$_3$], was reported in the 1980s as a by-product of the synthesis of another iridium complex. [22] However, it wasn't until 1999 that this complex was used in an OLED device, when Baldo *et al*. created a green emitting device using *fac*-[Ir(ppy)$_3$] as a dopant.[23] Emission from this species is believed to arise from a mixed state possessing both MLCT and intra-ligand IL π-π* character.[24–26] Molecular orbital theory suggests that the LUMO and HOMO of the phenylpyridine ligand are partially situated on the pyridyl moiety and the phenyl moiety respectively meaning that the ligand can be selectively functionalised to tune the emission wavelength.[27] Functionalisation of the pyridyl ligand can alter the level of the LUMO, whilst the HOMO remains unchanged as long as the phenyl moiety remains un-functionalised. A typical way in which this strategy is employed is in the substitution of a carbon atom in the pyridyl part of the ligand with a nitrogen atom to create a pyrazine moiety.[28] The addition of this nitrogen atom decreases the LUMO level resulting in a reduction in the energy gap for both the ^{3}π-π* and ^{3}MLCT emission.

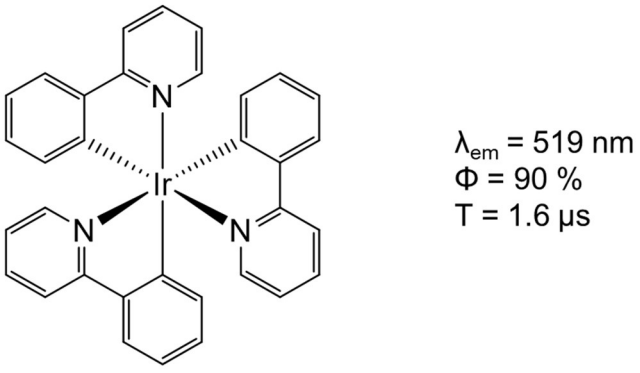

Figure 3.4: Structure and emission properties of fac-[Ir(ppy)$_3$]

In an effort to further manipulate the photophysical properties of phosphorescent iridium(III) complexes, design has since moved away from homoleptic tris-cyclometallated complexes and toward heteroleptic species.

A common ancillary ligand used in iridium chemistry is acetylacetonate (acac) which is formed by deprotonation of acetylacetone (Hacac). A study published by Lamansky *et al.* in 2001 reported a large series of bis-cyclometallated iridium complexes with a variety of functionalised acac ancillary ligands in an investigation into the emissive state of bis-cyclometallated complexes.[29] In another paper by the same authors, a series of bis-cyclometallated complexes were synthesised with three different ancillary ligands: acac, picolinate (pic) and *N*-methylsalicyliminate (sal) and it was found that the bis-cyclometallated species showed very similar emission profiles to their tris-cyclometallated counterparts.[30] The structure and binding modes of these ligands are shown in Figure 3.5.

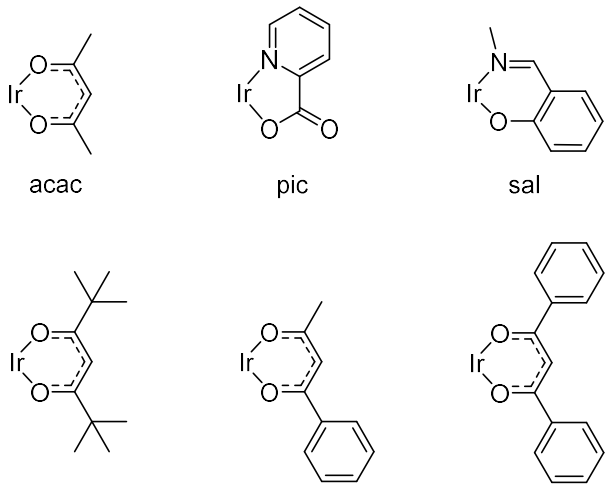

Figure 3.5: Ancillary ligands used in bis-cyclometallated iridium complexes.[30] Top) L-R) Acetylacetonate, picolinate and N-methylsalicyliminate. Bottom) Substituted acetylacetonate ligands.[29]

The same study found that the ancillary ligand did have a small effect upon emission wavelength. It was reported that the emission wavelength increased in the order pic < sal ~ acac which is proportional to the electron donating strengths of the ligands.

Some of the most recent neutral iridium(III) complexes reported are shown in Figure 3.6. The complex on the left of the figure was synthesised by Han *et al*. as part of a series of green emitting complexes which showed photoluminescent efficiency of up to 94%.[31] The central complex has a more unusual bis(diphenylphorothioyl)amide ancillary ligand. This complex, along with two similar species, when used as dopants in OLED devices, showed strong green emission at turn-on voltages as low as 2.8 V and quantum yields as high as 98%.[32]

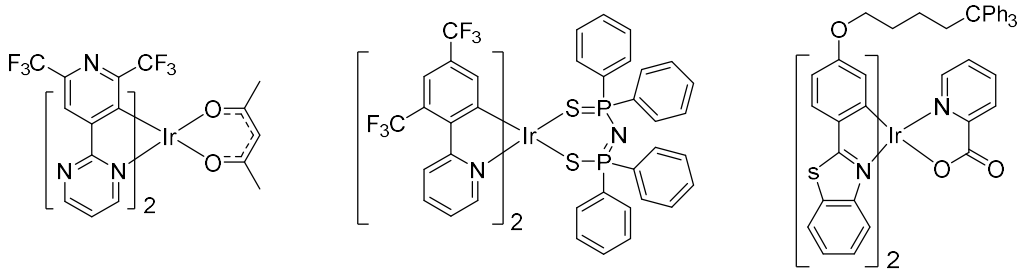

Figure 3.6: Recent neutral iridium(III) complexes synthesised for OLED applications.

The complex on the right of the figure was published as part of a study comparing acac and pic ancillary ligands. A series of six complexes were synthesised, three with pic ligands and three with acac, all with yellow to orange emission. The study reported very high quantum yields for the complexes of between 64 – 90%, but the study also noted that solid-state luminescence properties were much improved when a picolinic acid ligand was used.[33]

3.1.3. Picolinic Acid

Picolinic acid is a small organic molecule also known as pyridine-2-carboxylic acid. It is often used as a bi-dentate ligand in metal systems as it can coordinate through the nitrogen atom in the aromatic ring and through the oxygen in the carboxylic acid group.

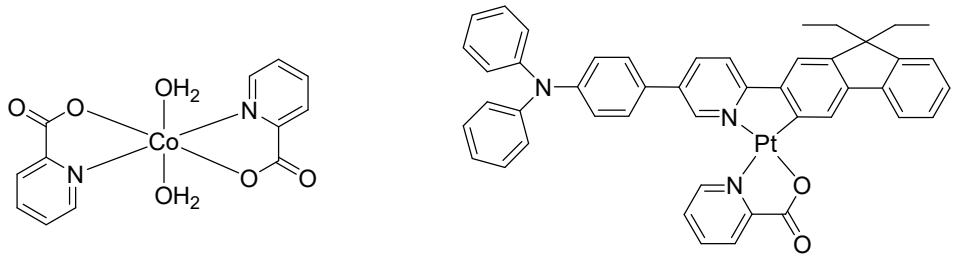

Figure 3.7: Transition metal complexes with a picolinic acid ligand.

Figure 3.7 shows two examples of picolinate used as a ligand in transition metal systems. The cobalt complex was reported in 2019, along with an analogous complex with methylated picolinate ligands, the complex shown above exhibited good activity as an inhibitor of α-glucosidase.[34] The platinum complex was reported along with a series of di-nuclear platinum complexes using functionalised picolinic acid ligands to link two platinum centres.[35]

As discussed previously, picolinate has also been used as a ligand in complexes of iridium(III). It is most often used as an ancillary ligand in bis-cyclometallated systems. One of the earliest reports of the use of picolinate in an iridium(III) complex was in 2001, discussed earlier, which investigated the effects of ancillary ligands derived from picolinic acid, acetylacetone and *N*-methylsalicylimine, upon a series of iridium complexes with different cyclometallating ligands.[30]

More recent examples of iridium complexes with picolinate ligands are shown in Figure 3.8. The left-most complex is a blue-emitting species reported in 2017 as part of a series of diphenylphosphoryl-substituted bis-cyclometallated iridium complexes investigated for their oxygen-sensing properties.[36] The central complex has a carbazole-functionalised benzimidazole cyclometallating ligand and shows strong green emission in solution, but was shown to have a lower wavelength emission and poorer efficiency in electrochemical devices than its acac analogue.[37]

Examples of red-emitting iridium complexes with a picolinic acid ligand are much less well known than blue- and green-emitting complexes. The complex shown on the right of Figure 3.8 is the only known example at time of writing. The complex has a 2-(thiophen-2-yl)quinoline cyclometallating ligand and shows emission at 647 nm.[38]

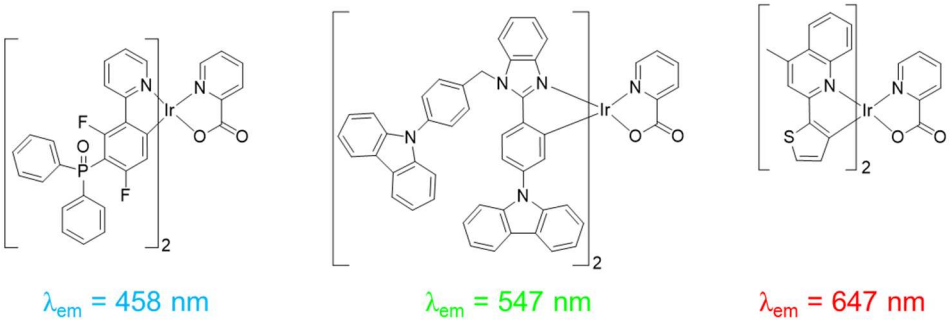

Figure 3.8: From left to right) Blue-, green- and red-emitting complexes of iridium(III) with a picolinate ligand.[36–38]

Red emission from neutral species is essential for applications such as high-quality white OLEDs (WOLEDs) and as such, demand is growing.[39] Picolinic acid could provide a convenient route to neutral red-emitting species as the synthetic route to these complexes uses the same iridium starting materials as the red-emitting cationic complexes reported in the previous chapter.

3.2. Aims

The aim of the work presented in this chapter was to build upon the results reported in chapter 2, where an emission tunability range of 30 nm was recorded across a series of seven bis-cyclometallated cationic iridium(III) complexes. In this study, a series of related neutral bis-cyclometallated complexes were synthesised bearing the same cyclometallating ligands used in the previous chapter, but with an anionic ancillary ligand replacing the neutral 2,2'-bipyridine ligand used in the cationic species.

The two anionic ligands utilised in this chapter were derived from picolinic acid, of which there are many reports in the literature, and the closely related pyrazinoic acid which has not previously been reported as an ancillary ligand in iridium(III) coordination chemistry. The photophysical properties of these complexes were studied and compared to their cationic analogues to investigate the effect of the ancillary ligand upon the emission wavelength of the complex.

3.3. Results and Discussion

3.3.1. Synthesis

The synthesis of the cyclometallating ligands used in this study has been previously reported and was discussed in further detail in chapter 2.[40] The general scheme for the synthesis of these ligands is shown below.

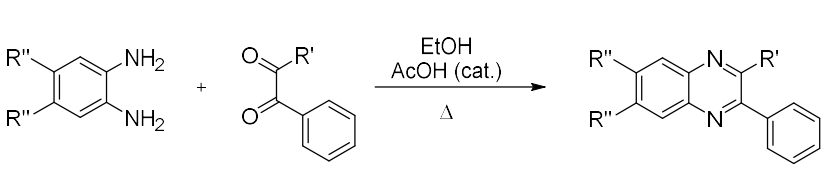

Scheme 3.1: Synthesis of cyclometallating ligands used in this study.

From these ligands, a series of chloro-bridged iridium(III) dimer compounds of formula $[\{Ir(L)_2(\mu\text{-}Cl)\}_2]$ were synthesised according to a method first published by Nonoyama.[41] The dimeric species were then used as starting materials for the synthesis of a series of neutral complexes. The proposed synthetic route to these complexes is shown in Scheme 3.2.

The synthesis is similar to that used for the cationic species, in that the iridium(III) dimer species is dissolved in 2-ethoxyethanol with a stoichiometric amount of ancillary ligand. However, for the synthesis of neutral complexes, two molar equivalents of potassium carbonate and silver nitrate were added to the reaction flask. The purpose of the potassium carbonate is to deprotonate the carboxylic acid group of the ancillary ligand, and the silver nitrate abstracts the chloride ions produced when the dimer species is split.

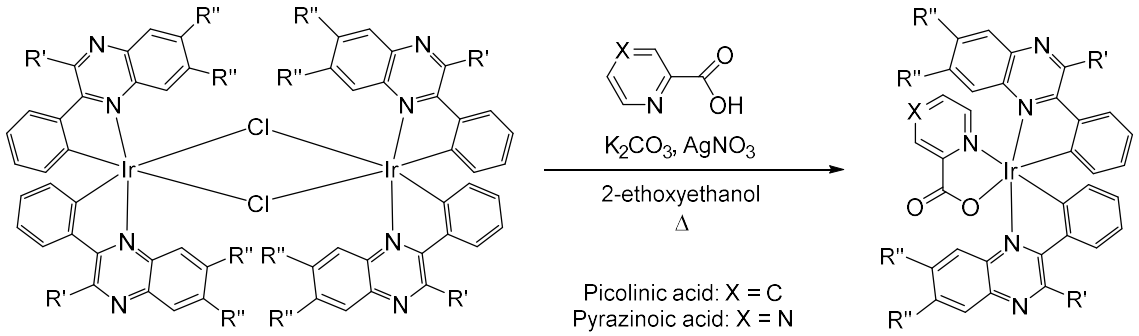

Scheme 3.2: Synthesis of neutral bis-cyclometallated complexes from chloro-bridged iridium(III) dimer species.

The ancillary ligands used in this study were picolinic acid and pyrazinoic acid. The first ligand to be investigated was picolinic acid and, following the procedure shown in Scheme 3.2, a series of seven novel neutral iridium(III) complexes was synthesised and the structure and yield of each complex is presented in the Figure 3.9. The yields of the isolated product vary from 12 – 97 %, suggesting that the reaction conditions may not be optimised for each species.

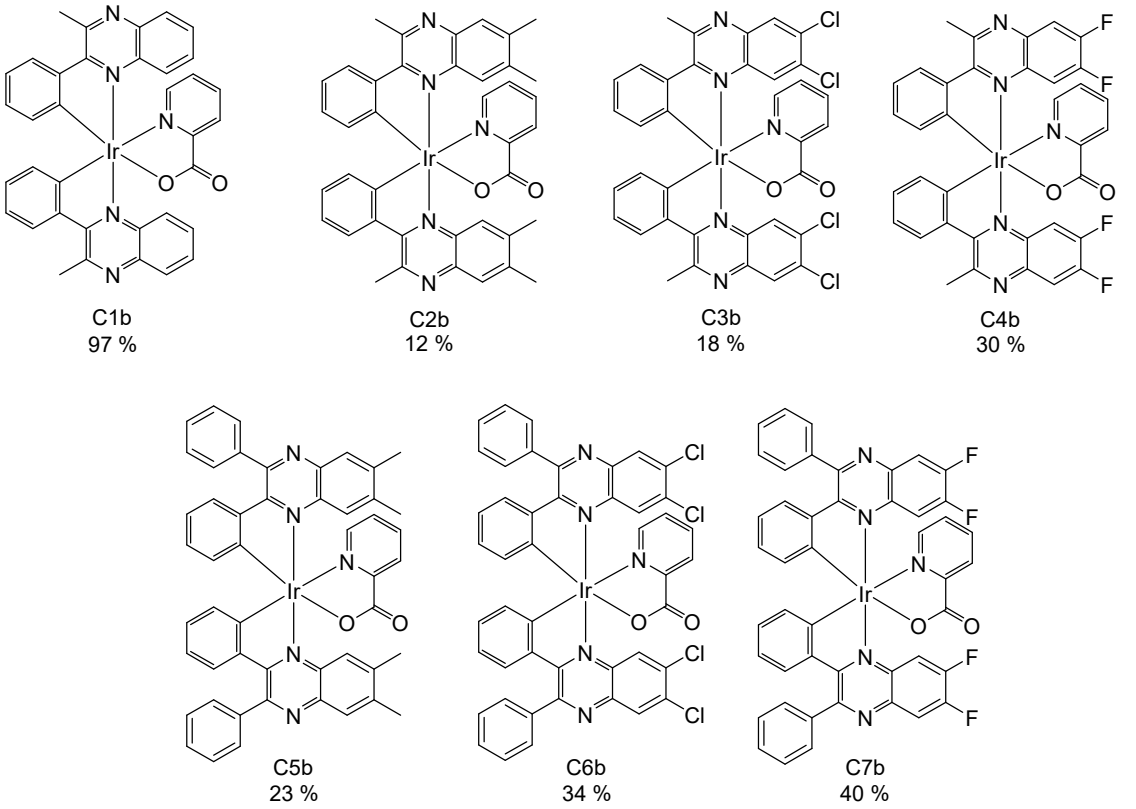

Figure 3.9: Structures of neutral bis-cyclometallated iridium(III) complexes of formula [Ir(L)$_2$(pic)]

The analogous synthetic approach was undertaken using pyrazinoic acid. For this series, four of the seven available starting materials were chosen to synthesise four novel neutral iridium(III) complexes show in Figure 3.10.

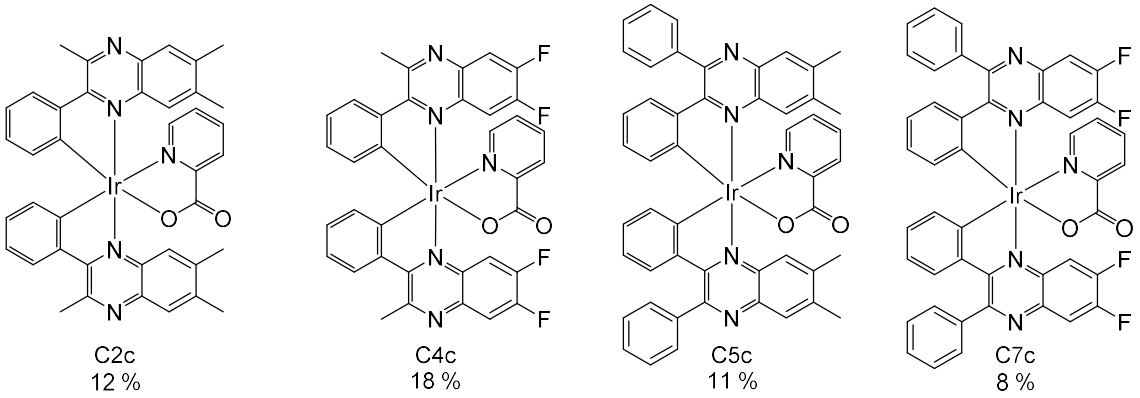

Figure 3.10:Structures of neutral bis-cyclometallated iridium(III) complexes of formula [Ir(L)$_2$(pyz)]

The yields recorded for this set of complexes are overall lower than those for the picolinic acid complexes. In fact, it was not possible to isolate complex C2c in a significant yield when following the proposed synthetic route outlaid in Scheme 3.2.

An alternative route to cationic bis-cyclometallated iridium(III) complexes that has been reported involves first splitting the chloro-bridged dimer with acetonitrile, before addition of the ancillary ligand.[42] Scheme 3.3 shows this method along with the alterations made to obtain a neutral product.

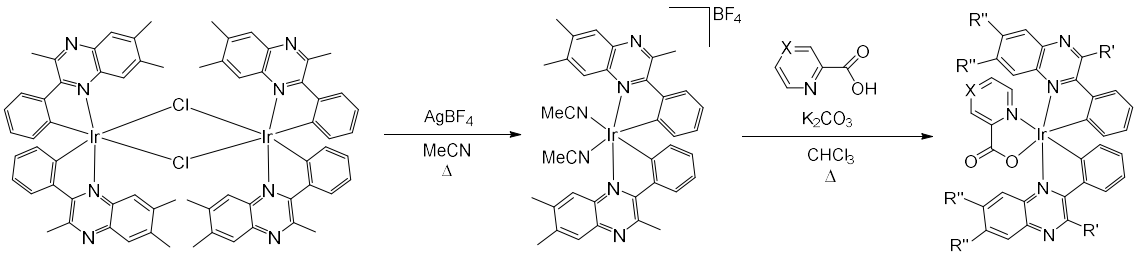

Scheme 3.3:Alternative synthetic route to complex C2c.

The advantage of this synthetic route is that the acetonitrile ligands on the cationic species formed from splitting the dimer in the presence of a silver salt are much more labile than the bridging chloride ligands of the dimer species.[43,44] This then makes the coordination of the pyrazinoic acid ligand more facile than in the previous synthesis. The second step of the new synthesis route uses chloroform as a solvent as it is very weakly coordinating so should not compete with the pyrazinoic acid.[45] Following this method, complex C2c was isolated in a yield comparable to that of the other pyrazinoate complexes suggesting that this route may result in higher yields if applied to other complexes in the series.

3.3.2. Characterisation

The complexes synthesised in this study were characterised by proton, carbon and fluorine NMR spectroscopy, in addition to high-resolution mass spectrometry. All of the complexes synthesised showed good solubility in organic solvents including chloroform, acetonitrile and acetone.

3.3.2.1. NMR Spectroscopy

One notable difference that can be observed in the NMR spectra of these complexes when compared with their cationic counterparts is increase in number of signals, arising from the loss of symmetry in the complex. As the anionic ancillary ligand is non-symmetrical, unlike 2,2'-bipyridine, the two cyclometallating ligands therefore become inequivalent. As a result, the proton NMR spectra of the neutral complexes are more complicated than those recorded for the cationic species.

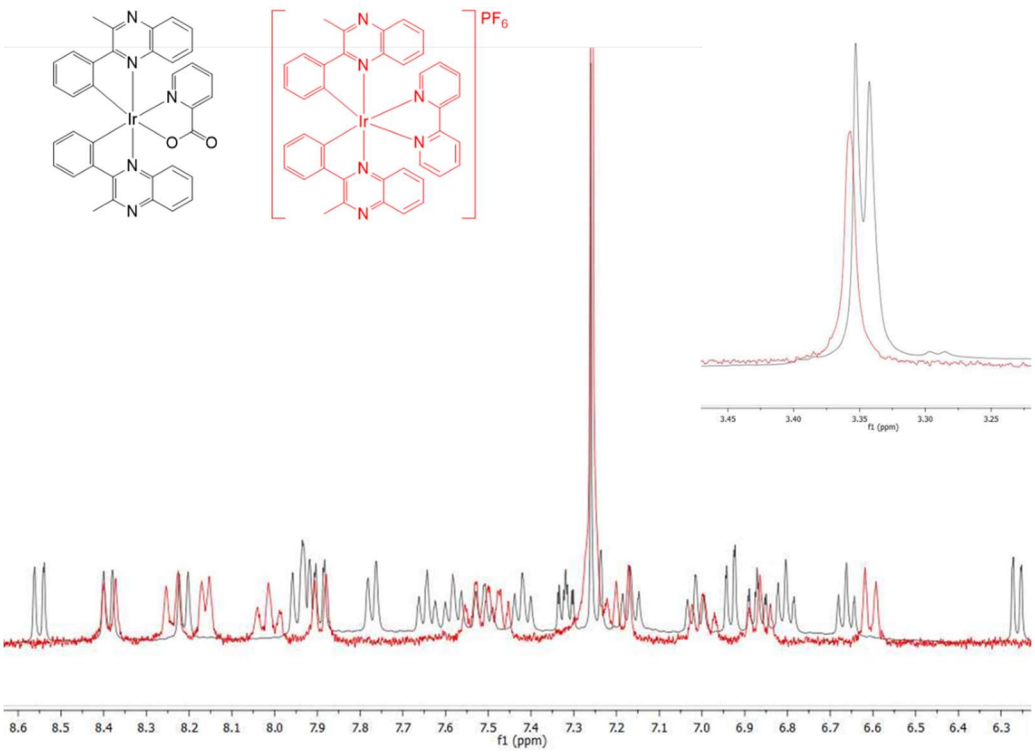

Figure 3.11: Comparison of the proton NMR spectra of C1b (black) and a cationic complex from chapter 2 bearing the same C^N ligand (red).

In Figure 3.11, the black trace spectrum is that recorded for the neutral complex C1b and the red spectrum is that recorded for the corresponding cationic complex, C1a, $[Ir(L1)_2(bipy)][PF_6]$. The inset of the figure shows the aliphatic region of the same spectra. The cationic complex shows a singlet as the methyl group of each cyclometallating ligand is equivalent. In the neutral complex, C1b, the signal splits into two singlets due to the difference in the environments caused by the non-symmetrical picolinate.

Other characteristic features that confirm coordination of the ligand to the metal centre include the doublet at 6.26 ppm which corresponds to the proton *ortho-* to the cyclometallating carbon atom on the quinoxaline ligand. As discussed in chapter 2, this is due to shielding caused by ring currents in adjacent ligands, however, as the complexes presented in this chapter are non-symmetrical, this effect is more pronounced in one cyclometallating ligand than the other. Therefore, a different signal is seen for each ligand with the doublet corresponding to the other cyclometallating ligand arising at 6.93 ppm.

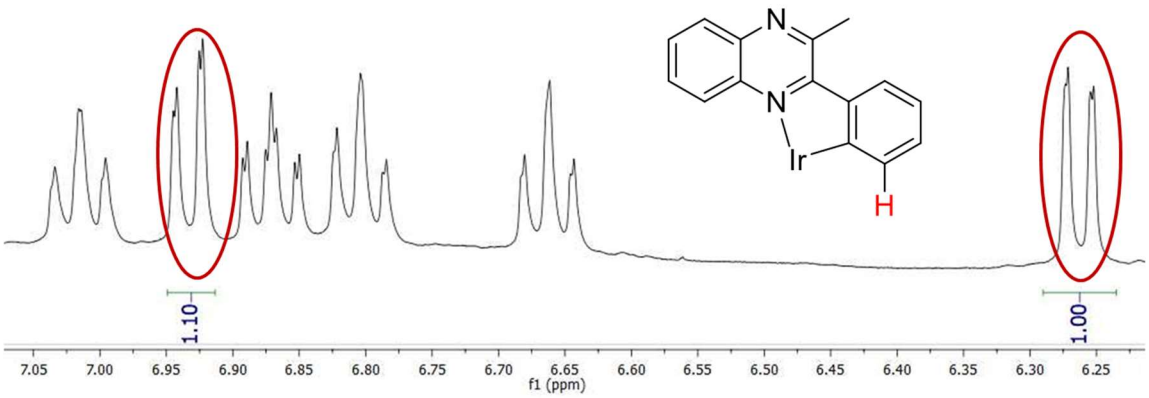

Figure 3.12: Inequivalency of protons ortho- to cyclometallating site. Circled signals correspond to proton highlighted in red.

The four fluorine-containing complexes were analysed by fluorine NMR and the data collected is tabulated below alongside the data collected for the corresponding cationic species, and the free ligands.

Table 3.1: Tabulated proton decoupled fluorine NMR data for fluorinated complexes C4b, C7b, C4c and C7c compared with free ligand and cationic counterparts.

Compound	**δ_F/ ppm**	**Compound**	**δ_F/ ppm**
HL4	-130.4	HL7	-130.0
$[Ir(L4)_2(bipy)][PF_6]$	-131.7, -133.7	$[Ir(L7)_2(bipy)][PF_6]$	-130.3, -132.7
$[Ir(L4)_2(pic)]$	-131.8, -132.9, -133.7, -134.0	$[Ir(L7)_2(pic)]$	-130.8, -131.5, -133.1, -133.6
$[Ir(L4)_2(pyr)]$	-125.01, -129.0, -129.5, -130.9	$[Ir(L7)_2(pyr)]$	-123.5, -128.1, -128.5, -130.5

The free ligands each show a single fluorine environment. In the case of ligand HL7, this is because the compound is symmetrical; ligand HL4 is not symmetrical but the two fluorine atoms are not significantly influenced by the non-symmetrical part of the ligand as they are too far

away. Two signals are observed in each cationic species as the fluorine environments become inequivalent upon coordination of the ligand to the metal centre. The number of signals observed then increases to four for each of the neutral species as each cyclometallating ligand becomes inequivalent meaning each fluorine atom in the complex is now in a unique environment.

The fluorine NMR chemical shifts in the complexes with a pyrazinoate ligand showed a higher δ_F value than the other complexes. This suggests that the ancillary ligand in these species is less electron donating to the metal centre, leaving the fluorine environments less shielded than those in the cationic species and those in the picolinate species.

3.3.2.2. Mass Spectrometry

All complexes in this study were also characterised by high-resolution mass spectrometry. In each case, the molecular ion peak was present with an isotope pattern consistent with iridium, and in some cases a fragment was present that contained both cyclometallating ligands, but without the ancillary ligand.

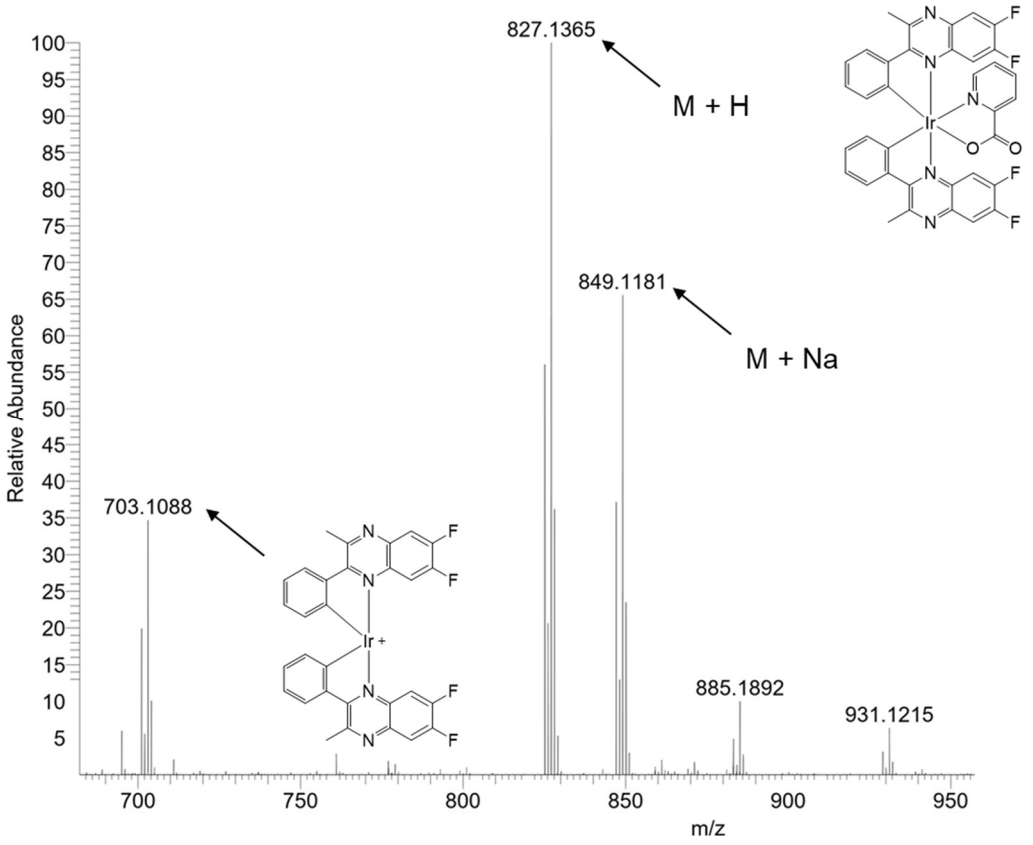

Figure 3.13: High-resolution mass spectrum recorded for C4c. Spectrum shows molecular ion peak, fragments and a sodium adduct.

The spectrum shown in Figure 3.13 is that recorded for complex C4c. The peak at 827.1365 amu is the protonated molecular ion peak, the peak at 849.1181 amu is an adduct formed from the molecular ion and a sodium ion present in the spectrometer. The peak at 703.1088 amu is a fragment that does not contain the ancillary ligand.

3.3.3. Electrochemistry

Cyclic voltammograms were recorded for each complex in the series to investigate the electrochemical properties. Each sample was dissolved in deoxygenated dichloromethane ($1x10^{-3}$ M) and measured using a platinum disc electrode (scan rate 200 mV s^{-1}, 0.1 M $[NBu_4][PF_6]$ used as electrolyte). The results are shown in Table 3.2.

Table 3.2: Redox potentials for picolinate complexes C1b-7b and pyrazinoate complexes C2c,4c, 5c and 7c. Cyclic voltammogramms recorded in DCM with NH_4PF_6 as an electrolyte. Scanning rate of 200 mV s^{-1} used. Values reported relative to Ag/Ag+ electrode with ferrocene as a reference.

Complex	**E_{ox}/ V**	**E_{red}/ V**	**Complex**	**E_{ox}/ V**	**E_{red}/ V**
C1b	+1.16	-1.42			
C2b	+1.11	-1.51	C2c	+1.18	-0.98
C3b	+1.27	-1.17			
C4b	+1.26	-1.05, -1.27	C4c	+1.24	-1.06
C5b	+1.09	-1.25	C5c	+1.19	-1.04, -1.42
C6b	+1.31	-1.12			
C7b	+1.30	-1.24	C7	+1.39	-1.15

The table shows that in the majority of cases, there is one oxidative process and one reductive process. The oxidative process was found to be irreversible and was attributed to the $Ir^{3+/4+}$ couple. As expected, the neutral complexes have lower oxidation potentials than their cationic counterparts $[Ir(L)_2(bipy)][PF_6]$. It is observed that the complexes with a pyrazonoate ligand have a more positive reduction potential than their picolinate counterparts while the substituents of the quinoxaline cyclometallating ligand also have an effect upon the redox potentials within each series of complexes. The halogenated species have higher oxidation potentials than those with methylated substituents. This could be due to the electron-withdrawing effects of these atoms reducing the electron density at the metal centre. Furthermore, the pyrazinoate species exhibit a more positive oxidation potential that the corresponding picolinate complexes, suggesting that the ancillary ligand also has a subtle effect upon the electrochemical properties. Ligand-based processes are assumed to be responsible for the reduction features observed.

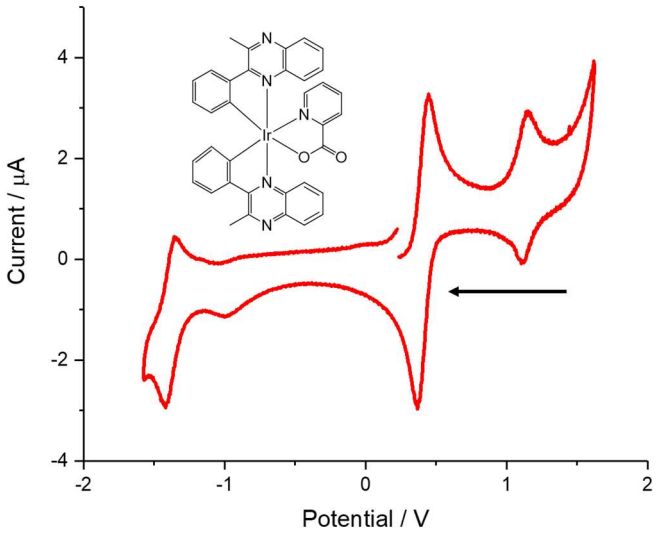

Figure 3.14: Cyclic voltammogram recorded for complex C1b in DCM with NH_4PF_6 as electrolyte. Potential reported relative to Ag/Ag^+ electrode. Fc/Fc^+ used as internal reference at +0.46 V. Scanning rate of 200 mV s^{-1}.

3.3.4. Photophysical Studies

3.3.4.1. UV-vis Absorption Spectra

The UV-vis absorption spectra of all complexes were recorded as solutions in chloroform at a concentration of 10^{-5} M. The results are collected in Table 3.3.

Table 3.3: UV-vis absorption data collected for all complexes, in $CHCl_3$ at $1x10^{-5}$ M.

Complex	λ_{abs} (ε) / nm ($M^{-1}cm^{-1}$)	Complex	λ_{abs} (ε) / nm ($M^{-1}cm^{-1}$)
C1b	491 (3700), 373 (17300)		
C2b	507 (3700), 381 (26000), 276 (116200)	C2c	480 (5100), 380 (27100), 267 (50200)
C3b	538 (2300), 389 (12500), 371 (11500), 300 (11500), 273 (21500)		
C4b	501 (4000), 377 (26300), 361 (23900), 272 (113200)	C4c	490 (4900), 374 (31000), 262 (50900)
C5b	501 (4700), 387 (28900), 300 (34200), 262 (50000)	C5c	489 (4400), 386 (24000), 271 (49000)
C6b	528 (4100), 396 (29800), 273 (90600)		
C7b	505 (3100), 387 (23100), 277 (3400)	C7c	494 (2900), 383 (15500), 272 (41200)

Figure 3.15 shows the spectra recorded for the picolinate complexes, while Figure 3.16 shows those recorded for the pyrazinoate complexes. In both sets of spectra, three distinct features

can be seen; a peak at around 500 nm arising from a metal-to-ligand charge transfer (MLCT) transition and features at around 375 and 275 nm from π-π* transitions.

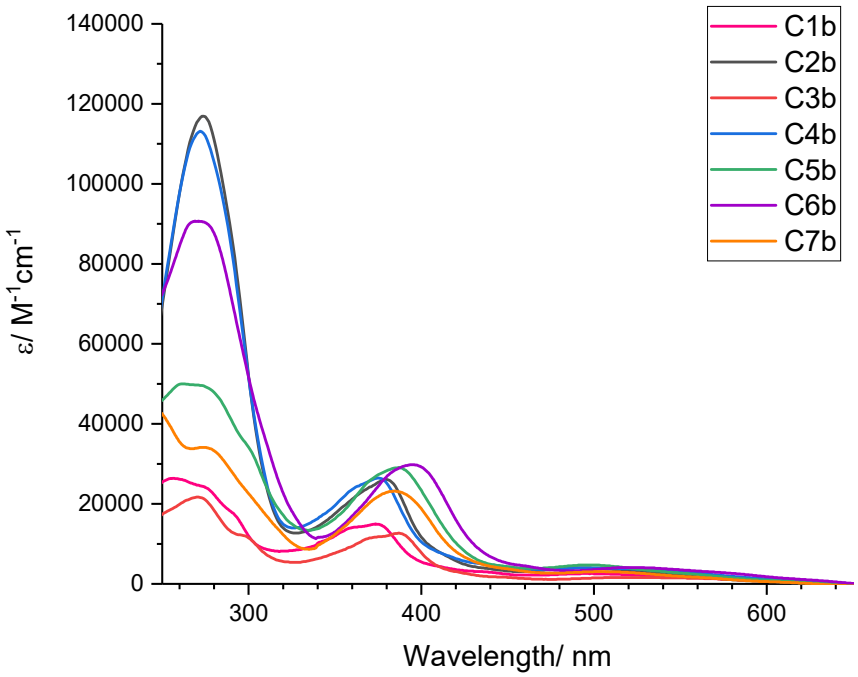

Figure 3.15: Left) UV-vis absorption spectra recorded for complexes C1b-7b. All samples recorded in chloroform at 10^{-5} M.

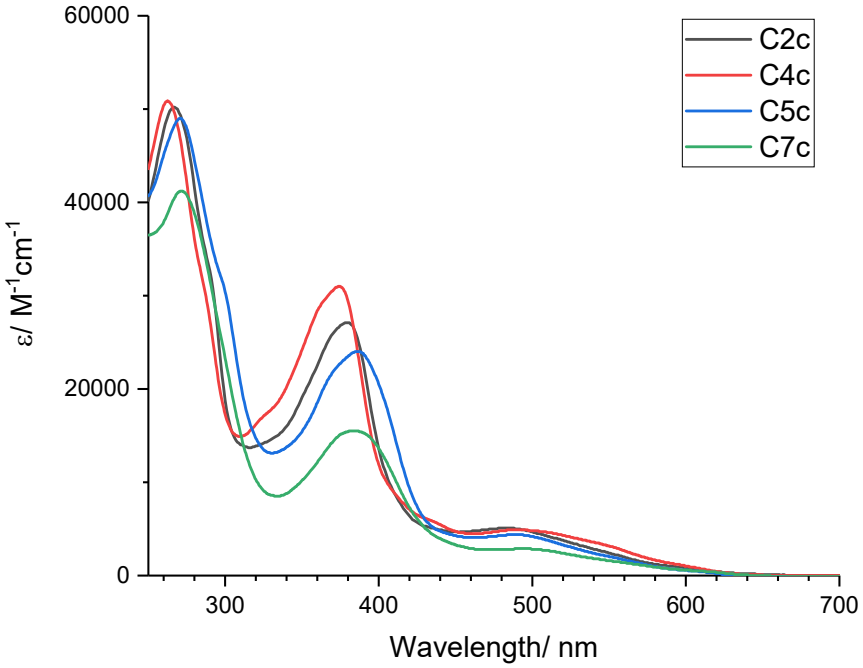

Figure 3.16: UV-vis absorption spectra recorded for complexes C2c, 4c, 5c and 7c. All samples recorded in chloroform at 10^{-5}M.

The molar extinction coefficients of the MLCT and the n-π* transitions have similar values across both series of complexes, however the value for the π-π* transition varies widely from around 20000 to 120000 $M^{-1}cm^{-1}$.

Figure 3.17 shows the MLCT absorption bands for three complexes with the same cyclometallating ligand, this shows the effect of the ancillary ligand upon this transition. There are subtle differences between the three species. In particular, this absorption band is slightly blue-shifted and appears less broad in the cationic species. The two neutral complexes have very similarly shaped absorption peaks, but the pyrazinoate complex shows a higher molar absorption coefficient at this peak than the picolinate complex.

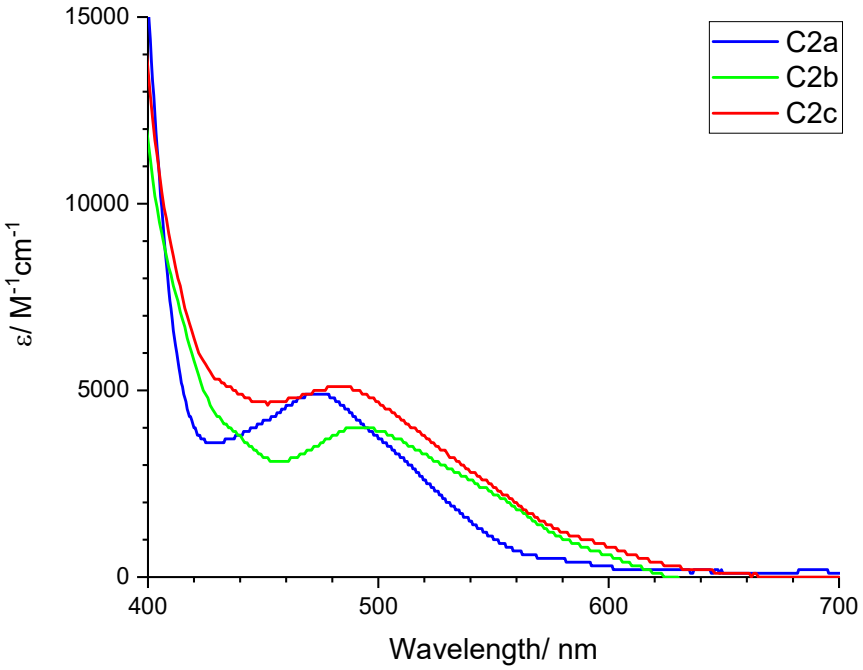

Figure 3.17: UV-vis spectra showing the effect of ancillary ligand on MLCT band. Overlaid spectra of cationic complex C2a, picolinate complex C2b and pyrazinoate complex C2c all recorded in chloroform at $1x10^{-5}$M.

3.3.4.2. Emission Data

The emission properties of the complexes were also investigated. Figure 3.18 shows the emission spectra of the picolinate complexes, while Figure 3.19 shows the spectra recorded for the pyrazinate complexes, all recorded in aerated chloroform. An excitation wavelength of 495 nm was used which corresponds to population of the MLCT excited states. The complexes with a picolinate ligand show an emission range of around 40 nm, with the species with ligand L2 having the shortest emission wavelength at 635 nm, and the longest emission wavelength of 677 nm arising from the complex with ligand L6.

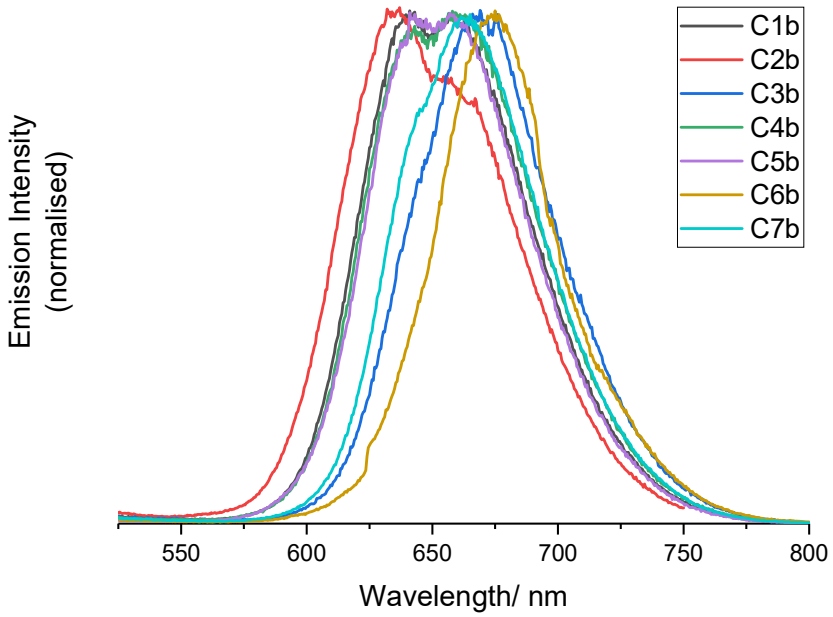

Figure 3.18: Normalised emission spectra recorded for complexes C1b-7b in aerated $CHCl_3$, λ_{ex} = 495 nm.

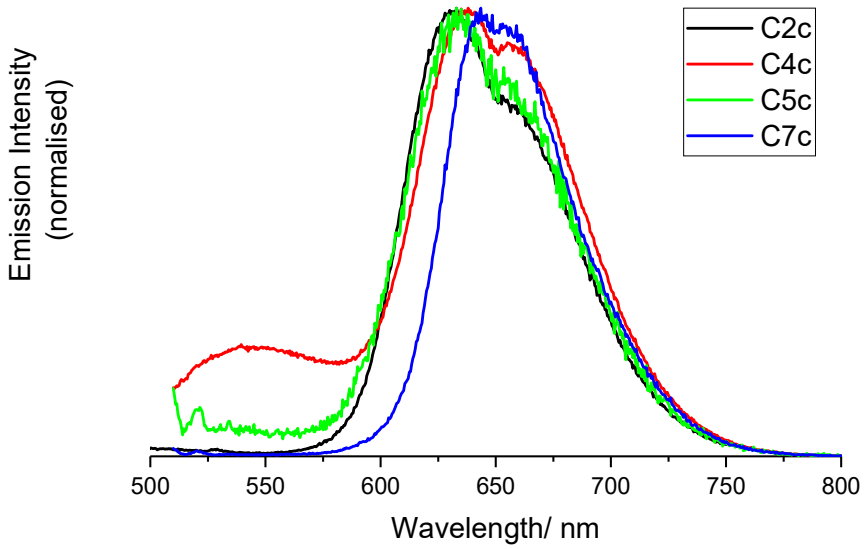

Figure 3.19: Normalised emission spectra recorded for complexes C2c, 4c, 5c and 7c in aerated $CHCl_3$, λ_{ex} = 495 nm.

The complexes with the pyrazinoate ligands show a modest range of emission wavelengths. The three complexes C2c, C4c and C5c all emit at 635 nm, whilst the complex C11 emits at 646 nm. For comparison, the emission spectra of three complexes bearing the same C^N ligand, L2, are shown in Figure 3.20. This figure shows that the ancillary ligand also has a subtle affect upon the wavelength of light emitted by the complex. The cationic complex bearing a 2,2'-bipyridine ancillary ligand shows the shortest emission wavelength at 615 nm, with both neutral complexes showing emission at around 635 nm.

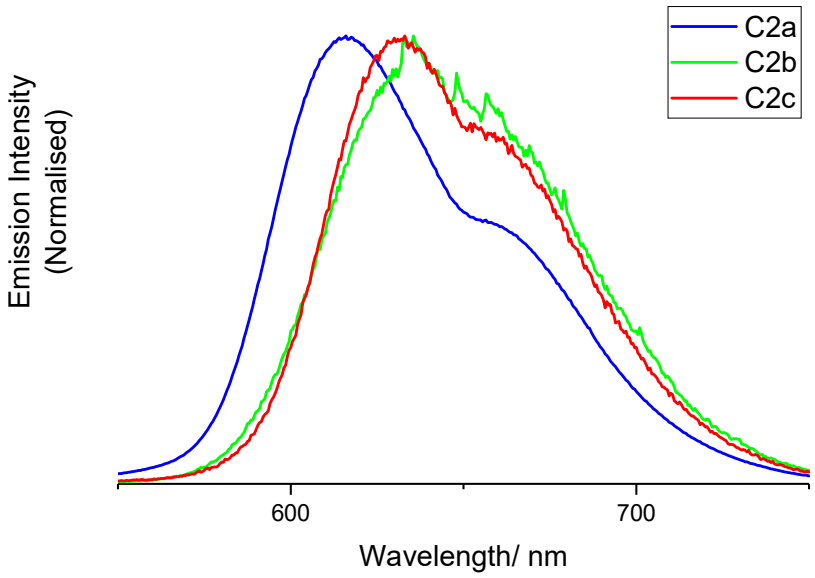

Figure 3.20: Overlaid absorption spectra of complexes bearing L2 with different ancillary ligands.

Figure 3.21 shows the absorption spectrum of C1b overlaid with the emission spectrum of the same complex to illustrate the Stokes' shift. The Stokes' shift occurs because the energy of emission is always less than that of absorption and can be measured by the difference in wavelength between the absorption maximum and the emission wavelength.[14] This complex shows a Stokes' shift of 157 nm. Large Stokes shifts are consistent with phosphorescence.

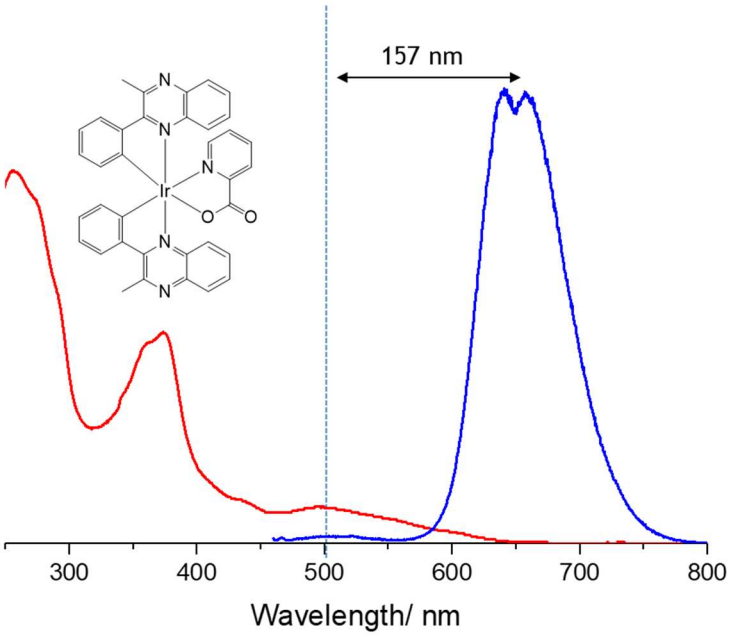

Figure 3.21: Absorption and emission spectra for complex C1b illustrating the Stokes shift.

Red light has a wavelength of between 622 – 780 nm.[46] All of the complexes synthesised in this chapter emit light in this range of the visible spectrum over a range of 42 nm. When these results are combined with the red-emitting complexes discussed in chapter 2, a total emission range of

60 nm is achieved across a series of 18 complexes. This means that it is possible to tune the emission of a complex to a particular 'shade' of red by careful selection of cyclometallating ligand substituents and ancillary ligand.

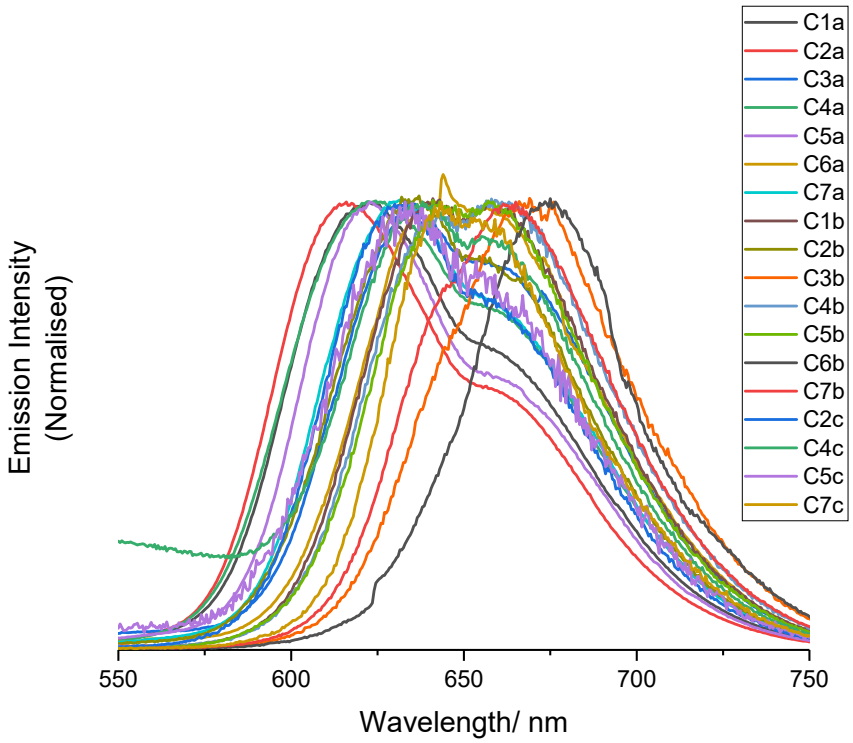

Figure 3.22: Overlaid emission spectra of all neutral complexes in this chapter, combined with the emission spectra of all cationic complexes from chapter 2.

3.3.4.3. Luminescence Lifetime

The luminescence lifetimes of the complexes studied in this chapter are tabulated below. Across each series, the cyclometallating ligand has an effect upon emission lifetime. For the picolinate complexes, the two methylated ligands, L2 and L5, gave the longest lifetime values of 333 and 321 ns respectively, whilst the chlorinated ligands, L3 and L6, give the shortest lifetime values at 275 and 294 ns. This is likely due to the heavy atom effect induced by the chlorine atoms, which can increase the rate of intersystem crossing.

However, in the pyrazinoate complex series, it is the fluorinated ligands L4 and L7 that give the longest-lived emission, with lifetime values of 402 and 454 nm respectively. In addition to this observation, the lifetimes recorded for the complexes with pyrazinoate ligands show longer values than those recorded for the corresponding picolinate complexes.

Table 3.4: Luminescent lifetimes recorded for neutral iridium(III) complexes. λ_{ex} = 295 nm, recorded in aerated $CHCl_3$

Complex	τ/ ns	Complex	τ/ ns
C1b	308		
C2b	333	C2c	350
C3b	275		
C4b	321	C4c	402
C5b	323	C5c	370
C6b	294		
C7b	323	C7c	454

Table 3.5 shows the collated data for both sets of neutral complexes compared with their cationic counterparts. While there is no distinct trend over the three series of complexes that links the cyclometallating ligand with the length of emission lifetime, there is a trend linking the ancillary ligand with emission lifetime. Overall, the cationic species have the longest emission lifetimes with the longest lifetime in the table being recorded for the cationic species with the fluorinated ligand, L7, at 539 ns. The complexes with a picolinate ligand generally have the shortest lifetimes in the series, with the chlorinated species, L4, having a lifetime of 321 ns

Table 3.5: A table listing the effect of ancillary ligand upon the luminescence lifetime of complexes with the same cyclometallating ligands. Λ_{ex} = 295 nm, all samples recorded in $CHCl_3$

Complex	τ/ ns	Complex	τ/ ns	Complex	τ/ ns
C2b	333	C2c	350	C2a	453
C4b	321	C4c	402	C4a	396
C5b	323	C5c	370	C5a	440
C7b	323	C7c	454	C7a	539

3.3.4.4. Quantum Yield

The quantum yield of each complex was measured, and the results are shown in Table 3.6. The measurements were recorded in aerated chloroform using $[Ru(bpy)_3][PF_6]_2$ as a standard.

There is no clear trend in the data that links either the cyclometallating ligand or the ancillary ligand to the quantum efficiency of the complex. The highest and lowest quantum yield values were recorded for pyrazinoate complexes with fluorinated cyclometallating ligands. The complex with L4, C4c, gave the highest value over both series at 8.9 %; whilst the complex C7c has the lowest quantum yield at 1.3 %. The picolinate complexes with these same ligands have the same quantum yield value and sit at halfway between the values recorded for their pyrazinoate analogues.

Table 3.6: Quantum yield values for all complexes with $[Ru(bpy)_3][PF_6]_2$ as a standard. (Φ_Δ = 0.018 in acetonitrile.[47]

Complex	Φ/ %	Complex	Φ/ %	Complex	Φ/ %
C1b	4.1			C1a	5.7
C2b	6.8	C2c	5.9	C2a	5.1
C3b	3.6			C3a	1.8
C4b	4.8	C4c	8.9	C4a	6.0
C5b	3.2	C5c	2.9	C5a	6.6
C6b	2.7			C6a	6.4
C7b	4.8	C7c	1.3	C7a	7.8

The last two columns of the table list the quantum yield values of the cationic complexes. These values also show no correlation between cyclometallating ligand and quantum yield. There is also no apparent trend when comparing the same cyclometallating ligand across a series of differing ancillary ligands.

Photoluminescent quantum yields of neutral red-emitting phosphors in solution reported in the literature are typically low. Many of these complexes have cyclometallating ligands based on phenylquinoline, with the highest quantum yield value recorded for methyl-substituted phenylquinoline complexes of iridium(III) with an acetylcacetone (acac) ligand recorded 14 %.[39] However, in 2015, a fluorine-substituted phenylquinoline complex with a picolinate ligand was synthesised which exhibited a quantum yield value of 65 %.[48] Although the complexes in this study have much lower values, this could be due to quenching by triplet oxygen in solution as these values were measured in aerated solvents, while the literature examples are unclear on whether the samples were de-aerated or not.

Table 3.7 shows the lifetime and quantum yield for each complex in this chapter alongside the calculated values for the rates of radiative, k_r, non-radiative, k_{nr}, decay. This table shows that the k_r values are relatively consistent across the series of complexes whilst the k_{nr} value shows much more variation. From this, it can be inferred that the photophysical properties of these complexes are dominated by non-radiative processes.

Table 3.7: Photophysical data collected for all neutral comlexes.

Complex	A τ/ ns	B Φ/ %	K_{nr}. 10^6 s^{-1}	K_r/ 10^5 s^{-1}
C1b	308	4.1	3.11	1.33
C2b	333	6.8	2.80	2.04
C3b	275	3.6	3.51	1.31
C4b	321	4.8	2.97	1.50
C5b	323	3.2	3.00	0.99
C6b	294	2.7	3.31	0.92
C7b	323	4.8	2.95	1.49
C2c	350	5.9	2.69	1.69
C4c	402	8.9	2.27	2.21
C5c	370	2.9	2.62	0.78
C7c	454	1.3	2.17	0.29

3.3.4.5. Solvent Studies

The complex C2c was chosen to investigate the effect of solvent upon the absorption and emission spectra of the pyrazinoic acid complex series. The extra heteroatom in the aromatic ring of the pyrazinoic acid could make the absorption and emission properties of the molecule more susceptible to solvent effects such as polarity and hydrogen bonding.

Figure 3.23 shows the UV-vis absorption spectra of C2c recorded in a variety of solvents with differing polarity and dielectric constant. The position of the MLCT absorption band does not change depending on the solvent, however the extinction coefficient of this peak does vary marginally, but not in line with polarity or dielectric constant of the solvent.

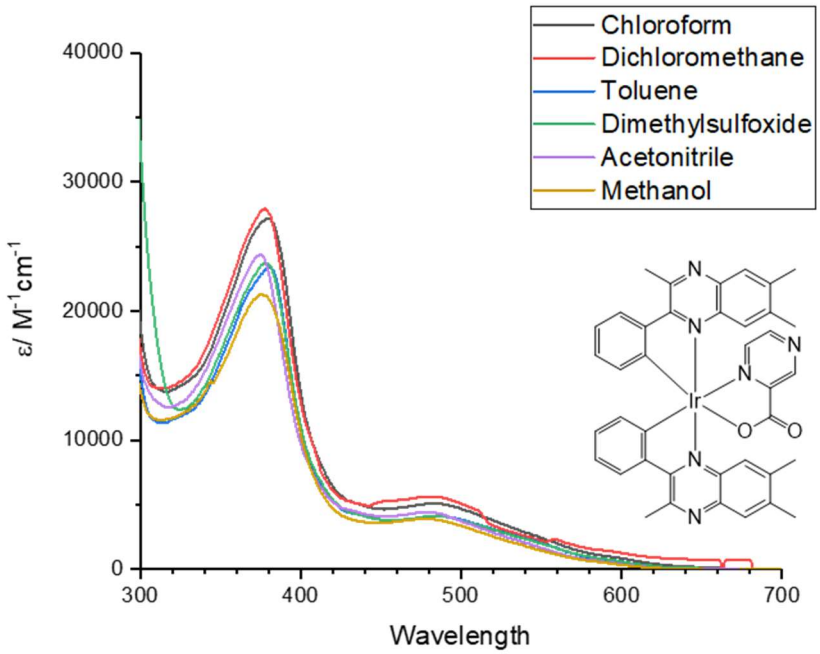

Figure 3.23: UV-vis absorption spectra recorded for complex C2c in different solvents. All spectra recorded at a concentration of 10^{-5} M.

The emission spectrum of the same complex was also recorded in different solvents. Unlike the absorption spectra, the position of the emission peak does change depending upon the solvent. The longest wavelength emission was observed in methanol at 662 nm and the shortest wavelength was recorded in toluene at 622 nm. As the emission wavelength increases with increasing polarity of the solvent, the complex is undergoing positive solvatochromism.

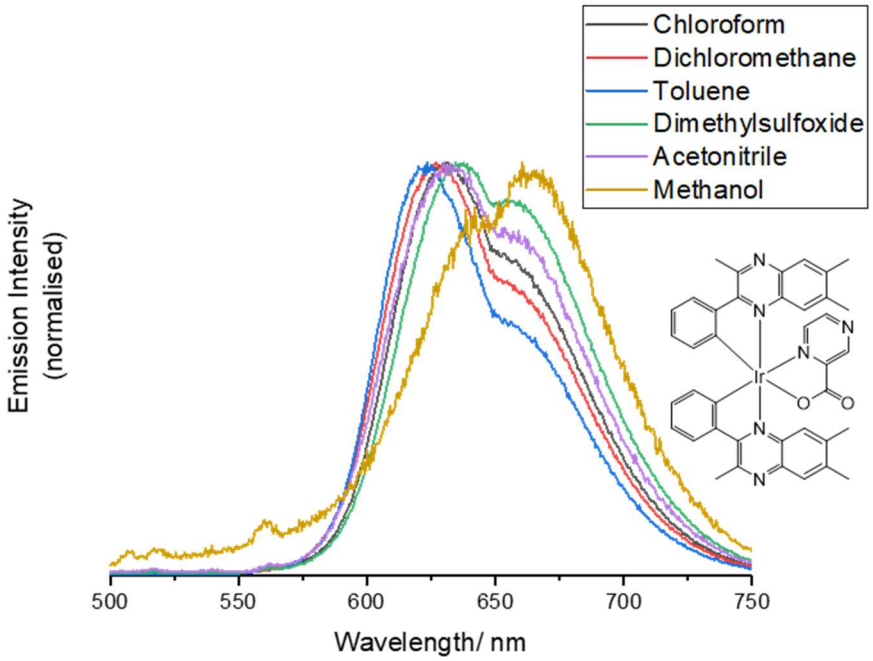

Figure 3.24: Emission spectra recorded for complex C2c in different solvents, showing positive solvatochromism. λ_{ex} = 495 nm.

The ^{3}MLCT excited state from which the complex emits creates a dipole moment in the molecule and depending upon the dielectric constant (ε) of the solvent, the solvent molecules arrange themselves around this dipole to varying degrees. The polar solvents stabilise this state, lowering the energy gap between the excited and ground states, leading to a bathochromic shift in emission. The change in emission wavelength between solvents is relatively small, at around 40 nm, suggesting that the excited state dipole is spread across the ligands and not concentrated on any particular one.

The hydrogen bonding ability of a solvent can also have an impact upon the emission wavelength. Methanol has a lower dielectric constant (see Table 3.8) than DMSO, but causes a larger bathochromic shift in emission wavelength, as its better ability to hydrogen-bond further stabilises the excited state. The most likely site of this hydrogen bonding is to one of the heteroatoms not involved in coordination.

In addition to this, the lifetime of the complex is also affected by a change in solvent. The general trend is that the luminescence lifetime increases with increasing dielectric constant of the solvent. However, the exception to this trend is acetonitrile, which despite having the second-highest dielectric constant, gives the shortest lifetime value. This may be attributed to the combination of high solubility of oxygen in acetonitrile and the low viscosity of the solvent.[49–51] These factors could help facilitate quenching of the luminescence lifetime by triplet oxygen, $^3O_2$.

Table 3.8: Emission and lifetime data recorded for complex C2c in different solvents along with their dielectric constants. [a] - λ_{ex} = 495 nm, [b] - λ_{ex} = 295 nm.

Solvent	λ_{em}/ nm[a]	τ/ ns[b]	Dielectric constant, ε
Chloroform	630	350	4.81
Dichloromethane	626	468	8.93
Toluene	622	253	2.38
Dimethyl sulfoxide	636	695	46.7
Acetonitrile	632	66	37.5
Methanol	662	630	32.7

3.3.5. Computational Studies

Extensive computational studies have been carried out upon ten of the eleven complexes reported in this chapter. This work was carried out by Thomas Stonelake and Dr Joseph Beames of Cardiff University and the findings are summarised below.

Density functional theory (DFT) calculations were found to support the experimental findings in this chapter. DFT was used to calculate the contribution of each moiety in the molecule to the HOMO and LUMO and these results are shown in Table 3.9. In the case of complex C1b, the quinoxaline ligands were responsible for 36 and 59 % of the contribution to the LUMO each, while the iridium centre and the picolinate ligand contributed only 4 and 1% respectively. These differ from the results calculated for the corresponding cationic complex, $[Ir(L1)_2(bipy)][PF_6]$, as the asymmetric picolinic acid ligand introduces inequivalency between the quinoxaline ligands. It was observed that where the complexes possessed a picolinate ligand, the quinoxaline ligands

formed pseudo-degenerate pairs. For example, the complex C2b showed LUMO contributions of 34 % and 60 % from quinoxaline ligands Q1 and Q2 respectively, whilst the LUMO+1 shows the opposite (Q1 = 60 %, Q2 = 34 %). These pseudo-degenerate pairs were not observed in the pyrazinoate complexes. Overall, the calculations suggest that the emissive state is almost entirely ligand-centred in character and not MLCT as previously supposed.

Table 3.9: A summary of the calculated percentage contributions to each MO from each part of the complex. Q1 and Q2 refer to the inequivalent quinoxaline ligands

Complex	Ir 5d		Q1		Q2		pic/pyz
	HOMO-1	HOMO	LUMO	LUMO+1	LUMO	LUMO+1	LUMO+2
C1b	43	40	36	59	59	36	96
C2b	37	39	34	60	60	34	96
C3b	41	39	40	55	55	40	94
C4b	40	39	39	56	56	39	96
C5b	21	38	38	57	57	38	94
C6b	21	38	42	53	53	41	6
C7b	16	38	41	54	54	41	90
C2c	28	38	48	47	38	39	77
C5c	10	37	41	35	47	48	76
C7c	8	37	44	46	49	46	89

The absorption spectrum of each complex was simulated and compared with that recorded experimentally. Figure 3.25 shows the results obtained for complex C1b and it can be seen that qualitatively, the simulated spectra are in good agreement with experiment, each featuring three components in decreasing intensity with increasing wavelength. However, the absolute energy of each transition is underestimated in the simulation as presented in Table 3.10.

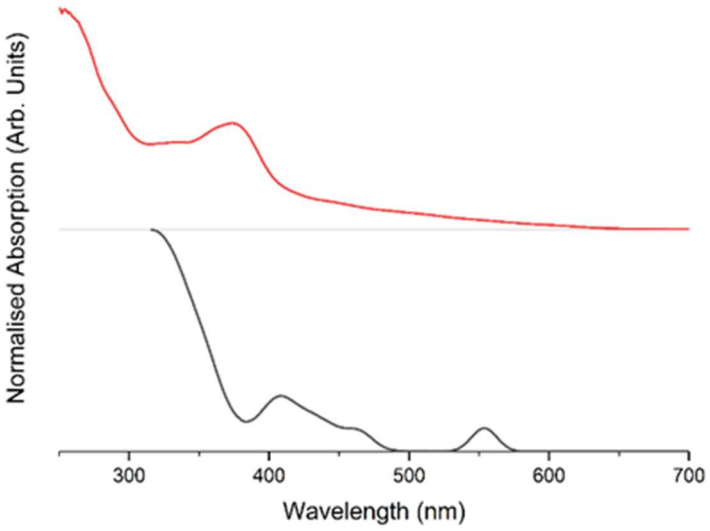

Figure 3.25: Comparison of experimental emission spectrum (red) and simulated emission spectrum (black) of complex C1b.

The calculations predict that there are no singlet transitions that occur above 500 nm and in each complex, there is a singlet-triplet absorption feature between 550 – 620 nm which corresponds well with the broad, low intensity feature observed experimentally.

The effect of ligand substitution was also studied. It is known that electron withdrawing groups of the cyclometallating ligands stabilise the HOMO, while electron donating groups have the opposite effect.[52–54] Here, it was calculated that complexes with fluoro- and chloro- substituted quinoxaline ligands exhibited lower energy values for frontier orbitals, with the HOMO typically being less stabilised than the LUMO. It has been suggested that this effect could be due to the quinoxaline rings contributing more to the LUMO than the HOMO. The result of this effect is that the HOMO – LUMO gap is slightly different depending upon the ligand substituents; the electron withdrawing substituents decrease this gap, while the electron donating methyl substituents lead to an increase. In addition to this, it was observed that the phenyl-substituted ligands have similar HOMO values to the methyl-substituted ligands, but have lower LUMO values.

Table 3.10: Absorption and emission values calculated for each complex. Experimental values for $T_1 \rightarrow S_0$ are written in parentheses

Complex	$S_0 \rightarrow S_1$ (nm)	$S_0 \rightarrow T_1$ (nm)	$T_1 \rightarrow S_0$ (nm)
C1b	424	578	697 (646)
C2b	419	568	689 (640)
C3b	440	608	739 (667)
C4b	428	586	710 (651)
C5b	425	579	705 (648)
C6b	445	618	751 (675)
C7b	434	597	722 (659)
C2c	416	563	685 (632)
C5c	422	573	703 (641)
C7c	431	589	714 (651)

The ancillary ligand also shows a similar effect. Both picolinate and pyrazinoate are electron withdrawing ligands, however the pyrazinoate has a slightly stronger effect due to the additional nitrogen atom in the aromatic ring. These electron withdrawing effects stabilise the HOMO and the LUMO, but the pyrazinoate ligand stabilises the HOMO more than the LUMO in comparison with picolinate. As a result of this, complexes with a pyrazinoate ligand exhibit slightly blue-shifted emission compared to their picolinate counterparts. The large metal contribution to the HOMO may be responsible for the differences in HOMO *vs.* LUMO stabilisation.

3.3.6. Transient Absorption Studies

Transient absorption studies were also carried out by Thomas Stonelake and Dr Joseph Beames of Cardiff University.

The transient absorption (TA) spectra recorded show three distinct features. The first of these features occurs at around 350 – 400 nm in all complexes which is attributed to the ground state bleach, the depletion of the ^{1}MLCT absorption band. The second of these features is a positive

going signal at between 400 – 500 nm which, in most cases, consists of two peaks. As the lifetime of this feature closely matched that of the $T_1 \rightarrow S_0$ emission decay kinetics, this was assigned as a triplet-triplet transition. This assignment was also supported by time dependent DFT calculations. The third feature observed is a broad, positive going feature at around 600 nm which was relatively weak. This was also assigned to a triplet-triplet transition.

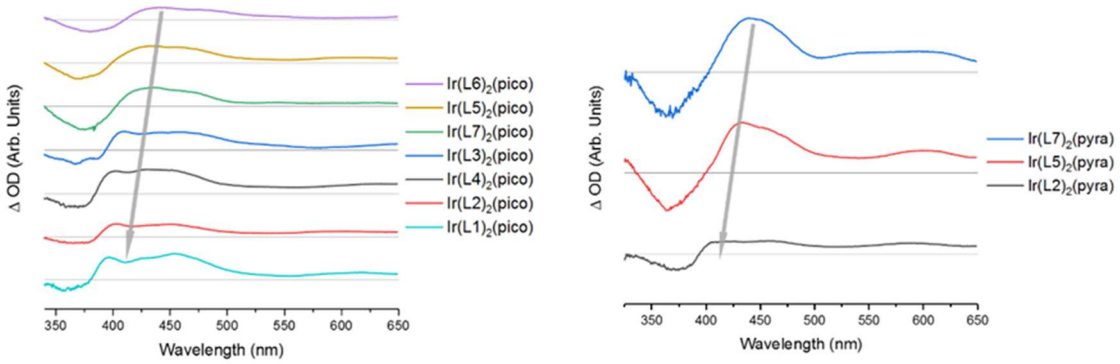

Figure 3.26: Left) TA spectra recorded for picolinate complexes C1b-7b. Right) TA spectra recorded for pyrazinoate complexes C2c, C5c and C7c

As mentioned previously, the LUMO of the picolinate complexes exhibits pseudo-degeneracy. This can be observed in the TA spectra as the structured absorption profiles in the 400 – 500 nm range. It is of note that these features were not observed in the previously reported spectra recorded for the cation species, $[Ir(L)_2(bipy)][PF_6]$. In addition to this, all complexes showed a red-shift relative to the complex C1, with the size of the shift depending upon quinoxaline substituents. Also, diphenyl substitution results in a greater red-shift than phenyl, methyl-substitution.

3.4. Conclusion

In this chapter of work, eleven novel neutral bis-cyclometallated iridium(III) complexes have been synthesised and fully characterised. The complexes utilised a series of seven cyclometallating ligands based upon quinoxaline, and two different ancillary ligands derived from picolinic acid and pyrazinoic acid.

These complexes showed emission between 635 and 677 nm in the red region of the spectrum, with the picolinate complexes showing a greater range in emission wavelength than the pyrazinoate analogues. When considered in combination with the structurally related cationic complexes synthesised in chapter two, the total emission range in the red region is over 60 nm.

In addition to this, the emission wavelength of each complex can be tuned to a lesser degree by changing the solvent used in the emission experiments. More polar solvents stabilise the ^{3}MLCT emitting state leading to a bathochromic shift in emission wavelength. This effect is much smaller than the effect of ligand substituents as the emitting state of these complexes is not purely MLCT in character as supported by DFT calculations.

3.5. Experimental

^{1}H and $^{13}C\{^{1}H\}$ NMR spectra were recorded on an NMR-FT Bruker 500 and 400 MHz spectrometer and recorded in $CDCl_3$, acetone-d_6, acetonitrile-d_3 and DMSO-d_6. ^{1}H and $^{13}C\{^{1}H\}$ NMR chemical shifts (δ) were determined relative to residual solvent peaks with digital locking and are given in ppm. Low-resolution mass spectra were obtained by the staff at Cardiff University. High-resolution mass spectra were carried out at the EPSRC National Mass Spectrometry Facility at Swansea University. UV-Vis studies were performed on a Shimadzu UV-1800 spectrophotometer as $CHCl_3$ solutions (1×10^{-5} M). Photophysical data were obtained on a JobinYvon–Horiba Fluorolog spectrometer fitted with a JY TBX picosecond photodetection module as $CHCl_3$ solutions. Emission spectra were uncorrected and excitation spectra were instrument corrected. The pulsed source was a Nano-LED configured for 459 nm output operating at 1 MHz. Luminescence lifetime profiles were obtained using the JobinYvon–Horiba FluoroHub single photon counting module and the data fits yielded the lifetime values using the provided DAS6 deconvolution software. Quantum yield measurements were obtained on aerated $CHCl_3$ solutions of the complexes using $[Ru(bpy)_3](PF_6)_2$ in aerated MeCN as a standard (Φ = 0.016).

For synthesis of ligands L1-L7 see chapter 2.

Synthesis of [Ir(L1)$_2$(pic)] C1b $[\{Ir(L1)_2(\mu\text{-}Cl)\}_2]$ (100 mg, 0.08 mmol) and 2-picolinic acid (2 eq., 18 mg, 0.16 mmol) were dissolved in 2-ethoxyethanol (10 mL) along with potassium carbonate (2 eq., 22 mg, 0.16 mmol) and silver nitrate (4 eq., 51 mg, 0.32 mmol). The reaction mixture was heated at reflux under a nitrogen atmosphere in a covered flask for 24 hours. The reaction mixture was then cooled to room temperature before the addition of cold water (20 mL) to form a dark red precipitate. The solid was collected by filtration to yield the product as a red powder (Yield = 107 mg, 97%). ^{1}H NMR (400 MHz, $CDCl_3$): δ_H 8.55 (1H, d, J_{HH} = 8.56 Hz), 8.39 (1H, d, J_{HH} = 8.56 Hz), 8.21 (1H, d, J_{HH} = 8.56 Hz), 7.97 – 7.87 (4H, m), 7.77 (1H, d, J_{HH} = 7.79 Hz), 7.64 (1H, t, J_{HH} = 7.42 Hz), 7.61 – 7.55 (1H, m), 7.54 – 7.48 (1H, m), 7.42 (1H, t, J_{HH} = 7.20 Hz), 7.34 – 7.30 (1H, m), 7.17 (1H, t, J_{HH} = 7.20 Hz), 7.02 (1H, t, J_{HH} = 7.20 Hz), 6.93 (1H, d, J_{HH} = 7.57 Hz), 6.90 – 6.85 (1H, m), 6.80 (1H, t, J_{HH} = 7.20 Hz), 6.66 (1H, t, J_{HH} = 7.53 Hz), 6.26 (1H, d, J_{HH} = 7.77 Hz), 3.35 (6H,overlapping s) ppm. ^{13}C $\{^{1}H\}$ NMR (100 MHz, $CDCl_3$): δ_C 145.5, 138.2, 137.1, 135.2, 131.1, 130.1, 129.9, 129.7, 129.5, 129.4, 128.9, 128.7, 127.9, 127.6, 127.5, 127.1, 124.5, 122.4, 121.7, 27.6 ppm. HRMS (ESI) found *m/z* 754.1789, calculated *m/z* 754.1790 for $[C_{36}H_{26}IrN_5O_2]H+$. UV vis. ($CHCl_3$) λ_{max} (ε / $dm^3mol^{-1}cm^{-1}$): 491 (3700), 373 (17300) nm. IR (solid) υ_{max} = 3723, 2962, 1630, 1507, 1578, 1564, 1526, 1481, 1451, 1425, 1387, 1334, 1321, 1289, 1260, 1219, 1194, 1165, 1015, 907, 841, 795, 758, 739, 662, 627, 592, 552, 407 cm^{-1}.

Synthesis of [Ir(L2)$_2$(pic)] C2b as C_1 but with $[\{Ir(L2)_2(\mu\text{-}Cl)\}_2]$ (100 mg, 0.07 mmol). Purified by column chromatography using DCM: MeOH (96:4) and product collected as first red band. Red solid (Yield = 13 mg, 12 %). ^{1}H NMR (400 MHz, $CDCl_3$): δ_H 8.36 (1 H, d, J_{HH} = 1.1 Hz), 8.36 – 8.31 (1 H, m), 8.19 (1 H, d, J_{HH} = 8.2 Hz), 7.96 – 7.92 (1 H, m), 7.83 (1 H, app. ddd), 7.69 (1 H, s), 7.66 – 7.62 (4 H, m), 7.32 (1 H, app. ddd), 7.13 (1 H, app. ddd), 7.03 (1 H, s), 6.99 (1 H, app. ddd), 6.86 (1 H, app. dd), 6.79 – 6.71 (1 H, m), 6.65 – 6.60 (1 H, m), 6.28 – 6.18 (1 H, m), 2.38 – 2.36 (6 H, overlapping s), 2.32 (6 H, s), 2.29 – 2.27 (6 H, overlapping s) ppm. $^{13}C\{^{1}H\}$ NMR (101 MHz, $CDCl_3$): δ_C 142.1, 137.8, 129.7, 129.4, 128.5, 127.6, 127.1, 126.3, 124.4, 122.0, 121.4, 27.9, 27.5, 20.3, 20.0, 19.7, 19.6 ppm. HRMS (ESI) found *m/z* 810.2415, calculated *m/z* 810. 2417 for $[C_{40}H_{34}IrN_5O_2]H+$. UV vis. ($CHCl_3$) λ_{max} (ε / $dm^3mol^{-1}cm^{-1}$): 507 (3700), 381 (26000), 276 (116200) nm. IR (solid) υ_{max} = 3362, 2915, 1655, 1601, 1578, 1562, 1526, 1483, 1408, 1335, 1321, 1287,

1269, 1219, 1163, 1121, 1059, 1047, 1034, 1024, 991, 903, 878, 839, 795, 758, 743, 733, 702, 691, 658, 629, 567, 476, 430 cm^{-1}.

Synthesis of [Ir(L3)$_2$(pic)] C3b as C_1 but with [{Ir(L3)$_2$(μ-Cl)}$_2$] (100 mg, 0.06 mmol). Purified by column chromatography using DCM: MeOH (95:5) and product collected as first red band. Red solid (Yield = 20 mg, 18%). ^{1}H NMR (400 MHz, $CDCl_3$): δ_H 8.83 (1 H, d, J_{HH} = 12.5 Hz), 8.42 (1 H, d, J_{HH} = 8.3 Hz), 8.29 – 8.19 (1 H, m), 8.06 (2 H, s), 8.04 (1 H, s), 7.96 – 7.90 (1 H, m), 7.84 (1 H, t, J_{HH} = 6.4 Hz), 7.76 (1 H, app. dt), 7.46 – 7.39 (1 H, m), 7.38 (1 H, s), 7.24 – 7.16 (1 H, m), 7.06 – 7.02 (1 H, m), 6.87 (1 H, d, J_{HH} = 3.8 Hz), 6.76 – 6.66 (1 H, m), 6.17 (1 H, app. dd), 3.47 – 3.23 (6 H, overlapping s) ppm. ^{13}C{^{1}H} NMR (126 MHz, $CDCl_3$): δ_C 171.2, 164.3, 154.8, 154.3, 152.5, 152.3, 151.8, 145.5, 145.0, 143.8, 139.5, 139.2, 139.1, 138.8, 138.7, 136.6, 136.3, 134.9, 134.7, 134.2, 133.2, 131.0, 130.6, 130.3, 130.0, 128.7, 128.4, 128.2, 127.8, 125.4, 122.7, 122.2, 28.0, 27.7 ppm. HRMS (ESI) found *m/z* 892.0191, calculated *m/z* 892.0195 for $[C_{36}H_{22}Cl_4IrN_5O_2]H^+$. UV vis. ($CHCl_3$) λ_{max} (ε / $dm^3mol^{-1}cm^{-1}$): 538 (2300), 389 (12500), 371 (11500), 300 (11500), 273 (21500) nm. IR (solid) υ_{max} = 3407, 3060, 1655, 1599, 1578, 1524, 1460, 1431, 1316, 1190, 1163, 1115, 1049, 1009, 963, 882, 855, 758, 725, 671, 646, 610, 556, 469, 436, 417 cm^{-1}.

Synthesis of [Ir(L4)$_2$(pic)] C4b as C_1 but with [{Ir(L4)$_2$(μ-Cl)}$_2$] (80 mg, 0.05 mmol). Purified by column chromatography, DCM used to elute ligand followed by DCM:MeOH (9:1) to elute product as red band. The product was then recrystallised from chloroform and hexane to give a red solid. (Yield = 27 mg, 30 %). ^{1}H NMR (400 MHz, $CDCl_3$): δ_H 8.81 (1H, d, J_{HH} = 0.4 Hz), 8.42 (1H, dd, J_{HH} = 8.3, 1.0 Hz), 8.25 – 8.21 (1H, m), 8.06 (1H, d, J_{HH} = 0.4 Hz), 8.04 (1H, d, J_{HH} = 0.4 Hz), 7.96 – 7.93 (1H, m), 7.83 – 7.78 (1H, m), 7.76 (1H, app. td), 7.44 – 7.40 (1H, m), 7.38 (1H, d, J_{HH} = 0.4 Hz), 7.23 – 7.17 (1H, m), 7.07 – 7.03 (1H, m), 6.86 (2H, d, J_{HH} = 3.9 Hz), 6.71 (1H, app. dt), 6.19 – 6.16 (1H, m), 3.33 (6H, overlapping s) ppm. ^{13}C{^{1}H} NMR (101 MHz, $CDCl_3$): δ_C 171.1, 153.9, 152.0, 145.4, 145.2, 144.1, 138.8, 136.7, 134.7, 130.7, 130.2, 129.9, 128.2, 128.0, 122.8, 122.2, 114.3, 31.6, 27.7, 27.5, 22.7, 14.2 ppm. ^{19}F{^{1}H} NMR (376 MHz, CD_3CN): δ_F -131.81 (d, $^3J_{FF}$ = 22.6 Hz), -132.90 (d, $^3J_{FF}$ = 22.6 Hz), -133.67 (d, $^3J_{FF}$ = 18.8 Hz), -134.03 (d, $^3J_{FF}$ = 18.8 Hz) ppm. HRMS (ESI) found *m/z* 826.1416, calculated *m/z* 826.1413 for $[C_{36}H_{22}F_4IrN_5O_2]H^+$. UV vis. ($CHCl_3$) λ_{max} (ε / $dm^3mol^{-1}cm^{-1}$): 501 (4000), 377 (26300), 361 (23900), 272 (113200) nm. IR (solid) υ_{max} = 3410, 3001, 1634, 1601, 1578, 1530, 1501, 1414, 1327, 1294, 1256, 1233, 1196, 1163, 1125, 1051, 1034, 995, 880, 843, 793, 758, 743, 729, 706, 694, 660, 637, 586, 476, 459, 434 cm^{-1}.

Synthesis of [Ir(L5)$_2$(pic)] C5b as C_1 but with [{Ir(L5)$_2$(μ-Cl)}$_2$] (100 mg, 0.06 mmol). Product purified by column chromatography using DCM:MeOH as the eluent. Product collected as the first red band and recrystallised from DCM and hexane to give a red solid. (Yield = 25 mg, 23 %). ^{1}H NMR (400 MHz, $CDCl_3$): δ_H 8.50 (1 H, s), 8.39 (1 H, d, J_{HH} = 5.3 Hz), 8.03 – 7.87 (3 H, m), 7.82 (1 H, s), 7.76 (3 H, m), 7.66 – 7.54 (6 H, m), 7.54 – 7.45 (3 H, m), 7.15 (1 H, s), 7.10 – 7.02 (1 H, m), 7.02 – 6.94 (1 H, m), 6.75 – 6.41 (4 H, m), 6.16 (1 H, d, J_{HH} = 7.5 Hz), 2.32 (6 H, s), 1.84 (6H, s) ppm. ^{13}C{^{1}H} NMR (101 MHz, $CDCl_3$): δ_C 145.7, 144.3, 139.5, 134.5, 130.5, 129.6, 129.4, 128.9, 128.0, 127.3, 124.2, 121.3, 20.7, 20.0, 19.9, 19.7 ppm. HRMS (ESI) found *m/z* 934.2731, calculated *m/z* 934.2731 for $[C_{50}H_{38}IrN_5O_2]H^+$. UV vis. ($CHCl_3$) λ_{max} (ε / $dm^3mol^{-1}cm^{-1}$): 501 (4700), 387 (28900), 300 (34200), 262 (50000) nm. IR (solid) υ_{max} = 3053, 1640, 1599, 1578, 1547, 1508, 1481, 1443, 1348, 1317, 1263, 1234, 1209, 1171, 1157, 1132, 1117, 1071,

1047, 1024, 1003, 974, 922, 876, 843, 833, 810, 774, 762, 743, 733, 698, 660, 640, 621, 608, 579, 540, 498, 490, 460, 440, 421 cm^{-1}.

Synthesis of [Ir(L6)$_2$(pic)] C6b as C_1 but with [{Ir(L6)$_2$(μ-Cl)}$_2$]. Product purified by column chromatography using DCM:MeOH as the eluent. Product collected as the first red band and recrystallised from DCM and hexane to give a red solid (Yield = 37 mg, 34%). ^{1}H NMR (400 MHz, $CDCl_3$): δ_H 8.94 (1 H, s), 8.32 (1 H, d, J_{HH} = 4.8 Hz), 8.20 (1 H, s), 8.16 (1 H, s), 8.08 (1 H, d, J_{HH} = 7.2 Hz), 7.98 (2 H, s), 7.86 (1 H, app. td), 7.79 (2 H, s), 7.67 (3 H, d, J_{HH} = 2.2 Hz), 7.64 – 7.60 (4 H, m), 7.52 (1 H, s), 7.20 – 7.14 (1 H, m), 7.07 (1 H, d, J_{HH} = 8.0 Hz), 6.77 – 6.71 (1 H, m), 6.70 – 6.78 (2 H, m), 6.65 – 6.54 (2 H, m), 6.11 – 6.09 (1 H, m) ppm. ^{13}C{^{1}H} NMR (126 MHz, $CDCl_3$): δ_C 171.3, 165.7, 163.7, 155.7, 154.4, 154.1, 152.6, 145.7, 144.6, 143.5, 139.8, 139.4, 139.3, 139.2, 139.1, 139.0, 139.0, 137.0, 136.2, 135.2, 134.9, 134.5, 133.5, 131.5, 131.2, 131.0, 130.8, 130.5, 130.4, 130.2, 129.5, 129.1, 128.9, 128.5, 128.3, 127.7, 125.3, 122.1, 121.6 ppm. HRMS (ESI) found *m/z* 1017.0534, calculated *m/z* 1017. 0537 for $[C_{46}H_{26}Cl_4IrN_5O_2]H+$. UV vis. ($CHCl_3$) λ_{max} (ε / $dm^3mol^{-1}cm^{-1}$): 528 (4100), 396 (29800), 273 (90600) nm. IR (solid) υ_{max} = 3410, 3000, 1632, 1597, 1578, 1562, 1543, 1508, 1458, 1443, 1429, 1406, 1387, 1346, 1317, 1256, 1198, 1163, 1132, 1115, 1069, 1044, 1022, 997, 959, 887, 878, 845, 808, 758, 745, 735, 725, 696, 673, 665, 652, 633, 606, 571, 515, 488, 476, 436, 415, 403 cm^{-1}.

Synthesis of [Ir(L7)$_2$(pic)] C7b *as C_1* but with [{Ir(L7)$_2$(μ-Cl)}$_2$] (90 mg, 0.05 mmol). Product collected as a red solid. (Yield = 39 mg, 40 %). ^{1}H NMR (400 MHz, $CDCl_3$): δ_H 8.67 (1H, app. dd), 8.41 (1H, d, J_{HH} = 5.4 Hz), 8.06 -8.04 (1H, m), 8.01 – 7.97 (2H, m), 7.90 – 7.84 (2H, m), 7.81 (2H, app. dd), 7.70 – 7.59 (8H, m), 7.22 – 7.18 (1H, m), 7.18 – 7.14 (1H, m), 7.07 – 7.03 (1H, m), 6.76 – 6.72 (1H, m), 6.70 – 6.68 (2H, m), 6.64 – 6.55 (2H, m), 6.10 – 6.07 (1H, m) ppm. ^{13}C {^{1}H} NMR (126 MHz, DMSO): δ_C 171.4, 153.5, 152.7, 151.8, 145.6, 145.1, 143.9, 139.1, 139.0, 136.4, 134.6, 131.1, 130.7, 130.6, 130.4, 130.2, 130.1, 129.1, 128.9, 128.4, 128.2, 122.2, 121.6 ppm. ^{19}F{^{1}H} NMR (376 MHz, CD_3CN): δ_F -130.18 (d, $^3J_{FF}$ = 22.6 Hz), -131.51 (d, $^3J_{FF}$ = 22.6 Hz), -133.10 (d, $^3J_{FF}$ = 18.8 Hz), -133.59 (d, $^3J_{FF}$ = 18.8 Hz) ppm. HRMS (ESI) found *m/z* 950.1726, calculated *m/z* 950.1728 for $[C_{46}H_{26}F_4IrN_5O_2]H+$. UV vis. ($CHCl_3$) λ_{max} (ε / $dm^3mol^{-1}cm^{-1}$): 505 (3100), 387 (23100), 277 (3400) nm. IR (solid) υ_{max} = 3412, 3042, 1649, 1601, 1578, 1522, 1499, 1445, 1427, 1327, 1294, 1273, 1258, 1227, 1165, 1126, 1069, 1044, 1024, 980, 874, 841, 808, 758, 745, 725, 700, 662, 640, 623, 615, 596, 530, 500, 488, 421 cm^{-1}.

Synthesis of [Ir(L2)$_2$(pyz)] C2c [Ir(L2)$_2$(MeCN)$_2$] (250 mg, 0.325 mmol), pyrazine carboxylic acid (50 mg, 0.4 mmol) and K_2CO_3 (55 mg, 0.4 mmol) were dissolved in a mixture of chloroform (20 mL) and ethanol (5 mL). The reaction mixture was heated at reflux for 48 hours. The reaction mixture was then filtered and a red solid collected. The solid was purified by silica gel chromatography (dichloromethane:methanol, 95:5) and collected as the first red band. Reprecipitation from DCM and Et_2O gave the product as a red solid. (Yield = 32 mg, 12 %); ^{1}H NMR (400MHz, $CDCl_3$): δ_H 8.93 (1H, d, J_{HH} = 1.1 Hz), 8.53 (1H, d, J_{HH} = 3.0 Hz), 8.29 (1H, d, J_{HH} = 7.8 Hz), 8.22 (1H, s), 8.12 (1H, d, J_{HH} = 7.7 Hz), 7.84 (1H, dd, J_{HH} = 3.0, 1.2Hz), 7.65 (1H, s), 7.61 (1H, s), 7.13-7.06 (1H, m), 6.97-6.90 (1H, m), 6.83 (1H, s), 6.80 (1 H, dd, J_{HH} = 7.8, 1.1 Hz), 6.75-6.69 (1H, m), 6.61-6.56 (1H, m), 6.13 (1H, dd, J_{HH} = 7.7, 1.0 Hz), 3.26 (3H, s), 3.24 (3H, s), 2.32 (3H, s), 2.25 (3H, s), 2.23 (3H, s), 1.72 (3H, s) ppm. ^{13}C{^{1}H} NMR (126MHz, $CDCl_3$): δ_C 170.0, 163.6, 161.5, 151.7, 151.2, 150.1, 149.8, 149.5, 148.3, 146.0, 145.7, 144.6, 142.5, 141.2, 140.1, 139.6, 139.5, 139.4, 139.0, 138.7, 136.7, 129.9, 129.5, 129.5, 129.1, 128.9, 127.4, 126.1, 123.9, 122.4, 122.0, 27.8, 27.5, 20.3, 20.00, 19.7 ppm. HRMS (ESI) found *m/z* of 811.2367, calculated *m/z*

811.2367 for $[C_{35}H_{21}F_4IrN_6O_2]H^+$. UV-vis ($CHCl_3$) λ_{max} (ε /$dm^3mol^{-1}cm^{-1}$) 480 (5100), 380 (27100), 267 (50200) nm. IR (solid) υ_{max} = 3408, 3050, 2918, 1649, 1578, 1524, 1483, 1449, 1406, 1344, 1319, 1217, 1163, 1034, 991, 870, 847, 793, 760, 723, 700, 627, 567, 473, 403 cm^{-1}.

Synthesis of [Ir(L4)$_2$(pyz)] C4c [{Ir(L4)$_2$(μ-Cl)}$_2$] (174 mg, 0.118 mmol), pyrazine carboxylic acid (28 mg, 0.236 mmol), potassium carbonate (33 mg, 0.236 mmol) and silver nitrate (80 mg, 0.472 mmol) were dissolved in 2-ethoxyethanol (10 mL). The reaction mixture was heated at reflux for 24 hours in the absence of light. The reaction mixture was cooled to room temperature and water (40 mL) added to form a brown precipitate. The precipitate was collected by filtration and purified by silica gel chromatography (dichloromethane:methanol, 95:5). First red band collected and dried *in vacuo* to yield [Ir(**L4**)$_2$pyr] as a red solid (Yield = 35mg, 18%). ^{1}H NMR (400 MHz, $CDCl_3$): δ_H 9.02 (1H, d, J_{HH} = 1.3 Hz), 8.63 (1H, d, J_{HH} = 3.0 Hz), 8.42-8.3 (2H, m), 8.15 (1H, d, J_{HH} = 7.6 Hz), 7.79 (1H, dd, J_{HH} = 3.0, 1.3 Hz), 7.75-7.62 (2H, m), 7.19-7.14 (1H, m), 7.04-6.98 (1H, m), 6.88 (1H, dd, J_{HH} = 11.7, 7.7 Hz) 6.85-6.79 (2H, m), 6.06 (1H, dd, J_{HH} = 7.7, 1.0 Hz), 3.28 (3H, s), 3.26 (3H, s) ppm. ^{13}C{^{1}H} NMR (101 MHz, $CDCl_3$): δ_C 167.0, 152.2, 151.8, 149.9, 149.2, 145.5, 145.0, 144.0, 138.9, 136.8, 134.6, 131.0, 130.5, 130.4, 129.9, 123.2, 122.7, 116.1, 115.9, 114.00, 110.8, 27.6, 27.5 ppm. ^{19}F{^{1}H} NMR (376 MHz, $CDCl_3$): δ_F -125.01 (d, $^3J_{FF}$ = 21.7 Hz), -128.95 (d, $^3J_{FF}$ = 22.0 Hz), -129.51 (d, $^3J_{FF}$ = 22.0 Hz), -130.85 (d, $^3J_{FF}$ = 21.7 Hz) ppm. HRMS found *m/z* 827.1365, calculated *m/z* 827.1365 for $[C_{35}H_{21}F_4IrN_6O_2]H^+$. UV-vis ($CHCl_3$) λ_{max} (ε /$dm^3mol^{-1}cm^{-1}$) 490 (4900), 374 (31000), 262 (50900) nm. IR (solid) υ_{max} = 3456, 3057, 1655, 1578, 1501, 1449, 1414, 1327, 1258, 1223, 1165, 1126, 1034, 995, 928, 876, 793, 731, 660, 637, 586, 474cm^{-1}.

Synthesis of [Ir(L5)$_2$(pyz)] C10 as [Ir(L4)$_2$(pyz)] but with [{Ir(L5)$_2$(μ-Cl)}$_2$] (200 mg, 0.118 mmol), pyrazine carboxylic acid (28 mg, 0.236 mmol), potassium carbonate (0.033g, 0.236mmol) and silver nitrate (80 mg, 0.472 mmol) were dissolved in 2-ethoxyethanol (10 mL). Product purified by silica gel chromatography (dichloromethane:methanol, 99:1), followed by (dichloromethane:methanol, 95:5) to elute red band, solvent was removed *in vacuo*, then reprecipitated from DCM and Et_2O to give [Ir(L5)$_2$pyr] as a red solid (Yield = 25 mg, 11 %). ^{1}H NMR (400 MHz, $CDCl_3$): δ_H 9.15 (1H, d, J_{HH} = 1.1Hz), 8.78 (1H, d, J_{HH} = 2.9Hz), 8.44 (1H, s), 8.31 (1H, dd, J_{HH} = 3.0, 1.3Hz), 7.98-7.73 (6H, m), 7.67-7.56 (6H, m), 7.08 (1H, dd, J_{HH} = 8.1, 1.1 Hz), 7.02 (1H, s), 7.00 (1H, dd, J_{HH} =8.0, 1.3 Hz), 6.75-6.61 (3H, m), 6.60-6.50 (2H, m), 6.13 (1H, dd, J_{HH} = 7.5, 1.1 Hz) 2.41 (3H, s), 2.41 (3H, s), 2.33 (3H, s), 1.89 (3H, s) ppm. ^{13}C{^{1}H} NMR (101 MHz, $CDCl_3$): δ_C 170.1, 163.0, 160.8, 153.5, 152.2, 150.7, 150.0, 149.9, 148.3, 146.6, 145.2, 144.1, 143.5, 141.5, 130.2, 129.9, 129.8, 129.5, 129.4, 128.9, 128.3, 126.1, 123.7, 121.8, 121.4, 20.8, 20.1, 20.0, 19.8 ppm. HRMS found *m/z* 935.2684, calculated *m/z* 935.2683 for $[C_{49}H_{37}IrN_6O_2]H^+$. UV-vis ($CHCl_3$) λ_{max} (ε /$dm^3mol^{-1}cm^{-1}$) 489 (4400), 386 (24000), 271 (49000) nm. IR (solid) υ_{max} = 3422, 3057, 1578, 1549, 1508, 1481, 1445, 1408, 1348, 1319, 1236, 1211, 1159, 1072, 1047, 1024, 1003, 974, 849, 810, 802, 762, 746, 731, 698, 642, 608, 579, 540, 492, 444 cm^{-1}.

Synthesis of [Ir(L7)$_2$(pyz)] C11 As [Ir(L4)$_2$(pyz)] but [{Ir(L7)$_2$(μ-Cl)}$_2$] (250 mg, 0.145 mmol), pyrazine carboxylic acid (41 mg, 0.290 mmol), potassium carbonate (42 mg, 0.290 mmol) and silver nitrate (98 mg, 0.58 mmol) were dissolved in 2-ethoxyethanol (10 mL). Product purified by silica gel chromatography (dichloromethane:methanol, 99:1) to elute yellow band, followed by (dichloromethane:methanol, 95:5) to elute red band, solvent was removed *in vacuo* to yield the product as a purple solid. Product was dissolved in DCM and recrystallised from hexane to give the product as a purple crystalline solid (Yield = 22 mg, 8 %). ^{1}H NMR (400 MHz, $CDCl_3$): δ_H 9.16 (d, J=1.2Hz, 1H), 8.85 (d, J=3.0Hz, 1H), 8.53 (dd, J=12.1, 8.1Hz, 1H), 8.30 (dd, J=3.0, 1.3Hz, 1H), 7.93 (dd, J=6.9, 2.7Hz, 2H), 7.88-7.74 (m, 4H), 7.65-7.53 (m, 6H), 7.14-6.97 (m, 3H), 6.74-

6.62 (m, 3H), 6.60-6.49 (m, 2H), 5.98 (dd, J=7.6, 1.0Hz, 1H); ^{13}C NMR (101 MHz, $CDCl_3$): δ_C 171.4, 165.7, 160.6, 154.0, 152.3, 151.6, 150.1, 148.2, 147.3, 143.1, 141.1, 139.9, 132.7, 131.5, 129.3, 128.2, 127.1, 125.2, 123.6, 121.7, 120.3 ppm. ^{19}F NMR (376 MHz, $CDCl_3$): δ_F -123.47 (d, $^3J_{FF}$ = 22.2 Hz), -128.13 (d, $^3J_{FF}$ = 21.7 Hz), -128.54 (d, $^3J_{FF}$ = 22.2 Hz), -130.53 (d, $^3J_{FF}$ = 21.7 Hz) ppm. HRMS found *m/z* 951.1677, calculated *m/z* 951.1677 for $[C_{45}H_{25}F_4IrN_6O_2]H+$. UV-vis ($CHCl_3$) λ_{max} (ε /$dm^3mol^{-1}cm^{-1}$): 494 (2900), 383 (15500), 272 (41200) nm. υ_{max} = 3422, 3044, 1649, 1576, 1501, 1329, 1227, 1163, 1126, 1069, 1045, 980, 874, 847, 808, 797, 758, 725, 700, 662, 640, 530, 419 cm^{-1}.

3.6. References

1. A. Kando, Y. Hisamatsu, H. Ohwada, T. Itoh, S. Moromizato, M. Kohno and S. Aoki, *Inorg. Chem.*, 2015, **54**, 5342–5357.
2. L. He, J.-J. Cao, D.-Y. Zhang, L. Hao, M.-F. Zhang, C.-P. Tan, L.-N. Ji and Z.-W. Mao, *Sens. Actuators B Chem.*, 2018, **262**, 313–325.
3. S. Yang, W. Che, H.-L. Wu, S.-F. Zhu and Q.-L. Zhou, *Chem. Sci.*, 2017, **8**, 1977–1980.
4. Y. Sun, N. C. Giebink, H. Kanno, B. Ma, M. E. Thompson and S. R. Forrest, *Nature*, 2006, **440**, 908–912.
5. L. Ying, C.-L. Ho, H. Wu, Y. Cao and W.-Y. Wong, *Adv. Mater.*, 2014, **26**, 2459–2473.
6. H. Sasabe and J. Kido, *J. Mater. Chem. C*, 2013, **1**, 1699–1707.
7. B. W. D'Andrade and S. R. Forrest, *Adv. Mater.*, 2004, **16**, 1585–1595.
8. R.-P. Xu, Y.-Q. Li and J.-X. Tang, *J. Mater. Chem. C*, 2016, **4**, 9116–9142.
9. R. C. Kwong, M. R. Nugent, L. Michalski, T. Ngo, K. Rajan, Y.-J. Tung, M. S. Weaver, T. X. Zhou, M. Hack, M. E. Thompson, S. R. Forrest and J. J. Brown, *Appl. Phys. Lett.*, 2002, **81**, 162–164.
10. M. Ikai, S. Tokito, Y. Sakamoto, T. Suzuki and Y. Taga, *Appl. Phys. Lett.*, 2001, **79**, 156–158.
11. F. Li, M. Zhang, G. Cheng, J. Feng, Y. Zhao, Y. Ma, S. Liu and J. Shen, *Appl. Phys. Lett.*, 2003, **84**, 148–150.
12. C. W. Tang and S. A. VanSlyke, *Appl. Phys. Lett.*, 1987, **51**, 913–915.
13. R. C. Evans, P. Douglas and C. J. Winscom, *Coord. Chem. Rev.*, 2006, **250**, 2093–2126.
14. J. R. Lakowicz, *Principles of Fluorescence Spectroscopy*, Springer Science & Business Media, 2007.
15. 1A. Vlček, *Coord. Chem. Rev.*, 1998, **177**, 219–256.
16. M . A. Baldo, D. F. O'Brien, Y. You, A. Shoustikov, S. Sibley, M. E. Thompson and S. R. Forrest, *Nature*, 1998, **395**, 151–154.
17. M. A. Baldo, M. E. Thompson and S. R. Forrest, *Pure Appl. Chem.*, 1999, **71**, 2095–2106.
18. P.-T. Chou and Y. Chi, *Chem. – Eur. J.*, 2007, **13**, 380–395.
19. J.-L. Liao, Y. Chi, C.-C. Yeh, H.-C. Kao, C.-H. Chang, M. A. Fox, P. J. Low and G.-H. Lee, *J. Mater. Chem. C*, 2015, **3**, 4910–4920.
20. Y-L. Tung, S.-W. Lee, Y. Chi, L.-S. Chen, C.-F. Shu, F.-I. Wu, A. J. Carty, P.-T. Chou, S.-M. Peng and G.-H. Lee, *Adv. Mater.*, 2005, **17**, 1059–1064.
21. G. Cheng, Q. Wan, W.-H. Ang, C.-L. Kwong, W.-P. To, P.-K. Chow, C.-C. Kwok and C.-M. Che, Advanced Optical Materials, 2019, 7, 1801452.
22. K. A. King, P. J. Spellane and R. J. Watts, *J. Am. Chem. Soc.*, 1985, **107**, 1431–1432.
23. M. A. Baldo, S. Lamansky, P. E. Burrows, M. E. Thompson and S. R. Forrest, *Appl. Phys. Lett.*, 1999, **75**, 4–6.
24. S. Sprouse, K. A. King, P. J. Spellane and R. J. Watts, *J. Am. Chem. Soc.*, 1984, **106**, 6647–6653.
25. A. P. Wilde and R. J. Watts, *J. Phys. Chem.*, 1991, **95**, 622–629.
26. M. G. Colombo, T. C. Brunold, T. Riedener, H. U. Guedel, M. Fortsch and H.-B. Buergi, *Inorg. Chem.*, 1994, **33**, 545–550.
27. H.-Y. Chen, Y. Chi, C.-S. Liu, J.-K. Yu, Y.-M. Cheng, K.-S. Chen, P.-T. Chou, S.-M. Peng, G.-H. Lee, A. J. Carty, S.-J. Yeh and C.-T. Chen, *Adv. Funct. Mater.*, 2005, **15**, 567–574.
28. M. S. Lowry and S. Bernhard, *Chem. – Eur. J.*, 2006, **12**, 7970–7977.
29. S. Lamansky, P. Djurovich, D. Murphy, F. Abdel-Razzaq, H.-E. Lee, C. Adachi, P. E. Burrows, S. R. Forrest and M. E. Thompson, *J. Am. Chem. Soc.*, 2001, **123**, 4304–4312.

30. S. Lamansky, P. Djurovich, D. Murphy, F. Abdel-Razzaq, R. Kwong, I. Tsyba, M. Bortz, B. Mui, R. Bau and M. E. Thompson, *Inorg. Chem.*, 2001, **40**, 1704–1711.
31. H.-B. Han, Z.-L. Tu, Z.-G. Wu and Y.-X. Zheng, *Dyes Pigments*, 2019, **160**, 863–871.
32. X. Liang, F. Zhang, Z.-P. Yan, Z.-G. Wu, Y. Zheng, G. Cheng, Y. Wang, J.-L. Zuo, Y. Pan and C.-M. Che, *ACS Appl. Mater. Interfaces*, 2019, **11**, 7184–7191.
33. K. Traskovskis, A. Ruduss, V. Kokars, I. Mihailovs, N. Lesina and A. Vembris, *New J. Chem.*, 2018, **43**, 37–47.
34. S. Altürk, D. Avcı, B. Z. Kurt, Ö. Tamer, A. Başoğlu, F. Sönmez, Y. Atalay and N. Dege, *J. Inorg. Organomet. Polym. Mater.*, , DOI:10.1007/s10904-019-01090-7.
35. A. Liang, Z. Liu, D. Liu, P. Cai, Z. Wang, W. Zhou, S. Hu, J. Tang, X. Zhang and M. Cai, *Opt. Mater.*, 2019, **88**, 551–557.
36. H. Yu, C. Liu, X. Lv, J. Xiu and J. Zhao, *Dyes Pigments*, 2017, **145**, 136–143.
37. T. Yu, F. Yang, X. Chen, W. Su, Y. Zhao, H. Zhang and J. Li, *New J. Chem.*, 2017, **41**, 2046–2054.
38. P. Tao, Y. Miao, Y. Zhang, K. Wang, H. Li, L. Li, X. Li, T. Yang, Q. Zhao, H. Wang, S. Liu, X. Zhou, B. Xu and W. Huang, *Org. Electron.*, 2017, **45**, 293–301.
39. D. H. Kim, N. S. Cho, H.-Y. Oh, J. H. Yang, W. S. Jeon, J. S. Park, M. C. Suh and J. H. Kwon, *Adv. Mater.*, 2011, **23**, 2721–2726.
40. K. A. Phillips, T. M. Stonelake, K. Chen, Y. Hou, J. Zhao, S. J. Coles, P. N. Horton, S. J. Keane, E. C. Stokes, I. A. Fallis, A. J. Hallett, S. P. O'Kell, J. M. Beames and S. J. A. Pope, *Chem. – Eur. J.*, 2018, **24**, 8577–8588.
41. M. Nonoyama, *Bull. Chem. Soc. Jpn.*, 1974, **47**, 767–768.
42. L. M. Groves, C. Schotten, J. Beames, J. A. Platts, S. J. Coles, P. N. Horton, D. L. Browne and S. J. A. Pope, *Chem. – Eur. J.*, 2017, **23**, 9407–9418.
43. K. R. Dunbar, *Comments Inorg. Chem.*, 1992, **13**, 313–357.
44. J. A. Davies and F. R. Hartley, *Chem. Rev.*, 1981, **81**, 79–90.
45. R. Díaz-Torres and S. Alvarez, *Dalton Trans*, 2011, **40**, 10742–10750.
46. E. Hecht, *Optics*, Pearson Education, Incorporated, 2017.
47. A. Juris, V. Balzani, F. Barigelletti, S. Campagna, P. Belser and A. von Zelewsky, *Coord. Chem. Rev.*, 1988, **84**, 85–277.
48. G. Sarada, J. Yoon, W. Cho, M. Cho, D. W. Cho, S. O. Kang, Y. Nam, J. Y. Lee and S.-H. Jin, *J. Mater. Chem. C*, 2015, **4**, 113–120.
49. M. Quaranta, M. Murkovic and I. Klimant, *Analyst*, 2013, **138**, 6243–6245.
50. T. Sato, Y. Hamada, M. Sumikawa, S. Araki and H. Yamamoto, *Ind. Eng. Chem. Res.*, 2014, **53**, 19331–19337.
51. C. J. Timpson, C. C. Carter and J. Olmsted, *J. Phys. Chem.*, 1989, **93**, 4116–4120.
52. K. K.-W. Lo, D. C.-M. Ng and C.-K. Chung, *Organometallics*, 2001, **20**, 4999–5001.
53. Q. Zhao, C. Huang and F. Li, *Chem. Soc. Rev.*, 2011, **40**, 2508–2524.
54. E. Baggaley, M. R. Gill, N. H. Green, D. Turton, I. V. Sazanovich, S. W. Botchway, C. Smythe, J. W. Haycock, J. A. Weinstein and J. A. Thomas, *Angew. Chem. Int. Ed Engl.*, 2014, **53**, 3367–3371.

4. Dual Visible/ Near-IR Emission from Organometallic Iridium(III) Complexes

4.1. Introduction

Chapters 2 and 3 have discussed the development of red-emitting bis-cyclometallated iridium(III) complexes and the fine-tuning of their emission wavelength. In this chapter, the focus is placed on the use of organic ligands that possess a higher degree of conjugation than those previously investigated, in an attempt to create a much larger bathochromic shift in emission wavelength.

4.1.1. Near Infrared

The near-infrared (NIR) region of the spectrum is commonly defined as 750-1500 nm.[1] In recent years, there has been a drive to develop compounds that emit in this range due to the many potential applications. Recently, NIR operating broadband light sources have been used clinically in ophthalmology and skin disease diagnosis,[2,3] as well as in the field of bioimaging with a particular focus on fluorescence spectroscopy.[4–6] Near-infrared wavelengths are advantageous in the fields of cellular and tissue imaging due to the low absorption of molecules in this region.[7] In addition to this, organic compounds with near-infrared emission have already found applications in the fields of night vision displays, sensors and optical communication.[8,9] The development of near-infrared emitting species is still continuing to expand, with the one of the main focuses now on the synthesis of long wavelength emitting inorganic complexes.

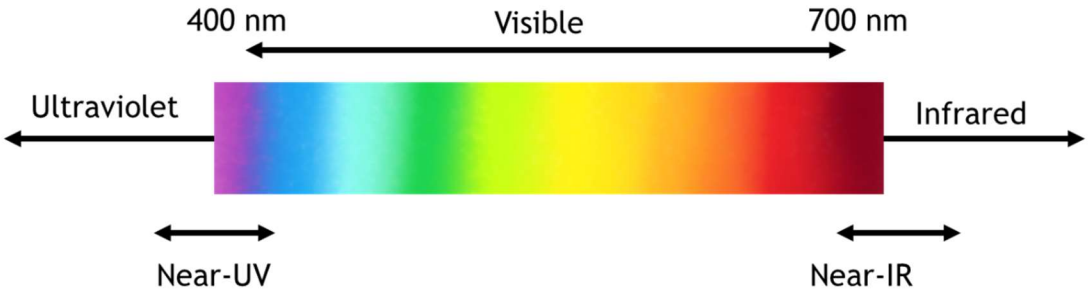

Figure 4.1: Illustration of electromagnetic spectrum from ultraviolet to infrared region.

In chapters 2 and 3 it was discussed that the number of red-emitting iridium complexes reported in the literature was much lower than those with green or blue emission, and it follows that the number of reports of iridium complexes with near-infrared emission is lower still. One of the earliest reports of a NIR emitting iridium complex was in 2006. Williams *et al.* synthesised a phosphorescent OLED using the iridium complex shown in the left of Figure 4.2 which exhibited emission at 720 nm.[10] The complex in the centre of the image was also developed with OLED applications in mind, this complex reported an emission peak at 716 nm, with a shoulder at 792 nm.[11] The final complex in the image has the longest reported emission wavelength of the three shown. This complex utilises a highly conjugated perylene diimide derived compound as the coordinating ligand and the reported emission wavelength was found to be 736 nm with another, less intense, peak at 824 nm when recorded as a film.[12]

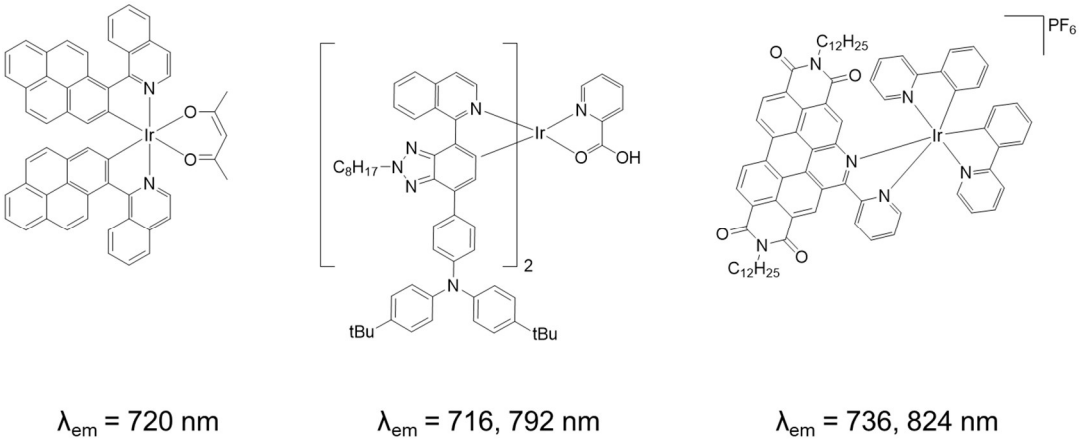

Figure 4.2: Examples of NIR-emitting iridium(III) complexes with OLED applications.[10–12]

The complexes shown in Figure 4.2 have relatively large, highly conjugated ligands. The rationale behind this is that increasing the conjugation of a cyclometallating ligand has been shown to bathochromically shift the emission wavelength of a complex.[13] The increased conjugation lowers the energy of the LUMO, whilst the position of the HOMO remains around the same, as a result there is a smaller energy gap leading to lower energy emission.[14,15]

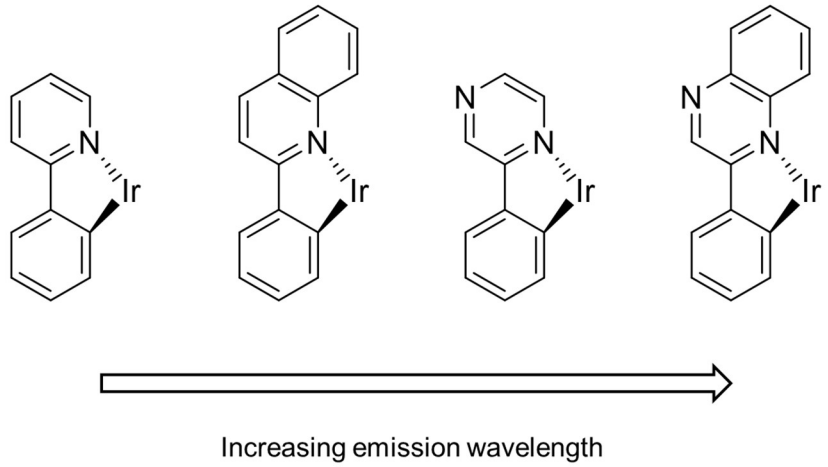

Figure 4.3: Conjugation and addition of heteroatoms results in a bathochromic shift in in emission wavelength.[8]

However, the literature suggests that it is not necessary to have quite as high a level of conjugation as seen in the previous examples as near-IR emission has been observed from complexes with simpler ligands. Figure 4.4 shows three examples of such complexes all of which have cyclometallating ligands based upon benzo[*g*]quinoxaline. The first complex in the figure was reported in 2012 by Tao *et al.* The cyclometallating ligands used in this complex are methyl-, phenyl-substituted benzo[*g*]quinoxaline with a di-phenylphenanthroline ancillary ligand and the complex showed a maximum emission wavelength of 935 nm.[16] The complex in the centre of the figure uses a benzo[*g*]quinoxaline ligand with two aryl substituents and a 2,2'-biquinoline ancillary ligand. This complex exhibited an emission wavelength of 852 nm.[17] The final complex shown has a very similar structure to the centre complex except that the cyclometallating ligand does not have methyl groups on the aryl substituent and the 2,2'-biquinoline ligand is replaced with 2-(quinolin-2-yl)quinoxaline (quqo) ligand. These small structural changes lead to a large

shift in emission wavelength as this complex emits at 970 nm, this latter work published after completion of the work described herein.[18]

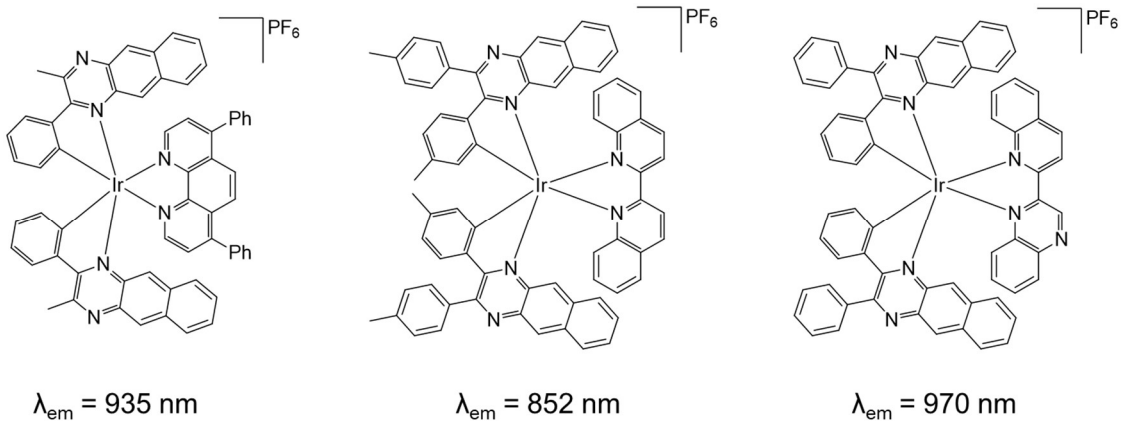

Figure 4.4: Near-IR emitting complexes with simpler cyclometallating ligands.[16,18,19]

The benzo[*g*]quinoxaline ligand is simply a more conjugated version of quinoxaline. Quinoxaline-based ligands have been the focus of chapters 2 and 3, and their complexes have shown emission in the red region. Therefore, complexes bearing benzo[*g*]quinoxaline-based ligands would form an appropriate comparison species and should undergo a bathochromic shift in respect to their quinoxaline counterparts.

4.2. Aims

Over the previous two chapters, series of complexes have been synthesised with quinoxaline-based cyclometallating ligands and the effects of substituents and ancillary ligands have been studied. The aims of this chapter were to investigate the effect of ligand conjugation and substituents in bis-cyclometallated iridium complexes.

In this study, four ligands based upon benzo[*g*]quinoxaline were synthesised and characterised. From these ligands, a series of cationic bis-cyclometallated iridium complexes were synthesised. These complexes were fully characterised and their photophysical properties investigated to understand the influence of an extended aromatic system on absorption and emission properties.

4.3. Results and Discussion

4.3.1. Synthesis of Ligands

The ligands used in this study were based upon benzo[*g*]quinoxaline and were synthesised *via* a condensation reaction between 2,3-diaminonaphthalene and a benzil derivative. Four different benzil derivatives were used to introduce electron-donating and electron withdrawing groups into the system; in addition to benzil these included 4,4'-dimethyl benzil, 4,4'-dibromobenzil and 4,4'-dimethoxy benzil. The general reaction scheme for the synthesis of these compounds was based upon the synthesis of pyrido-[2,3-*b*]pyrazine ligands, and is shown in Scheme 4.1.[20]

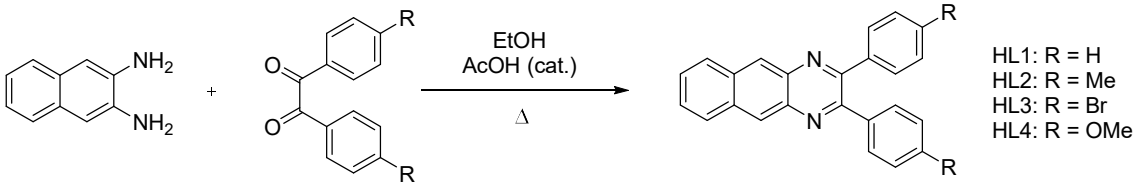

Scheme 4.1: Synthesis scheme for ligands HL1-4.

This synthetic route was used to isolate ligands HL1-3, but in the case of HL4 the solvent was substituted with tetrahydrofuran, with all other conditions retained. In all cases, the product formed as a yellow-brown precipitate which was collected by filtration and washed with methanol and used without further purification. High yields were recorded for all ligands at between 64 – 80 % suggesting that these conditions are an efficient route for condensation reactions.

Figure 4.5 shows the proton NMR spectrum recorded for the methoxy-substituted ligand, HL4. Some of the more interesting signals have been highlighted in the figure. The doublet at 6.90 ppm (highlighted in green) corresponds to the aromatic protons nearest to the methoxy group. The position of these protons varies from ligand to ligand as they experience the most influence from the functional group on the phenyl moiety. This signal is shifted most upfield in L4 due to the electron donating character of the functional group. In contrast to this, this signal is observed at its most downfield position in ligand HL3, at 7.45 ppm, due to the electron withdrawing bromo- substituent. The singlet highlighted in red in the spectrum arises from the aromatic protons at the centre of benzo[*g*]quinoxaline backbone. These appear as a singlet as the ligands are symmetrical and there are no nearby protons to cause splitting. The position of this signal varies by only 0.05 ppm across the series and in each case, this is the most downfield signal due to the close proximity of the electron-withdrawing nitrogen atoms in the adjacent aromatic ring. Finally, the singlet highlighted in blue at 3.85 ppm corresponds to the methyl groups of the methoxy substituent; these are downshifted from those in ligand HL2, which appear at 2.39 ppm, due to the electron withdrawing effect of the oxygen atom in the methoxy group.

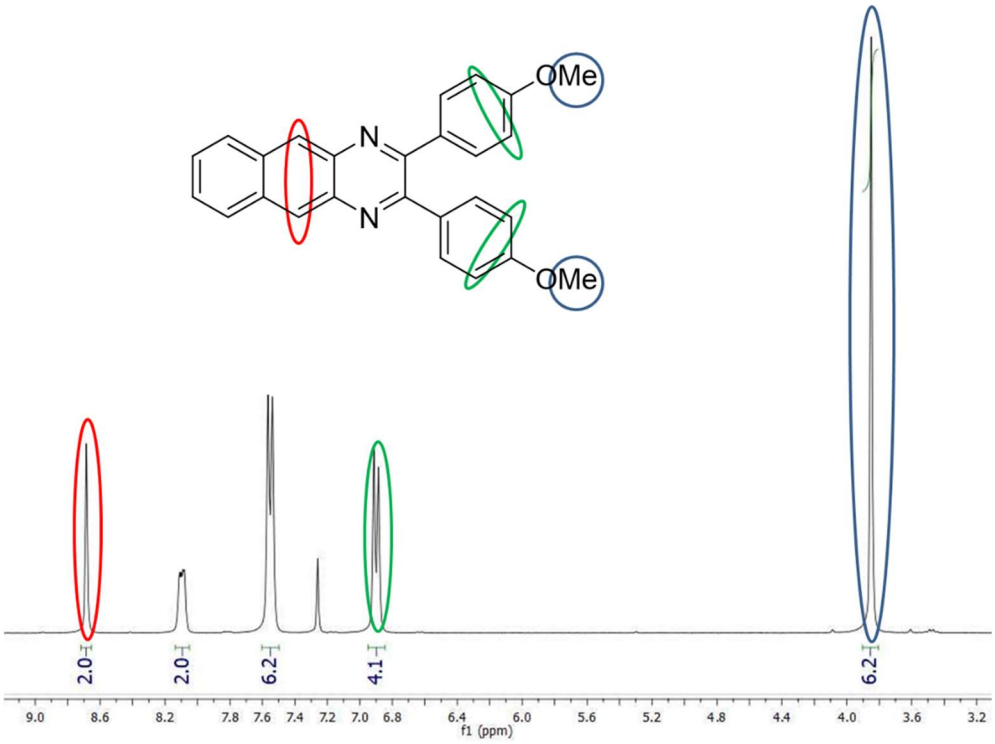

Figure 4.5: Proton NMR spectrum recorded for ligand HL4 in $CDCl_3$. Selected proton assignments are shown in circles.

For ligand HL3, it was possible to grow good quality, orange, blade-shaped single crystals *via* slow evaporation of a concentrated chloroform solution. These crystals were submitted to the University of Southampton for diffraction studies with the collection parameters reported in the experimental section of this chapter. The structure was refined in the $P2_{\frac{1}{n}}$ space group and it was observed that there is a single molecule in the asymmetric unit. The data collected confirmed the proposed structure of the ligand and the packing arrangement showed some long-range π-π interactions. Figure 4.7 shows the crystal structure, while Figure 4.6 shows the packing diagram. Furthermore, Table 4.1 and Table 4.2 show the bond lengths and bond angles recorded respectively.

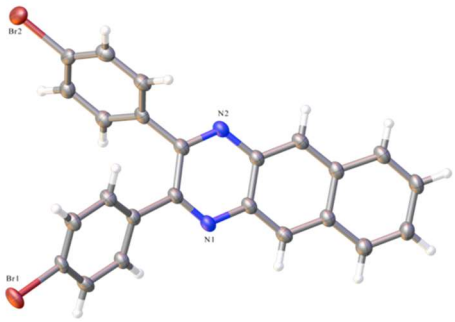

Figure 4.2: X-ray structure of ligand HL3. Ellipsoids drawn at 50 % probability. Crystal data: $C_{24}H_{14}Br_2N_2$, Mr = 490.19, monoclinic, P21/n (No. 14), a - 5.7963(2) Å, b = 21.8021(9) Å, c = 15.1661(6) Å, β = 91.211(3)˚, α = γ = 90 ˚, V = 1916.15(13) Å3, T = 100(2) K, Z = 4, Z' = 1, μ(MoKα) = 4.243 mm-1, 19907 reflections measured, 4396 unique (Rint = 0.0501) which were used in all calculations. The final wR2 was 0.1219 (all data) and R1 was 0.0491 (I>2(I)).

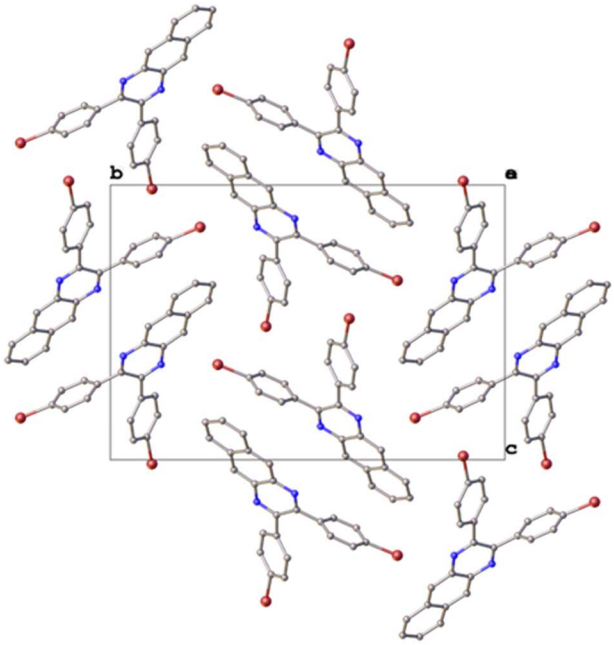

Figure 4.1: Packing diagram for ligand HL3 obtained from crystal data. Ellipsoids are drawn at 50 % probability.

Table 4.1: Selected bond length data for compound HL3.

Atom	Atom	Length/Å	Atom	Atom	Length/Å
Br1	C16	1.900(3)	C8	C9	1.362(5)
Br2	C22	1.902(3)	C9	C10	1.425(5)
N1	C1	1.305(5)	C10	C11	1.396(5)
N1	C12	1.377(4)	C11	C12	1.387(5)
N2	C2	1.310(4)	C13	C14	1.398(5)

N2	C3	1.385(4)	C13	C18	1.395(5)
C1	C2	1.463(5)	C14	C15	1.391(5)
C1	C13	1.497(4)	C15	C16	1.383(5)
C2	C19	1.490(5)	C16	C17	1.389(5)
C3	C4	1.393(5)	C17	C18	1.390(5)
C3	C12	1.431(5)	C19	C20	1.401(5)
C4	C5	1.399(5)	C19	C24	1.390(5)
C5	C6	1.430(4)	C20	C21	1.383(5)
C5	C10	1.442(5)	C21	C22	1.381(5)
C6	C7	1.368(5)	C22	C23	1.385(5)
C7	C8	1.422(5)			

Table 4.2: Selected bond angles for compound HL3.

Atom	Atom	Atom	Angle/°	Atom	Atom	Atom	Angle/°
C1	N1	C12	118.2(3)	N1	C12	C3	120.4(3)
C2	N2	C3	117.4(3)	N1	C12	C11	119.1(3)
N1	C1	C2	121.1(3)	C11	C12	C3	120.4(3)
N1	C1	C13	115.4(3)	C14	C13	C1	117.7(3)
C2	C1	C13	123.5(3)	C18	C13	C1	123.0(3)
N2	C2	C1	121.9(3)	C18	C13	C14	118.9(3)
N2	C2	C19	116.8(3)	C15	C14	C13	121.1(3)
C1	C2	C19	121.1(3)	C16	C15	C14	118.7(3)
N2	C3	C4	120.2(3)	C15	C16	Br1	118.8(3)
N2	C3	C12	120.4(3)	C15	C16	C17	121.5(3)
C4	C3	C12	119.5(3)	C17	C16	Br1	119.6(3)
C3	C4	C5	120.5(3)	C16	C17	C18	119.2(3)
C4	C5	C6	122.4(3)	C17	C18	C13	120.6(3)
C4	C5	C10	119.6(3)	C20	C19	C2	119.0(3)
C6	C5	C10	118.0(3)	C24	C19	C2	121.7(3)
C7	C6	C5	120.8(3)	C24	C19	C20	119.3(3)
C6	C7	C8	120.9(3)	C21	C20	C19	120.6(3)
C9	C8	C7	120.1(3)	C22	C21	C20	119.1(3)
C8	C9	C10	121.0(3)	C21	C22	Br2	118.5(3)
C9	C10	C5	119.2(3)	C21	C22	C23	121.7(3)
C11	C10	C5	119.3(3)	C23	C22	Br2	119.8(3)
C11	C10	C9	121.5(3)	C22	C23	C24	119.0(3)
C12	C11	C10	120.5(3)	C19	C24	C23	120.4(3)

4.3.2. Synthesis of Complexes

These compounds were then used as cyclometallating ligands with iridium(III). Firstly, the dimeric species [{Ir(L)$_2$(μ-Cl)}$_2$] was again prepared following the method first proposed by Nonoyama.[21] This dimeric species was then dissolved in 2-ethoxyethanol along with the appropriate cyclometallating ligand and heated at reflux for 24 hours. Upon cooling, a saturated aqueous solution of ammonium hexafluorophosphate was added to the reaction mixture causing the complex to crash out of solution as a hexafluorophosphate salt. Each complex was collected as a red solid and where further purification was required, this was carried out by column chromatography using a DCM/methanol mixture as an eluent. The general synthetic scheme is shown below.

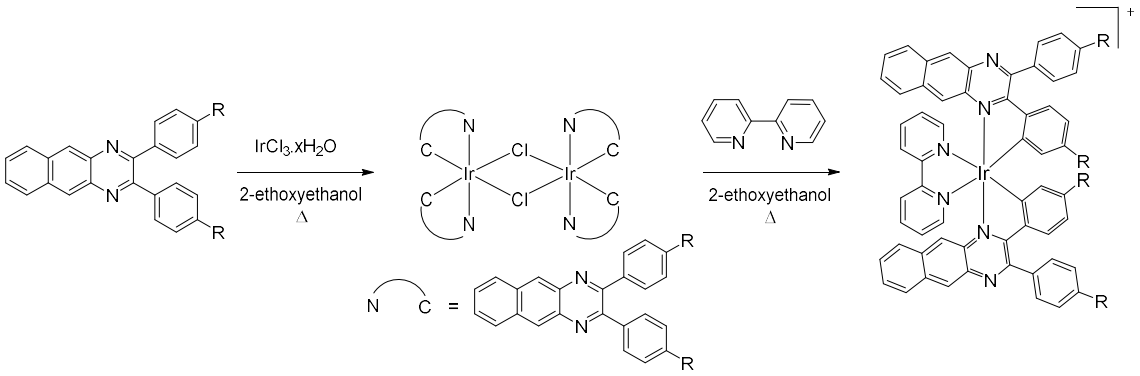

Scheme 4.2: Synthesis of bis-cyclometallated iridium(III) complexes.

Following this synthesis route, four complexes cationic bis-cyclometallated iridium(III) complexes were isolated as red solids. The structures and yields are shown in Figure 4.8.

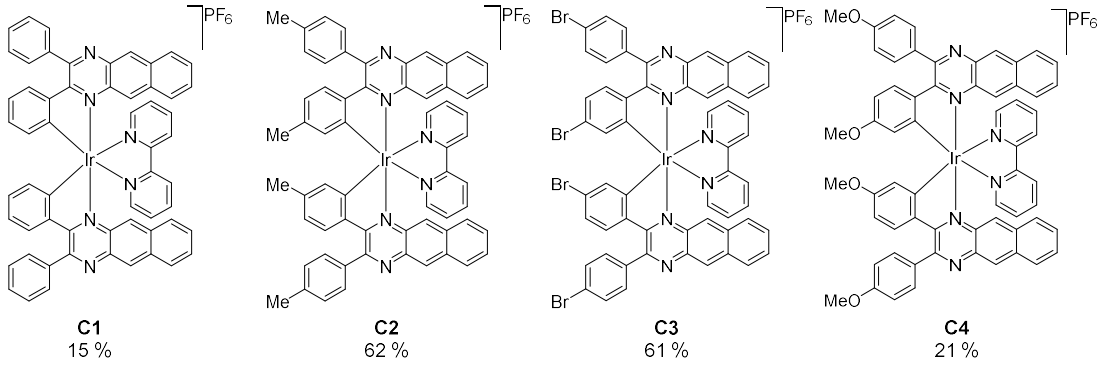

Figure 4.8: Structures and yields of complexes synthesised in this study.

Of the complexes synthesised, C2, C3 and C4 are novel with complex C1 first being reported in 2006,[22] and once more shortly after the completion of this work.[18] The complexes were characterised by proton NMR, carbon NMR spectroscopy and high-resolution mass spectrometry. Mass spectrometry was able to confirm the presence of the molecular ion peak and the correct isotope pattern in each case; an example spectrum is shown in Figure 4.9 while Figure 4.10 shows a comparison with theoretical data. The complexity of the peak cluster arises from the four bromine atoms, with bromine having two isotopes, ^{79}Br and ^{81}Br, in a 1:1 ratio abundance.

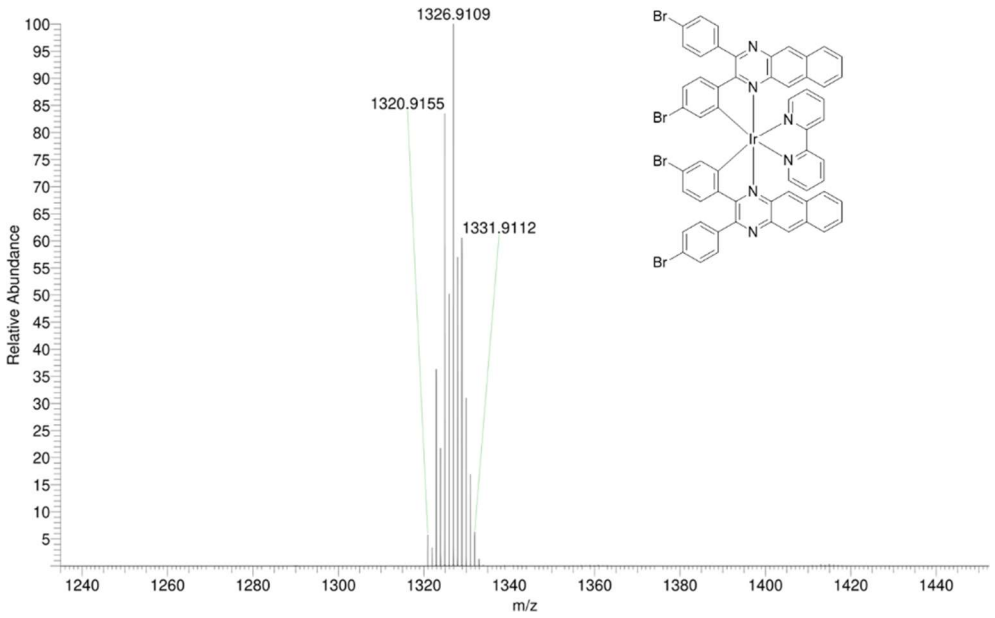

Figure 4.9: High-resolution mass spectrum recorded for complex C3.

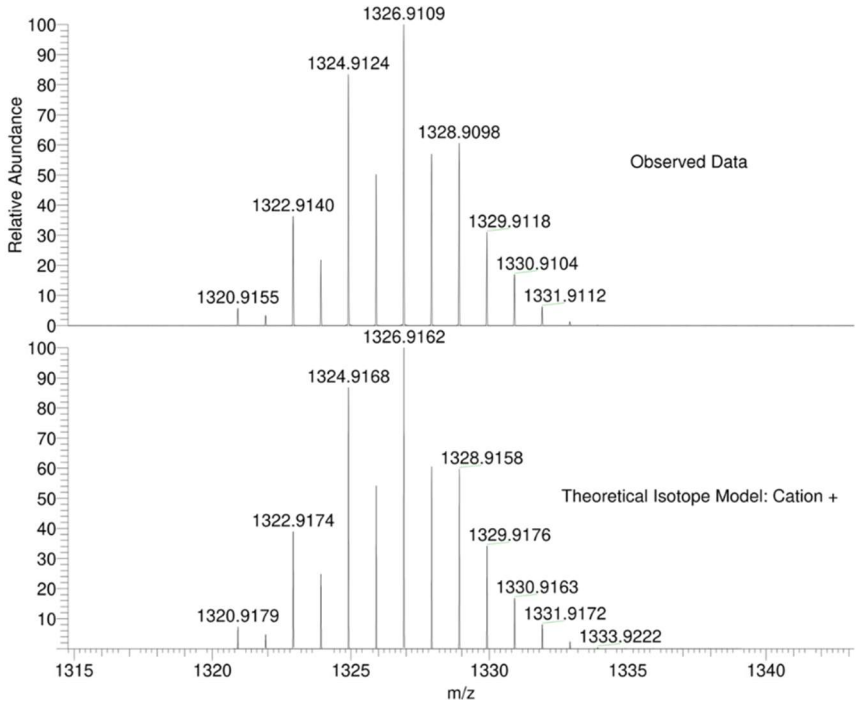

Figure 4.10: Observed mass spectrometry data for complex C3 compared with theoretical data for the same complex.

As discussed in chapters 2 and 3, proton NMR spectroscopy can be useful in determining the coordination of the ligand to the metal centre. The signal circled in red in Figure 4.11 relates to the proton adjacent to the cyclometallating site of the ligand. This signal experiences a large upfield shift due to experiencing the effects of the ring currents of the adjacent aromatic rings.

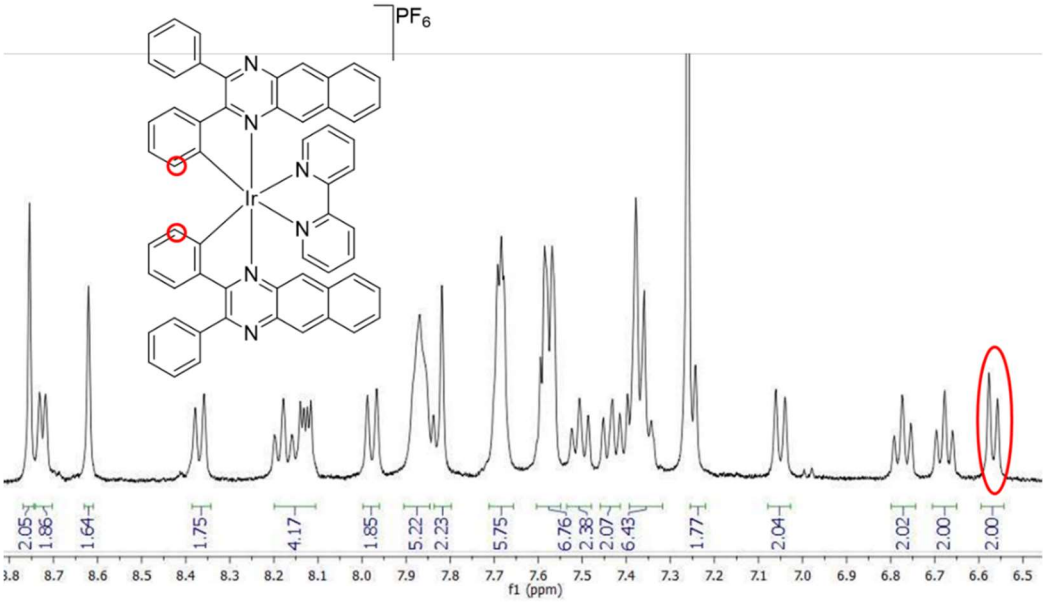

Figure 4.11: Proton NMR spectrum recorded for complex C1 showing the signal arising from proton adjacent to cyclometallating site. Recorded in $CDCl_3$, 400 MHz.

4.3.3. UV-Vis and Luminescence Spectroscopy

The ligands and complexes in this study were characterised by UV-vis absorption spectroscopy as well as luminescence spectroscopy and the results are discussed below.

Figure 4.12 shows the absorption spectra recorded for ligands HL1-4. All spectra were recorded as chloroform solutions at a concentration of $1x10^{-5}$ M and compare well with similar ligand systems in literature.[13,22–24] Each ligand shows strong π-π* transitions at 200 - 400 nm in the UV region. There is also a shoulder feature which extends beyond 450 nm and this is attributed to weak π-π* transitions as well as some n-π* transitions. It is also clear that the phenyl substituent effects the positions of these bands with the ligand L4 exhibiting the longest wavelength absorption, possibly due to the strong electron-donating character of the OMe groups.

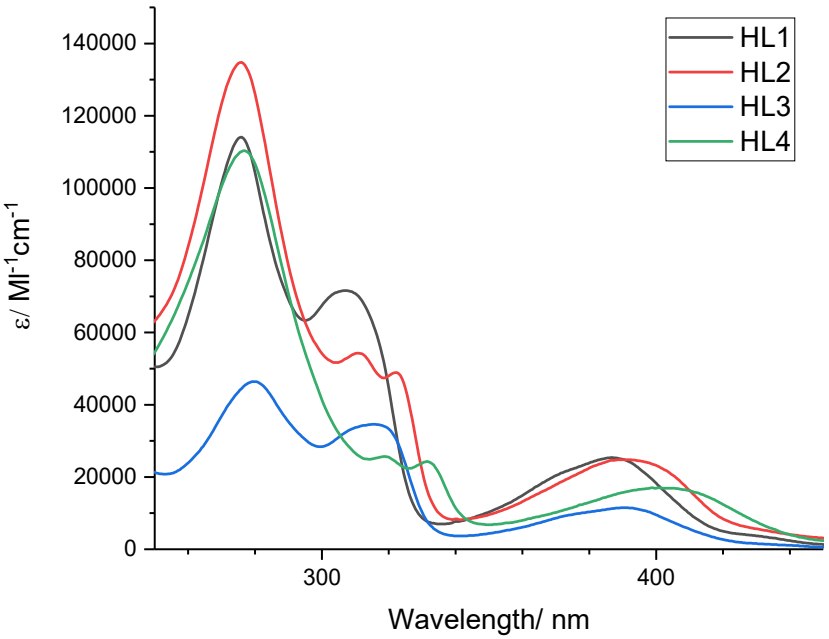

Figure 4.12: UV-Vis absorption spectra recorded for ligands HL1-4. Recorded in $CHCl_3$ at $1x10^{-5}$ M.

The emission spectra were also recorded for each ligand in the series. Luminescence in the visible region of the spectrum was observed for each species at between 400-550 nm, with some vibronic structure visible in the peak shape. The position of the emission peak varies depending upon the substituent, as observed in the absorption spectra. The ligand HL3 has the longest emission wavelength, while the ligand HL4 has the shortest. The lifetimes recorded for these species were all recorded at < 5 ns, which is in accordance with that expected from a π-π* fluorescent emitting state. The emission spectra are shown in Figure 4.13.

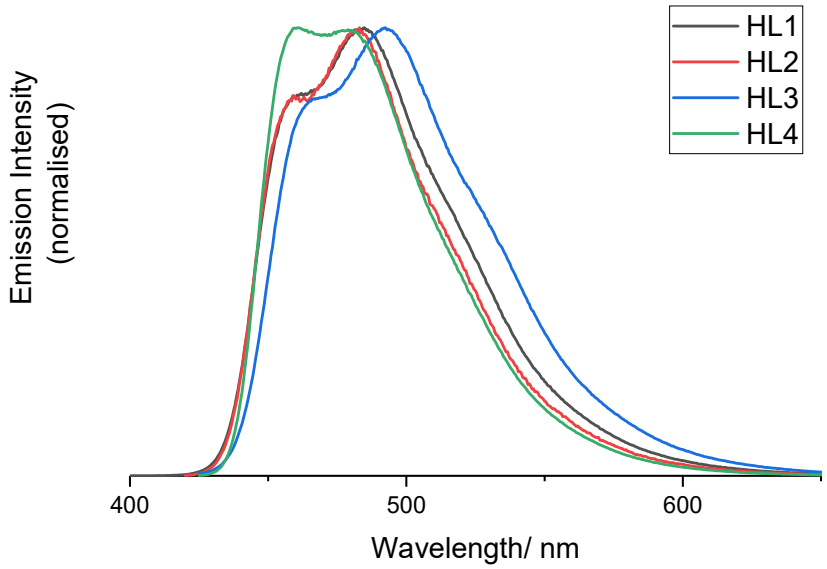

Figure 4.13: Emission spectra recorded for ligands HL1-4. Recorded as chloroform solutions, λ_{ex} = 400 nm.

The UV-vis absorption spectra of the complexes are shown in Figure 4.14 and show absorption signals in both the UV and visible regions. The peaks seen at 250-450 nm are ligand centred transitions that, upon coordination to the Ir(III) centre, become perturbed. It is also likely that there is some contribution from spin-allowed ^{1}MLCT transitions.

When compared to the absorption spectra of the ligand, additional absorption bands are observed at over 500 nm, this can be seen more clearly in Figure 4.15 where the absorption spectrum of ligand HL1 has been overlaid with the absorption spectrum of complex C1. The weak absorption bands at long wavelengths are likely to possess some spin-forbidden ^{3}MLCT character.[25] As a result, a strong bathochromic shift is observed in the complexes in this study relative to the substituted complexes with quinoxaline ligands investigated in chapter 2.[24] The reason for this is that the extended conjugation of the benzo[*g*]quinoxaline ligands lowers the energy of the MLCT transitions by stabilising the HOMO. The same small variations in absorption seen in the ligands, is also seen in the complexes; with complex C4 possessing the longest wavelength absorption just as ligand HL4 showed the lowest energy absorption of any ligand.

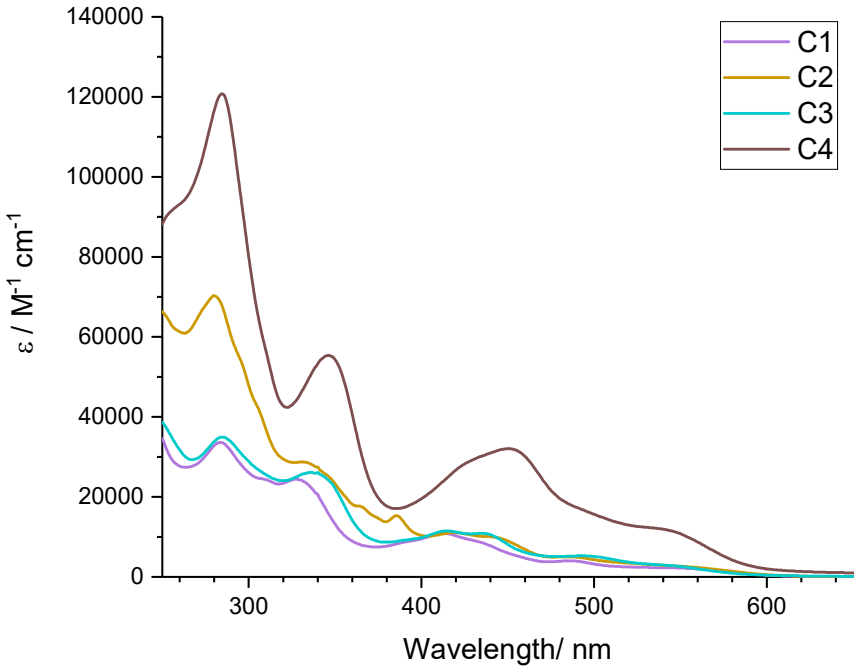

Figure 4.14: UV-vis absorption spectra recorded for complexes C1-4. Recorded as solutions in chloroform at 1x10^{-5} M.

Complex C1 has previously been reported in study from 2006 by Chen *et al.* and again, in 2017 by Wang *et al.*[22,18] Table 4.3 shows a comparison of the absorption data from each literature report in comparison with the data reported herein.

Table 4.3: Comparison of literature UV-vis absorption spectra with data recorded in this study for complex C1.

Complex	**λ_{abs}/ nm (ε/ M^{-1}cm^{-1})**
C1 ($CHCl_3$)	286 (33200), 329 (24200), 415 (10700), 490 (3900), 554 (2100)

Complex 1 (CH_2Cl_2) , Wang *et al.*, 2017[18]	327 (66000), 412 (29000), 486 (11000), 550 (6000), 673 (120), 742 (40)
Complex 3 (CH_2Cl_2) , Chen *et al.*, 2006[22]	412 (26000), 484 (9000), 540 (5000)

Each study is in agreement with absorption features at around 412, 490 and 550 nm, however the molar extinction coefficients reported in literature are around triple those found in this study. In addition to this, there is no report in the literature of features below 300 nm, contradictory to the absorption observed at 289 nm. Furthermore, in addition to all the peaks observed in this report, Wang *et al.* also observed very weak, broad absorptions at 673 and 742 nm which are not observed in the spectra reported here; in fact, no absorption above 600 nm is observed for any complex in this study.

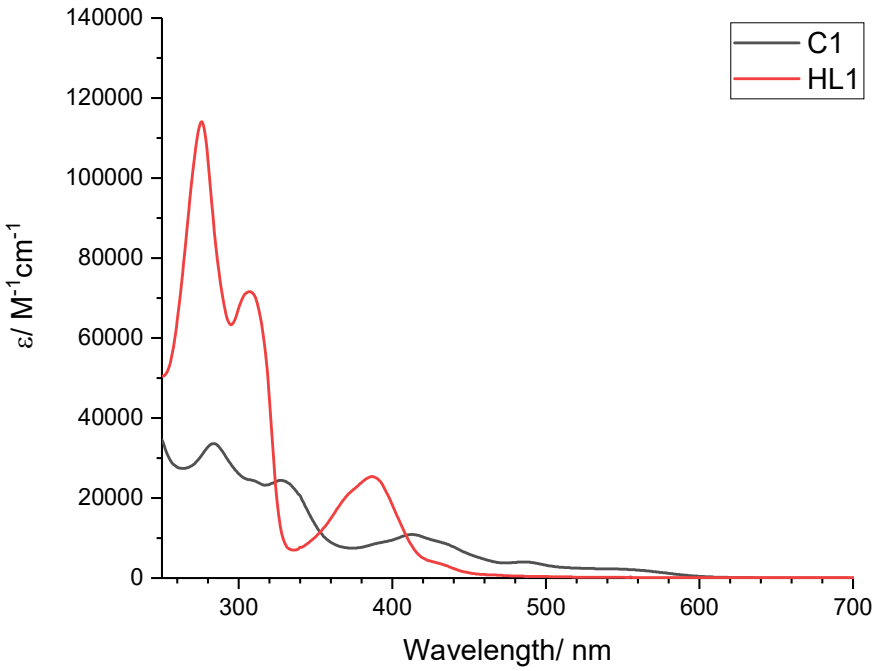

Figure 4.15: Overlaid absorption spectra of complex C1 (black) and ligand HL1 (red) showing additional bands observed in complex.

Luminescence spectra were recorded for each complex at room temperature in aerated chloroform solutions using an excitation wavelength of 470 nm. This wavelength was chosen as it corresponds to a strong absorption band in all of the complexes in this study. Emission spectra were first recorded in the 250 – 750 nm region and then repeated in the 850 – 1300 nm region.

The emission spectra shown in Figure 4.16 were the recorded for the visible region of the spectrum and show emission between 490 – 750 nm with vibronic structure in the peak shape of each complex. The spectra show almost no variation in the position of the emission peak with the four spectra being virtually superimposable. These observations do not correlate with the luminescent properties of the cationic iridium(III) phenyl quinoxaline complexes discussed in chapter 2, which showed phosphorescent emission between 620 – 650 nm from a ^{3}MLCT state.[24] It is also worth noting that the shape and position of these peaks differ from those of the free ligand, ruling out the possibility of decomposition in solution. The lifetime measurements for

these peaks were also measured and recorded at less than 10 ns, which suggests that these features may be due to intraligand transitions in the complexes.

As mentioned previously, complex C1 has twice been reported in literature yet neither study reports emission below 790 nm for this complex. In addition to this, a paper published by Chen *et al.* in 2019 reports cationic bis-cyclometallated complexes with ligands L2 and L4 with a series of different ancillary ligands.[17] This paper also reports no emission in the visible region of the spectrum. It appears likely that these reports did not scan the visible region of the spectrum for emission.

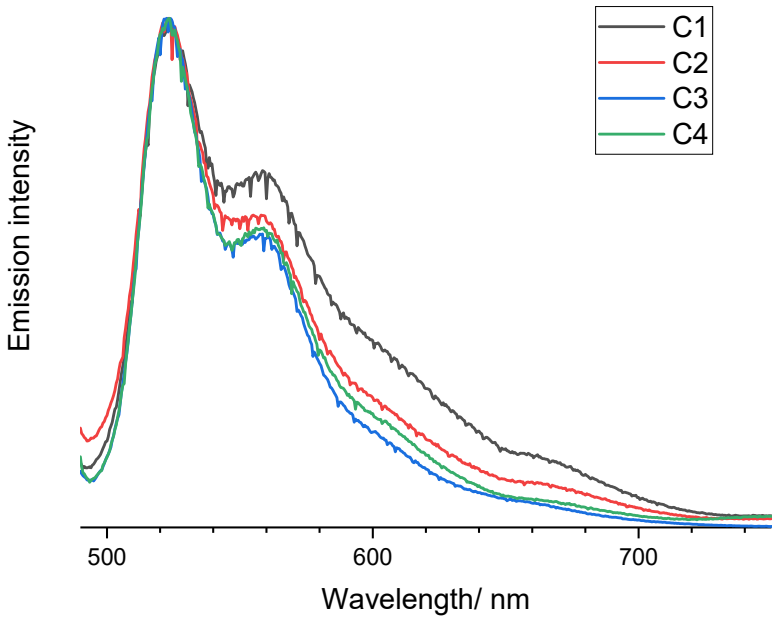

Figure 4.16: Visible emission spectra for complexes C1-4. Recorded in aerated $CHCl_3$, λ_{ex} = 470 nm.

The steady state experiments were then repeated to observe the near-IR region of the spectrum. These spectra were also recorded in aerated chloroform at room temperature using an excitation wavelength of 505 nm and collected at between 850 – 1300 nm. The emission spectra recorded are shown in Figure 4.17 and a compilation of the data recorded in both the visible and near-IR regions is recorded in Table 4.4.

Each of the complexes was excited using 505 nm light and, as Figure 4.17 shows, emission in the near-IR region was observed. Each complex exhibits a very broad emission profile which peaks between 915 – 950 nm and tails to around 1250 nm. The peak observed at around 1274 nm in each spectra is attributed to the spin relaxation of singlet oxygen ($^1O_2 \rightarrow {}^3O_2$). The presence of this feature not only confirms that the solvent used was aerated, but also suggests that there is an excited triplet state on a sensitiser molecule. This is further supported by lifetime measurements recorded for the complexes which all show values in the range of 116 – 162 ns which are concordant with triplet emission.

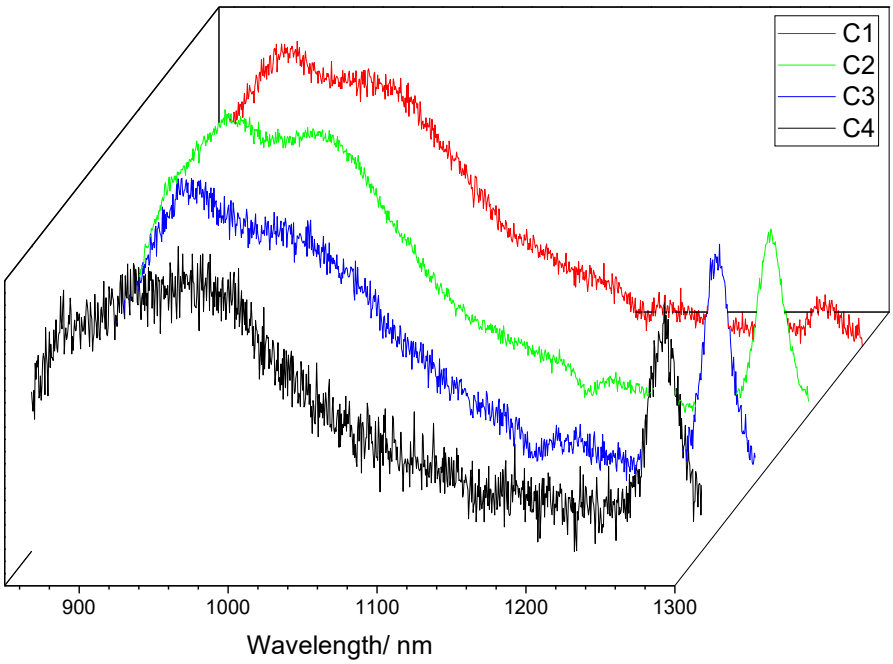

Figure 4.17: Steady state near-IR emission spectra pf the complexes. The peak at 1274 nm is due to the photogeneration of, and subsequent emission from, $^1O_2$. (Aerated $CHCl_3$, λ_{ex} = 505 nm)

These observations reported here are in good agreement with previous reports on related complexes with similar benzo[*g*]quinoxaline ligands.[17,18,22] Table 4.5 shows a comparison of the data recorded for complex C1 in this study with that reported for the same complex previously.

Table 4.4: Photophysical data recorded for ligands HL1-4 and complexes C1-4. [a] Recorded in aerated $CHCl_3$; [b] λ_{ex} = 405 nm; [c] λ_{ex} = 295 nm; [d] λ_{ex} = 505 nm; [e] λ_{ex} = 355 nm

Compound	**λ_{abs} / nm [a]**	**λ_{em} / nm[a,b] (τ / ns[c])**	**λ_{em} / nm[a,d] (τ / ns[e])**
HL1	386, 309, 276	485 (1.4)	-
HL2	391, 323, 312, 276	480 (1.1)	-
HL3	393, 318, 280	490 (1.8)	-
HL4	402, 332, 319, 276	480 (1.1)	-
C1	554, 490, 415, 329, 286	520 (4.9)	915 (119)
C2	554, 491, 445, 420, 388, 367, 334, 283	520 (7.0)	912 (148)
C3	554, 500, 439, 415, 340, 287	520 (2.9)	928 (116)
C4	554, 455, 348, 285	520 (<1)	949 (162)

*Table 4.5: Comparison of data recorded for complex C1 with data previously recorded for the same complex. * Lifetime stated is intrinsic lifetime, τ_0.*

Complex	λ_{em} / nm (τ/ ns)
C1 ($CHCl_3$)	520 (4.9), 915 (119)
Complex 1 (CH_2Cl_2) , Wang *et al.*, 2017[18]	794, 911, 965 (440)*
Complex 3 (CH_2Cl_2), Chen *et al.*, 2006[22]	922 (245)

4.3.4. Density Functional Theory Calculations

The calculations discussed in this section were carried out by Thomas Stonelake and Dr Joseph Beames (Cardiff University) and can be found in more detail in the publication at the end of this thesis.[26] The geometries of the complexes were optimised, and calculations included solvent effects. Also, the first five singlet excited states for each complex were determined using TD-DFT calculations on the stationary points and in addition to this, the phosphorescence and spin forbidden absorption bands were calculated.

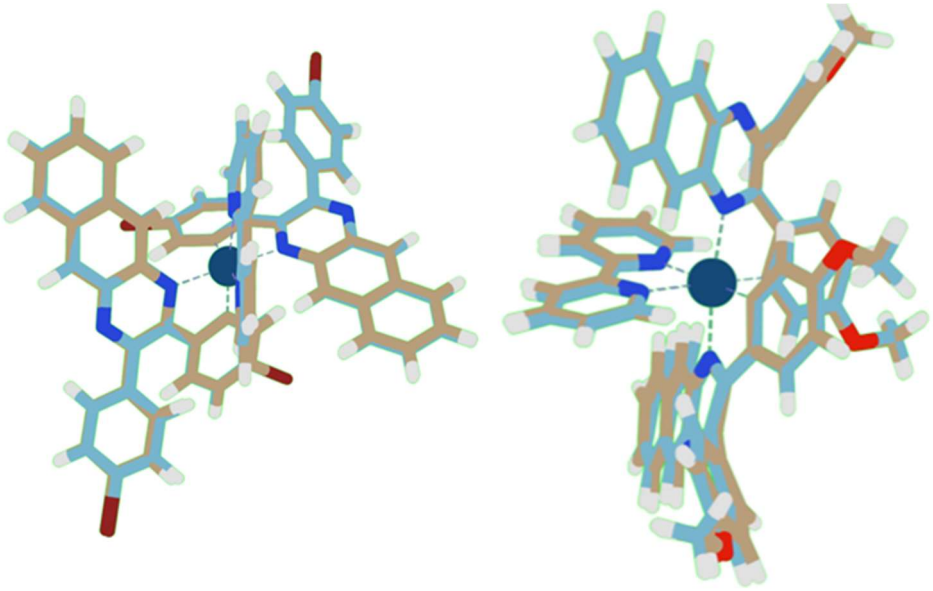

Figure 4.18: A comparison of the calculated geometries of the singlet and triplet excited states for complex C3 (left, RMSD = 0.185 Å) and C4 (right, RMSD = 0.149 Å).

Figure 4.18 shows the superimposed calculated structures of the complexes C3 and C4 in both the singlet and triplet excited states where it can be seen that there are slightly different degrees of distortion in the cyclometallated ligand in each excited state. Table 4.6 shows the composition of the HOMO and LUMO in each complex.

Table 4.6: Calculated HOMO and LUMO contributions for each complex.

	HOMO			
Compound	**Ir (5d)**	**C^N (1)**	**C^N (2)**	**Bpy**
C1	26 %	36 %	36 %	1 %
C2	26 %	37 %	36 %	1 %
C3	13 %	44 %	42 %	0 %
C4	16 %	40 %	43 %	1 %
	LUMO			
C1	3 %	48 %	47 %	1 %
C2	3 %	47 %	48 %	2 %
C3	3 %	49 %	46 %	3 %
C4	3 %	47 %	49 %	2 %

From the above table, it is seen that the cyclometallated ligands are predicted to have the largest contribution to the HOMO, with the contribution of the iridium centre varying between 13 – 26 %. This suggests that the emission is not purely ^{3}MLCT in character but consists of both MLCT and intraligand transitions. It is also worth noting that the 2,2'-bipyridine ligand has very little contribution to these molecular orbitals.

The vertical transitions for the complexes were calculated and are collated in Table 4.7. It was suggested that benzo[*g*]quinoxaline ligand centred transitions are responsible for the visible complex emission which is consistent with the similarity observed between the vibronic band shapes in the free ligand emission and in the complex emission.

Table 4.7: Calculated vertical transitions for complexes C1-4

Compound	**$S_1 \leftarrow S_0$ / nm**	**$T_1 \leftarrow S_0$ / nm**	**$T_1 \rightarrow S_0$ / nm**
C1	433	557	993
C2	434	602	980
C3	428	590	1019
C4	428	583	962

The electronic emission spectrum for the free ligand, HL1, was simulated as part of this study and Figure 4.19 shows this in comparison to the experimental emission spectra recorded for L1 and its corresponding complex C1.

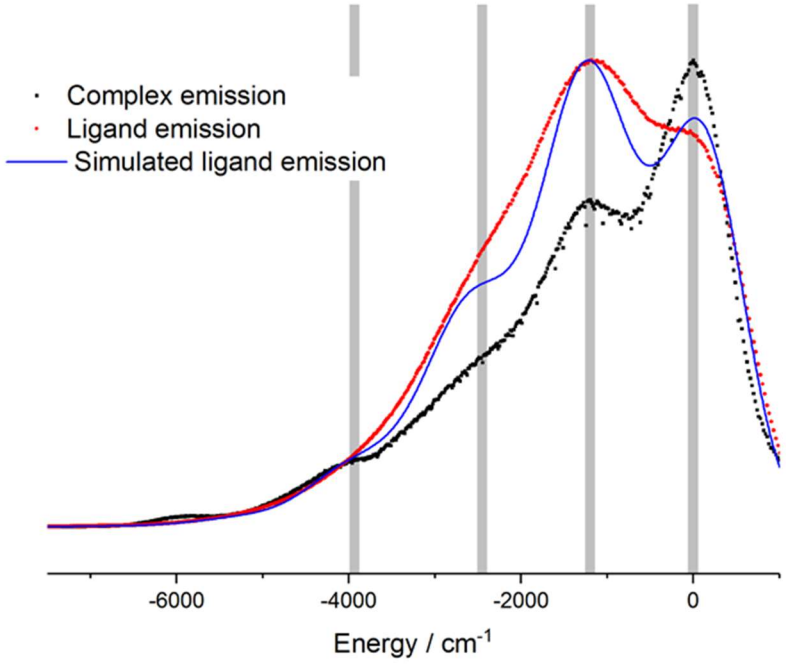

Figure 4.19: Franck - Condon simulation of the L1 A-X transition (blue), overlaid against the experimental emission spectra of the free ligand L1 (red) and the complex C1 (black). The spectra are offset by their respective vibronic origin, and are displayed as emission energy (cm^{-1}) relative to zero. The grey bars show different vibronic features.

The spectra show excellent agreement between simulation and experiment. In addition to confirming the assignment of the vibronic features, this figure shows the large similarity between the free ligand L1 and the same ligand in the complex.

Table 4.7 shows the calculated wavelengths for selected transitions. The data corelates very well with the experimental observations, but most importantly, the calculations predict near-IR emission from the complexes at between 962 – 1019 nm. The absorption spectra recorded also align well with the calculated spin-allowed and spin-forbidden transitions. Interestingly, the DFT calculations also predicted that differences in ligand structure should lead to significant differences in the emission energy, but only a small variation of 37 nm was observed over the series.

4.4. Conclusion

In this study, it has been shown that extending the conjugation of the cyclometallating ligand in a bis-cyclometallated iridium(III) complex system can result in large bathochromic shifts in emission wavelength, leading to near-IR emission. Ligands based upon benzo[*g*]quinoxaline have been shown to be excellent choice for Ir(III) complexes and DFT calculations have been able to reliably predict the transitions that dominate the lowest energy absorptions and phosphorescent emission properties of these complexes.

In addition to this, this study has also shown that these complexes simultaneously show emission in the visible region of the spectrum, centred at around 520 nm. This is in contrast with a number of recent publications which feature an identical complex along with several closely related complexes. These reports omit the visible feature in each case, instead focusing upon the near-infrared.

4.5. Experimental

All reactions were performed with the use of vacuum line and Schlenk techniques. Reagents were commercial grade and were used without further purification. ^{1}H and $^{13}C\{^{1}H\}$ NMR spectra were run on NMR-FT Bruker 300 or 400 spectrometers and recorded in $CDCl_3$. ^{1}H and $^{13}C\{^{1}H\}$ NMR chemical shifts (δ) were determined relative to internal TMS and are given in ppm. Low-resolution mass spectra were obtained by the staff at Cardiff University. High-resolution mass spectra were carried out by at the EPSRC National Mass Spectrometry Service at Swansea University. UV-Vis studies were performed on a Shimadzu UV-1800 as chloroform solutions (10^{-5} M). Photophysical data were obtained on a JobinYvon-Horiba Fluorolog spectrometer fitted with a JY TBX picosecond photodetection module as MeCN solutions. A Hamamatsu R5509-73 detector (cooled to -80 ˚C using a C9940 housing) was usedfor NIR luminescence measurements. For the NIR lifetimes the pulsed laser source was a Continuum Minilite Nd:YAG configured for 355 nm output. For all NIR emission data, a 850 nm band pass filter was used. Emission spectra were uncorrected and excitation spectra were instrument corrected. The pulsed source was a Nano-LED configured for 372 nm output operating at 1 MHz. Luminescence lifetime profiles were obtained using the JobinYvon-Horiba FluoroHub single photon counting module and the data fits yielded the lifetime values using the provided DAS6 deconvolution software.

Synthesis of HL1 To a stirred solution of benzil (322 mg, 1.6 mmol) in ethanol (15 mL) was added 2,3-diaminonaphthalene (250 mg, 1.6 mmol) and acetic acid (0.5 mL). The reaction mixture was heated at reflux under a nitrogen atmosphere for 24 hours. The reaction mixture was cooled to room temperature and a precipitate collected by filtration to give **L1** as a brown solid (Yield = 0.34 g, 64%). ^{1}H NMR (300 MHz, $CDCl_3$): δ_H 8.68 (s, 2H, CH), 8.05 (dd, J_{HH} = 3.21, 6.39 Hz, 2H), 7.50 (m, 6H), 7.30 (m, 6H) ppm. $^{13}C\{^{1}H\}$ NMR (101 MHz, $CDCl_3$): δ_C 154.2, 139.2, 138.0, 134.1, 129.8, 129.0, 128.6, 128.3, 127.6, 126.8 ppm. HRMS (ESI) found *m/z* 333.1387; calcd *m/z* 333.1386 for $C_{24}H_{16}N_2$+H . UV-vis. ($CHCl_3$) λ_{max} (ε / $dm^3\,mol^{-1}\,cm^{-1}$): 386 (25200), 309 (71500), 276 (114100) nm. Selected IR (solid) υ_{max} = 1607, 1508, 1441, 1346, 1248, 1175, 1013, 976, 876, 836, 760, 741, 691, 552, 500.0, 490, 467 cm^{-1}.

Synthesis of HL2 As **HL1** but with 4,4'-dimethylbenzil (376 mg, 1.6 mmol) and 2,3-diaminonaphthalene (250 mg, 1.6 mmol). Product collected as a brown solid (Yield = 0.41 g, 71%). ^{1}H NMR (300 MHz, $CDCl_3$) δ_H 8.73 (s, 2H), 8.12 (dd, J_{HH} = 3.2, 6.5 Hz, 2H), 7.57 (dd, J_{HH} = 3.1, 6.7 Hz, 2H), 7.49 (d, J_{HH} = 8.0 Hz, 4H), 7.19 (d, J_{HH} = 8.0 Hz, 4H), 2.41 (s, 6H) ppm. $^{13}C\{^{1}H\}$ NMR (101 MHz, $CDCl_3$) δ_C 154.3, 139.0, 138.0, 136.5, 134.0, 129.8, 129.0, 128.6, 127.4, 126.6, 21.4 ppm. HRMS (ESI) *m/z* found 361.1699; calcd *m/z* 361.1699 for $C_{26}H_{20}N_2$+H . UV-vis. ($CHCl_3$) λ_{max} (ε / $dm^3\,mol^{-1}\,cm^{-1}$): 391 (24800), 323 (48600), 312 (54200), 276 (134500) nm. Selected IR (solid) υ_{max} = 1607, 1508, 1445, 1346, 1247, 1174, 1109, 1013, 972, 878, 835, 819, 760, 559, 500, 490, 471, 421 cm^{-1}.

Synthesis of HL3 As **HL1** but with 4,4'-dibromobenzil (581 mg, 1.6 mmol) and 2,3-diaminonaphthalene (250 mg, 1.6 mmol). Product collected as a light brown solid (Yield = 0.56 g, 72%). ^{1}H NMR (400 MHz, $CDCl_3$) δ_H 8.66 (s, 2H), 8.05 (dd, J_{HH} = 3.2, 6.5 Hz, 2H), 7.52 (m, 2H), 7.46 (d, J_{HH} = 8.4 Hz, 4H), 7.38 (d, J_{HH} = 8.4 Hz, 4H) ppm. $^{13}C\{^{1}H\}$ NMR (101 MHz, $CDCl_3$) δ_C 152.6, 137.9, 137.8, 134.3, 131.7, 131.4, 128.6, 127.7, 127.0, 123.9 ppm. HRMS (ESI) found *m/z* 490.9569; calcd *m/z* 490.9576 for $C_{24}H_{15}Br_2N_2$+H. UV-vis. ($CHCl_3$) λ_{max} (ε / $dm^3mol^{-1}cm^{-1}$): 393 (11400), 318 (34300), 280 (46400) nm. Selected IR (solid) υ_{max} = 1605, 1510, 1445, 1344, 1246, 1173, 1109, 1053, 1011, 972, 880, 833, 795, 758, 745, 723, 656, 646, 623, 573, 557, 548, 532, 498, 471, 409 cm^{-1}.

Synthesis of HL4 As **HL1** but with anisil (427 mg, 1.6 mmol) and 2,3-diaminonaphthalene (250 mg, 1.6 mmol). Product collected as a light brown solid (Yield = 0.50 g, 80%). ^{1}H NMR (300 MHz, $CDCl_3$) δ_H 8.61 (s, 2H, CH), 8.02 (dd, J_{HH} = 3.0, 6.4 Hz, 2H), 7.48 (m, 6H), 6.83 (d, J_{HH} = 8.4, 4H), 3.78 (s, 6H) ppm. ^{13}C{^{1}H} (101 MHz, $CDCl_3$) δ_C 160.4, 153.8, 138.0, 133.9, 131.8, 131.3, 128.5, 127.2, 126.5, 113.8, 55.4 ppm. HRMS (ESI) found *m/z* 393.1593; calcd *m/z* 393.1598 for $C_{26}H_{21}N_2O_2$+H. UV-vis. ($CHCl_3$) λ_{max} (ε / $dm^3mol^{-1}cm^{-1}$): 402 (16900), 332 (24200), 319 (25600), 276 (110300) nm. Selected IR (solid) υ_{max} = 1605, 1578, 1541, 1508, 1445, 1414, 1344, 1275, 1246, 1173, 1109, 1051, 1015, 976, 891, 880, 853, 833, 795, 756, 747, 656, 646, 623, 592, 573, 557, 532, 525, 496, 474, 421 cm^{-1}.

Synthesis of $[Ir(C^N)_2Cl_2]_2$ $IrCl_3.xH_2O$ (1 eq.) and ligand, L (2 eq.) were dissolved in 2-ethoxyethanol (10 mL) and the reaction mixture heated at reflux for 48 hours. The reaction was then cooled to room temperature and water (30 mL) was added to form a dark brown precipitate. The solid was collected by filtration to yield $[(L)_2Ir(\mu\text{-}Cl_2)Ir(L)_2]$.

Synthesis of C1 $[\{Ir(L1)_2(\mu\text{-}Cl)\}_2]$ (195 mg, 0.11 mmol) and 2,2'-bipyridyl (36 mg, 0.23 mmol) were dissolved in 2-ethoxyethanol (10 mL) and heated at reflux for 24 hours under a nitrogen atmosphere. The reaction mixture was then cooled to room temperature and a saturated solution of aqueous ammonium hexafluorophosphate was added. Upon formation of a red precipitate, the mixture was filtered, and the precipitate washed with water and diethyl ether. The crude solid was purified by column chromatography using DCM followed by DCM/MeOH (9:1). Product collected as first red band with DCM/MeOH and dried in vacuo to give $[Ir(L1)_2(bipy)][PF_6]$ as a red solid (Yield = 38 mg, 15%). ^{1}H NMR (400 MHz, $CDCl_3$): δ_H 8.65 (d, J_{HH} = 5.6 Hz, 2H), 8.55 (s, 2H), 8.31 (d, J_{HH} = 8.8 Hz, 2H), 8.12 (app. t, J_{HH} = 8.8 Hz, 2H), 7.91 (d, J_{HH} = 8.4 Hz, 2H), 7.89-7.77 (m, 6H), 7.75 (s, 2H), 7.64-7.60 (m, 6H), 7.44 (app. t, J_{HH} = 8.8 Hz, 2H), 7.36 (app. t, J_{HH} = 6.4 Hz, 2H), 7.17 (s, 2H), 6.98 (d, J_{HH} = 8.8 Hz, 2H), 6.70 (app. t, J_{HH} = 5.6 Hz, 2H), 6.61 (app. t, J_{HH} = 7.2 Hz, 2H), 6.50 (d, J_{HH} = 7.2 Hz, 2H) ppm. ^{13}C{^{1}H} NMR (101 MHz, $CDCl_3$): δ_C 164.5, 155.8, 154.3, 153.8, 147.9, 144.3, 139.6, 134.6, 133.7, 132.5, 131.5, 130.4, 129.4, 129.4, 128.9, 128.8, 128.2, 128.0, 127.6, 125.4, 122.0, 119.5, 114.4, 77.4, 76.7 ppm. HRMS (ESI) found *m/z* 1011.2777; calcd *m/z* 1011.2786 for $C_{58}H_{38}IrN_8$. UV-vis. ($CHCl_3$) λ_{max} (ε / dm^3 mol^{-1} cm^{-1}): 554 (2100), 490 (3900), 415 (10700), 329 (24200), 286 (33200) nm. Selected IR (solid) υ_{max} = 1607, 1445, 1350, 1253, 835, 760, 738, 696, 574, 557, 500, 468 cm^{-1}.

Synthesis of C2 As **C1** but with $[\{Ir(L2)_2(\mu\text{-}Cl)\}_2]$ (56 mg, 0.03 mmol) and 2,2'-bipyridyl (10 mg, 0.07 mmol). Product collected as a red solid (Yield = 44 mg, 62%) ^{1}H NMR (400 MHz, $CDCl_3$): δ_H 8.67 (d, J_{HH} = 6.60 Hz, 2H), 8.59 (s, 2H), 8.53 (d, J_{HH} = 8.8 Hz, 2H), 8.21 (dd, J_{HH} = 7.72, 8.80 Hz, 2H), 7.98 (d, J_{HH} = 8.80 Hz, 2H), 7.78 (m, 8H), 7.50 (m, 6H), 7.42 (app. t, J_{HH} = 7.70, 2H), 7.24 (d, J_{HH} = 7.72 Hz, 2H), 7.03 (d, J_{HH} = 7.72 Hz, 2H), 6.65 (d, J_{HH} = 8.84 Hz, 2H), 6.43 (s, 2H), 2.57 (s, 6H), 1.94 (s, 6H) ppm. ^{13}C{^{1}H} NMR (101 MHz, $CDCl_3$): δ_C 164.8, 156.0, 148.0, 142.5, 141.7, 141.1, 140.5, 136.9, 136.3, 135.1, 134.0, 133.4, 132.3, 130.0, 129.1, 128.8, 128.5, 128.1, 128.0, 127.7, 127.5, 125.8, 123.8, 122.0, 21.8, 21.7 ppm. HRMS (ESI) found *m/z* 1067.3406; calcd *m/z* 1067.3413 for $C_{62}H_{46}IrN_6$. UV-vis. ($CHCl_3$) λ_{max} (ε / dm^3 mol^{-1} cm^{-1}): 554 (2500), 491 (4900), 445 (9700), 420 (11000), 388 (14900), 367 (16900), 334 (28300), 283 (69500) nm. Selected IR (solid) υ_{max} = 1586, 1503, 1445, 1398, 1359, 1314, 1257, 1211, 1177, 1138, 1069, 1042, 978, 833, 772, 635, 579, 556, 513, 471, 424, 407 cm^{-1}.

Synthesis of C3 As **C1** but with $[\{Ir(L3)_2(\mu\text{-}Cl)\}_2]$ (150 mg, 0.06 mmol) and 2,2'-bipyridyl (20 mg, 0.13 mmol). Product collected as a red solid (Yield = 75 mg, 61%). ^{1}H NMR (400 MHz, $CDCl_3$): δ_H 8.82 (d, J_{HH} = 8.80 Hz, 2H), 8.56 (s, 2H), 8.52 (d, J_{HH} = 6.40 Hz, 2H), 8.21 (app. t, J_{HH} = 8.40 Hz, 2H),

7.94 (d, J_{HH} = 7.20 Hz, 3H), 7.77 – 7.68 (m, 5H), 7.62 (s, 2H), 7.49 (app. t, J_{HH} = 8.40 Hz, 3H), 7.39 (app. t, J_{HH} = 6.00 Hz, 3H), 7.11 (d, J_{HH} = 7.20 Hz, 3H), 6.97 (m, 5H), 6.62 (s, 2H) ppm. $^{13}C\{^1H\}$ NMR (101 MHz, d6-acetone): δ_C 164.5, 155.8, 153.4, 149.6, 144.1, 141.0, 138.8, 137.5, 137.4, 136.8, 134.1, 133.7, 133.6, 132.3, 131.5, 129.3, 129.1, 128.5, 128.3, 127.9, 127.5, 126.5, 126.0, 124.8, 124.2, 122.4, 78.3 ppm. HRMS (ESI) found *m/z* 1326.9109; calcd *m/z* 1326.9162 for $C_{58}H_{34}Br_4IrN_6$. UV-vis. ($CHCl_3$) λ_{max} (ε / $dm^3\,mol^{-1}\,cm^{-1}$): 554 (2400), 500 (5100), 439 (10700), 415 (11500), 340 (26000), 287 (34800) nm. Selected IR (solid) υ_{max} = 1607, 1512, 1445, 1348, 1248, 1174, 1109, 1013, 878, 835, 760, 559, 500 cm^{-1}.

Synthesis of C4 As **C1** but with [{Ir(L4)$_2$(μ-Cl)}$_2$] (100 mg, 0.09 mmol) and 2,2'-bipyridyl (16 mg, 0.11 mmol). Product collected as a red solid (Yield = 27 mg, 21%). ^1H NMR (400 MHz, $CDCl_3$) δ_H 8.63 (d, J_{HH} = 4.64 Hz, 2H), 8.45 (s, 2H), 8.43 (d, J_{HH} = 8.00 Hz, 2H), 8.14 (app. t, J_{HH} = 9.28 Hz, 2H), 7.87 (d, J_{HH} = 8.12 Hz, 2H), 7.76 (m, 6H), 7.62 (s, 2H), 7.40 (dd, J_{HH} = 6.96, 8.12 Hz, 2H), 7.32 (dd, J_{HH} = 5.80, 9.28 Hz, 2H), 7.27 (s, 2H), 7.24 (s, 4H), 7.11 (d, J_{HH} = 8.52 Hz, 2H), 6.94 (d, J_{HH} = 8.16 Hz, 2H), 5.99 (s, 2H), 3.91 (s, 6H), 3.26 (s, 6H) ppm. $^{13}C\{^1H\}$ NMR (101 MHz, $CDCl_3$) δ_C 164.2, 161.4, 156.0, 148.2, 141.1, 137.2, 136.7, 136.2, 134.4, 134.0, 133.1 132.1, 130.5, 128.9, 128.4, 128.1, 127.5, 125.6, 121.6, 119.8, 114.7, 108.3, 55.6, 54.8 ppm. HRMS (ESI) found *m/z* 1131.3193; calcd *m/z* 1131.3209 for $C_{62}H_{46}IrN_6O_4$. UV-vis. ($CHCl_3$) λ_{max} (ε / $dm^3\,mol^{-1}\,cm^{-1}$): 554 (10000), 455 (31700), 348 (55200), 285 (120700) nm. Selected IR (solid) υ_{max} = 1580, 1503, 1447, 1400, 1358, 1246, 1224, 1173, 1134, 1020, 978, 870, 837, 810, 772, 687, 519, 471 cm^{-1}.

Crystal data collection parameters

Formula	$C_{24}H_{14}Br_2N_2$	***Z'***	1
$D_{calc.}$**/ g cm^{-3}**	1.699	**Wavelength/Å**	0.71075
μ**/mm^{-1}**	4.243	**Radiation type**	MoK_α
Formula Weight	490.19	Θ_{min}**/°**	2.687
Colour	orange	Θ_{max}**/°**	27.483
Shape	blade	**Measured Refl.**	19907
Size/mm^3	0.360×0.140×0.040	**Independent Refl.**	4396
***T*/K**	100(2)	**Reflections Used**	3812
Crystal System	monoclinic	R_{int}	0.0501
Space Group	$P2_1/n$	**Parameters**	253
***a*/Å**	5.7963(2)	**Restraints**	0
***b*/Å**	21.8021(9)	**Largest Peak**	1.511
***c*/Å**	15.1661(6)	**Deepest Hole**	-0.916
α/°	90	**GooF**	1.057
β/°	91.211(3)	wR_2 **(all data)**	0.1219
γ/°	90	wR_2	0.1166
V/Å^3	1916.15(13)	R_1 **(all data)**	0.0567
Z	4	R_1	0.0491

4.6. References

1. In *Van Nostrand's Scientific Encyclopedia*, American Cancer Society, 2007.
2. J. G. Fujimoto, C. Pitris, S. A. Boppart and M. E. Brezinski, *Neoplasia N. Y. N*, 2000, **2**, 9–25.
3. J. G. Fujimoto, *Nat. Biotechnol.*, 2003, **21**, 1361–1367.
4. J. V. Frangioni, *Curr. Opin. Chem. Biol.*, 2003, **7**, 626–634.
5. S. Luo, E. Zhang, Y. Su, T. Cheng and C. Shi, *Biomaterials*, 2011, **32**, 7127–7138.
6. J. Gao, X. Chen and Z. Cheng, *Curr. Top. Med. Chem.*, 2010, **10**, 1147–1157.
7. X. Zhang, S. Bloch, W. Akers and S. Achilefu, *Curr. Protoc. Cytom.*, 2012, **60**, 12.27.1-12.27.20.
8. H. Xiang, J. Cheng, X. Ma, X. Zhou and J. J. Chruma, *Chem. Soc. Rev.*, 2013, **42**, 6128.
9. G. Qian and Z. Y. Wang, *Chem. – Asian J.*, 2010, **5**, 1006–1029.
10. 10. E. L. Williams, J. Li and G. E. Jabbour, *Appl. Phys. Lett.*, 2006, **89**, 083506.
11. J. Yu, C. Xu, F. Meng, H. Tan, M. Li and W. Zhu, *Dyes Pigments*, 2019, **166**, 307–313.
12. J. Shi, J. Fan, Z. Qu, S. Wang and Y. Wang, *Dyes Pigments*, 2018, **154**, 263–268.
13. E. E. Langdon-Jones, A. J. Hallett, J. D. Routledge, D. A. Crole, B. D. Ward, J. A. Platts and S. J. A. Pope, *Inorg. Chem.*, 2013, **52**, 448–456.
14. C. Wang and K. M.-C. Wong, *Inorg. Chem.*, 2011, **50**, 5333–5335.
15. W.-J. Xu, S.-J. Liu, T.-C. Ma, Q. Zhao, A. Pertegás, D. Tordera, H. J. Bolink, S.-H. Ye, X.-M. Liu, S. Sun and W. Huang, *J. Mater. Chem.*, 2011, **21**, 13999.
16. R. Tao, J. Qiao, G. Zhang, L. Duan, L. Wang and Y. Qiu, *J. Phys. Chem. C*, 2012, **116**, 11658–11664.
17. G.-Y. Chen, B.-R. Chang, T.-A. Shih, C.-H. Lin, C.-L. Lo, Y.-Z. Chen, Y.-X. Liu, Y.-R. Li, J.-T. Guo, C.-W. Lu, Z.-P. Yang and H.-C. Su, *Chem. – Eur. J.*, 2019, **25**, 5489–5497.
18. L. Wang, H. Yin, P. Cui, M. Hetu, C. Wang, S. Monro, R. D. Schaller, C. G. Cameron, B. Liu, S. Kilina, S. A. McFarland and W. Sun, *Dalton Trans.*, 2017, **46**, 8091–8103.
19. G.-Y. Chen, B.-R. Chang, T.-A. Shih, C.-H. Lin, C.-L. Lo, Y.-Z. Chen, Y.-X. Liu, Y.-R. Li, J.-T. Guo, C.-W. Lu, Z.-P. Yang and H.-C. Su, *Chem. – Eur. J.*, , DOI:10.1002/chem.201805902.
20. B. R. Yeo, A. J. Hallett, B. M. Kariuki and S. J. A. Pope, *Polyhedron*, 2010, **29**, 1088–1094.
21. M. Nonoyama, *Bull. Chem. Soc. Jpn.*, 1974, **47**, 767–768.
22. H.-Y. Chen, C.-H. Yang, Y. Chi, Y.-M. Cheng, Y.-S. Yeh, P.-T. Chou, H.-Y. Hsieh, C.-S. Liu, S.-M. Peng and G.-H. Lee, *Can. J. Chem.*, 2006, **84**, 309–318.
23. C. Wang, L. Lystrom, H. Yin, M. Hetu, S. Kilina, S. A. McFarland and W. Sun, *Dalton Trans.*, 2016, **45**, 16366–16378.
24. K. A. Phillips, T. M. Stonelake, K. Chen, Y. Hou, J. Zhao, S. J. Coles, P. N. Horton, S. J. Keane, E. C. Stokes, I. A. Fallis, A. J. Hallett, S. P. O'Kell, J. M. Beames and S. J. A. Pope, *Chem. – Eur. J.*, 2018, **24**, 8577–8588.
25. L. M. Groves, C. Schotten, J. Beames, J. A. Platts, S. J. Coles, P. N. Horton, D. L. Browne and S. J. A. Pope, *Chem. – Eur. J.*, 2017, **23**, 9407–9418.
26. K. A. Phillips, T. M. Stonelake, P. N. Horton, S. J. Coles, A. J. Hallett, S. P. O'Kell, J. M. Beames and S. J. A. Pope, *J. Organomet. Chem.*, 2019, **893**, 11–20.

5. Exploratory Synthesis: Toward the synthesis of dicyanodibenzodioxin ligands and their rhenium(I) coordination chemistry

5.1. Introduction

The previous three chapters have focussed upon the synthesis and characterisation of cyclometallated iridium(III) complexes $[Ir(C\hat{}N)_2(N\hat{}L)]^n$. As discussed, the nature of the cyclometallated ligand can strongly influence the resultant electronics and thus luminescence properties of the complex in question. The following chapter takes a slightly different approach and considers the design and synthesis of a series of ligands based upon a rigid, conjugated dicyanodibenzodioxin core structure. These compounds are designed to act as chelating ligands in a wide range of metal complex systems including iridium(III) (see further discussion in Chapter 6), but within Chapter 5 the focus will be upon exploring their coordination chemistry with rhenium(I).

5.1.1. Dicyanodibenzodioxin Derivatives

Large, planar heterocyclic aromatic compounds have applications as biological luminescent sensors as well as in materials science.[1,2] This is because their large pi-systems lead to delocalisation of electron density and can give rise to multi-band optical spectra.[3] Dibenzodioxins are a branch of organic compounds that are known to have cytotoxic effects against certain tumour cell lines. It is understood that the dioxin core, which acts as a hydrogen-bond acceptor, and the planar geometry of these compounds are responsible for their strong DNA intercalation behaviour.[4–6]

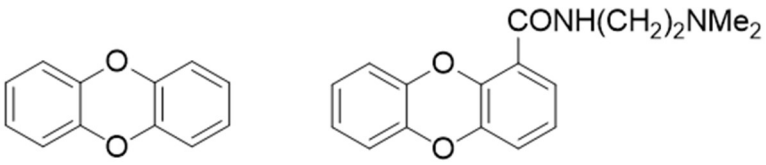

Figure 5.1: Left) Dibenzodioxin structure. Right) Cytotoxic derivative of dibenzodioxin.[5]

Dicycanobenzodioxins are similar in structure to dibenzodioxins, but as their name suggests, they possess two nitrile groups. These nitrile groups are electron withdrawing and can extend the pi-system which can alter the photophysical properties of the molecule, although these effects have not thoroughly been investigated.[7,8] In addition to this, dicyanodibenzodioxins could potentially have advantageous biological applications as they have exhibited cytotoxicity against the HeLa cell line and glioma cell line C6.[9]

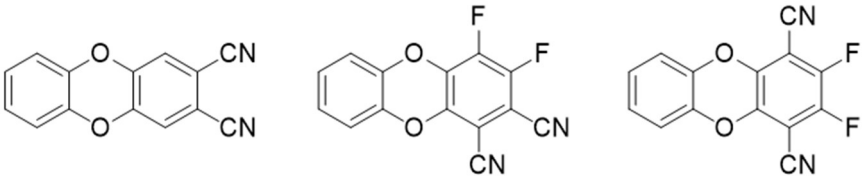

Figure 5.2: Examples of dicyanodibenzodioxin based compounds.[3]

The synthesis of these complexes is shown in Scheme 5.1. The reaction proceeds *via* a nucleophilic aromatic substitution reaction and means that many different analogues may be synthesised from di-hydroxy aromatic starting materials.

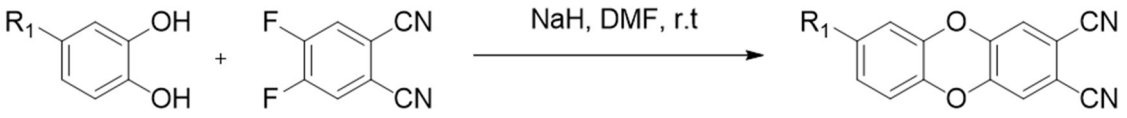

Scheme 5.1: Synthesis of dicyanodibenzodioxins.[1]

There are numerous reports in the literature of the use of this aromatic motif in the synthesis of polymeric chains using the compound tetrafluoroterephthalonitrile, also known as 2,3,5,6-tetrafluoro-1,4-dicyanobenzene, as a starting material.[10,11] These reports typically use potassium carbonate as the base instead of sodium hydride which suggests that formation of a second dioxin bridge is relatively facile due to the preorganised nature of the reacting functional groups. Scheme 5.2 shows a proposed route to how the use of tetrafluoroterephthalonitrile could form a compound with a second dioxin bridge.

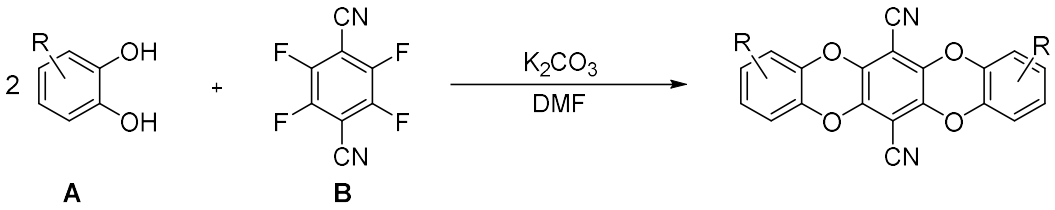

*Scheme 5.2: Proposed route to formation of second dioxin bridge. Where **A** is an aromatic diol and **B** is tetrafluoroterephthalonitrile.*

At present, there are no reports of the dicyanodibenzodioxin structure having been incorporated into a ligand system for transition metal chemistry. Thus, the aim of this work was to consider the introduction of a metal chelating site into this aromatic structure. As discussed later, one way to achieve this is by the use of 1,10-phenanthroline-5,6-diol as a dihydroxy starting material in the synthesis of the dicyanodibenzodioxins. Interestingly, the resulting target compound would have a similar structure to the known chelating ligand dipyridophenazine, dppz, and the use of a second 1,10-phenanthroline moiety would hypothetically result in a bridging ligand similar tetraazatetrapyridopentacene, tatpp. The structures of these known ligands along with the proposed dicyanodibenzodioxin based ligands are shown in Figure 5.3.

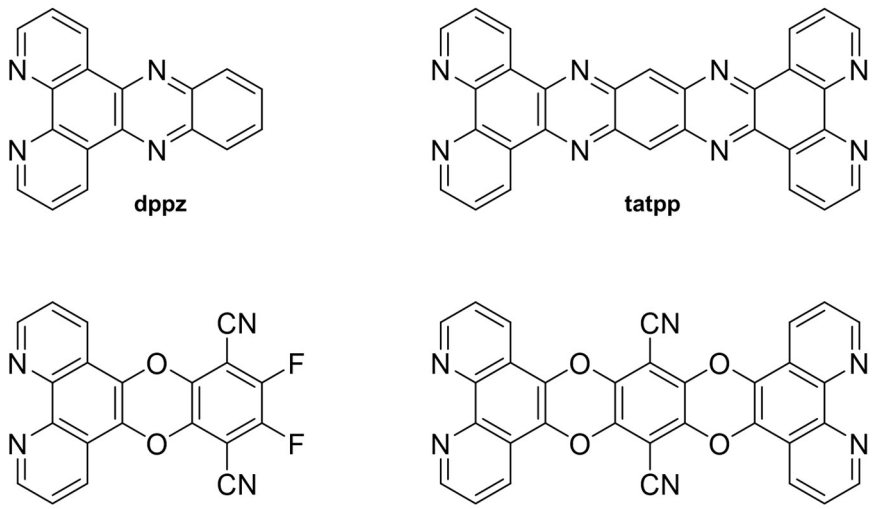

Figure 5.3: Structures of chelating ligands dppz and tatpp alongside the hypothetical structures of dicyanodibenzodioxin ligands.

The ligands dppz and tatpp have been very well reported in the literature, particularly in the context of ruthenium(II) coordination chemistry. Examples of ruthenium(II) complexes with these ligands are shown in Figure 5.4. As shown in the figure, the ligand tatpp can be used to bridge two ruthenium(II) complexes, something which may also be possible with the dicyanodibenzodioxin analogue. The complexes shown were reported in 2017 as part of a series of ruthenium(II) polypyridyl complexes investigated for their biological activity.[12] Polypyridyl dppz complexes of ruthenium(II) are of particular interest as these species have previously been shown to exhibit selective cytotoxicity toward cancer cell lines and have shown antitumor activity *in vivo*.[13] Importantly, these complexes can also act as luminescent probes for DNA as they show enhanced luminescence when intercalated into the DNA double-helix or when in organic solvents, but do not luminesce in water in the absence of DNA.[14,15]

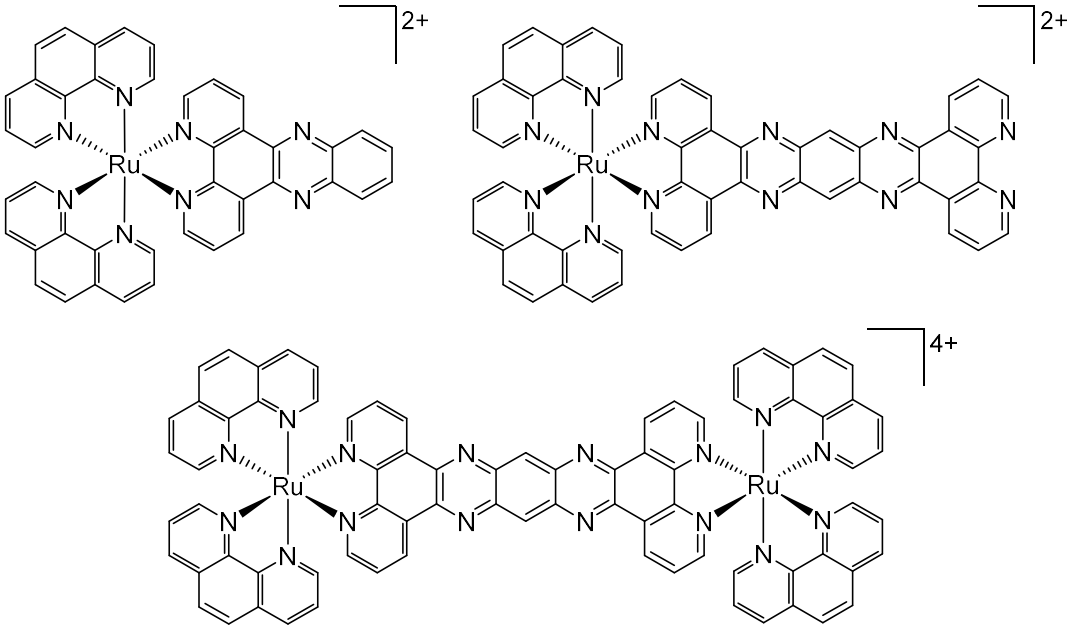

Figure 5.4: Examples of ruthenium(II) complexes with dppz and tatpp ligands.[12]

The ligand dppz has also been reported as a ligand in a tricarbonyl rhenium(I) complex. In 2008, the complex *fac*-[Re(CO)$_3$(dppz)Cl] was synthesised as part of a series of rhenium(I) tricarbonyl complexes with functionalised dppz ligands.[16] There are currently no reports of tatpp used as a ligand in mononuclear or dinuclear rhenium(I) tricarbonyl complexes in the primary literature, however their structures are also shown in Figure 5.5 for illustration.

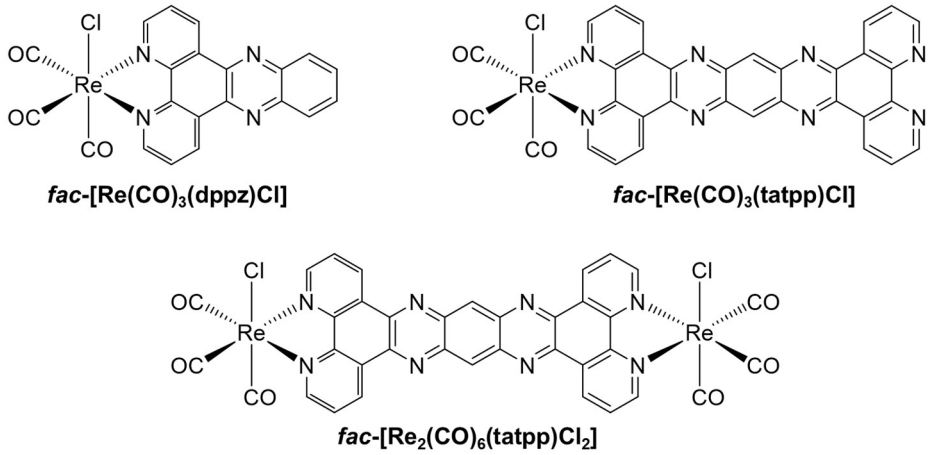

Figure 5.5: Rhenium(I) tricarbonyl complexes bearing dppz and hypothetical tatpp based structures.

5.1.2. Rhenium(I)

Like iridium(III) and ruthenium(II), rhenium(I) has a d^6 electron configuration.[17] Literature has shown that complexes of the form *fac*-$[Re(N^N)(CO)_3(L)]^{n+}$ (where N^N = a diimine ligand, L = monodentate ligand and n = 0 or 1) can exhibit phosphorescence at room temperature.[18–20] Emission from these complexes is typically assigned as arising from a ^{3}MLCT state.[21] The energy gap between the d orbitals of the rhenium centre and the π^* orbitals from the ligands is relatively small due to the large amount of back-bonding from the carbonyl ligands.[17] As a result of this, emission from this state is generally low in energy with emission usually occurring in the yellow-orange-red range of the visible spectrum. The lifetimes observed have been found to be in the range of $10^2 – 10^{-1}$ µs range, which is consistent with a triplet emitting state.[17]

Some of the simplest complexes of the formula *fac*-$[Re(N^N)(CO)_3(L)]^{n+}$ are shown below in Figure 5.6 along with some of their photophysical properties. The diimine used in the complex on the left is 2,2'-bipyridine, bpy, and when used as a ligand in a tricarbonylrhenium(I) complex results in an emission wavelength of 642 nm in DCM.[22] The complex in the centre of the figure has a 1,10-phenanthroline, phen, ligand. This complex has a shorter emission wavelength of 573 nm in acetonitrile, but has a much longer luminescent lifetime than the analogous bpy complex.[23] The final complex in the figure possesses a dipyridophenazine, dppz, ligand and has an emission wavelength of 600 nm and a luminescent lifetime of 0.04 µs, in degassed DCM, which is almost identical to that observed for the bpy complex.[24,25] From this, it can be determined that small changes to the structure of the diimine ligand can have a significant impact upon the photophysical properties of the complex as a whole.

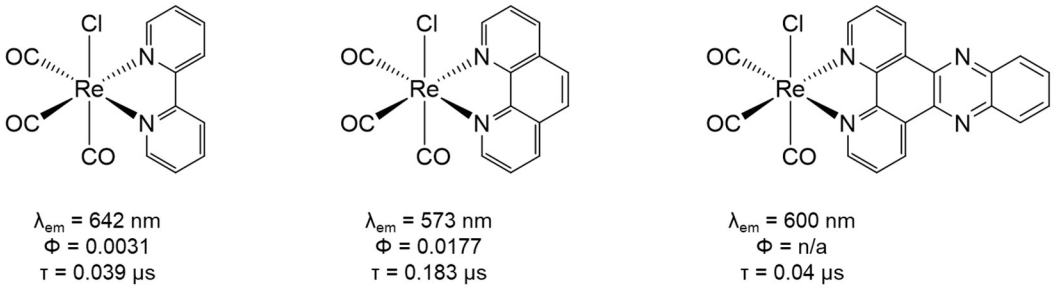

Figure 5.6: Structures and photophysical properties of simple tricarbonylrhenium(I) complexes. From left to right: [Re(bpy)(CO)$_3$Cl],[22] [Re(phen)(CO)$_3$Cl],[23] and [Re(dppz)(CO)$_3$Cl][24,25].

5.1.3. Rhenium Complexes in OLED Devices

Complexes of rhenium(I) have become of interest in many different applications. One of which is as a dopant in OLED devices. Rhenium complexes are not only attractive as dopants for their luminescent properties, but the neutral complexes can also be sublimed quite easily during the manufacturing process. The design of OLED devices has previously been discussed in detail in chapter three, but presented here are examples of rhenium(I) complexes designed for this purpose. The complex on the left of Figure 5.7 was reported by Chu *et al.* in 2014, which has a 1,10-phenanthroline diimine ligand and an axial [CNB(C_6F_5)$_3$] ligand, was used as a dopant in an electrochemical device that showed "sky-blue" emission at a wavelength of 538 nm.[26] The complex in the centre of the figure uses a functionalised 1,10-phenanthroline derivative as the diimine ligand to give a complex that has an emission wavelength of 570 nm.[27] The complex on the right of the figure was reported in 2006 and has a functionalised benzimidazole ligand and shows emission at 590 nm.[28]

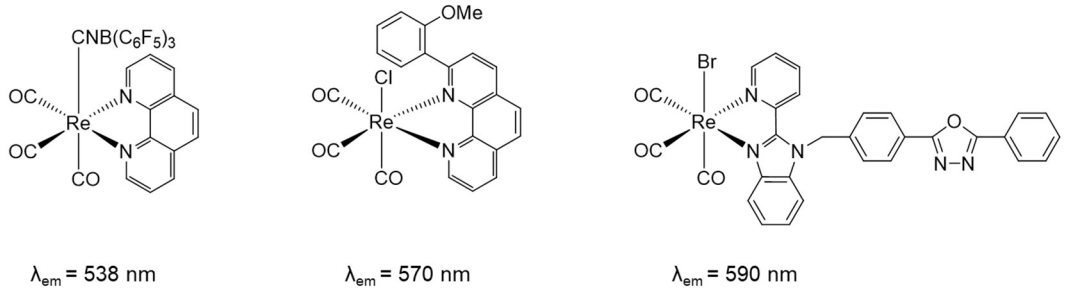

Figure 5.7: Examples of rhenium(I) complexes designed as OLED dopants.

5.1.4. Rhenium Complexes in Photocatalysis

Another application gathering extensive interest is the use of rhenium complexes as homogeneous catalysts in the reduction of CO_2 to CO. The photocatalytic activity of *fac*-[Re(bpy)(CO)$_3$Cl] was first reported by Hawecker *et al.* in 1986. The complex was found to be photocatalytic active after induction with visible light irradiation. The complex was also found to selectively reduce CO_2 to CO with the use of a tertiary amine as an electron donor.[29] Since then, other photocatalysts have been developed based upon similar complex structures. In 1996, Hori *et al*. reported that the complex *fac*-[Re(bpy)(CO)$_3${P(OEt)$_3$}]$^+$ showed improved

efficiency in the reduction of CO_2 compared to earlier catalysts which is believed to be due to the stability of the one-electron-reduced species *fac*-[Re(bpy$^{\cdot-}$)$(CO)_3${P$(OEt)_3$}].[30] A study in 2016 replaced the 2,2'-bipyridine ligand of the benchmark species *fac*-[Re(bpy)$(CO)_3$Br] with a series of pyridyl N-heterocyclic carbene ligands. The results showed that the complex *fac*-[Re(PyNHC-PhCF_3)$(CO)_3$Br] was able to outperform the benchmark species in the reduction of CO_2 both in the presence and in the absence of a photosensitiser species.[31]

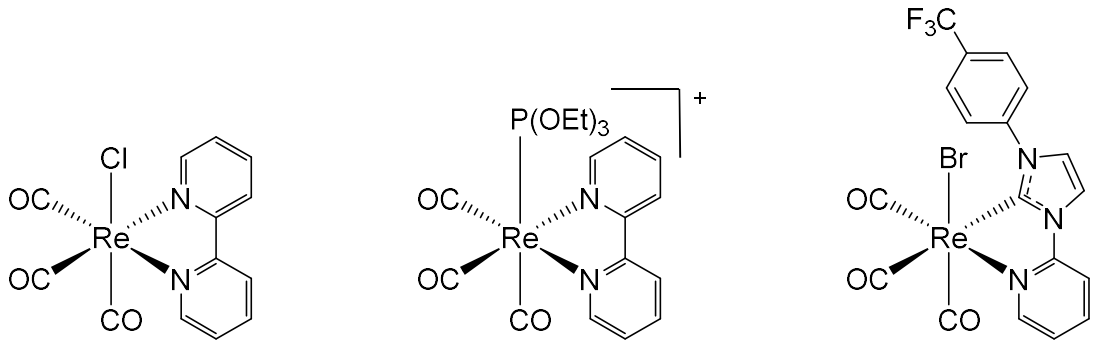

Figure 5.8: Structures of complexes used as photocatalysts for the reduction of CO_2 to CO. From left to right: [Re(bpy)$(CO)_3$Cl],[29] [Re(bpy)$(CO)_3${P$(OEt)_3$}],[30] and [Re(PyNHC-PhCF_3)$(CO)_3$Br].[31]

In recent years, the area of rhenium photocatalysts has diverged from the traditional 2,2'-bipyridine and 1,10-phenanthroline diimine ligands. Shown on the left of Figure 5.9 is part of a nanographene-rhenium complex synthesised in 2016 as a selective CO_2 reductant. The electron density is spread over the whole of the diimine ligand which lowers the electrical potential needed to drive the reaction. In addition to this, no photosensitiser is needed as the ligand absorbs a large range of the spectrum.[32] In 2019, a study published reports of a ruthenium(II)-rhenium(I) supramolecular photocatalyst for the reduction of CO_2. The bimetallic species used as part of the catalyst is shown on the right-hand side of Figure 5.9.[33]

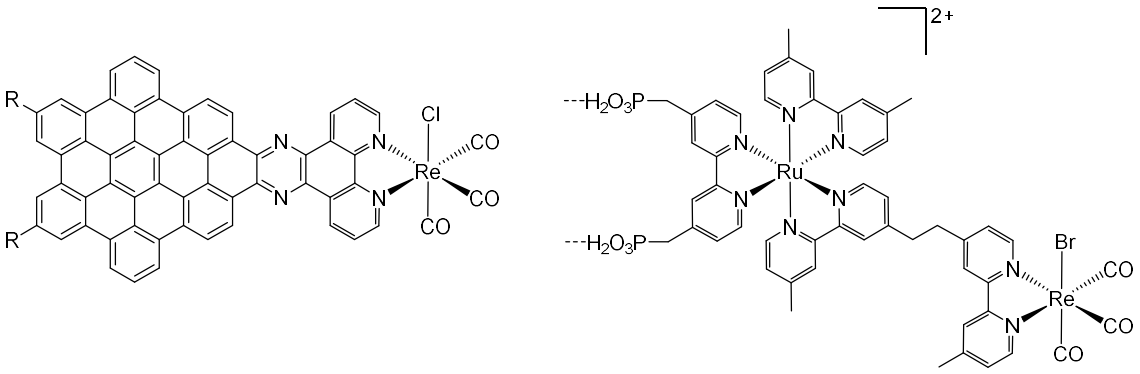

Figure 5.9: Recently published complexes for photocatalytic applications. Left) Nanographene-complexes reported by Qiao et al.[32] Right) Bimetallic Ru(II)-Re(I) complex used as part of a supramolecular photocatalyst by Kamata et al.[33]

5.1.5. Rhenium Complexes in Bioimaging

The field of bioimaging has also benefitted greatly from the development of luminescent rhenium(I) complexes. The large Stokes shift associated with these complexes overcomes the issue of auto fluorescence, while the low spin d^6 nature of tricarbonylrhenium(I) complexes makes them kinetically inert and so unlikely to interact with DNA. The first major study of tricarbonylrhenium(I) bisimine complexes as imaging agents was published in 2007 by Amoroso and Coogan *et al.*[34] A series of complexes of the form *fac*-$[Re(bisim)L(CO)_3]^+$ were synthesised, where bisim is a bisimine and L is pyridine or a derivative. Two examples of the complexes studied are shown in Figure 5.10. The complexes showed emission at around 550 nm which allows autofluorescence to be filtered out when imaging. In addition to this, the sulfonated complex shown in the figure showed very low toxicity, showing that complexes of this type may be promising future imaging agents.

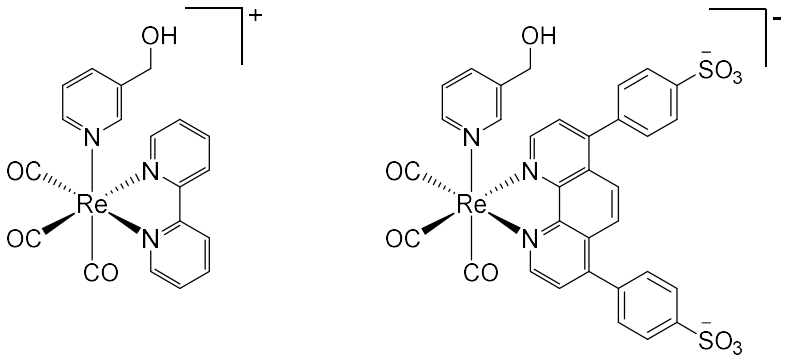

Figure 5.10: Some of the first examples of tricarbonylrhenium(I) complexes studied as biological imaging agents reported.[34]

Other developments in the field of bioimaging include the incorporation of biological substrates into the structure of the rhenium(I) complex. Work published by Lo *et al.* in 2015 describes three examples of cationic tricarbonylrhenium(I) complexes that incorporate the biological substrates into the structure through functionalisation of the axial pyridine ligand.[35] The biological substrates incorporated into the structure include estradiol, indole and biotin (Figure 5.11, clockwise from top). The aim of the study was to investigate how the photophysical properties of these complexes change upon binding of the biological substrate to its receptor. Common organic biotin-fluorophore compounds exhibit self-quenching upon binding to the avidin receptor, but this was not observed in the biotin-rhenium complex shown in Figure 5.11. In addition to this, it was found that the estradiol complex showed increased luminescence intensity and longer luminescent lifetime upon binding to estrogen receptors. As estrogen receptor content helps to provide accurate information on the index of hormone-dependent breast cancer,[36] this complex could have applications as an imaging agent for estrogen receptor-positive breast cancer.

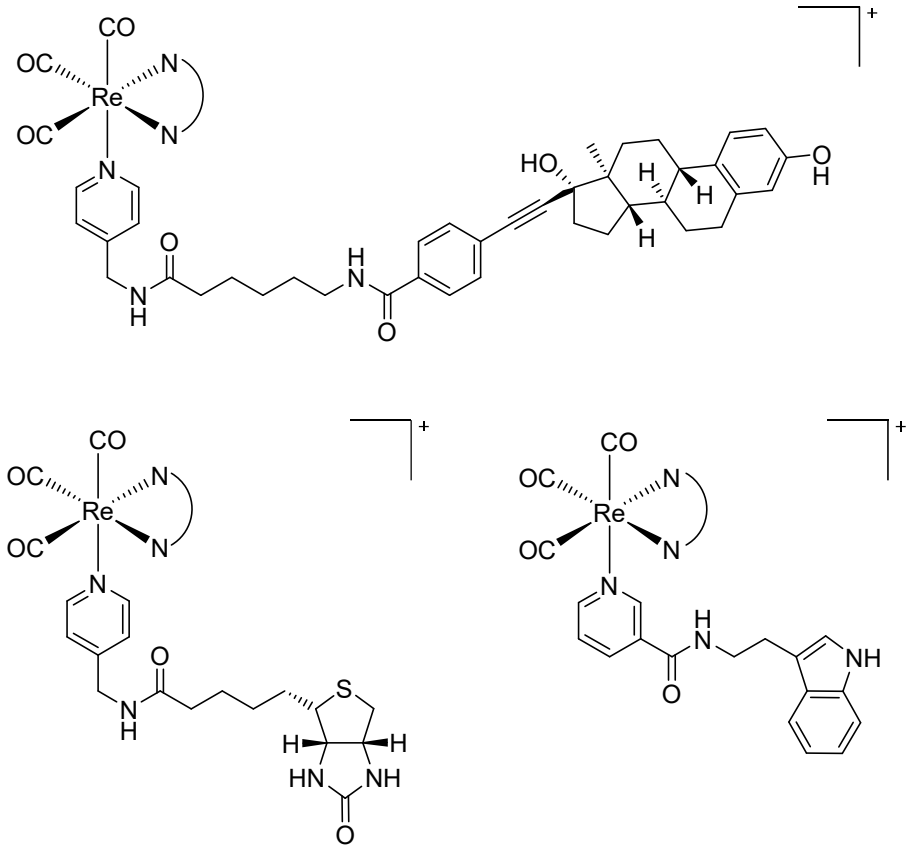

Figure 5.11: Biological imaging agents of Re(I) incorporating biological substrates.

More recent examples of tricarbonylrhenium(I) complexes are shown in Figure 5.12. The complex on the left was reported in 2017 by Langdon-Jones *et al.* The complex features an un-substituted 1,10-phenanthroline diimine ligand and has a 1,8-naphthalimide derivative in the axial position. The 1,8-naphthalimide-based ligand is fluorescent and depending upon the substituents, the emission from the complex as a whole can be modulated between ^{3}MLCT centred and ligand centred processes. This complex was found to be a viable cell imaging agent when tested with fission yeast cells.[37] The complex on the right of the figure was reported in 2019 and was found to have anti-cancer properties in addition to bioimaging applications. The complex was part of a study using non-steroidal anti-inflammatory drugs as the axial ligands in tricarbonylrhenium(I) complex systems. The complex shown uses aspirin as the axial ligand and was the only complex in the study that showed activity against cancer cell lines. The complex also showed no activity against non-tumorous mouse cells. Once inside the HeLa cell, the complex dissociates and produces the phosphorescent species $[Re(CO)_3(phen)]^+$ which accumulates in the mitochondria and was found to reversibly bind to hen egg white lysozyme (HEWL). The dissociated aspirin then inhibits the enzyme COX-2.[38]

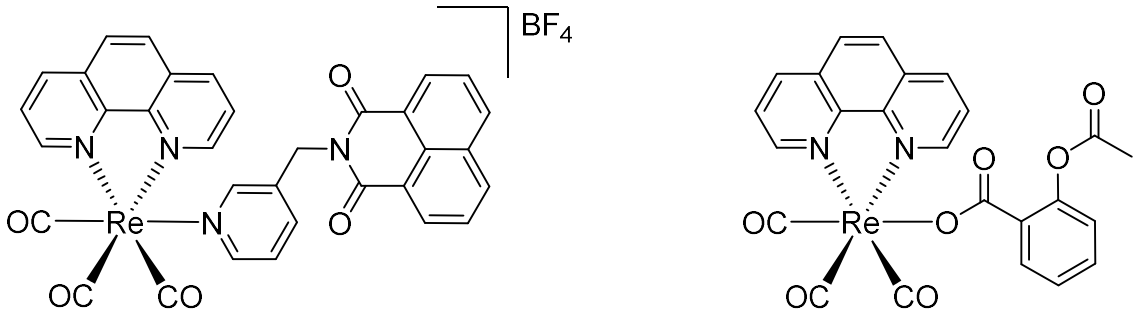

Figure 5.12: Rhenium(I) complexes developed as bioimaging agents.[37,38]

This work discussed here sets a precedent for the inclusion of biologically active compounds into the structure of luminescent inorganic complexes. Further work in this field could therefore include the incorporation of potentially cytotoxic compounds such as dicyanodibenzodioxins into rhenium complexes, and the possibility of dual action therapeutic and luminescence properties.

5.2. Aims

The aim of this work was to investigate synthetic pathways to a series of fluorescent dicyanobenzodioxin compounds that also demonstrate an ability to act as ligands. A metal coordination site was incorporated into these ligands by use of a conjugated 1,10-phenanthroline moiety to give a series of compounds with proposed structures of close similarity to ligands based upon dppz.

These new dicyanobenzodioxin-based ligands were then to be coordinated to rhenium(I) to give complexes of the formulation *fac*-[$Re(CO)_3(L)Br$] and to fully investigate the photophysical properties of these complexes. In addition to this, exchange of the axial bromide ligand in these complexes was to be carried out in order to form cationically charged species that optimise solubility characteristics.

5.3. Results and Discussion

5.3.1. Synthesis and characterisation of dicyanobenzodioxins

In this study, a series of four target compounds based upon the dicyanobenzodioxin core were synthesised and their photophysical properties investigated.

The first step in the synthesis of these compounds was the oxidation of 1,10-phenanthroline to 1,10-phenanthroline-5,6-dione following a procedure from literature.[39] This step was followed by a reduction to the corresponding diol form using hydrazine as the reductant (Scheme 5.3). This species can quickly oxidise in air and so is immediately used in the following step without further characterisation.

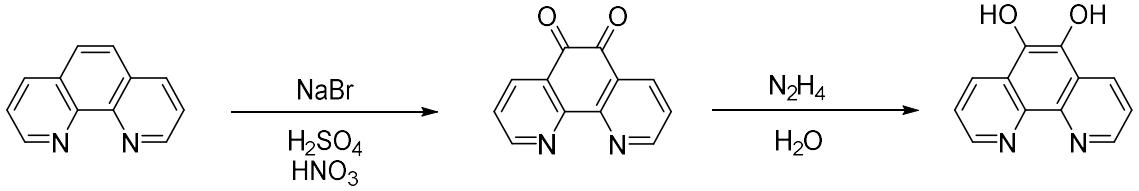

Scheme 5.3: Synthesis of 1,10-phenanthroline-5,6-diol from 1,10-phenanthroline.

In the next step, 1,10-phenanthroline-5,6-diol, was then dissolved in DMF and reacted with tetrafluoroterephthalonitrile (TFTPN) in the presence of potassium carbonate to form ligand **L1** (Scheme 5.4) as a bright green solid in 80% yield The product precipitated out of solution and so was collected by filtration and washed with water to remove excess K_2CO_3 with no further purification necessary. **L1** is a ligand in its own right, but also a valuable precursor to asymmetric dicyanobenzodioxin based ligands.

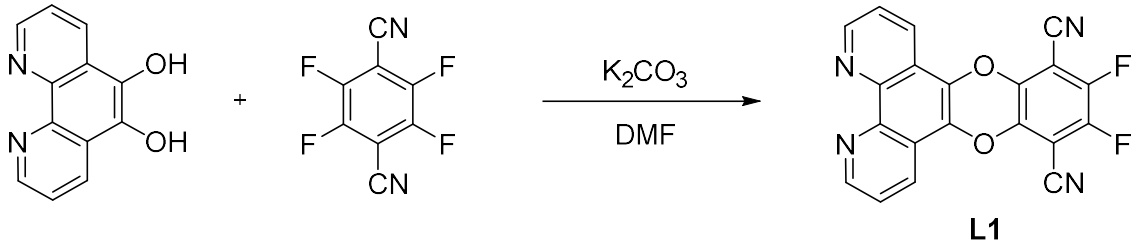

Scheme 5.4: Synthesis of ligand L1 from 1,10-phenanthroline-5,6-diol.

L1 was fully characterised by proton, carbon and fluorine NMR spectroscopy in addition to HRMS and IR spectroscopy. This section will discuss the analysis in detail. Figure 5.13 shows the proton NMR spectrum recorded for L1 in deuterated DMSO, with the proton assignments shown circled. The proton environment nearest to the nitrogen heteroatoms appears most downfield as a doublet at around 9.2 ppm. The splitting of the signal at around 8.0 ppm suggests it arises from the proton environment circled in red on the ligand, with the doublet at around 8.45 ppm arising from the final proton environment. When comparing these observations with the spectrum recorded for the 1,10-phenanthroline-5,6-dione precursor, a downfield shift of each proton environment is seen. The largest of these shifts occurs for the environment circled in red, which appears at 7.59 ppm in the dione species but is centred around 7.95 ppm in L1. As both the precursor and the product have the same number of protons and proton environments, the downfield shifts observed are indicative of the formation of the product.

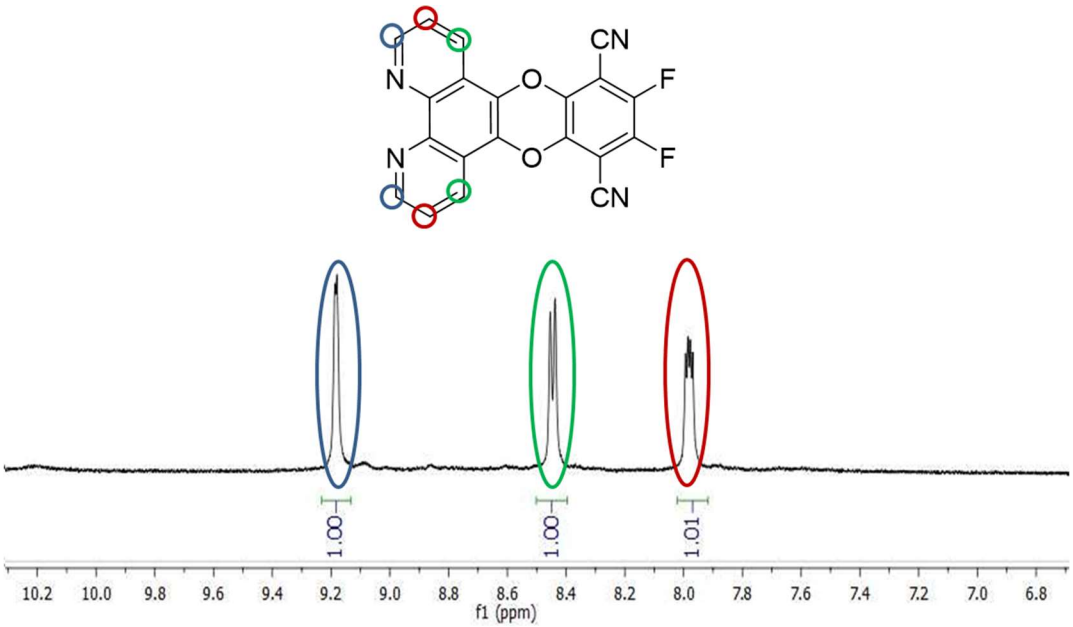

Figure 5.13: Proton NMR spectrum recorded for ligand L1 in deuterated DMSO with assignments for each proton (400 MHz).

The fluorine NMR spectrum shows a single signal at -132.30 ppm in deuterated DMSO. The signal is shifted upfield from that of the free tetrafluoroterephthalonitrile, which shows a single signal at -131.09 ppm in the same solvent. This shows that only one fluorinated species is present and that it is not the fluorinated starting material.

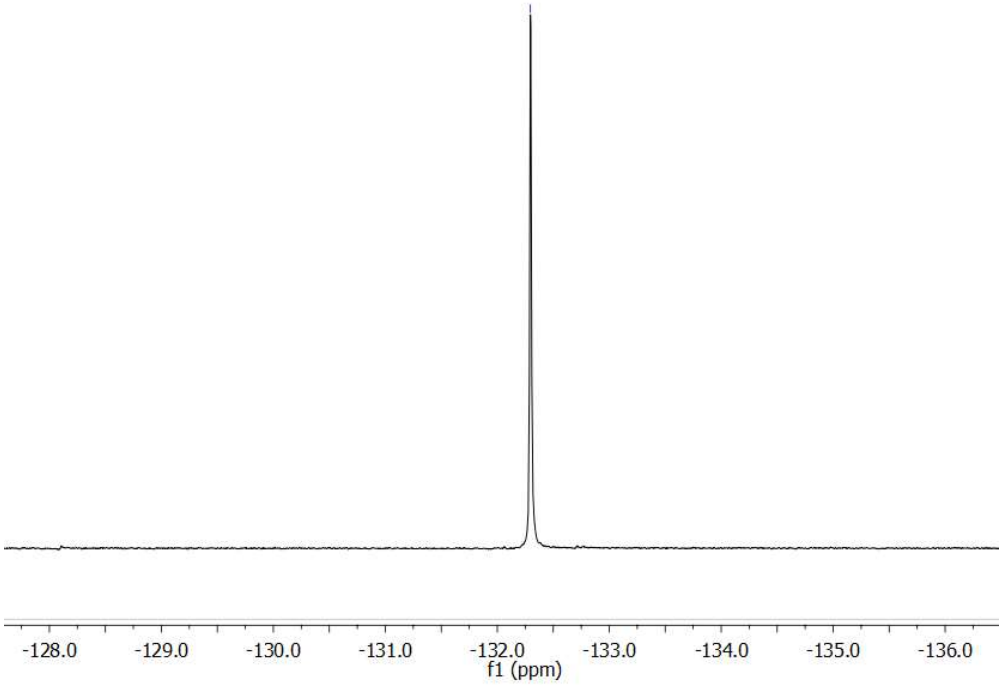

Figure 5.14: Fluorine NMR spectrum recorded for ligand L1 in deuterated DMSO (376 MHz).

The carbon NMR is shown in Figure 5.15, but was difficult to record due to the relatively poor solubility of L1 in organic solvents and as a result, the spectrum produced is very weak. The

number of peaks observed is consistent with the number of unique carbon environments in the compound, also a signal is observed at around 120 ppm which is consistent with a nitrile carbon environment.

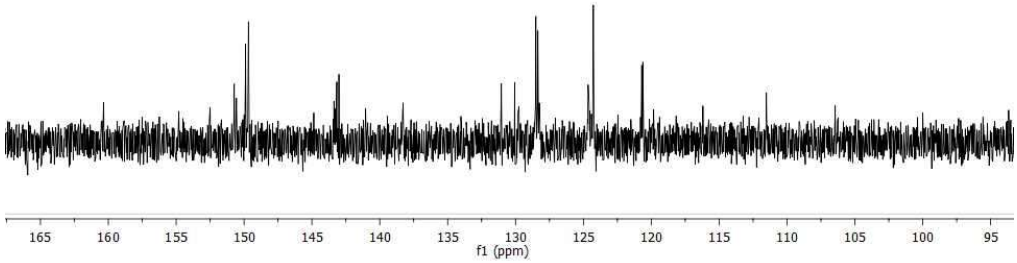

Figure 5.15: Carbon NMR spectrum recorded for ligand L1 in deuterated DMSO (126 MHz).

The IR spectrum recorded for ligand L1 is shown in Figure 5.16. The most distinctive feature in the spectrum is the relatively weak stretch at 2241 cm^{-1} is indicative of a C≡N stretch.

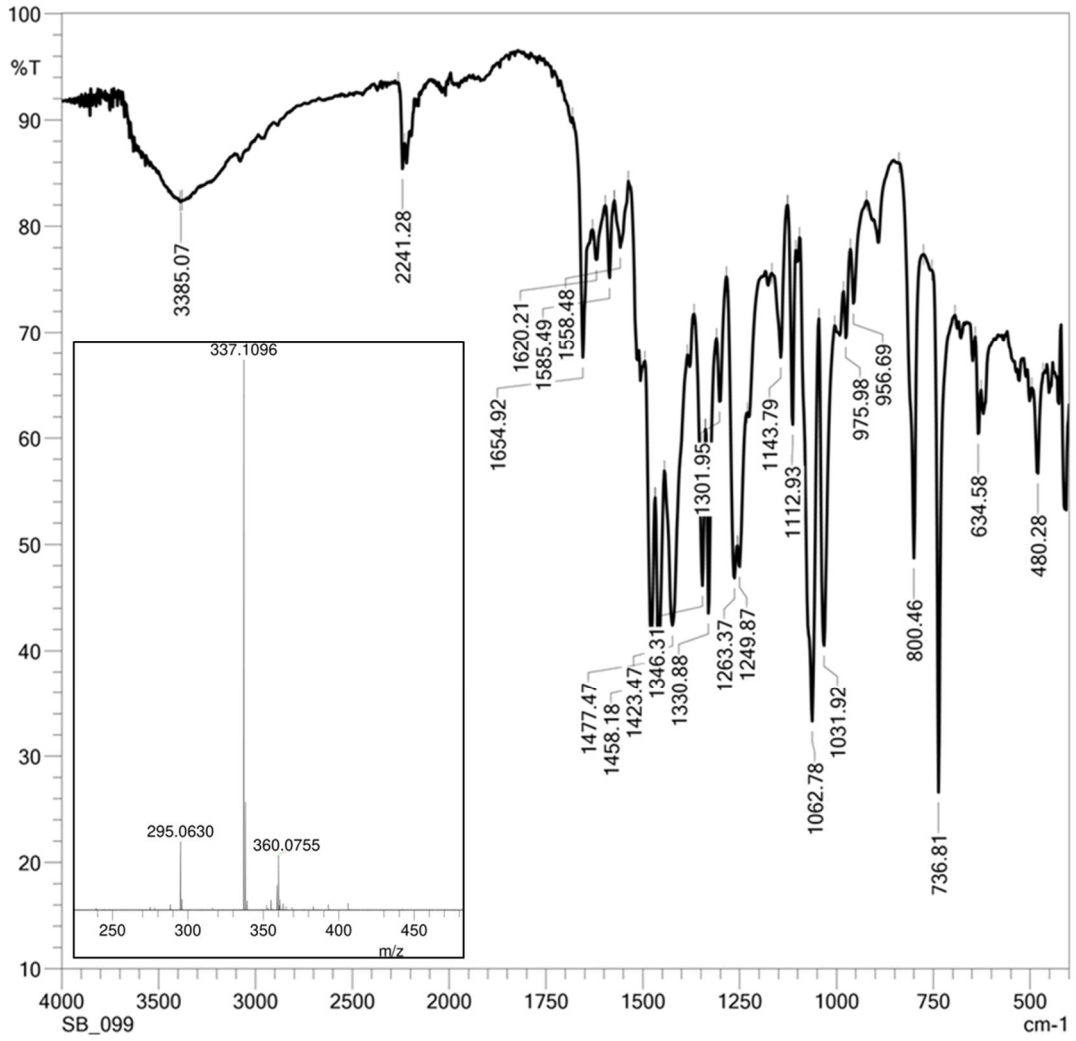

Figure 5.16: FTIR ATR spectrum recorded for ligand L1. Inset) HRMS (ASAP) data for L1 showing the molecular ion peak at 337.1096 amu.

The mass spectrometry data also correspond to synthesis of the desired compound L1. The inset of Figure 5.16 shows the high-resolution mass spectrometry data recorded for L1 showing the molecular ion peak present at 337.1096 amu. Therefore the characterisation is consistent with the proposed structure of ligand L1.

L1 was then used as the precursor for the synthesis of L2, L3 and L4. These were obtained by reacting L1 with the aromatic diols: catechol, 4-*tert*-butylcatechol and 2,3-dihydroxynaphthalene, respectively. Again, reaction in DMF with potassium carbonate yielded the ligands. The product of each reaction crashed out of a solution as a brightly coloured precipitate. Compounds L2 and L4 were green in colour, while ligand L3 was isolated as an orange solid.

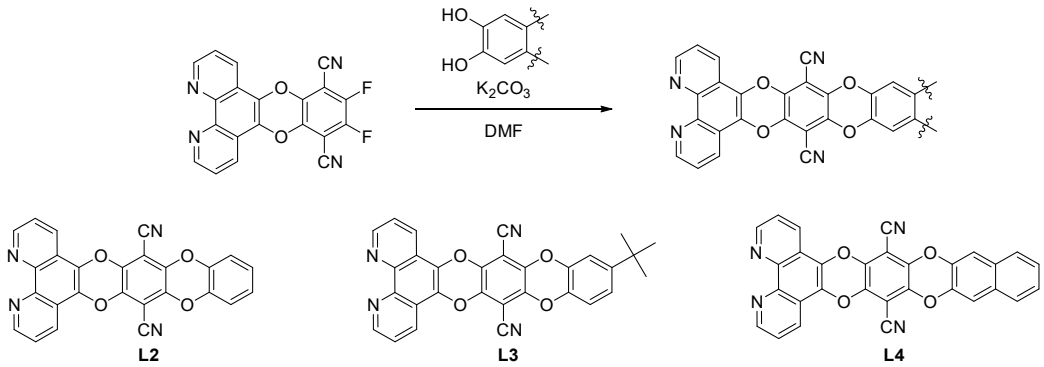

Scheme 5.5: Synthesis of ligands L2, L3 and L4.

The prepared compounds (Scheme 5.5), L1-4, each exhibited very poor solubility in common organic solvents. The planar structure of each molecule suggests that pi-stacking is most likely responsible for this property; this is also supported by L4, the most aromatic ligand, showing the least solubility. One impact of this limiting solubility is that it has not been possible to record good quality proton or carbon NMR data for L2, L3 and L4.

Figure 5.17 shows the proton NMR spectrum recorded for ligand L2 in deuterated DMSO. As the peaks do not rise significantly above the baseline, the integration of these signals is unreliable. The spectrum shows the same three signals as seen in the spectrum of L1, as expected, along with an additional multiplet signal at 7.19 ppm arising from the catechol moiety. It can be assumed that both starting materials, L1 and catechol, have been consumed in the reaction as they exhibit good solubility in DMSO and would result in much more intense peaks in the NMR spectrum. In addition to this, the absence of signals in the fluorine NMR spectrum suggests that there is no residual L1 remaining.

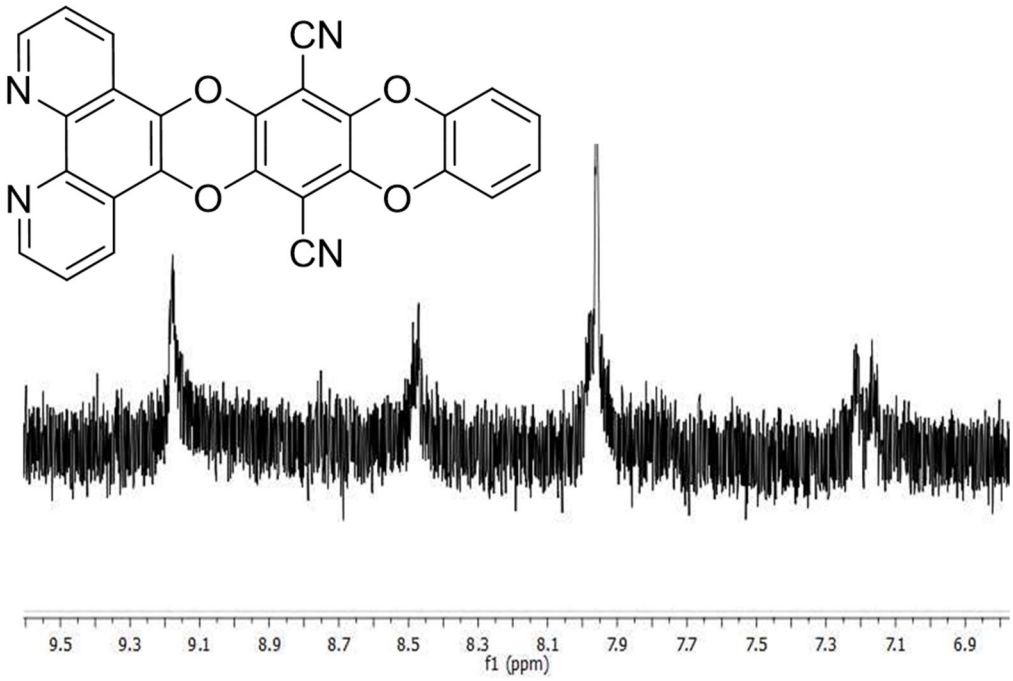

Figure 5.17: Proton NMR spectrum recorded for ligand L2 in deuterated DMSO.

It was not possible to obtain a proton NMR spectrum for ligand L3, however a very weak spectrum was recorded for ligand L4 using a 600 MHz instrument and recorded over 1024 scans. The spectrum showed no sign of excess starting material, however a number of very weak signals are present near the baseline which are possibly due to the formation of aggregates. A more intense set of signals is present in the aromatic region of the spectrum which together integrate correctly to the target compound. The proton NMR spectrum alone does not confirm confidently that the desired product has been synthesised, however in combination with the absence of signals in the fluorine NMR, it provides evidence that the starting materials, L1 and 2,3-dihydroxynaphthalene, have been consumed.

Therefore, in addition to NMR spectroscopy, high resolution mass spectrometry was employed to confirm the presence of the molecular ion peak. This was found to be present in the cases of L1, L2 and L3. The mass spectrum of ligand L2 is shown in Figure 5.18, where the [M + H] peak can be seen, it is also worth noting the absence of peaks corresponding to the starting material, L1.

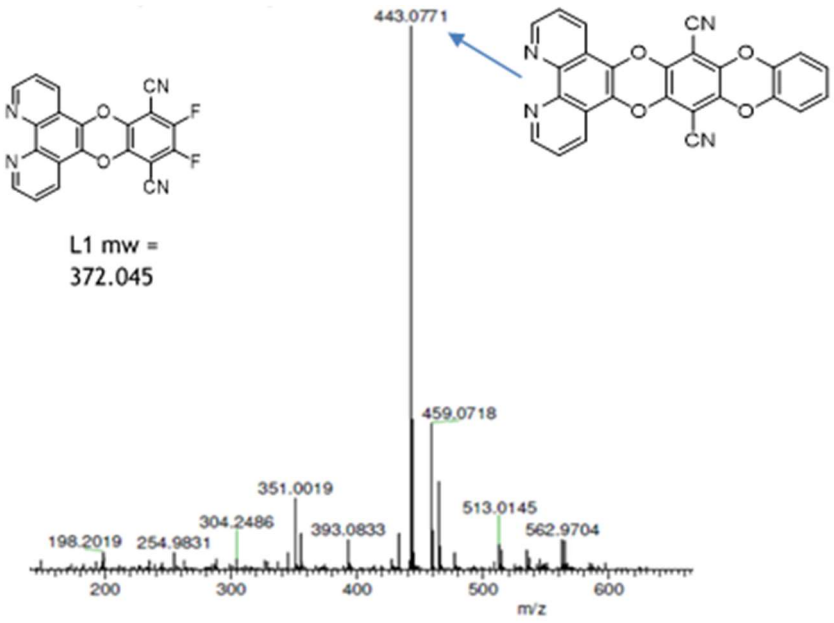

Figure 5.18: High resolution mass spectrum recorded for ligand L2 showing [M + H] peak. Peak for starting material is absent.

The poor solubility of ligand L4 also made recording mass spectrometry data difficult. The high-resolution mass spectrum recorded showed that the molecular ion peak is not present, but the starting material is also absent from the spectrum. A number of peaks with a higher mass value than that of the molecular ion were present, suggesting that the ligand may form adducts with other species in the spectrometer.

From this data it is possible to confirm the synthesis of ligands L1, L2 and L3. The data recorded for ligand L4 suggets that the starting materials are not present in the final product, however NMR spectroscopy and mass spectrometry have proved unsuccessful in confirming the presence of target compound L4.

Infra-red spectroscopy was used to identify the position of the nitrile stretches in each compound. These stretches are typically observed at between 2260 – 2220 cm^{-1} and appear with medium intensity. Table 5.1 lists the position of these signals for each ligand L1 - L4. It was not

possible to observe a nitrile stretch in the IR spectrum of ligand L3, however the mass spectrometry data is consistent with formation of the target product. Meanwhile, a nitrile stretch is present in the IR spectrum of ligand L4, meaning that while it is not possible to be certain of the structure of this compound, there are clearly nitrile groups present.

Table 5.1: Positions of nitrile stretch in infrared spectrum for ligands L1 - L4.

Ligand	**CN Stretch/ cm^{-1}**
L1	2241
L2	2237
L3	n/a
L4	2241

As discussed previously, the aim of this chapter was also to synthesise ligands with similar structure to the well-studied ligands dppz and tattp. The ligands L1 – L4 have a related structure to dppz, but to synthesise a ligand analogous to tattp, two metal coordination sites are required. Synthesis of a such a ligand was attempted using two equivalents of 1,10-phenanthroline-5,6-diol and one equivalent of tetrafluoroterephthalonitrile (Scheme 5.6). Analysis of the product of the reaction showed that only one equivalent of the diol species had reacted to give **L1**.

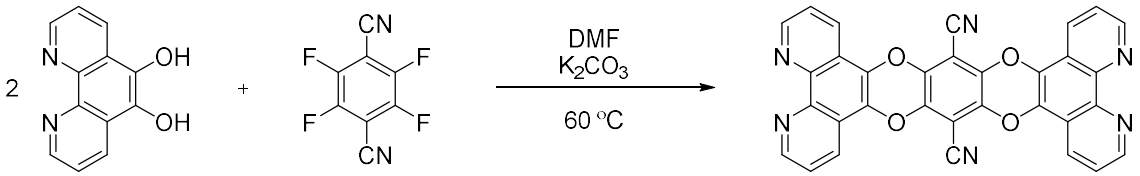

Scheme 5.6: Proposed synthetic route to tattp dicyanodibenzodioxin analogue.

A second attempt was made to isolate the bridging dicyanodibenzodioxin ligand using **L1** as a starting material with a further equivalent of 1,10-phenanthroline-5,6-diol (Scheme 5.7), but disappointingly no reaction was observed and **L1** was recovered. Although the reasons for this are currently unclear it may be that the limiting solubility of L1 in the solvent conditions is preventing efficient reaction.

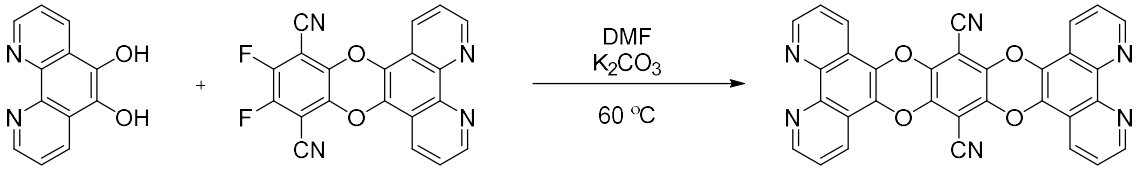

Scheme 5.7: Alternative route to bridging dicyanodibenzodioxin ligand.

As a result of this exploratory work, the focus of this work shifted to the coordination chemistry of ligands L1 - L4 only.

5.3.2. Coordination chemistry with rhenium(I)

Although the poor solubility of L1-L4 was noted, these four compounds were further investigated as ligands in rhenium(I) coordination chemistry. Each ligand was reacted in toluene at reflux in the presence of $[Re(CO)_5Br]$ and yielded a final complex of the form $[Re(CO)_3(L)Br]$.The synthesis of these complexes is shown in Scheme 5.8.

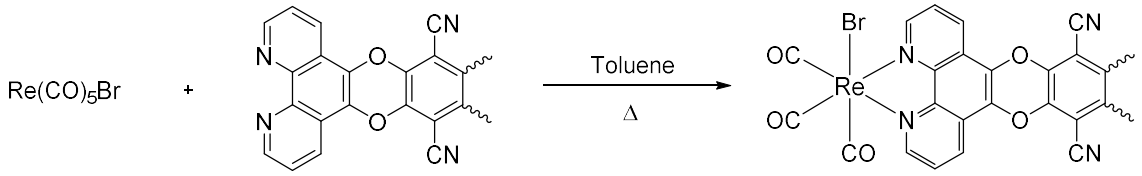

Scheme 5.8: Synthesis of rhenium complex from dioxin ligand.

The Re(I) complexes precipitated out of the reaction solution and were obtained in high yield by filtration. The proposed structures of these complexes are shown in Figure 5.19. The complexes were collected as brightly coloured powders ranging from green to orange in appearance.

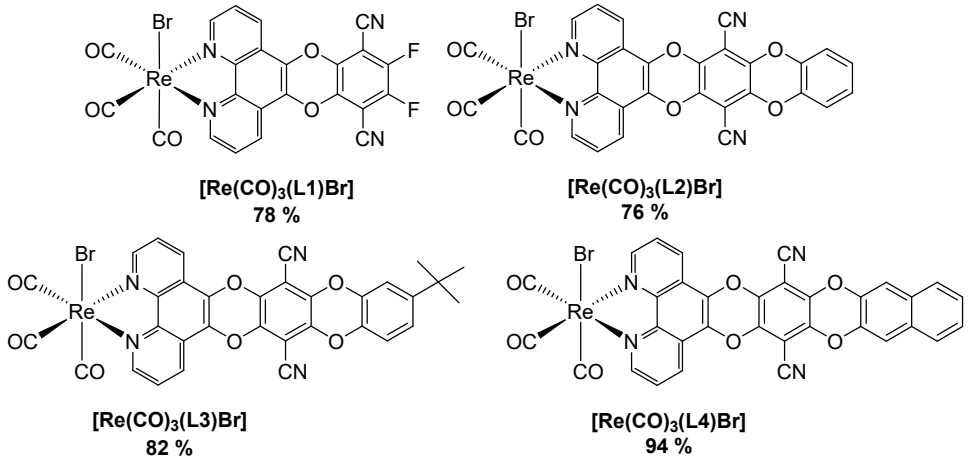

Figure 5.19: Structures and yields of tricarbonylrhenium complexes synthesised.

The four complexes were characterised by NMR spectroscopy, mass spectrometry and infrared spectroscopy. The NMR data collected from the complexes was of better quality than that collected for the free ligands due to improved solubility characteristics. The proton NMR spectrum shown in Figure 5.20 is that recorded for *fac*-$[Re(CO)_3(L3)Br]$. The spectrum shows clear peaks which integrate correctly to the number of protons in the complex. This is in great contrast with the free ligand, for which it was not possible to record a proton spectrum.

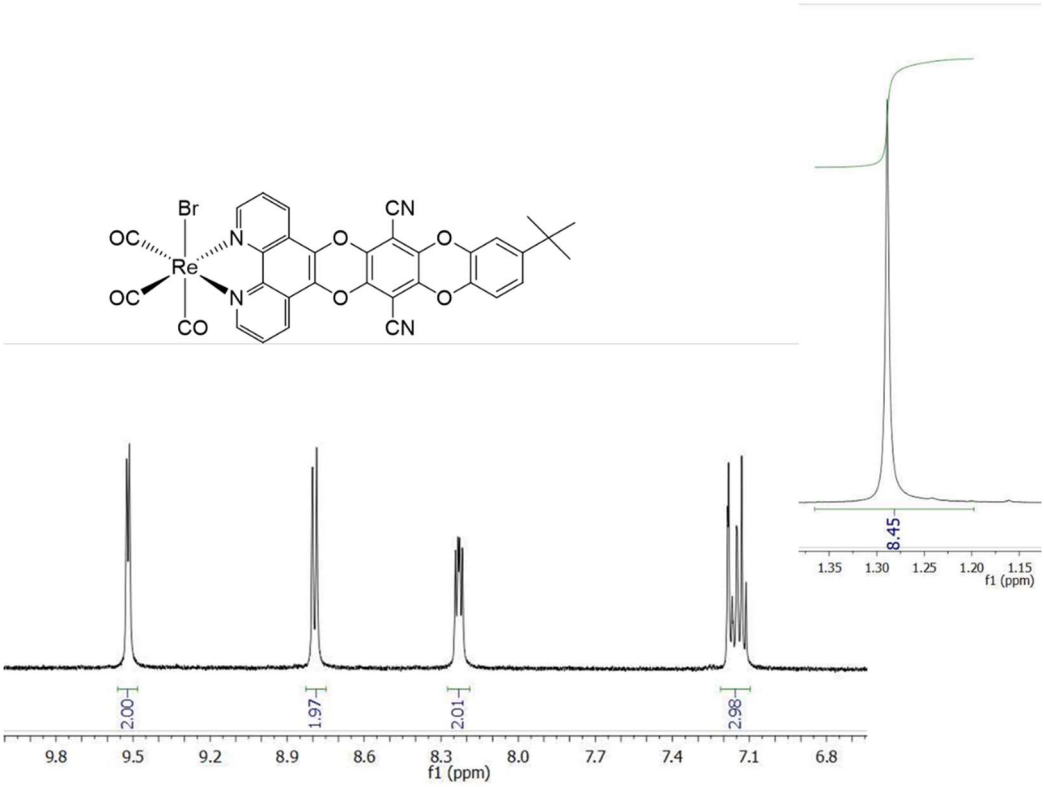

Figure 5.20: Proton NMR spectrum recorded for [Re(CO)$_3$(L3)Br].

The improved solubility of the complexes over their free ligands meant it was possible to obtain proton NMR data for every complex, however in the case of *fac*-[Re(CO)$_3$(L4)Br] the spectrum was still very weak due the low solubility of the complex. It was not possible to obtain carbon NMR data for any of the four complexes synthesised.

High resolution mass spectrometry was performed on each complex which was able to identify the sodium adduct of the molecular ion. Shown in Figure 5.21 is the high-resolution mass spectrum of complex *fac*-[Re(CO)$_3$(L1)Br]. The parent peak corresponds to [M + Na] and the peaks at lower amu values are fragments which do not correspond to either starting material.

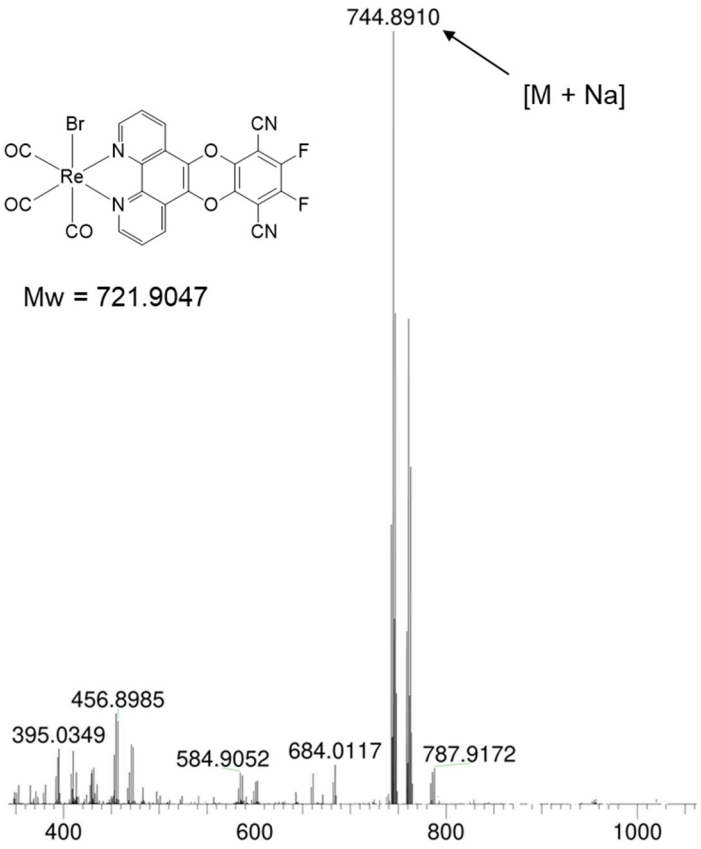

Figure 5.21: High-resolution mass spectrum of complex [Re(CO)$_3$(L1)Br] showing sodium adduct, [M + Na].

The complexes were also analysed using infrared spectroscopy. The nitrile stretch is no longer observable in the spectra, likely due to the much higher relative intensity of the carbonyl stretches in each complex. The position of the carbonyl stretches for each complex are shown in Table 5.2.

Table 5.2: Position of metal carbonyl stretches in the neutral rhenium complexes with dicyanodibenzodioxin ligands.

Complex	**CO stretch/ cm^{-1}**
[Re(CO)$_3$(L1)Br]	2031, 1929, 1877
[Re(CO)$_3$(L2)Br]	2019, 1902br
[Re(CO)$_3$(L3)Br]	2029, 1925, 1879
[Re(CO)$_3$(L4)Br]	2021, 1886br

The data shows that the complexes with ligands L2 and L4 show two carbonyl stretches, while the complexes with ligands L1 and L3 show three stretches. The coordination sphere of each neutral complex has a C_s symmetry and therefore, three carbonyl stretches are predicted in the IR spectrum (2A' + A''). Three stretches are observed in the case of complexes *fac*-[Re(CO)$_3$(L1)Br] and *fac*-[Re(CO)$_3$(L3)Br] with values that compare well with literature complexes of a similar structure.[40] The complexes with ligands L2 and L4 show only two stretches. In each

case, the lower energy stretch is broader than the one higher in energy suggesting it is composed of two overlapping stretches.

Full characterisation of the free ligands and of the neutral Re(I) complexes was not possible due to the limiting solubility of these species. In an attempt to further improve the solubility, the four neutral complexes were converted to their cationic analogues by exchanging the axial bromide ligand for an acetonitrile ligand following the synthesis route in Scheme 5.9. Here, acetonitrile was used as the solvent in the reaction; the silver tetrafloroborate, $AgBF_4$, was used to abstract the bromide ion to form AgBr while the BF_4^- ion becomes the counter ion for the cationic rhenium complex.

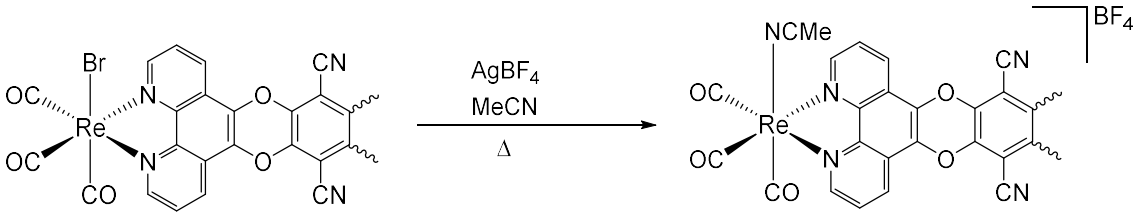

Scheme 5.9: Ligand exchange to give cationic complexes.

Following this route, four novel cationic complexes were isolated. The structures and yields of these complexes are shown in Figure 5.22. The isolated yields of these complexes were much lower than those of their neutral counterparts and vary largely between complexes. Higher yields were observed in cases where the neutral complex had better solubility in acetonitrile, as seen in the cases of complexes *fac*-$[Re(CO)_3(L1)(MeCN)][BF_4]$ and *fac*-$[Re(CO)_3(L3)(MeCN)][BF_4]$.

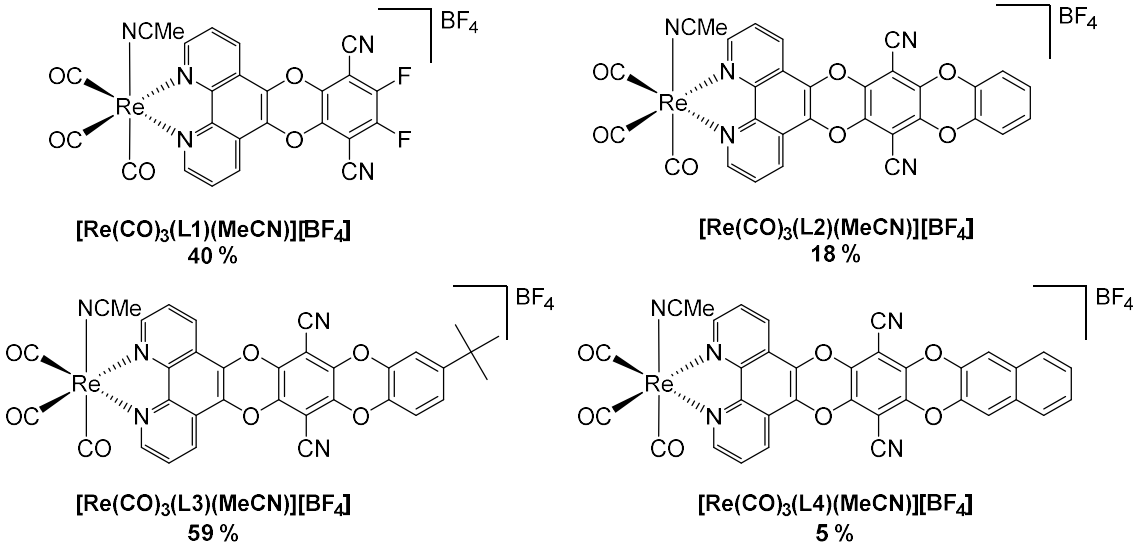

Figure 5.22: Structures and yields of cationic complexes with ligands L1 – L4.

This increased solubility resulted in higher quality proton NMR spectra and also meant it was possible to record carbon NMR data. Figure 5.23 shows the proton NMR recorded for complex *fac*-$[Re(CO)_3(L4)(MeCN)][BF_4]$.

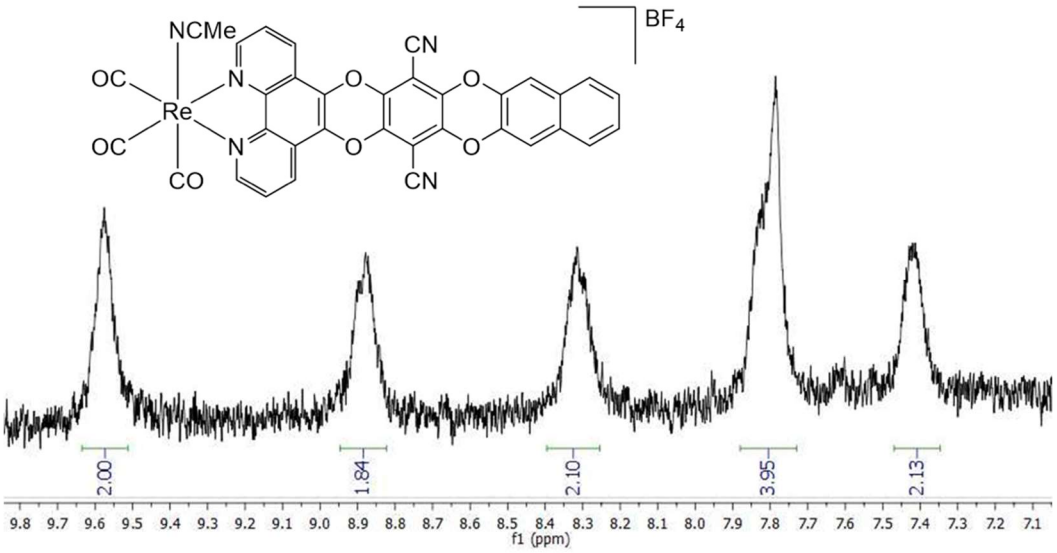

Figure 5.23: Proton NMR data for cationic complex $[Re(CO)_3(L4)(MeCN)][BF_4]$.

Carbon NMR data was collected for all complexes and the spectrum recorded for complex *fac*-$[Re(CO)_3(L3)(MeCN)][BF_4]$ is shown in Figure 5.24. The signal at 39.52 ppm is due to the deuterated DMSO. The *t*-butyl peaks can be clearly observed at 30.81 ($C(\mathbf{C}H_3)_3$) and 34.29 ($\mathbf{C}(CH_3)_3$) ppm respectively. Other signals of interest include the coordinated acetonitrile signals at 1.32 ppm and 93.58 ppm as well as a carbonyl peak arising at 195.72 ppm.

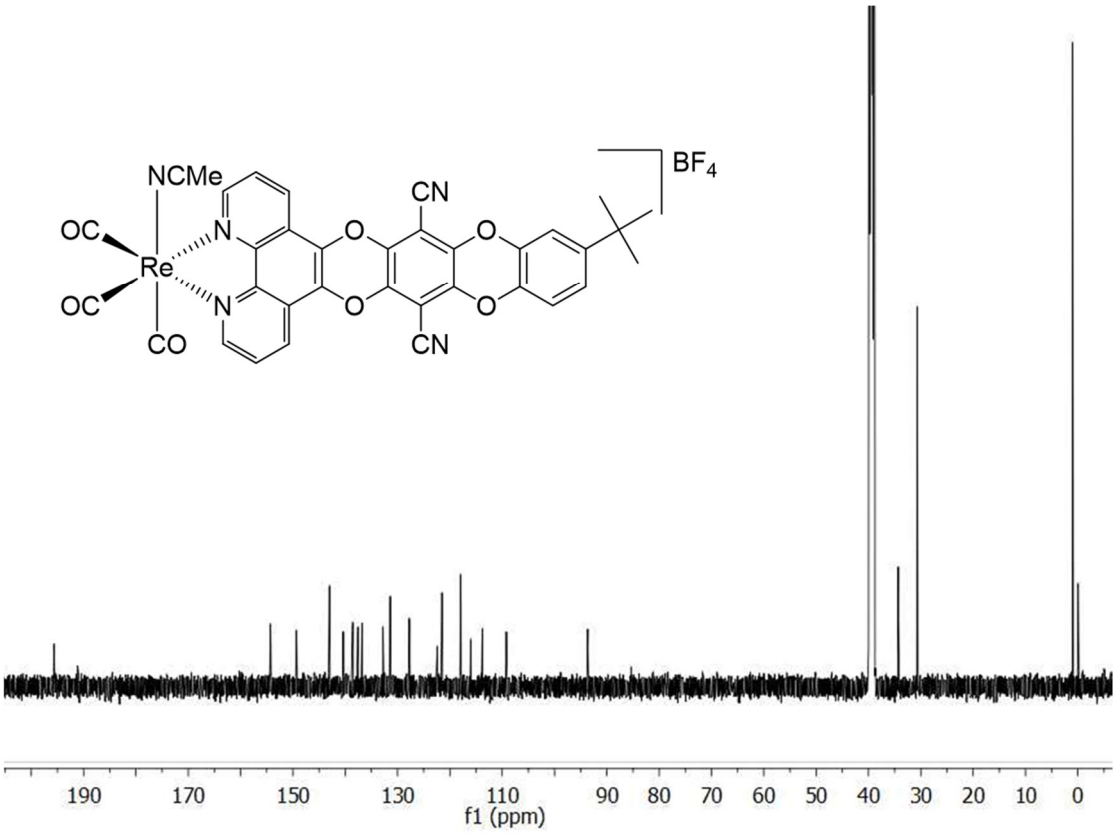

Figure 5.24: Carbon NMR spectrum recorded for complex $[Re(CO)_3(L3)(MeCN)][BF_4]$ in deuterated DMSO.

It was also possible to grow a good quality crystal for single crystal diffraction for the complex $[Re(CO)_3(L3)(MeCN)][BF_4]$. This crystal was grown *via* vapour diffusion of diisopropyl ether into a saturated acetonitrile solution of the complex.

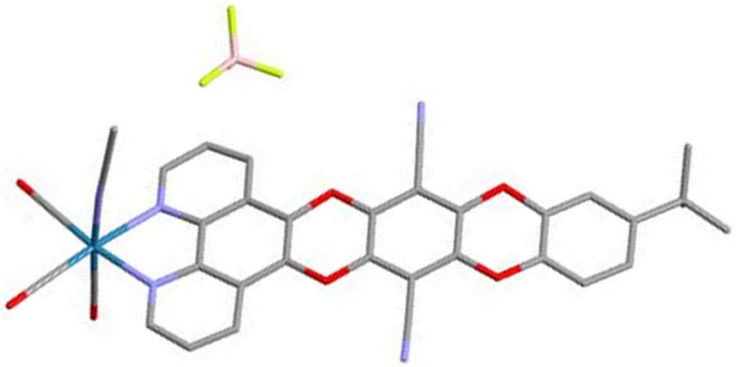

Figure 5.25: Crystal structure of complex $[Re(CO)_3(L3)(MeCN)][BF_4]$.

The structure recorded confirms that the target complex was synthesised. The following data tables show the bond lengths and bond angles of the coordination sphere. The rhenium – carbonyl bond lengths are around 1.91 – 1.94 Å and the rhenium – diimine bond lengths are between 2.17 – 2.18 Å which are consistent with literature reports of similar complexes.[40–42] In addition to this, the bite angle of the diimine ligand was measured at 76.20(8)˚ which compares closely with that measured for a phen ligand in a similar complex reported by Lo *et al.* in 2006.[41] It is also worth noting that the dicyanodibenzodioxin ligand is not completely planar, with the C_{CO}-Re-N angles measured at 172.19(9)˚ and 172.60(10)˚, making the geometry of the complex a distorted octahedron. This non-planarity has also been reported in tricarbonylrhenium(I) phen complexes.[42]

Table 5.3: Data collection parameters for complex $[Re(CO)_3(L3)(MeCN)][BF_4]$.

Formula	$C_{39}H_{27}B_{0.95}Br_{0.06}F_{3.77}N_7O_7Re$	***Z'***	1
$D_{calc.}$**/ g cm^{-3}**	1.699	**Wavelength/Å**	0.71075
***m*/mm^{-1}**	3.314	**Radiation type**	MoK_α
Formula Weight	978.21	Q_{min}**/°**	2.323
Colour	yellow	Q_{max}**/°**	27.483
Shape	block	**Measured Refl.**	88085
Size/mm^3	0.251×0.168×0.084	**Independent Refl.**	8767
***T*/K**	100(2)	**Reflections with I > 2(I)**	8428
Crystal System	triclinic	R_{int}	0.0237
Space Group	*P*-1	**Parameters**	548
***a*/Å**	8.68880(10)	**Restraints**	84
***b*/Å**	14.54320(10)	**Largest Peak**	2.158
***c*/Å**	16.6700(2)	**Deepest Hole**	-0.549
***a*/°**	106.8550(10)	**GooF**	1.092
***b*/°**	100.2890(10)	wR_2 **(all data)**	0.0600
***g*/°**	101.4630(10)	wR_2	0.0595
V/Å^3	1912.07(4)	R_1 **(all data)**	0.0244
Z	2	R_1	0.0231

Table 5.4: Selected bond lengths for the coordination sphere or complex $[Re(CO)_3(L3)(MeCN)][BF_4]$

Atom	**Atom**	**Length/Å**
Re(1)	N(1)	2.169(2)
Re(1)	N(2)	2.177(2)
Re(1)	N(41)	2.131(2)
Re(1)	C(31)	1.935(3)
Re(1)	C(32)	1.922(3)
Re(1)	C(33)	1.908(3)

Table 5.5: Selected bond angles in the coordination sphere of $[Re(CO)_3(L3)(MeCN)][BF_4]$

Atom	**Atom**	**Atom**	**Angle/°**
N(1)	Re(1)	N(2)	76.20(8)
N(41)	Re(1)	N(1)	82.64(8)
N(41)	Re(1)	N(2)	81.43(8)
C(31)	Re(1)	N(1)	172.19(9)
C(31)	Re(1)	N(2)	96.14(10)
C(31)	Re(1)	N(41)	94.83(11)
C(32)	Re(1)	N(1)	97.66(10)

C(32)	Re(1)	N(2)	172.60(10)
C(32)	Re(1)	N(41)	93.79(11)
C(32)	Re(1)	C(31)	89.87(12)
C(33)	Re(1)	N(1)	92.92(10)
C(33)	Re(1)	N(2)	95.72(10)
C(33)	Re(1)	N(41)	175.18(10)
C(33)	Re(1)	C(31)	89.33(12)
C(33)	Re(1)	C(32)	88.64(13)

These compounds were also analysed by IR spectroscopy and the results are shown in Table 5.6. The number of carbonyl stretches observed in each cationic complex is the same as in each neutral precursor. The coordination sphere of each of these complexes is pseudo C_{3v} in symmetry and as such, a total of two IR active stretches is predicted for each complex (A_1 + E). As observed in the neutral complexes, the cationic complexes with ligands L1 and L3 exhibit three IR carbonyl absorptions, which is likely due to the retention of the C_s symmetry exhibited by those complexes. The carbonyl stretches observed in the cationic complexes are higher in energy than those in the neutral complexes. This is because the d-orbitals in the cationic species are more diffuse resulting in a poorer overlap between the metal d orbitals and the antibonding orbital of the carbonyl ligand. The backbonding is weakened which strengthens the carbon – oxygen bond.

Table 5.6: Carbonyl infrared stretches for cationic rhenium complexes.

Complex	CO stretch/ cm^{-1}
$[Re(CO)_3(L1)(MeCN)][BF_4]$	2039, 1948, 1913
$[Re(CO)_3(L2)(MeCN)][BF_4]$	2035, 1902
$[Re(CO)_3(L3)(MeCN)][BF_4]$	2037, 1950, 1917
$[Re(CO)_3(L4)(MeCN)][BF_4]$	2033, 1906

5.3.3. Photophysical Data

The compound dipyridophenazine is similar in structure to the ligands synthesised in this work, however no photophysical data for this compound is available in the primary literature for comparison. Dicyanodibenzodioxin compounds with similar structures to ligands L1 – L4 have previously been reported in literature with photophysical data. Figure 5.26 shows three simple compounds with a dicyanodibenzodioxin core along with some of their photophysical properties. The absorption and emission maxima of compounds **a** and **b** are very similar despite a change in structure. However, the absorption maximum of compound **c** is longer than that recorded for **a** and **b** suggesting that larger structural changes can influence the photophysical properties of these types of compound.

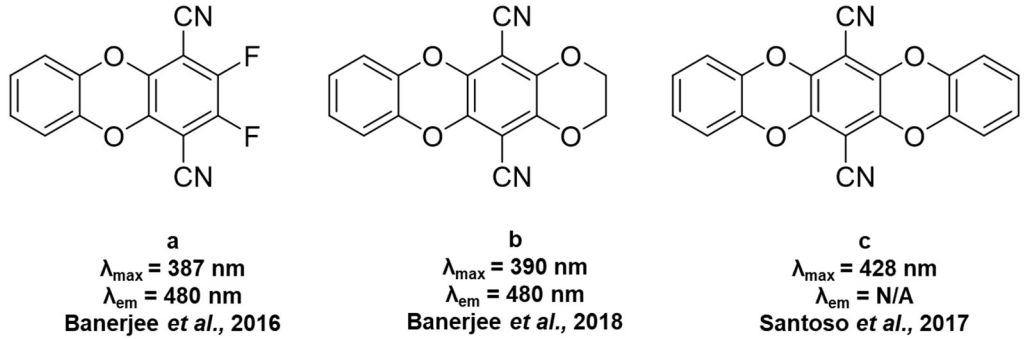

Figure 5.26: Examples of similar dioxin compounds from literature along with relevant photophysical data.[3,43,44]

Figure 5.27 shows the UV-vis absorption spectra of ligands L1-4. Each compound exhibits absorption features between 250 – 300 nm arising from π-π^* and also n-π^* transitions associated with the phenanthroline moiety and, in the cases of L2-4, the aryl moiety. Each species also shows a feature at between 400 and 450 nm. This feature is assigned to a charge transfer transition involving the accepting nitrile groups in each ligand. It appears that the aryl substituents have little to no effect upon the wavelength of this feature, however the intensity does differ between species, with the naphthyl substituted species, L4, having the highest molar extinction coefficient and the fluoro- substituted species having the lowest.

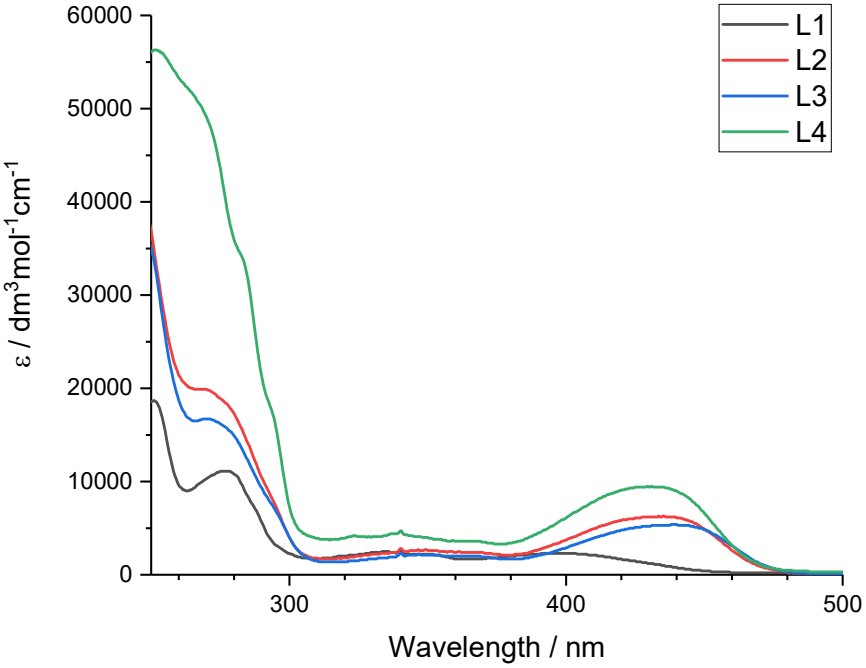

Figure 5.27: UV-vis absorption spectra recorded for ligands L1-4. Measured in $CHCl_3$ at a concentration of $1x10^{-5}$ M.

Literature compounds **a** and **b** both have absorption maxima of around 390 nm, which is also very close to the value of 400 nm recorded for ligand **L1**, suggesting that the phenanthroline moiety has little to no influence upon the absorption wavelength. Compound **c** has an additional aryl moiety in comparison to **a** and **b** and shows a red-shifted absorption wavelength of 428 nm. This is similar to the results observed for ligands L2-4 in respect to ligand **L1**. The effects discussed above are a result of the fact that dibenzodioxins and their related compounds contain oxygen atoms *para*- to one another separating aromatic parts of the compound and so there is no through-bond conjugation across the whole molecule. It is for this reason that the phenanthroline moiety exercises no influence over absorption. In addition to this, it has been observed that the use of electron withdrawing and electron donating groups can shift the absorption maxima of charge transfer transitions as is seen when replacing the fluoro substituents with an aryl dioxin substituent.[1]

The emission spectrum for each ligand is shown in Figure 5.28. The emission feature is broad and without any vibronic features. Across the series, there is minimal variation in emission wavelength maxima which suggests that the charge transfer transition responsible for this emission is unperturbed by the nature of the conjugated groups. The quantum yields and luminescent lifetimes of each ligand were also recorded. The lifetimes are all < 10 ns and suggest that a fluorescence process dominates emission. The data shows that ligands L2-4 have a quantum yield value that is over 10x that recorded for L1. Also, ligand L1 has a much shorter lifetime than ligands L2-4.

Table 5.7: Photophysical data for ligands L1-4.

Ligand	**Absorption wavelength $\lambda_{abs/\ nm}$**	**Emission Wavelength $\lambda_{em/\ nm}$**	**Quantum yield, Φ/ %**	**Lifetime, τ/ ns**
L1	400, 353, 277	490	0.2	2.2

L2	441, 350, 271	485	2.2	7.2
L3	445, 350, 273	489	2.9	8.1
L4	436	485	2.3	6.4

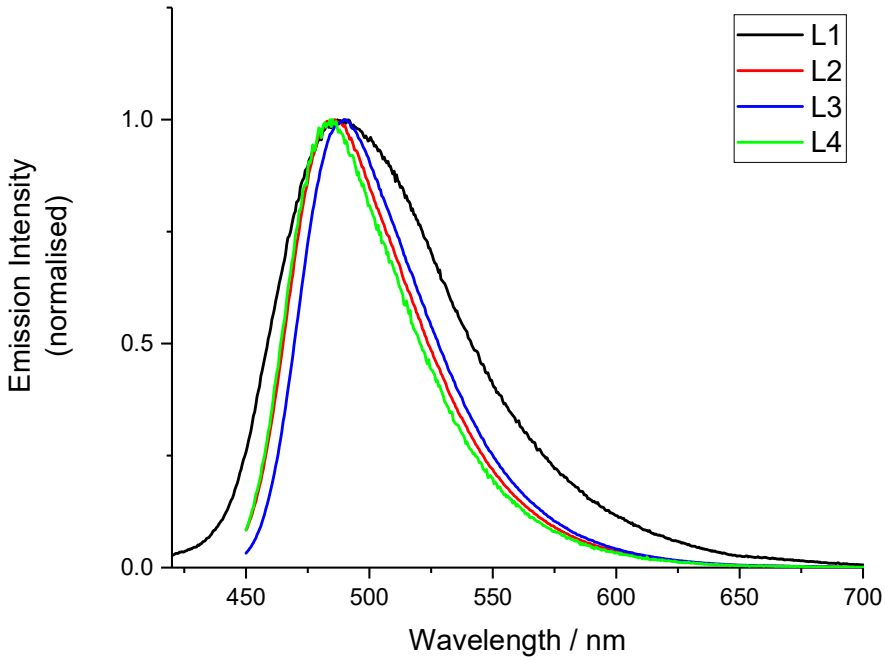

Figure 5.28: Normalised emission spectra recorded for ligands L1-4. Spectra recorded on $CHCl_3$ at room temperature.

The UV-vis absorption profiles for the neutral complexes of the form *fac*-[Re(CO)$_3$(L)Br] are shown in Figure 5.29. The spectra have the same general features as seen in the ligands, however the feature previously observed between 380 - 460 nm in the ligands now has a much broader profile of 340 – 460 nm. This can be ascribed to the overlapping metal-to-ligand charge transfer (MLCT) feature that is typically present in this region. This corresponds well with the absorption profile of the literature known complex *fac*-[Re(CO)$_3$(phen)Br] (where phen = 1,10-phenanthroline), which shows an ^{1}MLCT absorption maximum of 370 nm.[23] Also worthy of note is the large changes in intensity observed for the higher energy features. The molar extinction coefficient of the absorptions occurring around 280 nm for the complexes with ligands L1, L2 and L3 are around half of those observed in the free ligand. Interestingly, the molar extinction coefficient of this absorption in the complex *fac*-[Re(CO)$_3$(L4)Br] is over 5 times higher than that of the free ligand, rising from around 10000 $M^{-1}cm^{-1}$ in the free ligand to over 50000 $M^{-1}cm^{-1}$ in the complex.

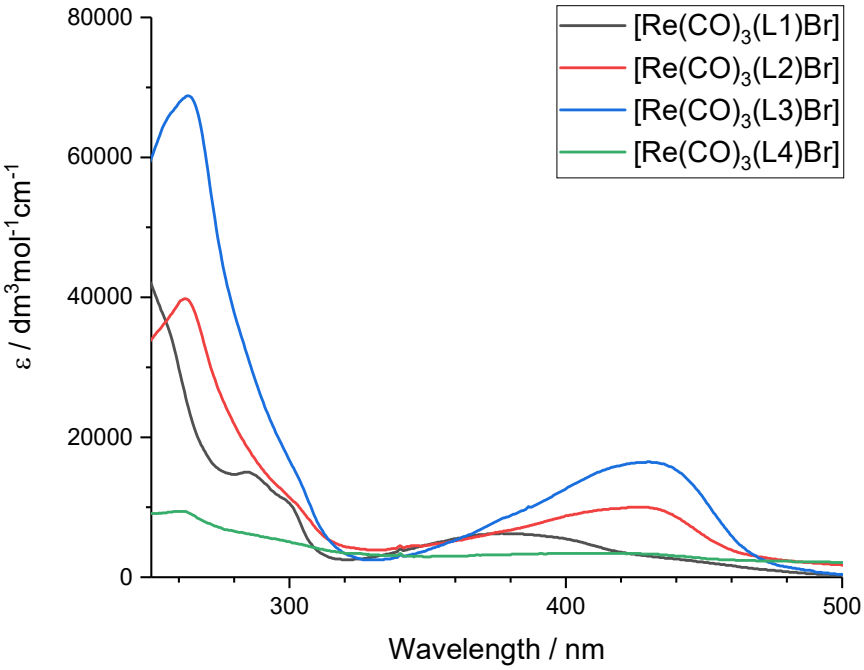

Figure 5.29: UV-vis absorption spectra recorded for neutral complexes fac-[Re(CO)₃(L)Br]. Samples recorded in $CHCl_3$ at concentration of 1x10 $^{-5}$ M.

The UV-vis absorption data of the complex *fac*-[Re(CO)$_3$(dppz-F$_2$)Cl] is also available in the literature for comparison. The most notable feature is that the longest wavelength absorption in the literature complex is around 40 nm shorter than that observed in *fac*-[Re(CO)$_3$(L1)Br]. The molar extinction coefficients are also much higher in the dppz-F$_2$ complex.

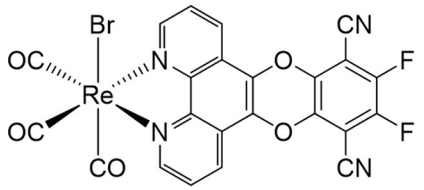

[Re(CO)$_3$(L1)Br]

λ_{max} (ε / M^{-1} cm^{-1}) = 442 (2500), 382 (6200), 300 (10700), 289 (1430)

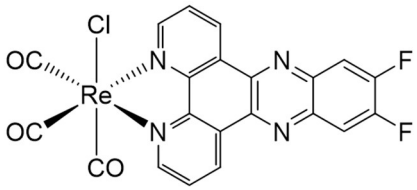

[Re(CO)$_3$(dppz-F$_2$)Cl]

λ_{max} (ε / M^{-1} cm^{-1}) = 400 (sh), 380 (9000), 360 (11000), 319 (14000), 276 (54000), 262 (sh)

Figure 5.30: Left) UV/vis absorption data recorded for complex [Re(CO)₃(L1)Br]. Right) UV-vis data from literature for complex [Re(CO)₃(dppz-F₂)Cl].[16]

The emission spectra of the synthesised complexes are shown in Figure 5.31. Two distinct emission peaks are seen for each complex, one centred around 490 nm and another centred at around 610 nm. The higher energy emission matches the emission observed from the free ligand, while the emission peak at 610 nm is in a similar range to the typical ^{3}MLCT emission observed from species such as *fac*-[Re(CO)$_3$(phen)Br]: λ_{em} = 570 nm, *fac*-[Re(CO)$_3$(phen)Cl]: λ_{em} = 573 nm and the complex *fac*-[Re(CO)$_3$(ephen)Cl]: λ_{em} = 585 nm (where ephen = 5,6-epoxy-1,10-phenanthroline).[23,42] The lack of through-bond conjugation in the ligand appears to effectively separate the molecule into two sections, with the central dicyanobenzodioxin moiety responsible for intraligand charge transfer, and the rhenium(I)-phenanthroline moiety responsible for the metal-to-ligand charge transfer. The result of this is dual emission in the

visible region of the spectrum. Furthermore, the intensity of the ^{3}MLCT emission relative to the ICT emission varies depending upon the aryl moiety used at the opposite end of the ligand to coordination. This creates the possibility of selectively tuning the relative intensity for desired applications.

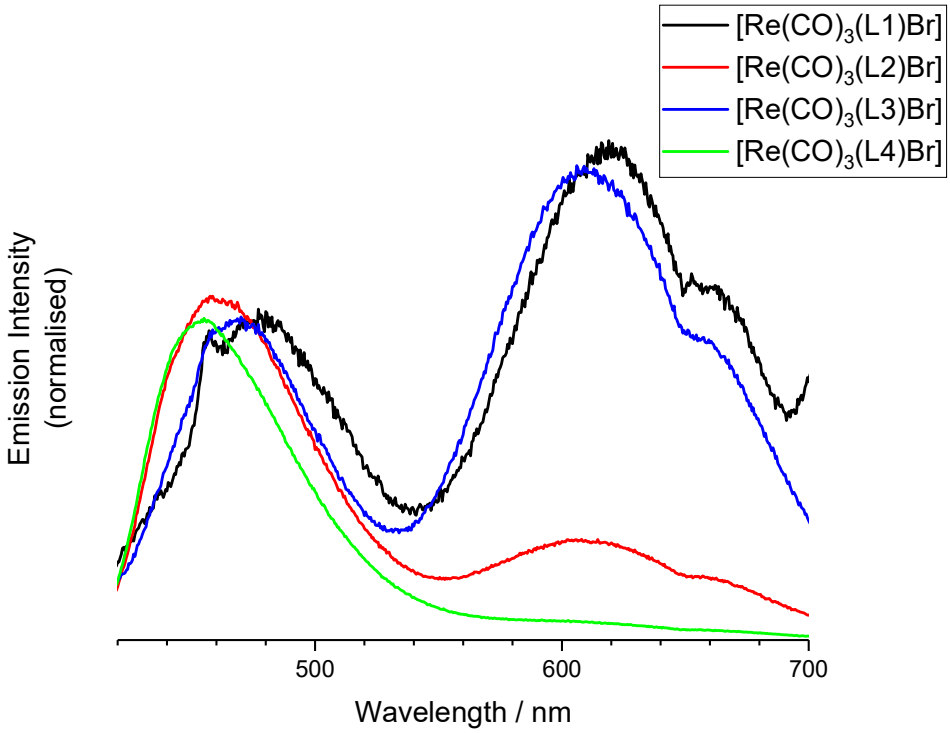

Figure 5.31: Steady state emission spectra recorded for complexes fac-[Re(CO)$_3$(L)Br] in CHCl$_3$.

The luminescence lifetime and quantum yield values were measured for the ^{3}MLCT emission peak and are reported in Table 5.8. This peak exhibits a much longer lifetime than the intraligand charge transfer peak of the free ligand with each complex showing a lifetime of over 80 ns and the longest emission lifetime recorded for the complex *fac*-[Re(CO)$_3$(L4)Br] at 131.6 ns. The quantum yield values were lower than those recorded for the free ligands, with the biggest difference observed for ligand L4. The free ligand shows a quantum yield of 2.3 % which decreases to only 0.38 % in the complex *fac*-[Re(CO)$_3$(L4)Br].

Table 5.8: Photophysical data for fac-[Re(CO)$_3$(L)Br] complexes.

Complex	**Absorption wavelength λ_{abs}/ nm**	**Emission wavelength λ_{em}/ nm**	**Quantum yield, Φ/ %**	**Lifetime, τ/ ns**
[Re(CO)$_3$(L1)Br]	442, 382, 300	477, 618	0.90	81.5
[Re(CO)$_3$(L2)Br]	427, 301, 264	462, 612	0.94	85.8
[Re(CO)$_3$(L3)Br]	434, 304, 265	464, 613	1.23	97.6
[Re(CO)$_3$(L4)Br]	417, 263	456	0.38	131.6 (95%), 6.6 (5%)

Comparative studies were then carried out for the corresponding cationic complexes of the form *fac*-[Re(CO)$_3$(L)(MeCN)][BF$_4$]. The UV-vis absorption spectra are shown in Figure 5.32. When comparing this data with that recorded for the neutral complexes it can be observed that molar extinction coefficient values for complexes *fac*-[Re(CO)$_3$(L2)(MeCN)][BF$_4$] and *fac*-[Re(CO)$_3$(L3)(MeCN)][BF$_4$] has decreased significantly for the feature between 370 – 460 nm while the values for *fac*[Re(CO)$_3$(L1)(MeCN)][BF$_4$] and *fac*-[Re(CO)$_3$(L4)(MeCN)][BF$_4$] remain similar.

Work published in 1982 by Caspar and Meyer directly compared the photophysical properties of the complexes *fac*-[Re(CO)$_3$(bpy)Cl] and *fac*-[Re(CO)$_3$(bpy)(MeCN)][PF$_6$]. Their results showed that the cationic complex showed a slightly higher energy MLCT absorption wavelength than the neutral complex.[45] A similar effect is not observed in the data recorded for the dicyanodibenzodioxin complexes, however this is likely due to the overlap between the MLCT absorption and the CT absorption of the ligand.

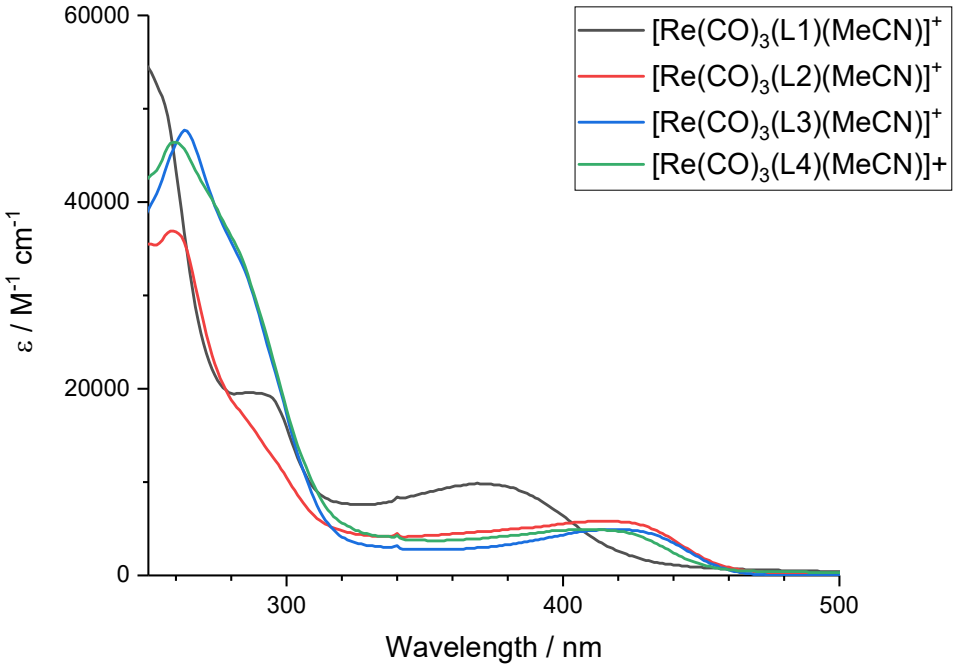

Figure 5.32: UV-vis absorption spectra recorded for cationic complexes fac-[Re(CO)$_3$(L)(MeCN)][BF$_4$]. Recorded in MeCN at concentration 1x10^{-5} M.

However, a much greater difference is present in the steady state emission data recorded for the cationic complexes. This data is presented in Figure 5.33 and shows that the emission peak assigned to a ^{3}MLCT transition in the neutral complexes is no longer present in the cationic complexes. Instead, the spectra recorded bare a strong resemblance to those recorded for the free ligand.

The work published by Caspar and Meyer in 1982 showed similar results when comparing the emission wavelengths of the complexes *fac*-[Re(CO)$_3$(bpy)Cl] and *fac*-[Re(CO)$_3$(bpy)(MeCN)][PF$_6$]. The chloride complex showed an emission wavelength of around 622 nm, but this shifted to 535 nm when the chloride was exchanged for an acetonitrile ligand.[45] This suggests that the peak observed in the cationic rhenium complex emission spectra may be two overlapping ^{3}MLCT and intraligand CT emission peaks.

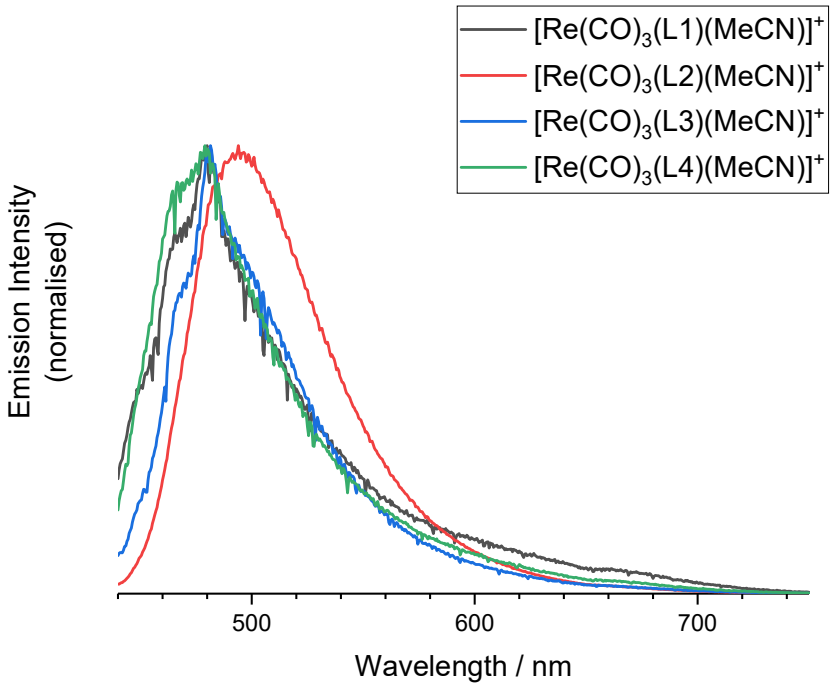

Figure 5.33: Steady state emission spectra recorded for complexes fac-[Re(CO)$_3$(L)(MeCN)][BF$_4$]. Measured in MeCN at room temperature.

The lifetime of each species was recorded in acetonitrile and the results are tabulated below. Unlike the free ligands, the lifetimes recorded for this emission peak are bi-exponential which may suggest two overlapping emission features. The lifetimes recorded are very short with both exponents being shorter than that of the neutral complex. The report by Caspar and Meyer suggests that a much longer emission lifetime should be observed in the cationic complex compared to the neutral complex, but as their measurements were recorded in deoxygenated solvents it may be that quenching by triplet oxygen is responsible for the shorter lifetimes observed in this study.

Table 5.9: Luminescence lifetimes recorded for complexes fac-[Re(CO)$_3$(L)(MeCN)][BF$_4$].Measurements recorded in MeCN at room temperature, λ_{ex} = 295 nm.

Complex	Lifetime/ ns
[Re(CO)$_3$(L1)(MeCN)][BF$_4$]	1.5 (43 %), 4.5 (57 %)
[Re(CO)$_3$(L2)(MeCN)][BF$_4$]	2.0
[Re(CO)$_3$(L3)(MeCN)][BF$_4$]	4.8 (54 %), 1.5 (46 %)

$[Re(CO)_3(L4)(MeCN)][BF_4]$	1.8 (66 %), 5.1 (34 %)

Further to this, one sample was chosen and the emission spectra re-recorded using a series of different excitation wavelengths. Figure 5.34 shows the results produced when the same sample of complex *fac*-$[Re(CO)_3(L3)(MeCN)]^+$ was excited at different wavelengths. When shorter excitation wavelengths are used, the most prominent peak is observed at between 370 – 420 nm. This peak corresponds to the phenanthroline moiety and matches well with literature reports of the emission spectrum of free 1,10-phenanthroline.[46]

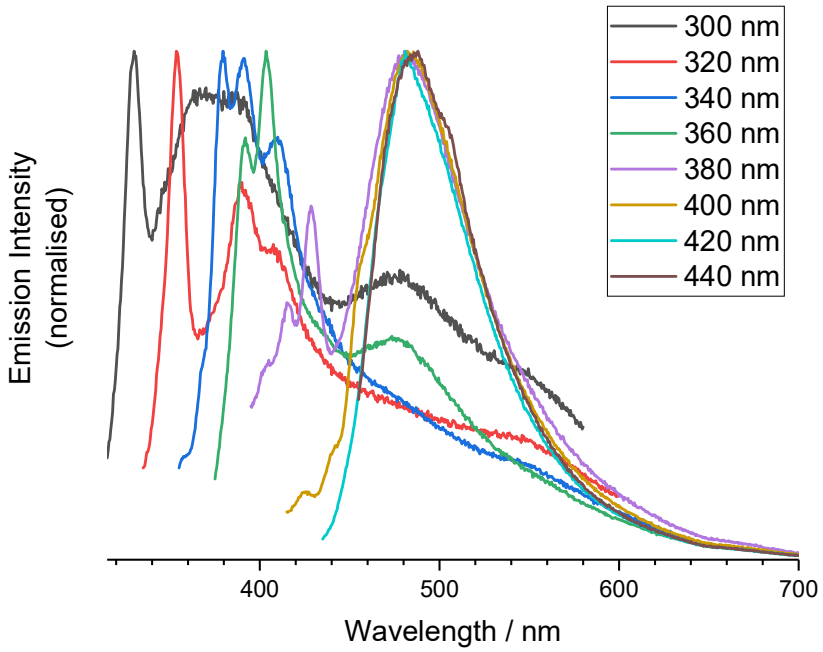

Figure 5.34: Steady state emission spectra recorded for complex fac-$[Re(CO)_3(L3)(MeCN)][BF_4]$ in MeCN using different excitation wavelengths.

Figure 5.35 shows the emission spectrum of complex $[Re(CO)_3(L3)(MeCN)]^+$ recorded in different solvents to show the effect of solvatochromism upon the complex. The emission wavelength varies widely depending upon the solvent used, from around 470 nm in tetrahydrofuran (THF) to almost 540 nm in the absence of solvent. With the exception of water, the more polar solvents, THF and methanol, resulted in the shorter wavelength emission; while non-polar solvents, chloroform and toluene, produced longer wavelength emission. This suggests that the compound may exhibit negative solvatochromism, implying a less dipolar excited state following the redistribution of electron density.

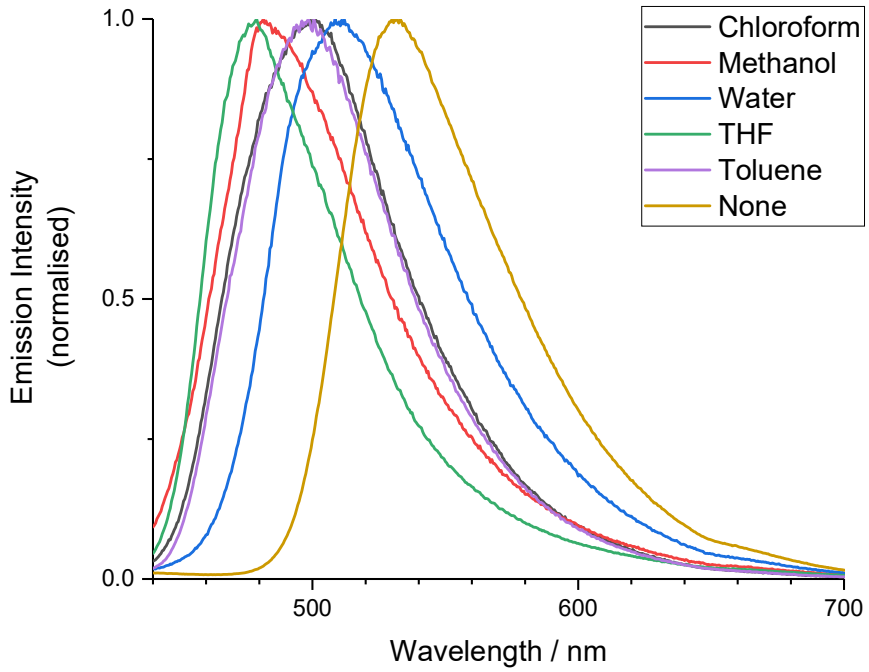

Figure 5.35: Steady state emission specta of complex fac-[Re(CO)$_3$(L3)(MeCN)][BF$_4$] recorded in different solvents using an excitation wavelength of 420 nm.

The luminescence lifetimes of complex [Re(CO)$_3$(L3)(MeCN)]$^+$ were re-recorded in each solvent and the results are shown in Table 5.10. It is clear from these results that the solvent has a large effect upon the lifetime of this species. The least polar solvent, chloroform and toluene, result in the longest-lived emission, whilst the shortest emission was recorded in the absence of solvent, with the next shortest lifetime recorded in methanol which is a polar, protic solvent.

Table 5.10: Luminescence lifetimes recorded for complex fac-[Re(CO)$_3$(L3)(MeCN)][PF$_6$] in different solvents. Measurements ecorded at room temperature, $\lambda_{ex} = 295\ nm$.

Solvent	Lifetime/ ns
Methanol	0.06 (19 %), 1.8 (81 %)
Chloroform	0.7 (69 %), 9.1 (31 %)
Water	0.09 (85 %), 3.7 (15 %)
THF	0.06 (25 %), 5.9 (75 %)
Toluene	1.0 (22 %), 0.2 (52 %), 9.4 (26 %)
None	0.6

It is clear from the photophysical data recorded that the ligand centred transition is always present and is not altered in position or intensity by complexation or substitution of other ligands in the complex. This provides evidence that the charge transfer transition is isolated upon the dicyanodibenzodioxin core of the ligand and independent of the phenanthroline and aryl substituents. Further to this, the intraligand charge transfer transition does not appear to influence the MLCT transition arising from the phenanthroline moiety, with the red emission peak in the neutral complexes bearing a large similarity to the literature known species *fac*-[Re(CO)$_3$(phen)Cl]. It is also likely that substitution of the axial chloride ligand with an acetonitrile ligand increases the energy of the ^{3}MLCT emission to match that of the intraligand charge transfer transition.

5.4. Conclusion

In this chapter, four novel ligands have been synthesised based upon dicyanodibenzodioxin derivatives. These were then used as ligands to synthesise eight novel rhenium complexes, four neutral and four cationic. Characterisation of the free ligands and of the neutral complexes proved difficult to complete due to low solubility, however, full characterisation was achieved for all cationic species with a crystal structure obtained for the complex *fac*-$[Re(CO)_3(L3)(MeCN)][BF_4]$.

The photophysical properties of all species were studied in depth. The neutral complexes were found to have dual emission arising from the separation of the intraligand charge transfer moiety at around 490 nm, and metal-to-ligand charge transfer moiety in the complex at around 610 nm. Exchange of the axial bromide ligand in the neutral complexes with an acetonitrile ligand gave the four cationic complexes. The emission peak of these complexes showed an increase in energy and coincided with the intraligand charge transfer peak resulting in green emission only.

This work has shown that the biologically active dicyanodibenzodioxin motif can be incorporated into a diimine ligand. Successful coordination of this compound to a tricarbonylrhenium(I) complex that shows dual green and red emission could lead to the development of biologically active luminescent probes.

5.5. Experimental

All reactions were performed with the use of vacuum line and Schlenk techniques. Reagents were commercial grade and were used without further purification. ^{1}H and $^{13}C\{^{1}H\}$ NMR spectra were run on NMR-FT Bruker 300 or 400 spectrometers and recorded in $CDCl_3$. ^{1}H and $^{13}C\{^{1}H\}$ NMR chemical shifts (δ) were determined relative to internal TMS and are given in ppm. Low-resolution mass spectra were obtained by the staff at Cardiff University. High-resolution mass spectra were carried out by at the EPSRC National Mass Spectrometry Service at Swansea University. UV-Vis studies were performed on a Shimadzu UV-1800 as chloroform solutions (10^{-5} M). Photophysical data were obtained on a JobinYvon-Horiba Fluorolog spectrometer fitted with a JY TBX picosecond photodetection module as MeCN solutions. Emission spectra were uncorrected and excitation spectra were instrument corrected. The pulsed source was a Nano-LED configured for 372 nm output operating at 1 MHz. Luminescence lifetime profiles were obtained using the JobinYvon-Horiba FluoroHub single photon counting module and the data fits yielded the lifetime values using the provided DAS6 deconvolution software.

Synthesis of 1,10-phenanthroline-5,6-dione To a solution of sulfuric acid (40 mL, conc) and nitric acid (20 mL, conc) on ice, was added 1,10-phenanthroline (4.0 g, 0.02 mol) and sodium bromide (4.0g, 0.04 mol). The ice was removed and the reaction flask heated at reflux for 4 hours. The reaction mixture was cooled to room temperature and poured over ice before neutralisation with sodium hydroxide pellets (18 g, 0.5 mol), followed by sodium hydroxide solution (100 mL, 10 M). The crude product was then extracted into chloroform (3x 500 mL), dried over $MgSO_4$ and the solvent removed *in vacuo*. Purification was carried out by trituration in hot ethanol (10 mL) to yield 1,10-phenanthroline-5,6-dione as a yellow solid. (Yield = 2.02 g, 48 %), ^{1}H NMR (300 MHz, $CDCl_3$) δ_H 9.12 (2 H, dd, J_{HH} = 4.6, 1.8 Hz), 8.71 – 8.33 (2 H, m), 7.67 – 7.46 (2 H, m).

Synthesis of 1,10-phenanthroline-5,6-diol To a stirred solution of 1,10-phenanthroline-5,6-dione (1.0 g, 4.8 mmol) in degassed water (40 ml) was added hydrazine hydrate (432 mg, 14.4 mmol) at room temperature. Once the evolution of gas had begun to subside, the reaction mixture was filtered and the precipitate collected was washed with diethyl ether (100 mL) and dried *in vacuo*. The yellow product was used in subsequent steps without further characterisation.

Synthesis of Ligand L1 To a solution of tetrafluoroteraphthalonitrile (1.0 g, 5.0 mmol) in acetone (60 mL) was added 1,10-phenanthroline-5,6-diol (961 mg, 5.0 mmol) and K_2CO_3 (1.40 g, 10.0 mmol). The reaction mixture was heated at reflux for 24 hours, after which time a green precipitate formed. After cooling to room temperature, the precipitate was collected by filtration and washed with acetone (20 mL), water (20 mL) and diethyl ether (50 mL) to give compound 1 as a green solid. (Yield = 1.48 g, 80 %). ^{1}H NMR (400 MHz, DMSO) δ_H 9.16 (1 H, s), 8.38 (1 H, s), 7.99 – 7.92 (1 H, m) ppm. $^{13}C\{^{1}H\}$ NMR (126 MHz, $CDCl_3$): δ_C 149.98, 146.49, 144.27, 142.78, 139.65, 128.84, 127.87, 123.01, 118.41, 106.31 ppm. $^{19}F\{^{1}H\}$ NMR (376 MHz, DMSO): δ_F -132.30 ppm. HRMS (ASAP) found *m/z* = 373.0533, calculated *m/z* = 373.0532 for $C_{20}H_6F_2N_4O_2$. UV vis. ($CHCl_3$) λ_{max} (ε / $dm^3mol^{-1}cm^{-1}$): 402 (2300), 339 (2300), 280 (10800), 252 (18500) nm. IR (solid) υ /

cm^{-1}: 3385, 2241, 1655, 1620, 1585, 1477, 1458, 1423, 1346, 1331, 1302, 1263, 1250, 1144, 1113, 1063, 1032, 976, 957, 800, 737, 635, 480.

Synthesis of Ligand L2 To a solution of compound 1 (120 mg, 0.33 mmol) in dimethylformamide (5 mL) was added catechol (43 mg, 0.39 mmol) and K_2CO_3 (136 mg, 0.98 mmol). The reaction mixture was heated at 60 ˚C for 24 hours. Upon cooling, water (30 mL) was added to form a brown precipitate. The precipitate was collected by filtration and washed with diethyl ether (25 mL) to give compound 2 as a dark brown solid. (Yield = 80 mg, 55 %). HRMS (ASAP) found *m/z* = 443.0771, calculated *m/z* = 443.0775 for $C_{26}H_{10}N_4O_4$+H. UV vis. ($CHCl_3$) λ_{max} (ε / $dm^3mol^{-1}cm^{-1}$): 436 (6300), 350 (2700), 273 (19400) nm. IR (solid) υ / cm^{-1}: 3383, 3013, 2237, 1661, 1632, 1587, 1454, 1346, 1329, 1304, 1267, 1248, 1113, 1088, 1063, 1026, 962, 802, 752, 737, 635, 559, 503, 419, 411.

Synthesis of Ligand L3 As synthesis of compound 2, but with compound 1 (300 mg, 0.81 mmol) and tert-butylcatechol (147 mg, 0.89 mmol). Product collected as a brown solid. (Yield = 245 mg, 61 %). HRMS (ASAP) found *m/z* = 499.1388, calculated *m/z* = 499.1401 for $C_{30}H_{18}N_4O_4$+H. UV vis. ($CHCl_3$) λ_{max} (ε / $dm^3mol^{-1}cm^{-1}$): 448 (5000), 349 (2100), 295 (7100), 273 (16600) nm. IR (solid) υ / cm^{-1}: 3362, 2955, 1663, 1630, 1508, 1456, 1344, 1329, 1300, 1265, 1113, 1088, 1063, 1030, 968, 864, 843, 804, 737, 627, 407.

Synthesis of Ligand L4 As synthesis of compound 2, but with compound 1 (150 mg, 0.40 mmol) and 2,3-naphthalenediol (71 mg, 0.44 mmol). Product collected as a dark purple solid. (Yield = 85 mg, 43 %) UV vis. ($CHCl_3$) λ_{max} (ε / $dm^3mol^{-1}cm^{-1}$): 433 (9400), 342 (4300), 294 (17200), 284 (33600), 267 (50700), 254 (56000) nm. IR (solid) υ / cm^{-1}: 3379, 2241, 1655, 1630, 1585, 1508, 1450, 1346, 1329, 1271, 1252, 1171, 1115, 1086, 1063, 1030, 966, 899, 870, 802, 737, 619, 480, 451, 411.

Synthesis of complex [Re(CO)$_3$(L1)Br] Compound 1 (100 mg, 0.25 mmol) and $Re(CO)_5Br$ (100 mg, 0.27 mmol) were stirred in toluene (25 ml) and heated at reflux for 24 hours. The cooled reaction mixture was filtered to give complex 1 as a green solid. (Yield = 140 mg, 78 %). ^{1}H NMR (500 MHz, DMSO): δ_H 9.53 (2 H, d, J_{HH} = 4.3 Hz), 8.81 (2 H, d, J_{HH} = 8.1 Hz), 8.31 – 8.18 (2 H, m). HRMS (ASAP) found *m/z* = 744.8910, calculated *m/z* = 744.8922 for $C_{23}H_6BrF_2N_4O_5Re$+Na. UV vis. ($CHCl_3$) λ_{max} (ε / $dm^3mol^{-1}cm^{-1}$): 442 (2500), 382 (6200), 300 (10700), 289 (14300) nm. IR (solid) υ / cm^{-1} : 2031.04, 1928.82, 1894.10, 1876.74, 1664.57, 1487.12, 1465.90, 1352.10, 1273.02, 1091.71, 1072.42, 1049.28, 966.34, 817.82, 748.38, 725.23, 522.71, 414.70, 405.05.

Synthesis of complex [Re(CO)$_3$(L2)Br] Compound 2 (80 mg, 0.18 mmol) and $Re(CO)_5Br$ (73 mg, 0.18 mmol) were stirred in toluene and heated at reflux for 24 hours. The cooled reaction mixture was filtered to give complex 2 as a green solid. (Yield = 105 mg, 76 %). ^{1}H NMR (400 MHz, DMSO): δ_H 9.52 (2 H, m), 8.78 (2 H, m), 8.23 (2 H, m), 7.16 (4 H, m). HRMS (ASAP) found *m/z* = 791.9272, calculated *m/z* = 791.9274 for $C_{29}H_{10}BrN_4O_7Re$. UV vis. ($CHCl_3$) λ_{max} (ε / $dm^3mol^{-1}cm^{-1}$): 427 (10000), 301 (11200), 264 (39300) nm. IR (solid) υ / cm^{-1} : 2019, 1902, 1659, 1634, 1495, 1429, 1350, 1331, 1308, 1273, 1252, 1125, 1090, 1072, 1051, 997, 976, 812, 772, 739, 725, 644, 627, 527, 484, 434, 424, 411, 401.

Synthesis of complex [Re(CO)$_3$(L3)Br] Compound 4 (100 mg, 0.20 mmol) and $Re(CO)_5Br$ (74 mg, 0.18 mmol) were stirred in toluene (25 mL) and heated at reflux for 24 hours. The cooled reaction mixture was filtered to give complex 4 as an orange solid. (Yield = 125 mg, 82 %). ^{1}H NMR (500 MHz, DMSO): δ_H 9.51 (2 H, d, J_{HH} = 5.0 Hz), 8.78 (2 H, d, J_{HH} = 7.9 Hz), 8.22 (2 H, dd,

J_{HH} = 8.1, 4.9 Hz), 7.20 – 7.07 (3 H, m), 1.28 (9 H, s). HRMS (ASAP) found *m/z* = 870.9780, calculated *m/z* = 870.9797 for $C_{33}H_{18}BrN_4O_7Re$+Na. UV vis. ($CHCl_3$) λ_{max} (ε / $dm^3mol^{-1}cm^{-1}$): 434 (16300), 304 (1400), 265 (68300) nm. IR (solid) υ / cm^{-1} : 2029, 1924, 1879, 1661, 1634, 1462, 1427, 1350, 1329, 1277, 1125, 1090, 1072, 1051, 995, 978, 814, 725, 640, 621, 523, 467, 403.

Synthesis of complex [Re(CO)$_3$(L4)Br] Compound 3 (70 mg, 0.14 mmol) and $Re(CO)_5Br$ (71 mg, 0.14 mmol) were stirred in toluene (25 mL) and heated at reflux for 24 hours. The cooled reaction mixture was filtered to give complex 3 as a dark brown solid. (Yield = 111 mg, 94 %). ^{1}H NMR (500 MHz, DMSO): δ_H 8.50 (2 H, d, J_{HH} = 3.4 Hz), 7.90 – 7.85 (2 H, m), 7.45 (2 H, m), 7.25 (2 H, m), 7.16 (4 H, m). UV vis. ($CHCl_3$) λ_{max} (ε / $dm^3mol^{-1}cm^{-1}$): 417 (3400), 263 (9300) nm. IR (solid) υ / cm^{-1} : 2021, 1886, 1605, 1512, 1458, 1329, 1279, 1258, 1169, 1126, 1090, 1072, 1049, 980, 908, 816, 772, 723, 523, 478, 414, 401.

Synthesis of [Re(CO)$_3$(L1)MeCN][BF$_4$] A solution of $Re(CO)_3$(L1)Br (300 mg, 0.42 mmol) and silver tetrafluoroborate, $AgBF_4$, (1.5 eq., 121 mg, 0.62 mmol) in acetonitrile (50 mL) was heated at reflux for 24 hours in the absence of light. Upon cooling, the reaction mixture was filtered through Celite™ and the filtrate dried *in vaccuo*. The crude solid was taken up in acetonitrile and reprecipitated by addition of diethyl ether. A green precipitate was collected by filtration and washed with diethyl ether to give $[Re(CO)_3(L1)MeCN][BF_4]$ (Yield = 128 mg, 40%). ^{1}H NMR (400 MHz, Acetone): δ_H 9.69 (2 H, ddd, J_{HH} = 5.1, 3.5, 1.3 Hz), 9.09 – 9.03 (2 H, m), 8.46 – 8.36 (1 H, m), 2.78 (3 H, s). HRMS (ESI) found *m/z* = 684.0151, calculated *m/z* = 684.0129 for $C_{25}H_9F_2N_5O_5Re$+. UV vis. (CH_3CN) λ_{max} (ε / $dm^3mol^{-1}cm^{-1}$): 375 (9800), 295 (19000), 248 (55000) nm. IR (solid) υ_{max} = 2039, 1948, 913, 1663, 1589, 1481, 1468, 1431, 1356, 1265, 1070, 1051, 989, 822, 727, 642, 625, 523, 478, 409 cm^{-1}.

Synthesis of [Re(CO)$_3$(L2)MeCN][BF$_4$] As $[Re(CO)_3(L1)MeCN][BF_4]$ but with $Re(CO)_3$(L2)Br (300 mg, 0.38 mmol), and $AgBF_4$ (**1.5 eq**, 110 mg, 0.57 mmol). Product collected as green/yellow solid (Yield = 56 mg, 18%). ^{1}H NMR (300 MHz, DMSO): δ_H 9.57 (2 H, d, J_{HH} = 6.0 Hz), 8.89 (1 H, d, J_{HH} = 7.8 Hz), 8.30 (2 H, m), 7.19 (4 H, m), 2.16 (3 H, s). HRMS (ESI) found *m/z* = 754.0375, calculated *m/z* = 754.0372 for $C_{31}H_{13}N_5O_7Re$+. UV vis. (CH_3CN) λ_{max} (ε / $dm^3mol^{-1}cm^{-1}$): 422 (5700), 261 (36600) nm. IR (solid) υ_{max} = 2035, 1902, 1663, 1634, 1460, 1433, 1354, 1306, 1275, 1250, 1130, 1051, 976, 812, 762, 725, 644, 590, 532, 520, 419, 411, 403 cm^{-1}.

Synthesis of [Re(CO)$_3$(L3)MeCN][BF$_4$] As $[Re(CO)_3(L1)MeCN][BF_4]$ but with $Re(CO)_3$(L3)Br (300 mg, 0.35 mmol) and $AgBF_4$ (**1.5 eq.**, 103 mg, 0.53 mmol). Product collected as an orange solid (Yield = 186 mg, 59%). ^{1}H NMR (300 MHz, DMSO): δ_H 9.56 (2 H, d, J_{HH} = 4.8 Hz), 8.88 (2 H, d, J_{HH} = 8.1 Hz), 8.37 – 8.23 (2 H, m), 7.18 (1 H, s), 7.13 (2 H, s), 2.15 (3 H, s), 1.28 (9 H, s) ppm. ^{13}C{^{1}H} NMR (126 MHz, DMSO): δ_C 195.6, 154.2, 149.2, 142.9, 140.3, 140.2, 138.5, 137.4, 137.5, 136.7, 132.7, 131.3, 127.7, 122.3, 121.4, 117.8, 115.9, 113.7, 109.1, 93.6, 93.5 34.2, 30.6, 0.9, 0.1 ppm. HRMS (ESI) found *m/z* = 810.0989, calculated *m/z* = 810.0998 for $C_{35}H_{21}N_5O_7Re$+. UV vis. (CH_3CN) λ_{max} (ε / $dm^3mol^{-1}cm^{-1}$): 425 (4800), 283 (33900), 264 (47600) nm. IR (solid) υ_{max} = 3553, 2037, 1917, 1634, 1464, 1433, 1418, 1352, 1331, 1273, 1072, 1016, 980, 895, 816, 766, 725, 714, 644, 627, 518.85, 433.98 cm^{-1}.

Synthesis of [Re(CO)$_3$(L4)MeCN][BF$_4$] As $[Re(CO)_3(L1)MeCN][BF_4]$ but with $Re(CO)_3$(L4)Br (300 mg, 0.36 mmol) and $AgBF_4$ (**1.5 eq.**, 103 mg, 0.53 mmol). Product collected as a dark green solid (Yield = 14 mg, 5%). ^{1}H NMR (300 MHz, DMSO): δ_H 9.58 (2 H, m), 8.88 (2 H, m), 8.32 (2 H, m), 7.79 (4 H, m), 7.41 (2 H, m), 2.07 (3 H, s). HRMS (ESI) found *m/z* = 804.0517, calculated *m/z* = 804.0529 for $C_{35}H_{15}N_5O_7Re$+. UV vis. (CH_3CN) λ_{max} (ε / $dm^3mol^{-1}cm^{-1}$): 425 (4500), 261 (46400),

234 (42200) nm. IR (solid) υ_{max} = 2035, 1902, 1663, 1460, 1433, 1354, 1306, 1275, 1250, 1130, 1051, 976, 812, 762, 725, 644, 590, 532, 521, 419, 411, 403 cm^{-1}.

5.6. References

1. S. Banerjee, A. Chattopadhyay, A. Banerjee, M. Haridas, P. Saini, M. Das, M. S. Majik and Y. K. Maurya, *Bioorg. Med. Chem. Lett.*, 2015, **25**, 753–757.
2. S. S. Bag, S. Ghorai, S. Jana and C. Mukherjee, *RSC Adv.*, 2013, **3**, 5374–5377.
3. S. Banerjee, A. A. Phadte, A. Chattopadhyay, J. R. D. Fernandes, A. V. Savardekar, A. Banerjee and K. S. Singh, *Tetrahedron Lett.*, 2018, **59**, 3787–3791.
4. J. Fabian, H. Nakazumi and M. Matsuoka, *Chem. Rev.*, 1992, **92**, 1197–1226.
5. H. H. Lee, B. D. Palmer, M. Boyd, B. C. Baguley and W. A. Denny, *J. Med. Chem.*, 1992, **35**, 258–266.
6. B. D. Palmer, G. W. Rewcastle, G. J. Atwell, B. C. Baguley and W. A. Denny, *J. Med. Chem.*, 1988, **31**, 707–712.
7. G. Qian and Z. Y. Wang, *Chem. – Asian J.*, 2010, **5**, 1006–1029.
8. J. C. Rojas, A. K. Bruchey and F. Gonzalez-Lima, *Prog. Neurobiol.*, 2012, **96**, 32–45.
9. B. P. Sullivan, D. J. Salmon and T. J. Meyer, *Inorg. Chem.*, 1978, **17**, 3334–3341.
10. J. Vile, M. Carta, C. G. Bezzu, B. M. Kariuki and N. B. McKeown, *Polymer*, 2014, **55**, 326–329.
11. R. Short, M. Carta, C. G. Bezzu, D. Fritsch, B. M. Kariuki and N. B. McKeown, *Chem. Commun.*, 2011, **47**, 6822.
12. N. Alatrash, E. S. Narh, A. Yadav, M.-J. Kim, T. Janaratne, J. Gabriel and F. M. MacDonnell, *ChemMedChem*, 2017, **12**, 1055–1069.
13. A. Yadav, T. Janaratne, A. Krishnan, S. S. Singhal, S. Yadav, A. S. Dayoub, D. L. Hawkins, S. Awasthi and F. M. MacDonnell, *Mol. Cancer Ther.*, 2013, **12**, 643–653.
14. C. Metcalfe and J. A. Thomas, *Chem. Soc. Rev.*, 2003, **32**, 215–224.
15. A. E. Friedman, J. C. Chambron, J. P. Sauvage, N. J. Turro and J. K. Barton, *J. Am. Chem. Soc.*, 1990, **112**, 4960–4962.
16. M. K. Kuimova, W. Z. Alsindi, A. J. Blake, E. S. Davies, D. J. Lampus, P. Matousek, J. McMaster, A. W. Parker, M. Towrie, X.-Z. Sun, C. Wilson and M. W. George, *Inorg. Chem.*, 2008, **47**, 9857–9869.
17. R. C. Evans, P. Douglas and C. J. Winscom, *Coord. Chem. Rev.*, 2006, **250**, 2093–2126.
18. L. Sacksteder, M. Lee, J. N. Demas and B. A. DeGraff, *J. Am. Chem. Soc.*, 1993, **115**, 8230–8238.
19. H. Kunkely and A. Vogler, *Inorg. Chem. Commun.*, 2002, **5**, 391–394.
20. K. Koike, J. Tanabe, S. Toyama, H. Tsubaki, K. Sakamoto, J. R. Westwell, F. P. A. Johnson, H. Hori, H. Saitoh and O. Ishitani, *Inorg. Chem.*, 2000, **39**, 2777–2783.
21. M. Wrighton and D. L. Morse, *J. Am. Chem. Soc.*, 1974, **96**, 998–1003.
22. K. R. J. Thomas, J. T. Lin, H.-M. Lin, C.-P. Chang and C.-H. Chuen, *Organometallics*, 2001, **20**, 557–563.
23. P. Kurz, B. Probst, B. Spingler and R. Alberto, *Eur. J. Inorg. Chem.*, 2006, **2006**, 2966–2974.
24. C. Fu, M. Li, Z. Su, Z. Hong, W. Li and B. Li, *Appl Phys Lett*, 4.
25. M. R. Waterland, K. C. Gordon, J. J. McGarvey and P. M. Jayaweera, *J. Chem. Soc. Dalton Trans.*, 1998, **0**, 609–616.
26. W.-K. Chu, C.-C. Ko, K.-C. Chan, S.-M. Yiu, F.-L. Wong, C.-S. Lee and V. A. L. Roy, *Chem. Mater.*, 2014, **26**, 2544–2550.
27. X. Liu, H. Xia, W. Gao, Q. Wu, X. Fan, Y. Mu and C. Ma, *J. Mater. Chem.*, 2012, **22**, 3485–3492.
28. Z. Si, J. Li, B. Li, F. Zhao, S. Liu and W. Li, *Inorg. Chem.*, 2007, **46**, 6155–6163.

29. J. Hawecker, J.-M. Lehn and R. Ziessel, *Helv. Chim. Acta*, 1986, **69**, 1990–2012.
30. H. Hori, F. P. A. Johnson, K. Koike, O. Ishitani and T. Ibusuki, *J. Photochem. Photobiol. Chem.*, 1996, **96**, 171–174.
31. A. J. Huckaba, E. A. Sharpe and J. H. Delcamp, *Inorg. Chem.*, 2016, **55**, 682–690.
32. X. Qiao, Q. Li, R. N. Schaugaard, B. W. Noffke, Y. Liu, D. Li, L. Liu, K. Raghavachari and L. Li, *J. Am. Chem. Soc.*, 2017, **139**, 3934–3937.
33. R. Kamata, H. Kumagai, Y. Yamazaki, G. Sahara and O. Ishitani, *ACS Appl. Mater. Interfaces*, 2019, **11**, 5632–5641.
34. A. J. Amoroso, M. P. Coogan, J. E. Dunne, V. Fernández-Moreira, J. B. Hess, A. J. Hayes, D. Lloyd, C. Millet, S. J. A. Pope and C. Williams, *Chem. Commun.*, 2007, 3066–3068.
35. K. K.-W. Lo, *Acc. Chem. Res.*, 2015, **48**, 2985–2995.
36. G. Gelbfish, A. Davidson, S. Kopel, B. Schreibman, J. Gelbfish, G. Degenshein, B. Herz and J. Cunningham, *Ann. Surg.*, 1988, **207**, 75–79.
37. E. E. Langdon-Jones, C. F. Williams, A. J. Hayes, D. Lloyd, S. J. Coles, P. N. Horton, L. M. Groves and S. J. A. Pope, *Eur. J. Inorg. Chem.*, 2017, **2017**, 5279–5287.
38. J. Skiba, A. Kowalczyk, P. Stączek, T. Bernaś, D. Trzybiński, K. Woźniak, U. Schatzschneider, R. Czerwieniec and K. Kowalski, *New J. Chem.*, 2019, **43**, 573–583.
39. J. Wang, A. K. Khanamiryan and C. C. Leznoff, *J. Porphyr. Phthalocyanines*, 2004, **08**, 1293–1299.
40. F. L. Thorp-Greenwood, M. P. Coogan, A. J. Hallett, R. H. Laye and S. J. A. Pope, *J. Organomet. Chem.*, 2009, **694**, 1400–1406.
41. K. K.-W. Lo, K. H.-K. Tsang and N. Zhu, *Organometallics*, 2006, **25**, 3220–3227.
42. A. A. Martí, G. Mezei, L. Maldonado, G. Paralitici, R. G. Raptis and J. L. Colón, *Eur. J. Inorg. Chem.*, 2005, **2005**, 118–124.
43. S. Banerjee, A. Chattopadhyay, P. Saini and K. S. Singh, *Synlett*, 2016, **27**, 799–804.
44. B. Santoso, P. Yanaranop, H. Kang, I. K. H. Leung and J. Jin, *Macromolecules*, 2017, **50**, 3043–3050.
45. J. V. Caspar and T. J. Meyer, *J. Phys. Chem.*, 1983, **87**, 952–957.
46. G. Accorsi, A. Listorti, K. Yoosaf and N. Armaroli, *Chem. Soc. Rev.*, 2009, **38**, 1690–1700.

6. Summary and Further Work

6.1. Summary

This thesis has explored the synthesis and characterisation of luminescent transition metal complexes, beginning with the design of cyclometallating ligands in iridium(III) systems, followed by studying the effects of ancillary ligand upon emission and ending with the design of novel diimine ligands.

The work of chapter 2 investigated the effects of cyclometallating ligand substituents upon the luminescent properties of cationic bis-cyclometallated iridium(III) complexes. It was found that these changes in ligand structure led to a tuning range of 30 nm across the series. Chapter 3 then expanded upon this work by investigating the role of ancillary ligand in the bis-cyclometallated iridium(III) systems developed in chapter 2. This work found that changing the ancillary ligand could further extend the range of emission wavelengths using the same cyclometallating ligands as the work in chapter 2.

Bis-cyclometallated iridium(III) systems also formed the basis of chapter 4. Ligands with a benzo[*g*]quinoxaline structure were used to study how the extent of conjugation influences the emission properties of a complex. The results showed that each complex showed emission in the near infra-red region of the spectrum.

Chapter 5 focussed upon the synthesis of a series of novel diimine compounds and their coordination chemistry with rhenium in a series of tricarbonylrhenium(I) complexes. From this work, a series of four novel diimine ligands were synthesised incorporating a dicyanodibenzodioxin segment into their structure, as well as eight novel rhenium(I) complexes. The results showed that the neutral series of complexes showed two emission peaks, with the longer wavelength peak varying in intensity depending upon the structure of the diimine ligand.

6.2. Future Work

Chapter 5 presented the synthesis of a series of novel diimine ligands with a structure based around dicyanodibenzodioxin and their coordination chemistry with rhenium(I). This work showed that incorporation of these ligands into a neutral tricarbonylrhenium(I) complex resulted in dual emission from the species, with the intensity of red emission varying with ligand structure. It is therefore of interest to investigate whether these novel diimine ligands could influence the photophysical properties of other luminescent transition metal complexes. The experiments presented in this chapter form the foundation of future work to this end.

Chapter 2 reported series of iridium(III) complexes with quinoxaline-based cyclometallating ligands and the literature known diimine ligand 2,2’-bipyridine. Chapter 3 showed that substitution of 2,2’-bipyridine with picolinic acid or pyrazinoic acid further influenced the photophysical properties. As an extension of this work, the dicyanodibenzodioxin ligand L1 from chapter 5 was used as an ancillary ligand in one of these iridium complexes. The proposed synthetic route is shown in Scheme 6.1.

The synthesis makes use of the bis-acetonitrile iridium(III) complex synthesised in chapter 3 as the iridium(III) starting material. This was chosen over the μ-chloro-bridged dimeric iridium species used in chapter 2 due to the increased lability of acetonitrile ligands over the bridging chloride ligands. To overcome the low solubility of ligand L1 in common organic solvents, nitromethane was used as the reaction solvent due to its high boiling point and is only weakly coordinating.

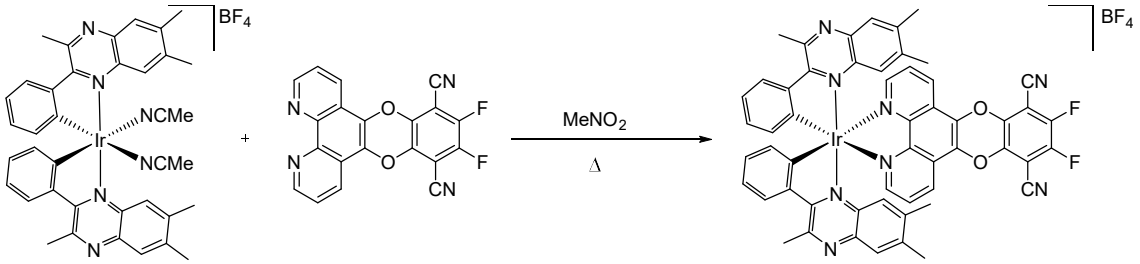

Scheme 6.1: Proposed synthesis of bis-cyclometallated iridium(III) complexes with dioxin-based ligands.

The experimental procedure for this reaction is described below:

$[Ir(quin)_2(MeCN)_2][BF_4]$ (200 mg, 0.23 mmol) and ligand L1 (96 mg, 0.25 mmol) were dissolved in nitromethane (10 mL) and heated at reflux for 48 hours under a nitrogen atmosphere. Upon cooling, the solvent was removed *in vaccuo* and the crude solid taken up in chloroform. The solution was filtered to remove a green precipitate and the dark red solution purified by column chromatography using DCM/MeOH (95:5) as the eluent. Small fractions were collected from a wide red band and two fractions were shown to contain one species by TLC. These were dried and recrystallised using vapour diffusion of diisopropyl ether into a saturated solution of the product in MeCN. The red coloured crystals grown were submitted for single crystal x-ray diffraction. The crystal structure of this complex is shown in Figure 6.1 with the crystal data in the appendix of this work.

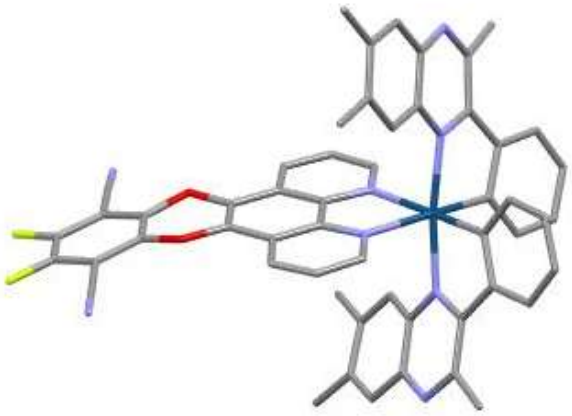

Figure 6.1: Crystal structure obtained by single crystal x-ray diffraction.

The crystal data shows that the target complex was isolated, however, the low yield suggests that the reaction conditions require adjustment in order to give yields high enough for full analysis.

The future of this work lies in using each diimine ligand from chapter 5 as ancillary ligands in iridium complexes, beginning with those systems outlaid in chapter 2 and then in the near-infrared systems of chapter 4. The photophysical properties should then be fully investigated and, if appropriate, followed by cell imaging studies.

Table 6.1: Crystal data collection parameters for iridium complex with dicyanodibenzodioxin ligand

Formula	$C_{62}H_{53}BF_6IrN_9O_3$	***Z'***	1
$D_{calc.}$**/ g cm^{-3}**	1.546	**Wavelength/Å**	0.71075
μ**/mm^{-1}**	2.487	**Radiation type**	MoK_α
Formula Weight	1289.14	Θ_{min}**/°**	1.688
Colour	red	Θ_{max}**/°**	27.483
Shape	block	**Measured Refl.**	189143
Size/mm^3	0.140×0.120×0.040	**Independent Refl.**	12698
***T*/K**	100(2)	**Reflections with I > 2(I)**	11479
Crystal System	monoclinic	R_{int}	0.0485
Space Group	$P2_1/n$	**Parameters**	872
***a*/Å**	12.1642(2)	**Restraints**	587
***b*/Å**	12.8238(2)	**Largest Peak**	1.704
***c*/Å**	35.8981(6)	**Deepest Hole**	-0.593
α/°	90	**GooF**	1.064
β/°	98.4850(10)	wR_2 **(all data)**	0.0797
γ/°	90	wR_2	0.0769
V/Å^3	5538.50(16)	R_1 **(all data)**	0.0352
Z	4	R_1	0.0303

7. Appendix

ChemPubSoc Europe

DOI: 10.1002/chem.201801007

CHEMISTRY A European Journal Full Paper

Ligand Effects | *Hot Paper*

Ligand-Tuneable, Red-Emitting Iridium(III) Complexes for Efficient Triplet–Triplet Annihilation Upconversion Performance

Kaitlin A. Phillips,[a] Thomas M. Stonelake,[a] Kepeng Chen,[b] Yuqi Hou,[b] Jianzhang Zhao,[b] Simon J. Coles,[c] Peter N. Horton,[c] Shannon J. Keane,[a] Emily C. Stokes,[a] Ian A. Fallis,[a] Andrew J. Hallett,[d] Sean P. O'Kell,[d] Joseph M. Beames,*[a] and Simon J. A. Pope*[a]

Abstract: A series of substituted 2-phenylquinoxaline ligands have been explored to finely tune the visible emission properties of a corresponding set of cationic, cyclometallated iridium(III) complexes. The electronic and redox properties of the complexes were investigated through experimental (including time-resolved luminescence and transient absorption spectroscopy) and theoretical methods. The complexes display absorption and phosphorescent emissions in the visible region that are attributed to metal to ligand charge-transfer transitions. The different substitution patterns of the ligands induce variations in these parameters. Time-dependent DFT studies support these assignments and show that there is likely to be a strong spin-forbidden contribution to the visible absorption bands at $\lambda = 500$–600 nm. Calculations also reliably predict the magnitude and trends in triplet emitting wavelengths for the series of complexes. The complexes were assessed as potential sensitisers in triplet–triplet annihilation upconversion experiments by using 9,10-diphenylanthracene as the acceptor; the methylated variants performed especially well with impressive upconversion quantum yields of up to 39.3%.

Introduction

Photoactive metal coordination compounds continue to find broadening application in several disciplines, such as electroluminescence, photovoltaics, photocatalysis, and bioimaging. In particular, organometallic iridium(III) complexes are extremely attractive because a wide range of ligand architectures exist and can be developed to allow tuning of the excited-state properties of such complexes.[1] A more recent development in their potential application is in the field of triplet–triplet annihilation (TTA) upconversion,[2] for which such species, through a limited number of studies,[3] appear to be well suited for use as sensitisers that stimulate fluorescence from an appropriate annihilator acceptor molecule. TTA upconversion is of great interest due to the benefits that such processes can provide to the disciplines outlined earlier. A small number of reports have described the use of Ir^{III} complexes for TTA upconversion,[4] with the best performing, to date, being pyrene-conjugated species of the type $[Ir(ppy)_2(L)]PF_6$ (ppy = 2-phenylpyridine), which have demonstrated highly efficient upconversion quantum yields of up to 31.6% (the highest value yet reported).[5] Typically, the sensitiser should possess good molar absorption at the wavelength of excitation and a long triplet lifetime.[6]

Our own work into luminescent Ir^{III} complexes has included the development of low-energy emitting species that luminesce in the red part of the visible spectrum. The requisite cyclometallating ligands are based upon core ligand structures of 2-phenylquinoline[7] or 2-phenylquinoxaline,[8] and these can provide interesting species with related pyrene derivatives that also show capability as potent photo-oxidation sensitisers.[9] Other studies have reported extending the emission wavelengths of Ir^{III} complexes into the near-infrared (NIR) region.[10]

Herein, we have focused upon the development of poly-substituted quinoxaline ligands to tune the emission of a new series of cationic cyclometallated Ir^{III} complexes. The ability to finely tune the excited-state character and energy of the complex is essential when considering applications such as TTA upconversion. The structural and spectroscopic characterisation of these complexes, together with detailed theoretical analysis, has provided further insight into the species and their application to TTA upconversion. We report herein a world-leading

[a] K. A. Phillips, T. M. Stonelake, S. J. Keane, Dr. E. C. Stokes, Dr. I. A. Fallis, Dr. J. M. Beames, Prof. S. J. A. Pope
School of Chemistry, Main Building, Cardiff University
Cardiff, CF10 3AT (UK)
E-mail: beamesj@cardiff.ac.uk
popesj@cardiff.ac.uk

[b] K. Chen, Y. Hou, Prof. J. Zhao
State Key Laboratory of Fine Chemicals
Dalian University of Technology, Dalian 116024 (P.R. China)

[c] Prof. S. J. Coles, Dr. P. N. Horton
UK National Crystallographic Service, Chemistry
University of Southampton, Highfield, Southampton, SO17 1BJ (UK)

[d] Dr. A. J. Hallett, Dr. S. P. O'Kell
STG Aerospace, Brecon House
Cwmbran, NP44 3AB (UK)

Supporting information and the ORCID number(s) for the author(s) of this article can be found under https://doi.org/10.1002/chem.201801007. Information on the data underpinning the results presented here, including how to access them, can be found in the Cardiff University data catalogue at http://doi.org/10.17035/d.2018.0050717410.

TTA upconversion efficiency of 39.3% from one of the iridium complexes within our series of newly synthesised phosphors.

Results and Discussion

All ligands (Scheme 1) were synthesised by heating the required phenyldiamine with benzil or 1-phenyl-1,2-propanedione in ethanol in the presence of acetic acid. The ligands were reacted with iridium trichloride to generate the chloro-bridged dimetallic [{Ir(L)$_2$-μ-Cl}$_2$] species,[11] which were subsequently reacted with bpy in 2-ethoxyethanol at 120° to yield the corresponding monometallic species [Ir(L)$_2$(bpy)]PF$_6$ following precipitation with a saturated aqueous solution of NH_4PF_6. These reaction conditions are known to favour the *cis*-C,C and *trans*-N,N coordination mode for the cyclometallating ligand at Ir^{III} and have been supported by structural data.[12] Other studies have shown that the mutual *cis*-C,C and *cis*-N,N arrangement of certain cyclometallating ligands can be achieved under different reaction conditions.[13] If required, further purification was achieved by means of column chromatography (silica) by eluting a major red band with CH_2Cl_2/MeOH (95/5). All complexes (Scheme 1) were isolated as reddish brown air-stable solids. Ligand L1 has been previously reported, but all characterisation data are included in the Experimental Section for convenience and comparison.[14]

The complexes were characterised by means of multinuclear NMR, IR, UV/Vis, transient absorption (TA) and luminescence spectroscopies, as well as HRMS, cyclic voltammetry and XRD. ^{1}H NMR spectra provided clear evidence for the formation of the complexes with characteristic shifts in the various resonances associated with the quinoxaline ligands. In particular, the proton adjacent to the cyclometallated carbon was shifted upfield in all cases; this was indicative of the shielding effect of coordination to iridium(III). For [Ir(L1)$_2$(bpy)]PF$_6$, [Ir(L2)$_2$(bpy)]PF$_6$ and [Ir(L3)$_2$(bpy)]PF$_6$, the methyl resonance(s) were shifted away from the corresponding free-ligand values. ^{19}F{^{1}H} NMR spectroscopy was used to analyse [Ir(L4)$_2$(bpy)]PF$_6$ and [Ir(L7)$_2$(bpy)]PF$_6$ and revealed observable differences in the ^{19}F resonances in the spectra (Table 1). Firstly, for the ligand-based fluorine atoms, typical shifts were observed at $\delta \approx -131$ ppm; these were subtly shifted upon coordination in comparison with the free ligands. A loss of chemical equivalence in the L7 fluorine atoms was anticipated upon cyclometallation through the expected coordination mode, and this manifested in a ^3J(F,F) coupling of around 22 Hz.[15] Both complexes showed an additional chemical shift $\delta \approx -73$ ppm, which is assigned to the non-coordinating hexafluorophosphate. Examples of obtained NMR spectra are shown in Figures S1–S5 in the Supporting Information. The observations from the NMR spectroscopy data are consistent with the presence of a single isomer of complex in each case.

Table 1. ^{19}F{^{1}H} NMR chemical shift and coupling constant values for the fluorinated ligands and complexes.

Compound	Ligand δ (^3J(F,F)) [ppm]	PF_6^- δ (^1J(F,P)) [ppm]
L4	−130.4 (d, 21 Hz), −131.2 (d, 21 Hz)	
[Ir(L4)$_2$(bpy)]PF$_6$	−131.7 (d, 22 Hz), −133.7(d, 22 Hz)	−72.6 (d, 712 Hz)
L7	−129.9 (s)	
[Ir(L7)$_2$(bpy)]PF$_6$	−130.3 (d, 22 Hz), −132.7 (d, 22 Hz)	−72.6 (d, 700 Hz)

HRMS data were obtained for each of the complexes; these confirmed the proposed formulations and showed the expected isotopic distributions in each case. The dichloro species, in particular, produced distinct spectra. Supporting IR data principally indicated the presence of the coordinated ligands in each case and the hexafluorophosphate counter anion at $\tilde{\nu} \approx 840$ cm^{-1}.

X-ray crystallography

X-ray-quality single crystals were obtained for two of the methylated species [Ir(L2)$_2$(bpy)]PF$_6$, [Ir(L5)$_2$(bpy)]PF$_6$ and the difluoro variant [Ir(L7)$_2$(bpy)]PF$_6$ through a vapour diffusion methodology (diethyl ether into solutions of the complexes in acetonitrile). Data collection parameters are reported in Table S1 in the Supporting Information, whereas key bond length/angle data are shown in Tables S2 and S3. Each complex adopts a distorted octahedral geometry at Ir^{III}, with substituted quinoxaline ligands chelating in an N^C manner (Figure 1). The obtained structures confirm the expected *cis*-

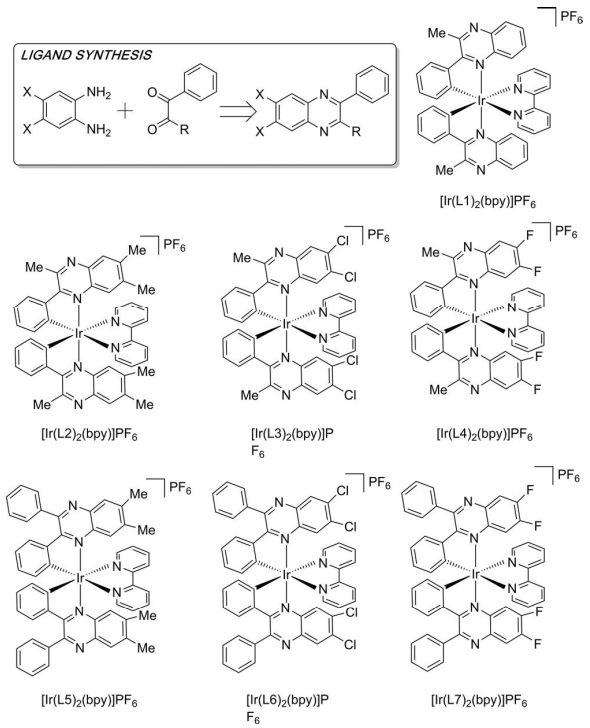

Scheme 1. Structures of the heteroleptic Ir^{III} complexes synthesised in this study and the generalised route to the ligands (top and inset). bpy = 2,2′-bipyridine.

C,C and *trans*-N,N arrangements of the cyclometallating ligands that are retained, irrespective of the quinoxaline ligand substitution. The observation support previous assertions about the stronger *trans* influence of the phenyl group over N-heterocycle donors.[16] Bond lengths to Ir^{III} lie in the typical range expected for such species. Additional packing diagrams shown in the Supporting Information reveal that intermolecular π–π contacts are present between phenyl rings on the quinoxaline ligands of neighbouring complexes.

Figure 2 shows a comparison of the experimental crystal structure of $[Ir(L5)_2(bpy)]PF_6$ with the computationally optimised structure. These results demonstrate that the computational method chosen serves to adequately reproduce the crystal structure (RMSD < 0.5 Å); the majority of the discrepancy is introduced by the position of the methyl substituent groups, which is likely to be derived from a combination of errors in crystallography and DFT. This is to be expected given the low-frequency vibrational motions associated with both the flexing and torsional motions of these methyl groups. Some discrepancy is observed with the bpy position, such that the computed geometry is closer to that of C_2 symmetry.

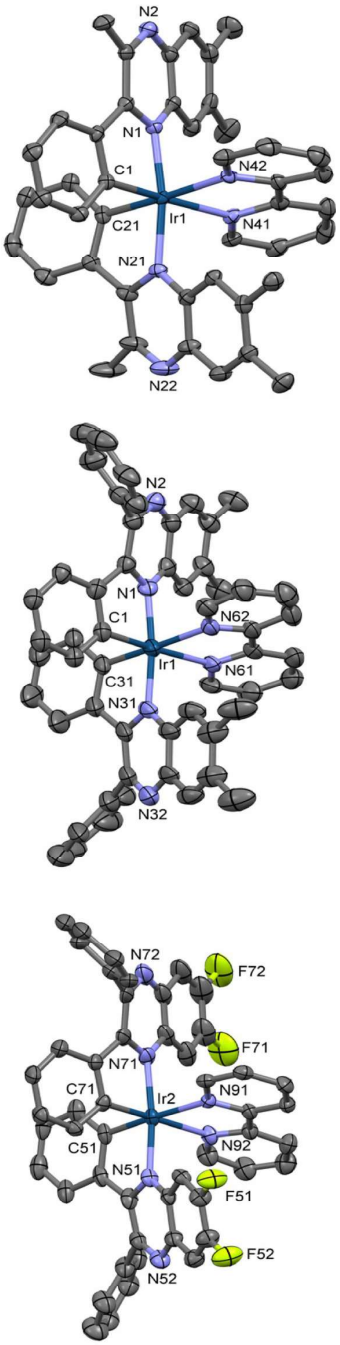

Figure 1. X-ray structures of the complexes $[Ir(L2)_2(bpy)]PF_6$, $[Ir(L5)_2(bpy)]PF_6$ and $[Ir(L7)_2(bpy)]PF_6$ (top to bottom). Anions and solvents of crystallisation are omitted.

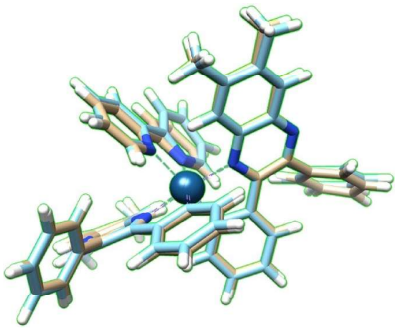

Figure 2. Overlay of the crystal structure (blue) and DF-DFT//B3LYP/6-31G*(SDD) optimised structures (brown) for $[Ir(L5)_2(bpy)]PF_6$. The structures exhibit a root-mean-square deviation (RMSD) of 0.3 Å.

Electronic properties of the complexes

The UV/Vis absorption properties of the complexes were determined as solutions in chloroform. Between $\lambda = 260$ and 400 nm, the complexes show a composite of high-probability transitions that overlap with one another. The bands are generally ascribed to the different ligand-centred transitions related to the coordinated quinoxaline and bpy ligands. They are likely to comprise of various $\pi \rightarrow \pi^*$ transitions, with the possibility of weaker $n \rightarrow \pi^*$ transitions arising from the heterocyclic quinoxaline core. The spectra show a strong feature at $\lambda = 400$–450 nm and a weaker, broad, lower energy band with a maximum at $\lambda = 474$–498 nm (the associated molar absorption coefficients are about $5 \times 10^3\ M^{-1}\,cm^{-1}$); these transitions are likely to possess some metal to ligand charge-transfer (MLCT) character. The positioning of these bands is clearly dependent upon the substitution of the cyclometallated quinoxaline ligand: the halogenated complexes show the longest wavelength values, whereas the methylated analogues are, in contrast, hypsochromically shifted (Figure 3). All visible-region features showed a weaker, lower energy shoulder that extended to $\lambda \approx 600$ nm in these complexes. For related iridium(III)

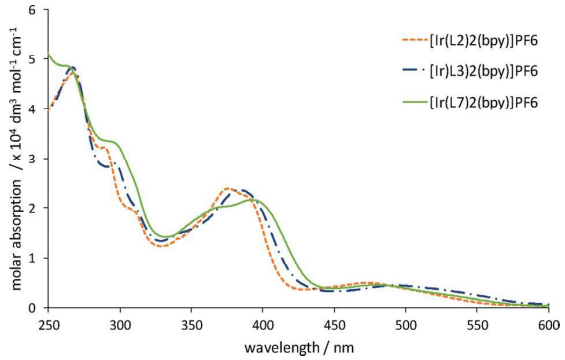

Figure 3. Absorption spectra of $[Ir(L2)_2(bpy)]PF_6$, $[Ir(L3)_2(bpy)]PF_6$ and $[Ir(L7)_2(bpy)]PF_6$ in chloroform.

complexes, this observation has been previously attributed to the transition to the spin-forbidden ^{3}MLCT state. Further discussion of the nature of these electronic transitions is provided below.

The electrochemical characteristics of the complexes were studied in de-oxygenated dichloromethane. The cyclic voltammograms were measured by using a platinum disc electrode (scan rate $\upsilon = 200\ mV\,s^{-1}$, 1×10^{-3} M solutions, 0.1 M $[NBu_4][PF_6]$ as a supporting electrolyte). Each complex showed an irreversible oxidation process between +1.4 and +1.6 V, which was assigned to a $Ir^{3+}/^{4+}$ process. The methyl-substituted complexes of L1, L2 and L5 possessed the lowest E_{ox} values; this was consistent with the anticipated electron-donating ability of the quinoxaline ligands. An irreversible signal at around −0.9 V was also observed and assigned to a ligand-centred reduction.

Density functional theory (DFT)

Figure S8 in the Supporting Information illustrates the Kohn–Sham frontier orbitals for $[Ir(L1)_2(bpy)]PF_6$ in chloroform. The orbitals are shown at the minimum-energy geometry on the S_0 surface. The orbitals illustrate that the occupied molecular orbitals (MOs) have strong Ir 5d character, whereas the unoccupied orbitals are more ligand centred. This is confirmed through MO decomposition analysis (see Table S4 in the Supporting Information; GaussSum Package):[17] the HOMO has equal MO contributions from the metal (33%) and two identical quinoxaline ligands (33 and 33%), with a negligible contribution from bpy (1%). In contrast, the LUMO is predominantly centred on the quinoxalines (48 and 47%). All complexes exhibit similar orbital contributions; however, derivatives $[Ir(L5–L7)_2(bpy)]PF_6$ have slightly reduced metal contributions to the HOMO of between 28 and 30%. The contributions from the quinoxaline ligands are necessarily almost degenerate, given the symmetric nature of the system. These orbital descriptions afford further analysis of the excited states of this system. Time-dependent (TD) DFT calculations suggest the character of all singlet excited states (that lie in a region of interest, $250\ nm < \lambda < 750\ nm$) are reasonably mixed; however, most of the occupied MOs have sizeable Ir 5d contributions, of which the HOMO-1 is the notable exception. All unoccupied orbitals are ligand centred, with <5% metal contributions; therefore, each state will possess a significant degree of ^{1}MLCT character. The longest wavelength singlet excitation is predicted to be at $\lambda = 405$ nm, and does not account for the broad, structure-less feature observed in the absorption spectrum at $\lambda_{max} \approx 475$ nm, typically attributed to the formally spin forbidden $T_1 \leftarrow S_0$ transition, which may become weakly allowed due to spin–orbit effects. This is in reasonable agreement with the energy of the T_1 state at the geometry of the S_0 ground-state minimum, which corresponds to a predicted ^{3}MLCT band at $\lambda = 514$ nm. These transitions all compare qualitatively favourably with the observed UV/Vis spectrum of $[Ir(L1)_2(bpy)]PF_6$ (Figure 4).

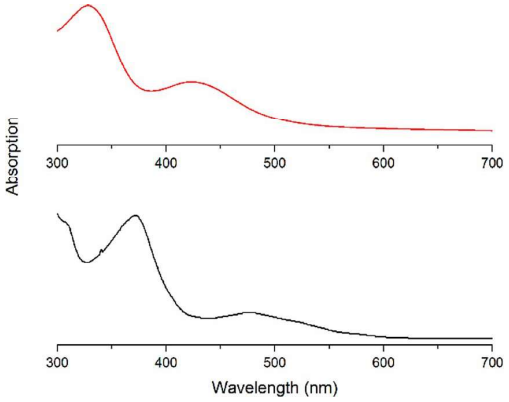

Figure 4. A comparison of the experimental absorption spectrum of $[Ir(L1)_2(bpy)]PF_6$ (black) with the TD-DFT//CAM-B3LYP/6-31G*(SDD) convoluted absorption spectrum (red), which was computed by using the method described in the text. The red line is a summation of spin-allowed and -forbidden transition energies, for which all spin-forbidden transitions are assigned an identical oscillator strength; the total summative transition strength is chosen to best illustrate the spectrum.

Optimisation of triplet $[Ir(L1)_2(bpy)]PF_6$, affords an examination of the spin-forbidden emission bands of the complex. This procedure leads to a significant underestimation of the energy of the spin-forbidden band: the computed vertical transition occurs at $\lambda = 719$ nm, whereas the experimental observation of this band is at $\lambda_{max} \approx 630$ nm. This observation could be attributed to the evolution of the system from an initially prepared singlet photoexcited state into a higher lying triplet state from which emission occurs (TD-DFT calculations suggest, for example, that there are three additional triplet states within 0.3 eV of T_1 within the Franck–Condon region). However, Kasha's rule would suggest that ^{3}MLCT emission occurs after photoexcitation at the S_0 minimum-energy geometry, whereupon it is assumed that the intersystem crossing (ISC), internal conversion (IC) and internal vibrational energy redistribution (IVR) processes occur rapidly in the excited states, such that phosphorescence occurs from the relaxed T_1 geometry. The T_1 geometry relaxation primarily involves additional buckling of a single quinoxaline ligand and a more subtle change in bpy.

Despite the relatively subtle changes in the triplet-state geometry, these complexes exhibit a range of low-frequency vi-

brational modes, leading to a very broad Franck–Condon envelope for these electronic transitions. A cursory investigation of the emission band profile of $[Ir(L1)_2(bpy)]PF_6$ at 298 K, by utilising the Franck–Condon procedures in the Gaussian 09 suite,[18] exclusive of Herzberg–Teller interactions, shows that indeed the emission profile will be broad, and spans the wavelength region over which phosphorescence is observed, leading to the conclusion that emission is indeed observed from T_1. Such a methodology is quantitatively problematic for a system of this size and with such a number of low-frequency vibrational modes, but provides a qualitative depiction of the complex emission. As shown in Figure S9 in the Supporting Information, this simulation provides good agreement with the experimentally recorded emission band, and reasonably well reproduces both the λ_{max} value and the band contour. From the simulation, it can be extracted that the band profile is predominantly formed by a progression in mixed C–C stretching/C–C–C bending modes localised on the quinoxaline ligands ($\approx$1400 cm^{-1}). This is in good agreement with the electron density change induced by the ^{3}MLCT emission. These vibronic features are broadened by multiple combinations of low-frequency modes. In addition, the calculations illustrate that the adiabatic transition values are a more appropriate model of emission band positions (Table 2). These data illustrate that the dichloro complexes exhibit substantial bathochromic shifts, which is in good agreement with experimental results.

A more complete investigation of the vibronic band shapes and Franck–Condon effects was performed on the $S_1/T_1 \leftarrow S_0$ computed spectral features for $[Ir(L1)_2(bpy)]PF_6$. Photoabsorption cross sections were computed by sampling over the ground-state (S_0) geometries accessible at room temperature by means of a nuclear ensemble method, as implemented in the Newton-X computational suite.[19,20] In this case, 2000 geometries (N_s) were sampled from an uncoupled harmonic oscillator Wigner distribution, such that they described a ground-state (S_0) quantum distribution, with excitation energies (E_{0n}) and oscillator strengths (f_{0n}) for the first 10 singlet states (N_n) and first 5 triplet states, computed at each geometry (R_k), and then summed (with a $\delta = 0.2$ eV Lorentzian convolution [red]) to construct the photoabsorption cross section [$\sigma(E)$; Eq. (1)].

$$\sigma(E) = \frac{\pi e^2 \gamma}{2mc\varepsilon_0} \sum_{I\neq 0}^{N_s} \frac{1}{N_n^I} \sum_{k}^{N_n^I} f_{0I}(R_k)\, g(E - E_{0n}(R_I), \delta) \qquad (1)$$

This methodology can be used to provide band shapes and relative cross sections for electronic transitions, but, unlike the Franck–Condon method described above, does not reproduce vibronic progressions. It is worth noting that the refractive index for all calculations is assumed to be one. This assessment of band shapes is extremely computationally costly and has only been applied to $[Ir(L1)_2(bpy)]PF_6$, to demonstrate the accuracy of the band assignments.

Given the remarkable agreement between the absorption spectrum of $[Ir(L1)_2(bpy)]PF_6$ and the computational spectral simulation, the relative band positions of all complexes have been computed and are displayed in Table 2.

The complexes showed emission properties in the visible region (Figure 5). Steady-state measurements in both chloroform (Table 3) and toluene (Table 4) confirmed that the complexes emitted with a broad feature at $\lambda = 550$–750 nm. The coordinated quinoxaline ligands modulate the emission energy of the complexes, with the trimethylated species $[Ir(L2)_2(bpy)]PF_6$ revealing the highest energy emission, and the

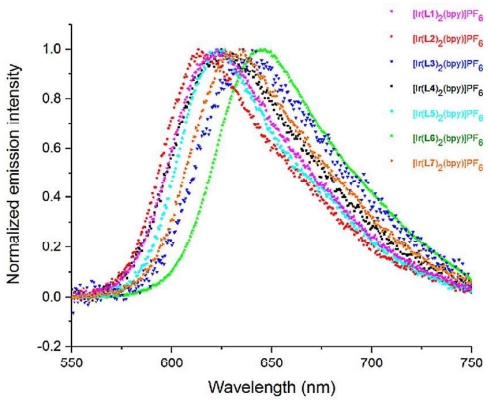

Figure 5. Normalised emission spectra of complexes (in chloroform; $\lambda_{ex} = 355$ nm).

Table 2. Computed spectral properties for all complexes; experimentally observed band positions are given in parentheses. The experimental spin-allowed absorption band positions are taken from the band onsets, whereas the spin-forbidden parameters are λ_{max} values for the respective bands. The last three rows, with L5–L7, are phenyl-substituted analogues of L2–L4, respectively. Both vertical and adiabatic emission energies are reported; the latter in italics.

Compound[a]	$S_1 \leftarrow S_0$ [nm][a]	$T_1 \leftarrow S_0$ [nm][b]	$T_1 \rightarrow S_0$ [nm][b]
$[Ir(L1)_2(bpy)]PF_6$	405 (372)	541 (477)	691, *607* (627)
$[Ir(L2)_2(bpy)]PF_6$	402 (402)	533 (474)	698, *605* (617)
$[Ir(L3)_2(bpy)]PF_6$	419 (406)	565 (500)	708, *630* (634)
$[Ir(L4)_2(bpy)]PF_6$	409 (394)	552 (480)	692, *612* (624)
$[Ir(L5)_2(bpy)]PF_6$	406 (417)	540 (479)	723, *618* (624)
$[Ir(L6)_2(bpy)]PF_6$	423 (428)	572 (501)	730, *642* (645)
$[Ir(L7)_2(bpy)]PF_6$	414 (418)	555 (483)	716, *626* (632)

[a] Recorded in chloroform. [b] In chloroform; $\lambda_{ex} = 355$ nm.

Table 3. Emission data of the complexes recorded in chloroform. The last three rows, with L5–L7, are phenyl-substituted analogues of L2–L4, respectively.

Compound	λ_{em}[a,b] [nm]	τ[a,c] [μs]	Φ_{em}[a]	k_r ($s^{-1} \times 10^5$)	k_{nr} ($s^{-1} \times 10^6$)
$[Ir(L1)_2(bpy)]PF_6$	627	0.46	5.7	1.2	2.1
$[Ir(L2)_2(bpy)]PF_6$	617	0.45	5.1	1.1	2.1
$[Ir(L3)_2(bpy)]PF_6$	634	0.34	1.8	0.32	2.9
$[Ir(L4)_2(bpy)]PF_6$	624	0.40	6.0	1.5	2.4
$[Ir(L5)_2(bpy)]PF_6$	624	0.44	6.6	1.5	2.1
$[Ir(L6)_2(bpy)]PF_6$	645	0.31	6.4	2.1	3.0
$[Ir(L7)_2(bpy)]PF_6$	632	0.54	7.8	1.4	1.1

[a] In chloroform. [b] In chloroform; $\lambda_{ex} = 480$ nm. [c] Luminescence lifetime in chloroform; $\lambda_{ex} = 459$ nm. [d] Quantum yield with $[Ru(bpy)_3][PF_6]_2$ as a standard ($\Phi_\Delta = 0.018$ in acetonitrile).[21]

Table 4. Emission and upconversion data of the complexes recorded in toluene. The last three rows, with L5–L7, are phenyl-substituted analogues of L2–L4, respectively.

Compound	λ_{em} [a,b] [nm]	τ_{obsd} [b] [µs]	τ_{obsd} [c] [µs]	Φ_{UC} [d] [%]
$[Ir(L1)_2(bpy)]PF_6$	618	0.41	2.2	25.9
$[Ir(L2)_2(bpy)]PF_6$	609	0.38	2.3	39.3
$[Ir(L3)_2(bpy)]PF_6$	656	0.38	0.8	0.1
$[Ir(L4)_2(bpy)]PF_6$	638	0.39	1.8	2.0
$[Ir(L5)_2(bpy)]PF_6$	617	0.37	2.0	9.6
$[Ir(L6)_2(bpy)]PF_6$	660	0.35	1.8	1.0
$[Ir(L7)_2(bpy)]PF_6$	646	0.38	1.3	4.0

[a] In toluene (1.0×10^{-5} M). [b] Luminescence lifetime in air, $\lambda_{ex}=510$ nm. [c] Luminescence lifetime in deaerated toluene, $\lambda_{ex}=510$ nm. [d] TTA upconversion quantum yield (Φ_{UC}) with diiodo-BODIPY (BODIPY = 4,4-difluoro-4-bora-3*a*,4*a*-diaza-*s*-indacene) as a standard ($\Phi_F=0.027$ in acetonitrile).

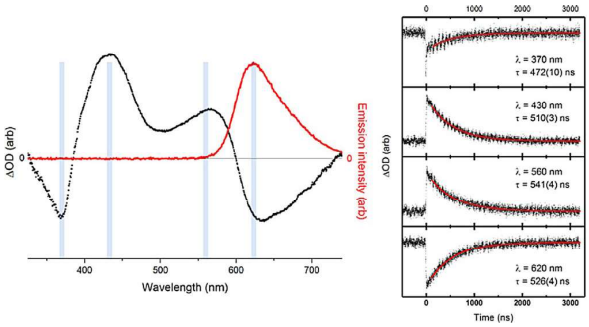

Figure 6. Left: TA spectrum of $[Ir(L1)_2(bpy)]PF_6$ shown in black, overlaid with the emission spectrum of the same complex shown in red. Right: TA lifetime measurements made at selected wavelengths, highlighted as grey bars in the right-hand figure. The red traces indicate mono-exponential fits to these measurements, with corresponding lifetimes displayed in each panel. Recorded in chloroform; $\lambda_{ex}=355$ nm.

dichloro analogues displaying the largest bathochromic shifts within the series. The shift to longer wavelength upon chlorination is a result of changing electronic character of the system, as demonstrated clearly by the reproducibility of this trend in the $T_1\leftarrow S_0$ TD-DFT calculations (Table 2), and equally borne out by the shift in $S_1\leftarrow S_0$ band onsets. However, the cause of the reduced emission lifetimes for the chlorinated species cannot be deconvoluted from a mixture of electronic and relativistic effects, and indeed an increase in ISC rates (supported by increased k_{nr} contributions) may be anticipated for the dichloro species.

To validate the hypothesis that chlorine substitution of the quinoxaline ligands leads to an increase S_0/T_1 spin–orbit couplings (SOCs), SOC elements have been computed from linear response (LR) TD-DFT calculations at the T_1 minimum-energy geometries for $[Ir(L1)_2(bpy)]PF_6$ and $[Ir(L6)_2(bpy)]PF_6$. Values are generated by utilising a Breit–Pauli spin–orbit operator-based approach, as recently implemented in the PySOC computational suite. These calculations suggest that the SOC elements, $<S_0|H_{SO}|T_1>$, evaluated as the root of the squared sum of the *ms* sublevels, is larger (5%, 149 vs. 142 cm^{-1}) for the chlorinated $[Ir(L6)_2(bpy)]PF_6$ complex than that for $[Ir(L1)_2(bpy)]PF_6$. This change is characteristic of a reduced T_1 lifetime for the chloro-substituted systems and, along with the electronic shift in the potential-energy surfaces, serves to explain the photophysics of the molecule.

Experimental time-resolved luminescence lifetime measurements showed mono-exponential decay character in each case, which was consistent with a single emitting state. These observed lifetimes confirmed the phosphorescent nature of the emission for all complexes, and corresponding degassed measurements indicated sensitivity to quenching via $^3O_2$, with lifetimes typically extending into the microsecond domain. Thus, all photophysical data are consistent with an emitting state that possesses significant ^{3}MLCT character.

TA spectroscopy

TA spectroscopy was carried out on solutions of each of the complexes in chloroform. All spectra are similar in appearance, and once again complex $[Ir(L1)_2(bpy)]PF_6$ has been chosen as an example for further discussion. The spectrum shown in Figure 6 is illustrative of the TA spectra for all of the complexes described herein. From short to long wavelength, the spectrum shows a ground-state bleaching (negative ΔOD) at $\lambda=355$ nm, two features corresponding to putative triplet–triplet absorptions in the visible region ($\lambda_{max}\approx430$ and 560 nm, respectively) and finally a long-wavelength emission attributed to the spin-forbidden $T_1\rightarrow S_0$ radiative transition. The two triplet absorption bands are consistent with TD-DFT calculations, which suggests that there is a set of strong $T_n\leftarrow T_1$ absorption bands at $\lambda<600$ nm. The longest wavelength, negative peak is assigned based on the similarity between the TA feature (Figure 6, black) and emission profile (red).

Each feature, including the ground-state bleaching and recovery, and the phosphorescence, exhibit similar TA lifetimes (Figure 6, right), which suggests that each peak relates to the same photoexcitation, ISC process and deactivation. This is attributed to the formation of the lowest triplet state, through prompt S_1/T_1 ISC, and compares relatively well with the observed lifetime from time-resolved emission measurements.[22] Figure 7 displays a comparison of TA spectra for the complexes

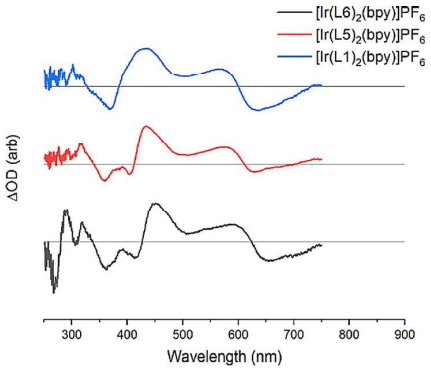

Figure 7. TA spectra of several sample complexes. The spectra show qualitatively similar features. Recorded in chloroform; $\lambda_{ex}=355$ nm.

$[Ir(L1)_2(bpy)]PF_6$, $[Ir(L5)_2(bpy)]PF_6$ and $[Ir(L6)_2(bpy)]PF_6$. Each spectrum shows qualitatively similar features, with the exception of the ground-state bleaching at $\lambda < 450$ nm, which appears to be a clear doublet in the case of $[Ir(L5)_2(bpy)]PF_6$ and $[Ir(L6)_2(bpy)]PF_6$, but does not show the same spectral shape for $[Ir(L1)_2(bpy)]PF_6$. For each of the complexes, the temporal evolution (Figure 8) of the four TA features described in Figure 7 has been analysed in an analogous fashion, and is shown in Table S5 in the Supporting Information, alongside the spin-forbidden emission lifetimes, which are duplicated from Table 2.

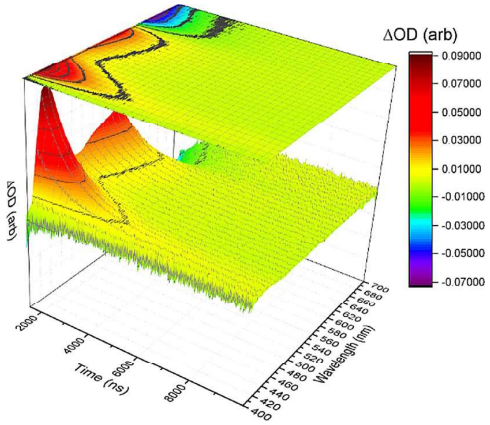

Figure 8. Sample time-resolved TA data for $[Ir(L6)_2(bpy)]PF_6$ prior to spectral deconvolution. The data is shown from $t = 1800$ ns for clarity purposes only.

TTA upconversion measurements

TTA upconversion luminescence experiments were conducted in degassed toluene by using the complexes as the donor component and 9,10-diphenylanthracene (DPA) as the acceptor. The spectra in Figure 9 show the emission spectra recorded in degassed toluene for these upconversion experiments. In each case, the graphs contain superimposed emission profiles for the native complex and the mixture of complex/DPA following excitation at $\lambda = 510$ nm. The DPA triplet excited state is at $\lambda = 700$ nm (1.77 eV), and therefore, lies below the triplet emitting level of all of the complexes in the series. Direct irradiation of DPA with $\lambda = 510$ nm does not produce any emission. In contrast, for the majority of mixtures of complex/DPA, the fluorescence from DPA was observed at $\lambda = 400$–500 nm, which was therefore indicative of an upconversion process. This was most pronounced for $[Ir(L1)_2(bpy)]PF_6$, $[Ir(L2)_2(bpy)]PF_6$ and $[Ir(L5)_2(bpy)]PF_6$, which displayed concomitant quenching of the ^{3}MLCT emission band at $\lambda = 600$–700 nm.

These observations were quantitatively supported by the measured quantum yields for upconversion (Table 4), which showed significant variation across the series of complexes. Interestingly, the methylated variants performed best, amongst which $[Ir(L1)_2(bpy)]PF_6$ and $[Ir(L2)_2(bpy)]PF_6$ displayed remarkable efficiencies of 26 and 39%, respectively. The latter is the highest recorded value for TTA upconversion with a triplet sensitiser.

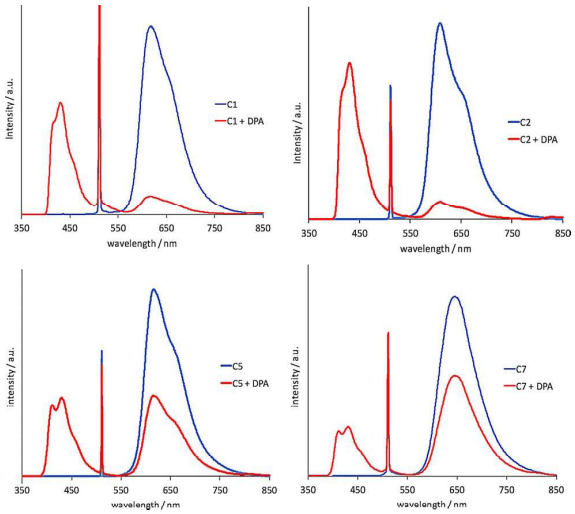

Figure 9. Clockwise from top left: the upconversion fluorescence spectra of C1 ($[Ir(L1)_2(bpy)]PF_6$), C2 ($[Ir(L2)_2(bpy)]PF_6$), C7 ($[Ir(L7)_2(bpy)]PF_6$) and C5 ($[Ir(L5)_2(bpy)]PF_6$) as photosensitisers in toluene. DPA was the acceptor. Excitation was achieved with a continuous laser at $\lambda = 510$ nm (noted as the incident peak in the spectra) and power density of 5.2 mW under a deaerated atmosphere. c(sensitiser) $= 1.0\times10^{-5}$ M; c(DPA) $= 1.6\times10^{-3}$, 1.6×10^{-3}, 2.6×10^{-4} and 2.0×10^{-4} M, respectively; 20 °C.

In comparison, the upconversion performance was contrastingly low ($\leq 1\%$) for both dichloro species, $[Ir(L3)_2(bpy)]PF_6$ and $[Ir(L6)_2(bpy)]PF_6$. Previous reports in the literature have highlighted high molar absorption coefficients in the visible region and long triplet excited-state lifetimes as advantageous attributes for triplet sensitisers.[23] It is notable that these complexes possess modest triplet-state lifetimes and molar absorption values of around 5000 $M^{-1}cm^{-1}$ in the visible region at $\lambda \approx 500$ nm. The luminescence data in toluene revealed a larger variation in emission properties, with the methylated variants displaying the highest emission energies and longest triplet-state lifetimes. The poorly performing dichloro derivatives show the longest wavelength emission maxima and shortest triplet lifetimes. The difluoro-substituted complexes perform slightly better than that of the dichloro analogues; this probably reflects the longer triplet lifetime values.

The visual representation of upconversion was photographically recorded for the best performing methylated complexes (Figure 10). The variation in visual appearance can be plotted by using the CIE coordinates (Figure 11), and conveniently demonstrates the tuneability of the system. The observed red emission of the parent triplet sensitisers is dramatically shifted upon the addition of DPA to give new CIE coordinates.

Conclusion

The use of substituted quinoxaline ligands as cyclometallating units for iridium(III) has proven to be a highly efficient route towards the development of high-performance sensitisers for

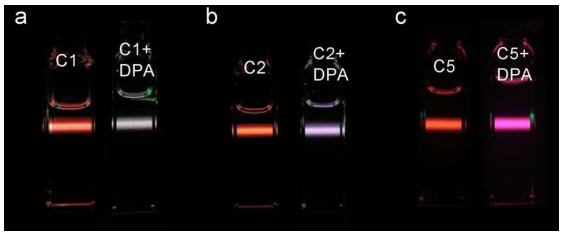

Figure 10. Photographs of the emission of selected triplet sensitisers C1 ($[Ir(L1)_2(bpy)]PF_6$), C2 ($[Ir(L2)_2(bpy)]PF_6$) and C5 ($[Ir(L5)_2(bpy)]PF_6$) alone and the upconversion with DPA in toluene. Excitation was achieved with a continuous laser of $\lambda = 510$ nm and power density of 5.2 mW under a deaerated atmosphere. c(sensitisers) $= 1.0\times10^{-5}$ M; c(DPA) = a) 1.6×10^{-3}, b) 1.6×10^{-3}, and c) 2.0×10^{-4} M; 20 °C.

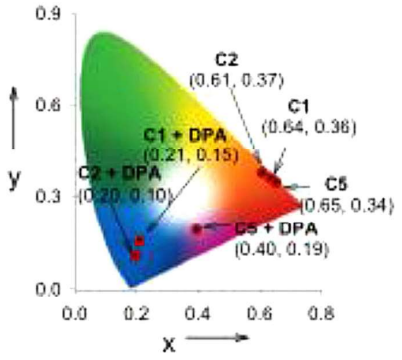

Figure 11. The CIE coordinate changes of triplet sensitisers C1 ($[Ir(L1)_2(bpy)]PF_6$), C2 ($[Ir(L2)_2(bpy)]PF_6$) and C5 ($[Ir(L5)_2(bpy)]PF_6$) before and after the addition of DPA. Excitation was achieved with a continuous laser of $\lambda = 510$ nm and power density of 5.2 mW under a deaerated atmosphere. Before: c(sensitisers) $= 1.0\times10^{-5}$ M. After the addition of DPA: c(DPA) was 1.6×10^{-3} M for C1, 1.6×10^{-3} M for C2, 2.0×10^{-4} M for C4 and 2.0×10^{-4} M for C5; 20 °C.

TTA upconversion. Methylation of the coordinated quinoxaline heterocycle increases the energy and lifetime of the triplet-state emission, and thus, enhances performance. In contrast, although chloro substitution bathochromically shifts the absorption and emission profiles, the dramatic reduction in triplet-state lifetime for the complex of L3 proves unfavourable with respect to TTA upconversion efficiency. We attribute this, with supporting calculations, to the enhancement in ISC, assisted by the chlorine substituents, leading to more rapid non-radiative deactivation of the ^{3}MLCT state.

Experimental Section

X-ray crystallography

Crystals of $[Ir(L2)_2(bpy)]PF_6$, $[Ir(L5)_2(bpy)]PF_6$ and $[Ir(L7)_2(bpy)]PF_6$ suitable for XRD were obtained and mounted on a MITIGEN holder in perfluoroether oil on a Rigaku FRE+ diffractometer equipped with either VHF Varimax confocal mirrors and an AFC12 goniometer and HyPix 6000 detector diffractometer ($[Ir(L5)_2(bpy)]PF_6$), or HF Varimax confocal mirrors and an AFC12 goniometer and HG Saturn 724+ detector diffractometer ($[Ir(L2)_2(bpy)]PF_6$ and $[Ir(L7)_2(bpy)]PF_6$).[24] The crystal was kept at $T = 100(2)$ K during data collection. By using Olex2,[25] the structure was solved with the ShelXT[26] structure solution program, with the intrinsic phasing solution method. The model was refined with version 2014/7 of ShelXL[27] by using least squares minimisation. All non-hydrogen atoms were refined anisotropically and difference Fourier syntheses were employed in positioning idealised hydrogen atoms that were allowed to ride on their parent carbon atoms. For sample $[Ir(L5)_2(bpy)]PF_6$, there was highly disordered solvent (assumed to be either MeCN, diethyl ether or a mixture) that could not be suitably modelled. As such, solvent masking within Olex2 was applied. Due to the quality of the crystals for sample $[Ir(L7)_2(bpy)]PF_6$, a significant number of restraints (RIGU, SADI, BUMP) were required.
CCDC-1825271, 1825273 and 1825272 contain the supplementary crystallographic data for $[Ir(L2)_2(bpy)]PF_6$, $[Ir(L5)_2(bpy)]PF_6$ and $[Ir(L7)_2(bpy)]PF_6$. These data can be obtained free of charge from The Cambridge Crystallographic Data Centre.

Computational methods

Electronic structure calculations were all performed by using density-fitted DFT within the Gaussian 09 computational chemistry suite.[18] All calculations were performed by using the Stuttgart–Dresden (SDD) effective core potential and basis set in the treatment of iridium, in combination with the 6-31G* basis set for all other light atoms. Full geometry optimisations were performed for the cationic complexes by utilising the self-consistent reaction field model (SCRF), which treated the solvent implicitly as a dielectric continuum. In all cases, the solvent chosen was chloroform, which was consistent with that utilised in the both final synthesis and in the majority of spectroscopic measurements. Chloroform was characterised by an electrical permittivity of $\varepsilon = 4.7113$ within the calculations. This computational method modelled the solvent as surrounding a cavity in which the solute resided, and this cavity was characterised by using an integral equation formalism for the polarisable continuum model (IEFPCM). This model represented the system in equilibrium during, for example, an optimisation routine: in all excited-state calculations, a non-equilibrium solvent model was used.
All geometry optimisations were performed by using an ultrafine grid and very tight convergence criteria, and the minima were confirmed as stationary points through the computation of harmonic vibrational frequencies, each of which showed no imaginary components. These stationary points were used in single-point TD-DFT calculations to compute vertical excitation energies. All TD-DFT calculations were undertaken by using a linear response approach. All TD-DFT calculations were also performed with a long-range corrected hybrid functional (CAM-B3LYP).
Phosphorescence and spin-forbidden absorption bands were investigated by using unrestricted DFT to compute parameters associated with the first triplet state (T_1), with an identical methodology to that used for the singlet states. Decomposition of the MO character was performed by using the GaussSum software package. Crystal structure overlays with optimised computational structures were performed by using the Chimera software package, which was also used to calculate RMSD values for these comparative structures.[28]

TA measurements

TA measurements were performed by using an Edinburgh Instruments LP920 spectrometer. All spectra were collected by using a pump wavelength of $\lambda = 355$ nm (third harmonic of a Continuum Surelite II Nd:YAG laser system). The probe light for these measure-

ments was a xenon lamp, which afforded spectral generation at 300 nm $< \lambda <$ 800 nm. Wavelength-dependent spectra were recorded with a 2.05 nm spectral resolution, collected by using an Andor ICCD camera, and integrated over the first 500 ns after the pump laser pulse. The spectra are presented as $\Delta OD_{Xe\ lamp}$, which is simply referred to as ΔOD. Lifetime data was generated by using a photomultiplier to collect time-resolved signals; the bandwidth of these data were identical to that of the camera resolution (2.05 nm). The lifetime data was fitted by using the Origin 2017 software package, and each data set was fitted by using a mono-exponential function, with no evidence of multi-exponential components. Uncertainties in lifetimes were taken from the least squares fitting algorithm, and were not indicative of the uncertainties in multiple fits or data sets.

Cyclic voltammetry

Electrochemical studies were carried out by using a Parstat 2273 potentiostat, in conjunction with a three-electrode cell. The auxiliary electrode was a platinum wire and the working electrode was a platinum (1.0 mm diameter) disc. The reference was a silver wire separated from the test solution by a fine porosity frit and an agar bridge saturated with KCl. Solutions (10 mL CH_2Cl_2) were 1.0×10^{-3} mol dm^{-3} in the test compound and 0.1 mol dm^{-3} in [N*n*Bu$_4$][PF$_6$] as the supporting electrolyte. Under these conditions, $E^{0\prime}$ for the one-electron oxidation of [Fe(η-C_5H_5)$_2$], added to the test solutions as an internal calibrant, was +0.46 V.[29] Unless specified, all electrochemical values were set at $\upsilon = 200$ mV s^{-1}.

TTA upconversion

Associated luminescence spectra were recorded on a Shimadzu RF-5301PC spectrofluorometer. The fluorescence and phosphorescence lifetimes were measured on an OB920 fluorescence/phosphorescence lifetime instrument (Edinburgh, UK) with an EPL picosecond pulsed diode laser ($\lambda = (510 \pm 10)$ nm, pulse width: 119.9 ps, maximum average power: 5 mW). All compounds in flash photolysis experiments were deaerated with N_2 for about 10 min and the gas was maintained during measurements.

A continuous laser ($\lambda = 510$ nm) was used for upconversion and the power of the laser beam was 5.2 mW. The diameter of the spot of the $\lambda = 510$ nm laser was about 3 mm. The mixed solution (with different triplet sensitisers and acceptor) was deaerated for 10 min before the experiment, and the gas flow was maintained during measurements. The upconverted fluorescence was recorded with a RF 5301PC spectrofluorometer. To repress laser scattering, a small black box was put behind the fluorescent cuvette as a beam dump to trap the laser.

The upconversion quantum yields (Φ_{UC}) of all complexes in toluene were determined by using the fluorescence quantum yield of diiodo-BODIPY ($\Phi_F = 2.7\%$ in acetonitrile) as a standard. The upconversion quantum yield was obtained from Equation (2), in which Φ, A, I and η are the quantum yield, absorbance, integrated photoluminescence intensity and refractive index, respectively. Symbols with std and sam are the corresponding parameters for the standard used in the measurement of quantum yield and samples to be measured, respectively.

$$\Phi_{UC} = 2\Phi_{std}\left(\frac{1-10^{-A_{std}}}{1-10^{-A_{sam}}}\right)\left(\frac{I_{sam}}{I_{std}}\right)\left(\frac{\eta_{sam}}{\eta_{std}}\right)^2 \quad (2)$$

Synthesis of L1

1-Phenyl-1,2-propanedione (2.0 mL, 15 mmol) and 1,2-diaminobenzene (1.60 g, 15 mmol) were dissolved in ethanol (30 mL) with acetic acid (1 mL). The reaction mixture was heated at reflux for 24 h under a nitrogen atmosphere. The mixture was cooled to room temperature and the solvent was removed in vacuo. The crude product was taken up in dichloromethane (20 mL) and washed with hydrochloric acid (0.1 M, 2×20 mL). The organic phase was dried over $MgSO_4$ and dried in vacuo to yield a low-melting-point, yellow solid (3.26 g, 81%). UV/Vis ($CHCl_3$): λ_{max} (ε) = 325 nm (9400 dm^3 mol^{-1} cm^{-1}); IR (solid): $\tilde{\nu}$ = 3061, 3032, 2961, 1952, 1813, 1686, 1611, 1578, 1557, 1508, 1495, 1483, 1443, 1431, 1395, 1375, 1341, 1248, 1217, 1188, 1132, 1117, 1074, 1030, 1005, 993, 974, 950, 921, 897, 868, 818, 797, 708, 679, 619, 608, 575, 559, 496, 467, 436, 409, 401 cm^{-1}; ^{1}H NMR (400 MHz; $CDCl_3$): δ = 8.10 (d, *J*(H,H) = 8.37 Hz, 1H), 8.05 (d, *J*(H,H) = 8.37 Hz, 1H), 7.67–7.75 (m, 3H), 7.65 (d, *J*(H,H) = 7.15 Hz, 2H), 7.44–7.54 (m, 3H), 2.77 (s, 3H; Me), 2.51 ppm (s, 3H; Me); ^{13}C{^{1}H} NMR (75 MHz, $CDCl_3$): δ = 155.7, 153.3, 142.0, 141.7, 139.8, 130.5, 130.0, 129.8, 129.7, 129.3, 129.1, 25.2 ppm; HRMS: *m/z* calcd for $C_{15}H_{12}N_2$: 220.1073; found: 220.1072.

Synthesis of L2

Same procedure as that described for L1, but with 1-phenyl-1,2-propanedione (246 mg, 1.7 mmol) and 1,2-diamino-4,5-dimethylbenzene (250 mg, 1.8 mmol). The product was collected as a low-melting-point, brown solid (361 mg, 86%). UV/Vis ($CHCl_3$): λ_{max} (ε) = 339 (11200), 269 (11400), 262 nm (21800 dm^3 mol^{-1} cm^{-1}); IR (solid): $\tilde{\nu}$ = 3060, 3030, 2961, 1654, 1483, 1445, 1398, 1373, 1337, 1252, 1217, 1204, 1157, 1123, 1076, 1024, 1003, 988, 920, 876, 870, 858, 785, 768, 739, 706, 696, 644, 629, 610, 559, 532, 494, 478, 440, 420, 403 cm^{-1}; ^{1}H NMR (300 MHz, $CDCl_3$): δ = 7.85 (s, 1H), 7.80 (s, 1H), 7.64–7.62 (m, 2H), 7.53–7.44 (m, 3H), 2.74 (s, 3H; Me), 2.50 (s, 3H; Me), 2.48 ppm (s, 3H); ^{13}C{^{1}H} NMR (101 MHz, $CDCl_3$): δ = 153.9, 151.3, 140.3, 140.0, 139.6, 139.3, 129.0, 128.8, 128.5, 128.3, 127.3, 24.2, 20.4, 20.3 ppm; HRMS: *m/z* calcd for $C_{17}H_{16}N_2$: 249.1386; found: 249.1385.

Synthesis of L3

Same procedure as that described for L1, but with 1-phenyl-1,2-propanedione (190 mg, 1.3 mmol) and 1,2-diamino-4,5-dichlorobenzene (250 mg, 1.4 mmol). Upon cooling to room temperature, a white precipitate formed and was collected by filtration. The precipitate was washed with methanol to yield the product as a white solid (283 mg, 73%). UV/Vis ($CHCl_3$) λ_{max} (ε) = 342 (12800), 268 nm (30700 dm^3 mol^{-1} cm^{-1}); IR (solid): $\tilde{\nu}$ = 3088, 1753, 1697, 1587, 1543, 1491, 1441, 1412, 1389, 1371, 1325, 1246, 1209, 1180, 1169, 1107, 1078, 1022, 1005, 993, 976, 955, 930, 897, 878, 845, 795, 768, 748, 706, 658, 635, 629, 613, 594, 550, 509, 490, 461, 428, 417 cm^{-1}; ^{1}H NMR (300 MHz, $CDCl_3$): δ = 8.22 (s, 1H), 8.17 (s, 1H), 7.66–7.62 (m, 2H), 7.58–7.52 (m, 3H), 2.77 ppm (s, 3H); ^{13}C{^{1}H} NMR (75 MHz, $CDCl_3$): δ = 155.9, 154.0, 140.0, 139.8, 138.3, 133.7, 129.5, 129.1, 128.9, 128.7, 110.0, 24.5 ppm; HRMS: *m/z* calcd for $C_{15}H_{10}Cl_2N_2$: 291.0264; found: 291.0268.

Synthesis of L4

Same procedure as that described for L1, but with 1-phenyl-1,2-propanedione (230 mg, 1.6 mmol) and 1,2-diamino-4,5-difluorobenzene (250 mg, 1.7 mmol). Upon cooling to room temperature, a white precipitate formed and was collected by filtration and

washed with methanol. The product was collected as a white solid (225 mg, 55%). UV/Vis ($CHCl_3$) λ_{max} (ε) = 326 nm (13000 $dm^3 mol^{-1} cm^{-1}$); IR (solid): $\tilde{\nu}$ = 3030, 1630, 1572, 1553, 1497, 1450, 1373, 1356, 1339, 1256, 1227, 1200, 1142, 1078, 1015, 1005, 988, 928, 897, 874, 866, 791, 772, 752, 712, 706, 667, 619, 611, 584, 544, 484, 447, 419, 405 cm^{-1}; ^{1}H NMR (300 MHz, $CDCl_3$): δ = 7.87–7.77 (m, 2H), 7.65–7.62 (m, 2H), 7.56–7.49 (m, 3H), 2.76 ppm (s, 3H); $^{13}C\{^1H\}$ NMR (101 MHz, $CDCl_3$): δ = 138.4, 129.3, 128.9, 128.7, 114.8, 114.0, 24.3 ppm; $^{19}F\{^1H\}$ NMR (376 MHz, $CDCl_3$): δ = −130.38 (d, ^3J(F,F) = 21.2 Hz), −131.17 ppm (d, ^3J(F,F) = 21.2 Hz); HRMS: *m/z* calcd for $C_{15}H_{10}F_2N_2$: 257.0885; found; 257.0888.

Synthesis of L5

Benzil (357 mg, 1.7 mmol) and 1,2-diamino-4,5-dimethylbenzene (250 mg, 1.8 mmol) were dissolved in ethanol (15 mL) and acetic acid (1 mL). The reaction mixture was heated at reflux under a nitrogen atmosphere for 24 h. The mixture was then cooled to room temperature and a white precipitate was collected by filtration and washed with methanol (413 mg, 78%). UV/Vis ($CHCl_3$): λ_{max} (ε) = 356 (13900), 281 (24600), 269 (31800), 254 nm (44900 $dm^3 mol^{-1} cm^{-1}$); IR (solid): $\tilde{\nu}$ = 2974, 1749, 1549, 1531, 1493, 1474, 1460, 1445, 1416, 1400, 1375, 1346, 1335, 1263, 1211, 1179, 1153, 1074, 1059, 1022, 1003, 966, 932, 870, 849, 814, 783, 773, 762, 741, 725, 691, 633, 608, 598, 556, 530, 519, 492, 476, 436, 413 cm^{-1}; ^{1}H NMR (300 MHz, $CDCl_3$): δ = 7.92 (s, 2H), 7.51–7.48 (m, 4H), 7.35–7.31 (m, 6H), 2.49 ppm (s, 6H; Me); $^{13}C\{^1H\}$ NMR (75 MHz, $CDCl_3$): δ = 152.5, 140.6, 140.2, 139.4, 129.8, 128.5, 128.2, 110.0, 20.5 ppm; HRMS: *m/z* calcd for $C_{22}H_{18}N_2$: 311.1543; found: 311.1542.

Synthesis of L6

The same procedure as that described for L5 was used, but with benzil (273 mg, 1.3 mmol) and 1,2-diamino-4,5-dichlorobenzene (250 mg, 1.4 mmol). The product was collected as a white solid (367 mg, 80%). UV/Vis ($CHCl_3$): λ_{max} (ε) = 362 (19400), 254 nm (61300 $dm^3 mol^{-1} cm^{-1}$); IR (solid): $\tilde{\nu}$ = 3067, 3024, 2980, 1589, 1535, 1491, 1452, 1439, 1393, 1337, 1254, 1190, 1109, 1074, 1061, 1020, 999, 964, 920, 883, 874, 831, 814, 766, 733, 719, 692, 640, 621, 606, 598, 546, 511, 488, 480, 444, 426, 419, 409 cm^{-1}; ^{1}H NMR (300 MHz, $CDCl_3$): δ = 8.29 (s, 2H), 7.52–7.49 (m, 4H), 7.37–7.35 ppm (m, 6H); $^{13}C\{^1H\}$ NMR (101 MHz, $CDCl_3$): δ = 154.5, 140.0, 138.4, 134.4, 129.8, 129.3, 128.4 ppm; HRMS: *m/z* calcd for $C_{20}H_{12}Cl_2N_2$: 351.0450; found: 351.0450.

Synthesis of L7

The same procedure as that described for L5 was used, but with benzil (336 mg, 1.6 mmol) and 1,2-diamino-4,5-difluorobenzene (250 mg, 1.7 mmol). The product was collected as an orange solid (296 mg, 58%). UV/Vis ($CHCl_3$): λ_{max} (ε) = 343 (14900), 261 nm (16800 $dm^3 mol^{-1} cm^{-1}$); IR (solid): $\tilde{\nu}$ = 3051, 1597, 1568, 1541, 1456, 1435, 1352, 1342, 1246, 1217, 1194, 1175, 1152, 1142, 1082, 1072, 1055, 1022, 1001, 972, 939, 918, 872, 818, 785, 772, 760, 752, 719, 700, 677, 623, 610, 573, 542, 521, 498, 438, 424, 419 cm^{-1}; ^{1}H NMR (300 MHz, $CDCl_3$): δ = 7.91 (app. td, *J* = 1.37, 9.35 Hz, 2H), 7.51–7.48 (m, 4H), 7.41–7.31 ppm (m, 6H); $^{13}C\{^1H\}$ NMR (75 MHz, $CDCl_3$): δ = 154.3, 154.1, 153.7, 150.9, 150.7, 138.51, 138.48, 129.8, 129.1, 128.4, 114.7 ppm; $^{19}F\{^1H\}$ NMR (376 MHz, $CDCl_3$): δ = −129.86 ppm; HRMS: *m/z* calcd for $C_{20}H_{12}F_2N_2$: 319.1041; found: 319.1044.

Complex synthesis

$IrCl_3 \cdot x H_2O$ (1 equiv) and ligand L (2 equiv) were dissolved in 2-ethoxyethanol (10 mL) and the reaction mixture was heated at reflux for 48 h. The reaction was then cooled to room temperature and water (30 mL) was added to form a dark brown precipitate. The solid was collected by filtration and assumed to yield [{Ir(L)$_2$μ-Cl}$_2$], which was used without further purification.

Synthesis of [Ir(L1)$_2$(bpy)]PF$_6$

[{Ir(L1)$_2$μ-Cl}$_2$] (100 mg, 0.075 mmol) and bpy (0.025 g, 0.16 mmol) were dissolved in 2-ethoxyethanol (10 mL) and heated at reflux for 24 h under a nitrogen atmosphere. The reaction mixture was then cooled to room temperature and a saturated solution of aqueous ammonium hexafluorophosphate was added. Upon formation of a red precipitate, the mixture was filtered and the precipitate washed with water and diethyl ether to yield the product as a red solid (0.08 g, 68%). UV/Vis ($CHCl_3$): λ_{max} (ε) = 477 (2500), 372 (13200), 253 nm (27900 $dm^3 mol^{-1} cm^{-1}$); IR (solid): $\tilde{\nu}$ = 1605, 1578, 1530, 1449, 1427, 1387, 1348, 1261, 1215, 1196, 1165, 1130, 1016, 1001, 897, 837, 770, 750, 731, 704, 660, 627, 592, 557, 459, 420, 415, 405 cm^{-1}; ^{1}H NMR (300 MHz, $CDCl_3$): δ = 8.39 (d, *J*(H,H) = 8.31 Hz, 2H), 8.24 (d, *J*(H,H) = 8.31 Hz, 2H), 8.17 (d, *J*(H,H) = 5.32 Hz, 2H), 8.01 (app. t, *J*(H,H) = 7.86 Hz, 2H), 7.90 (d, *J*(H,H) = 8.31 Hz, 2H), 7.45–7.57 (m, 4H), 7.16–7.24 (m, 2H), 7.00 (app. t, *J*(H,H) = 7.69 Hz, 2H), 6.86 (app. t, *J*(H,H) = 7.69 Hz, 2H), 6.61 (d, *J*(H,H) = 7.60 Hz, 2H), 3.36 ppm (s, 6H; Me); $^{13}C\{^1H\}$ NMR (400 MHz, $CDCl_3$): δ = 163.7, 155.1, 152.6, 152.0, 146.6, 144.0, 140.4, 140.0, 139.7, 135.1, 130.9, 130.5, 130.4, 130.1, 129.2, 127.6, 124.8, 123.6, 123.2, 27.5 ppm; HRMS: *m/z* calcd for $C_{40}H_{30}IrN_6$: 787.2158; found: 787.2148.

Synthesis of [Ir(L2)$_2$(bpy)]PF$_6$

The product was collected as a red solid (133 mg, 94%). UV/Vis ($CHCl_3$) λ_{max} (ε) = 474 (4800), 391 (22100), 376 (23900), 309 (19300), 390 (32300), 268 nm (47200 $dm^3 mol^{-1} cm^{-1}$); IR (solid): $\tilde{\nu}$ = 1601, 1582, 1560, 1526, 1483, 1445, 1396, 1375, 1342, 1323, 1267, 1219, 1171, 1134, 1063, 993, 835, 795, 768, 737, 702, 660, 627, 556, 474, 434, 420, 403 cm^{-1}; ^{1}H NMR (400 MHz, [D$_6$]acetone): δ = 8.57–8.54 (m, 2H), 8.49 (dd, *J*(H,H) = 8.3, 1.2 Hz, 2H), 8.41 (app. dt, *J*(H,H) = 8.2, 1.0 Hz, 2H), 8.16 (ddd, *J*(H,H) = 8.3, 7.6, 1.6 Hz, 2H), 7.86–7.81 (m, 2H), 7.66 (s, 2H), 7.24 (ddd, *J*(H,H) = 8.3, 7.1, 1.3 Hz, 2H), 7.17 (s, 2H), 6.86–6.79 (m, 2H), 6.70 (dd, *J*(H,H) = 7.7, 1.3 Hz, 2H), 3.34 (s, 6H; Me), 2.30 (s, 6H; Me), 1.81 ppm (s, 6H; Me); $^{13}C\{^1H\}$ (101 MHz, [D$_6$]acetone): δ = 164.6, 156.8, 154.0, 153.4, 149.6, 146.4, 142.7, 142.1, 141.5, 140.7, 140.1, 136.5, 132.1, 131.6, 130.0, 129.7, 125.6, 125.2, 124.3, 28.2, 20.4, 20.1 ppm; HRMS: *m/z* calcd for $C_{44}H_{38}IrN_6$: 843.2784; found: 843.2783.

Synthesis of [Ir(L3)$_2$(bpy)]PF$_6$

The same procedure as that described for [Ir(L1)$_2$(bpy)]PF$_6$ was used, but with [{Ir(L3)$_2$Cl}$_2$] (100 mg, 0.06 mmol) and bpy (20 mg, 0.1 mmol). The product was collected as a red solid (61 mg, 46%). UV/Vis ($CHCl_3$): λ_{max} (ε): 500 (4500), 383 (23700), 298 (28900), 266 nm (48200 $dm^3 mol^{-1} cm^{-1}$); IR (solid): $\tilde{\nu}$ = 1603, 1576, 1528, 1464, 1447, 1381, 1315, 1265, 1188, 1165, 1132, 1113, 1061, 1026, 1009, 962, 895, 870, 843, 824, 772, 739, 729, 673, 664, 646, 637, 608, 556, 467, 428, 419, 403 cm^{-1}; ^{1}H NMR (400 MHz, [D$_6$]acetone): δ = 8.60 (d, *J*(H,H) = 8.4 Hz, 2H), 8.51 (dd, *J*(H,H) = 5.6, 3.6 Hz, 3H), 8.48 (s, 1H), 8.26–8.18 (m, 2H), 8.13 (d, *J*(H,H) = 1.2 Hz, 2H), 7.92–7.83 (m, 2H), 7.59 (s, 2H), 7.31 (dd, *J*(H,H) = 8.3, 6.7 Hz, 2H), 6.97–

6.89 (m, 2H), 6.86 (s, 1H), 6.84 (s, 1H), 3.41 ppm (s, 6H); $^{13}C\{^1H\}$ NMR (126 MHz, [D6]DMSO): δ = 165.6, 155.1, 154.8, 153.8, 147.3, 143.9, 140.8, 138.8, 138.4, 135.3, 133.2, 132.6, 132.1, 131.5, 129.8, 129.3, 125.1, 125.0, 123.4, 27.3 ppm; HRMS: *m/z* calcd for $C_{40}H_{26}Cl_4IrN_6$: 925.0558; found: 925.0548.

Synthesis of $[Ir(L4)_2(bpy)]PF_6$

The product was collected as a red solid (133 mg, 97%). UV/Vis ($CHCl_3$): λ_{max} (ε) = 480 (2400), 375 (13200), 311(11800), 288 (15400), 262 nm (25800 $dm^3 mol^{-1} cm^{-1}$); IR (solid): $\tilde{\nu}$ = 1065, 1578, 1533, 1501, 1447, 1341, 1331, 1252, 1233, 1196, 1128, 1063, 1036, 997, 878, 841, 795, 772, 741, 731, 689, 660, 638, 586, 557, 476, 451, 428, 422, 407 cm^{-1}; ^1H NMR (400 MHz, [D_6]acetone): δ = 8.58 (dd, *J*(H,H) = 8.3, 1.2 Hz, 2H), 8.54 (ddd, *J*(H,H) = 5.5, 1.6, 0.8 Hz, 2H), 8.47 (dt, *J*(H,H) = 8.2, 1.0 Hz, 2H), 8.25–8.18 (m, 2H), 7.92–7.81 (m, 4H), 7.34–7.20 (m, 4H), 6.95–6.88 (m, 2H), 6.84–6.79 ppm (m, 2H); $^{13}C\{^1H\}$ NMR (101 MHz, [D_6]acetone): δ = 155.6, 152.8, 147.8, 144.4, 140.5, 135.3, 131.5, 131.1, 128.9, 124.8, 123.3 ppm; ^{19}F NMR (376 MHz, [D_6]acetone): δ = −72.63 (d, *J* = 711.7 Hz), −131.73 (d, *J* = 21.9 Hz), −133.10 ppm (d, *J* = 21.9 Hz); HRMS: *m/z* calcd for $C_{40}H_{26}F_4IrN_6$: 859.1781; found: 859.1780.

Synthesis of $[Ir(L5)_2(bpy)]PF_6$

The same procedure as that described for $[Ir(L1)_2(bpy)]PF_6$ was used, but with $[\{Ir(L5)_2Cl\}_2]$ (150 mg, 0.09 mmol) and bpy (29 mg, 0.2 mmol). The product was collected as a red solid (124 mg, 63%). UV/Vis ($CHCl_3$): λ_{max} (ε) = 479 (6500), 400 (29300), 362 (24800), 297 (49000), 269 nm (71300 $dm^3 mol^{-1} cm^{-1}$); IR (solid): $\tilde{\nu}$ = 1603, 1580, 1479, 1447, 1348, 1321, 1234, 1207, 1159, 1134, 1074, 1024, 1001, 974, 833, 810, 775, 748, 737, 729, 700, 658, 640, 608, 577, 557, 542, 446, 432, 415 cm^{-1}; ^1H NMR (400 MHz, [D_6]acetone): δ = 9.10 (dt, *J*(H,H) = 5.1, 2.2 Hz, 2H), 8.61–8.52 (m, 2H), 8.34–8.25 (m, 2H), 8.24–8.15 (m, 2H), 7.96 (dt, *J*(H,H) = 6.7, 2.7 Hz, 4H), 7.78 (s, 2H), 7.74–7.65 (m, 6H), 7.34 (s, 2H), 7.18 (ddd, *J*(H,H) = 8.2, 2.9, 1.5 Hz, 2H), 6.78–6.72 (m, 2H), 6.69–6.63 (m, 2H), 6.61–6.54 (m, 2H), 2.35 (s, 6H), 1.94 ppm (s, 6H); $^{13}C\{^1H\}$ NMR (101 MHz, [D_6]acetone): δ = 162.6, 156.1, 153.6, 152.8, 149.3, 144.9, 142.8, 141.5, 140.8, 140.4, 139.9, 139.4, 135.2, 131.4, 130.5, 130.1, 129.6, 129.4, 129.2, 124.8, 124.0, 122.4, 19.4, 19.0 ppm; HRMS: *m/z* calcd for $C_{54}H_{42}IrN_6$: 967.3099; found: 967.3086.

Synthesis of $[Ir(L6)_2(bpy)]PF_6$

The same procedure as that described for $[Ir(L1)_2(bpy)]PF_6$ was used, but with $[\{Ir(L6)_2Cl\}_2]$ (100 mg, 0.05 mmol) and bpy (19 mg, 0.1 mmol). The product was collected as a red solid (48 mg, 37%). UV/Vis: λ_{max} (ε) = ($CHCl_3$) 501(7300), 404 (35300), 299 (54600), 268 nm (87500 $dm^3 mol^{-1} cm^{-1}$); IR (solid): $\tilde{\nu}$ = 1603, 1576, 1524, 1493, 1445, 1433, 1406, 1383, 1342, 1317, 1258, 1186, 1165, 1132, 1115, 1072, 1045, 1026, 1001, 961, 880, 839, 826, 766, 734, 698, 673, 648, 635, 606, 577, 557, 532, 517, 486, 474, 451, 434, 419 cm^{-1}; ^1H NMR (300 MHz, [D_6]acetone): δ = 8.98 (ddd, *J*(H,H) = 5.5, 1.7, 0.7 Hz, 2H), 8.60 (dt, *J*(H,H) = 8.2, 1.0 Hz, 2H), 8.30 (td, *J*(H,H) = 7.9, 1.6 Hz, 2H), 8.23–8.15 (m, 4H), 7.99–7.90 (m, 4H), 7.69 (q, *J*(H,H) = 2.2, 1.8 Hz, 8H), 7.25–7.15 (m, 2H), 6.81–6.62 ppm (m, 6H); $^{13}C\{^1H\}$ NMR (101 MHz, [D_6]acetone): δ = 166.4, 157.3, 156.9, 155.1, 149.9, 145.3, 142.2, 141.0, 140.7, 140.6, 136.5, 136.2, 133.4, 132.8, 131.9, 131.7, 130.8, 130.6, 126.7, 126.4, 123.8 ppm; HRMS: *m/z* calcd for $C_{50}H_{30}Cl_4IrN_6$: 1049.0872; found: 1049.0839.

Synthesis of $[Ir(L7)_2(bpy)]PF_6$

The same procedure as that described for $[Ir(L1)_2(bpy)]PF_6$ was used, but with $[\{Ir(L7)_2Cl\}_2]$ (100 mg, 0.06 mmol) and bpy (19 mg, 0.1 mmol). The product was collected as a red solid (108 mg, 83%). UV/Vis ($CHCl_3$) λ_{max} (ε) = 483 (4500), 396 (21600), 367 (20200), 297 (33100), 265 nm (48600 $dm^3 mol^{-1} cm^{-1}$); IR (solid): $\tilde{\nu}$ = 1603, 1578, 1503, 1447, 1429, 1335, 1275, 1260, 1223, 1204, 1163, 1126, 1072, 1043, 1026, 980, 874, 835, 810, 758, 739, 700, 660, 640, 623, 615, 557, 536, 498 cm^{-1}; ^1H NMR (400 MHz, [D_6]acetone): δ = 9.10–9.06 (m, 2H), 8.63 (d, *J*(H,H) = 8.2 Hz, 2H), 8.35 (tt, *J*(H,H) = 8.0, 1.4 Hz, 2H), 8.22 (m, 2H), 8.01 (tt, *J*(H,H) = 8.5, 4.4 Hz, 6H), 7.79–7.68 (m, 6H), 7.55 (dt, *J*(H,H) = 8.2, 1.5 Hz, 1H), 7.46–7.37 (m, 2H), 7.28–7.20 (m, 2H), 6.87–6.79 (m, 2H), 6.77–6.72 (m, 2H), 6.69 ppm (dt, *J*(H,H) = 7.8, 1.3 Hz, 2H); $^{13}C\{^1H\}$ NMR (101 MHz, [D_6]acetone): δ = 157.5, 150.1, 142.4, 140.8, 136.7, 133.3, 132.6, 131.8, 130.8, 126.6, 124.0, 117.9 ppm; $^{19}F\{^1H\}$ NMR (376 MHz, [D_6]acetone): δ = −72.64 (d, *J* = 699.9 Hz), −130.30 (d, *J* = 21.7 Hz), −132.66 ppm (d, *J* = 21.7 Hz); HRMS: *m/z* calcd for $C_{50}H_{30}F_4IrN_6$: 983.2095; found: 983.2088.

Acknowledgements

Cardiff University (Knowledge Economy Skills Scholarship to K.A.P.) and STG Aerospace are thanked for financial support. We thank the staff of the Engineering and Physical Sciences Research Council (EPSRC) Mass Spectrometry National Service (Swansea University) for providing MS data and the Engineering and Physical Sciences Research Council (EPSRC) UK National Crystallographic Service at the University of Southampton. J.M.B. acknowledges Dr. James A. Platts for helpful discussions regarding the Gaussian calculations.

Conflict of interest

The authors declare no conflict of interest.

Keywords: absorption · density functional calculations · iridium · ligand effects · upconversion

[1] a) S. Ladouceur, E. Zysman-Colman, *Eur. J. Inorg. Chem.* **2013**, 2985; b) A. Ruggi, F. W. B. van Leeuwen, A. H. Velders, *Coord. Chem. Rev.* **2011**, *255*, 2542; c) K. K-W. Lo, M.-W. Louie, K. Y. Zhang, *Coord. Chem. Rev.* **2010**, *254*, 2603; d) A. F. Henwood, E. Zysman-Colman, *Chem. Commun.* **2017**, *53*, 807.

[2] a) T. N. Singh-Rachford, F. N. Castellano, *Coord. Chem. Rev.* **2010**, *254*, 2560; b) S. Baluschev, T. Miteva, V. Yakutkin, G. Nelles, A. Yasuda, G. Wegner, *Phys. Rev. Lett.* **2006**, *97*, 143903.

[3] a) J. Peng, X. Jiang, X. Guo, D. Zhao, Y. Ma, *Chem. Commun.* **2014**, *50*, 7828; b) P. Duan, N. Yanai, N. Kimizuka, *Chem. Commun.* **2014**, *50*, 13111; c) J. Sun, F. Zhong, X. Yi, J. Zhao, *Inorg. Chem.* **2013**, *52*, 6299; d) J. Ma, X. Cui, F. Wang, X. Wu, J. Zhao, K. Li, *J. Org. Chem.* **2014**, *79*, 10855; e) Y. Lu, N. McGoldrick, F. Murphy, B. Twamley, X. Cui, C. Delaney, G. M. O. Maille, J. Wang, J. Zhao, S. M. Draper, *Chem. Eur. J.* **2016**, *22*, 11349; f) J. Sun, W. Wu, H. Guo, J. Zhao, *Eur. J. Inorg. Chem.* **2011**, 3165; g) J. Sun, W. Wu, J. Zhao, *Chem. Eur. J.* **2012**, *18*, 8100; h) C. E. McCusker, F. N. Castellano, *Inorg. Chem.* **2015**, *54*, 6035; i) P. Wang, Y. H. Lee, W. Kim, W. Yang, X. Cui, W. Ji, J. Zhao, D. Kim, *J. Phys. Chem. C* **2017**, *121*, 11117.

[4] For examples, see: a) X. Yi, P. Yang, D. Huang, J. Zhao, *Dyes Pigm.* **2013**, *96*, 104; b) L. Ma, H. Guo, Q. Li, S. Guo, J. Zhao, *Dalton Trans.* **2012**, *41*, 10680; c) X. Yi, C. Zhang, S. Guo, J. Ma, J. Zhao, *Dalton Trans.* **2014**, *43*,

1672; d) X. Chu, M. Guan, L. Niu, Y. Zeng, Y. Li, Y. Zhang, Z. Zhu, B. Wang, *ACS Appl. Mater. Interfaces* **2014**, *6*, 19011.
[5] Y. Lu, J. Wang, N. McGoldrick, X. Cui, J. Zhao, C. Caverly, B. Twamley, G. M. O. Maille, B. Irwin, R. Conway-Kenny, S. M. Draper, *Angew. Chem. Int. Ed.* **2016**, *55*, 14688; *Angew. Chem.* **2016**, *128*, 14908.
[6] J. Zhao, W. Wu, J. Sun, S. Guo, *Chem. Soc. Rev.* **2013**, *42*, 5323.
[7] R. A. Smith, E. C. Stokes, E. E. Langdon-Jones, J. A. Platts, B. M. Kariuki, A. J. Hallett, S. J. A. Pope, *Dalton Trans.* **2013**, *42*, 10347.
[8] E. E. Langdon-Jones, A. J. Hallett, J. D. Routledge, D. A. Crole, B. D. Ward, J. A. Platts, S. J. A. Pope, *Inorg. Chem.* **2013**, *52*, 448.
[9] A. J. Hallett, N. White, W. Wu, X. Cui, P. N. Horton, S. J. Coles, J. Zhao, S. J. A. Pope, *Chem. Commun.* **2012**, *48*, 10838.
[10] For examples, see: a) J. Xue, L. Xin, J. Hou, L. Duan, R. Wang, Y. Wei, J. Qiao, *Chem. Mater.* **2017**, *29*, 4775; b) L. Wang, H. Yin, P. Cui, M. Hetu, C. Wang, S. Monro, R. D. Schaller, C. G. Cameron, B. Liu, S. Kilina, S. A. McFarland, W. Sun, *Dalton Trans.* **2017**, *46*, 8091.
[11] M. Nonoyama, *Bull. Chem. Soc. Jpn.* **1974**, *47*, 767.
[12] a) A. B. Tamayo, B. D. Alleyne, P. I. Djurovich, S. Lamansky, I. Tsyba, N. M. Ho, R. Bau, M. E. Thompson, *J. Am. Chem. Soc.* **2003**, *125*, 7377; b) S. Lamansky, P. Djurovich, D. Murphy, F. Abdel-Razzaq, R. Kwong, I. Tsyba, M. Bortz, B. Mui, R. Bau, M. E. Thompson, *Inorg. Chem.* **2001**, *40*, 1704; c) M. C. Colombo, T. C. Brunold, T. Riedener, H. U. Gudel, M. Fortsch, H.-B. Burgi, *Inorg. Chem.* **1994**, *33*, 545.
[13] J. M. Fernández-Hernández, C.-H. Yang, J. I. Beltran, V. Lemaur, F. Polo, R. Fröhlich, J. Cornil, L. De Cola, *J. Am. Chem. Soc.* **2011**, *133*, 10543.
[14] a) S. Ammermann, C. Hrib, P. G. Jones, W.-W. du Mont, W. Kowalsky, H.-H. Johannes, *Org. Lett.* **2012**, *14*, 5090; b) E. Matteucci, A. Baschieri, A. Mazzanti, L. Sambri, J. Avila, A. Pertegas, H. J. Bolink, F. Monti, E. Leoni, N. Armaroli, *Inorg. Chem.* **2017**, *56*, 10584.
[15] N. Castillo, C. F. Matta, R. J. Boyd, *J. Chem. Inf. Model.* **2005**, *45*, 354.
[16] a) M. Polson, S. Fracasso, V. Bertolasi, M. Ravaglia, F. Scandola, *Inorg. Chem.* **2004**, *43*, 1950; b) M. Albrecht, *Chem. Rev.* **2010**, *110*, 576; c) B. J. Coe, S. J. Glenwright, *Coord. Chem. Rev.* **2000**, *203*, 5.
[17] N. M. O'Boyle, A. L. Tenderholt, K. M. Langner, *J. Comput. Chem.* **2008**, *29*, 839.
[18] Gaussian 09, Revision C.01, M. J. Frisch, G. W. Trucks, H. B. Schlegel, G. E. Scuseria, M. A. Robb, J. R. Cheeseman, G. Scalmani, V. Barone, G. A. Petersson, H. Nakatsuji, X. Li, M. Caricato, A. Marenich, J. Bloino, B. G. Janesko, R. Gomperts, B. Mennucci, H. P. Hratchian, J. V. Ortiz, A. F. Izmaylov, J. L. Sonnenberg, D. Williams-Young, F. Ding, F. Lipparini, F. Egidi, J. Goings, B. Peng, A. Petrone, T. Henderson, D. Ranasinghe, V. G. Zakrzewski, J. Gao, N. Rega, G. Zheng, W. Liang, M. Hada, M. Ehara, K. Toyota, R. Fukuda, J. Hasegawa, M. Ishida, T. Nakajima, Y. Honda, O. Kitao, H. Nakai, T. Vreven, K. Throssell, J. A. Montgomery, Jr., J. E. Peralta, F. Ogliaro, M. Bearpark, J. J. Heyd, E. Brothers, K. N. Kudin, V. N. Staroverov, T. Keith, R. Kobayashi, J. Normand, K. Raghavachari, A. Rendell, J. C. Burant, S. S. Iyengar, J. Tomasi, M. Cossi, J. M. Millam, M. Klene, C. Adamo, R. Cammi, J. W. Ochterski, R. L. Martin, K. Morokuma, O. Farkas, J. B. Foresman, and D. J. Fox, Gaussian, Inc., Wallingford CT, **2016**.
[19] M. Barbatti, M. Ruckenbauer, F. Plasser, J. Pittner, G. Granucci, M. Persico, H. Lischka, *Wiley Interdiscip. Rev.: Comput. Mol. Sci.* **2014**, *4*, 26.
[20] M. Barbatti, G. Granucci, M. Ruckenbauer, F. Plasser, R. Crespo-Otero, J. Pittner, M. Persico, H. Lischka, NEWTON-X: A package for Newtonian dynamics close to the crossing seam. Version 2, 2016, http://www.newtonx.org.
[21] A. Juris, V. Balzani, F. Barigelletti, S. Campagna, P. Belser, A. von Zelewsky, *Coord. Chem. Rev.* **1988**, *84*, 85.
[22] L. M. Groves, C. Schotten, J. Beames, J. A. Platts, S. J. Coles, P. N. Horton, D. L. Browne, S. J. A. Pope, *Chem. Eur. J.* **2017**, *23*, 9407.
[23] D. Dzebo, K. Börjesson, V. Gray, K. Moth-Poulsen, B. Albinsson, *J. Phys. Chem. C* **2016**, *120*, 23397.
[24] S. J. Coles, P. A. Gale, *Chem. Sci.* **2012**, *3*, 683.
[25] O. V. Dolomanov, L. J. Bourhis, R. J. Gildea, J. A. K. Howard, H. Puschmann, *J. Appl. Crystallogr.* **2009**, *42*, 339.
[26] G. M. Sheldrick, *Acta Crystallogr. Sect. A* **2015**, *71*, 3.
[27] G. M. Sheldrick, *Acta Crystallogr. Sect. C* **2015**, *71*, 3.
[28] E. F. Pettersen, T. D. Goddard, C. C. Huang, G. S. Couch, D. M. Greenblatt, E. C. Meng, T. E. Ferrin, *J. Comput. Chem.* **2004**, *25*, 1605. http://www.cgl.ucsf.edu/chimera.
[29] N. G. Connelly, W. E. Geiger, *Chem. Rev.* **1996**, *96*, 877.

Manuscript received: February 27, 2018
Accepted manuscript online: April 18, 2018
Version of record online: June 7, 2018

Journal of Organometallic Chemistry 893 (2019) 11–20

Contents lists available at ScienceDirect

Journal of Organometallic Chemistry

journal homepage: www.elsevier.com/locate/jorganchem

Dual visible/NIR emission from organometallic iridium(III) complexes

Kaitlin A. Phillips [a], Thomas M. Stonelake [a], Peter N. Horton [b], Simon J. Coles [b], Andrew J. Hallett [c], Sean P. O'Kell [c], Joseph M. Beames [a, **], Simon J.A. Pope [a, *]

[a] School of Chemistry, Main Building, Cardiff University, Museum Avenue, Cardiff, CF10 3AT, United Kingdom
[b] UK National Crystallographic Service, Chemistry, Faculty of Natural and Environmental Sciences, University of Southampton, Highfield, Southampton, England, SO17 1BJ, United Kingdom
[c] STG Aerospace, Brecon House, Cwmbran, NP44 3AB, United Kingdom

ARTICLE INFO

Article history:
Received 12 February 2019
Received in revised form
15 April 2019
Accepted 20 April 2019
Available online 25 April 2019

Keywords:
Iridium
Luminescence
Ligands
DFT

ABSTRACT

A series of four substituted benzo[*g*]quinoxaline species have been synthesised and utilised as cyclometalating ligands for iridium(III). The ligands (**L1-L4**) were synthesised and isolated in good yield following the condensation of 2,3-diaminonaphthalene with benzil and three of its derivatives. The substituent modulated electronic properties of **L1-L4** were dominated by intraligand $\pi-\pi^*$ transitions, with the fluorescence profile demonstrating vibronic features attributed to the highly conjugated nature of the chromophore. Iridium(III) complexes of the form $[Ir(\mathbf{L})_2(bipy)]PF_6$ were synthesised from **L1-L4** in two steps. The electronic properties of the complexes reveal absorption in the UV-vis. region with spin forbidden metal-to-ligand charge transfer (MLCT) transitions possibly contributing at longer wavelengths to ca. 600 nm. Steady state luminescence (aerated, room temperature) on solutions of the complexes showed dual emissive properties in the visible and near-infra red (NIR) regions. Firstly, a vibronically structured emission in the visible region (ca. 525 nm) was attributed to ligand centred fluorescence (lifetime < 10 ns). Secondly, a broad emission peak in the NIR (ca. 950 nm) which extended to around 1200 nm was observed with corresponding lifetimes of 116–162 ns, indicative of triplet excited state emission.

1. Introduction

The development and study of molecular species that are luminescent in the near-infra red (NIR) region continues to attract significant attention. Such studies have been motivated by the many applications (some postulated, others realised) that can benefit from NIR luminescent materials [1]. A range of optoelectronic devices can utilise NIR wavelengths. In the realm of bioimaging, it has long been argued that the use of fluorescence microscopy as a research and diagnostic tool can greatly benefit from the use of NIR excitation and emission wavelengths [2]. The optical properties of biological tissue are such that its relative transparency in parts of the NIR region can greatly improve optical imaging potential. Achieving NIR luminescence from molecular species has therefore become an ongoing challenge. From a photophysical perspective, consideration of the nature of the excited emitting state and suppression of non-radiative deactivation pathways (particularly where the energy gap between the ground and excited state is small) is a key challenge.

Lanthanide coordination compounds have been successfully developed in this regard with Nd(III), Er(III) and Yb(III) species demonstrating long-lived emission in the 880–1550 nm window [3]. Uniquely, such species possess metal centred (4*f*) excited states that can give rise to NIR emission. Whilst demonstrating attractive emission properties, the limiting aspect of such systems is overcoming the inherently poor molar absorption coefficients associated with 4*f*-4*f* transitions [4]. Over the last two decades a wide range of functionalised ligand systems have been developed to address these challenges [5].

In contrast, only a relatively small number of reports have described NIR emission from *d*-metal complexes. Most commonly such observations are often defined at low temperature (*i.e.* in a frozen matrix) or under deoxygenated conditions. Of course, both approaches seek to minimise non-radiative quenching of the excited emitting state. For several decades, Cr(III) complexes have

* Corresponding author.
** Corresponding author.
E-mail addresses: beamesj@cardiff.ac.uk (J.M. Beames), popesj@cardiff.ac.uk (S.J.A. Pope).

https://doi.org/10.1016/j.jorganchem.2019.04.019

been known to demonstrate emission from a *d*-centred excited state (^{2}E) which typically emits around 780 nm, and work continues to maximise these properties [6]. A small number of Ru(II) [7], Os(II) [8], and Pt(II) [9] complexes have also been reported to demonstrate luminescence in the NIR region. Strategies can include lowering the energy of charge transfer (CT) excited states or facilitating the population of low-lying ligand-centred triplet states through efficient spin orbit coupling (SOC) facilitated by the heavy metal atom of the complex.

Cyclometalated Ir(III) complexes have also, very recently, been investigated in this context. Neutral Ir(III) complexes based on 1-(benzo[*b*]thiophen-2-yl)-isoquinolinate show emission between 680 and 850 nm and have been successfully processed into phosphorescent organic light-emitting devices [10]. Ir(III) complexes with boron-dipyrromethane (BODIPY) conjugated ligands have shown interesting NIR absorption and emission properties with particularly long triplet state lifetimes [11]. Wong and co-workers have demonstrated highly tuneable emission properties for Ir(III) complexes using both conjugation and substitution strategies on the cyclometalating ligands [12]. This has allowed the emission to be tuned in the range 420–729 nm with successful application shown within light emitting diodes. Two further reports of cationic Ir(III) complexes that incorporate benzo[*g*]quinoxaline cyclometalated ligands have been previously described by Chen et al. [13] and Sun and co-workers [14]. The extended conjugation of these ligands, *versus* the red wavelength emission observed from previous studies on 2-phenylquinoxaline analogues [15], appears to bathochromically shift the emission wavelength into the NIR region. Building on these reports, we herein describe a further series of Ir(III) organometallic complexes based on substituted benzo[*g*] quinoxaline ligands, providing further evidence that these species are viable NIR emitters, even under ambient conditions (room temperature, aerated solution).

2. Results and discussion

2.1. Synthesis and characterisation

The ligands (**L1-L4**) were synthesised in a single step by the condensation reaction of 2,3-diaminonaphthalene with a benzil derivative in the presence of acetic acid. The ligands (Scheme 1) were isolated in good yield and characterised using a range of analytical and spectroscopic techniques. All relevant data is presented in the experimental section. Good quality single crystals were obtained for the dibromo-substituted derivative **L3** following slow evaporation of a concentrated chloroform solution. The orange blade shaped crystals were submitted to diffraction studies and the structure was refined in the $P2_1/n$ space group and there is a single molecule in the asymmetric unit. The data confirmed the proposed structure (Figs. 1 and 2), with a packing arrangement supported by some long range intermolecular π-π interactions.

The complexes (Scheme 2) were synthesised according to the well known Nonoyama route [16] that first isolates the chloro-bridged dimeric Ir(III) species, $[(L)_2Ir\text{-}(\mu\text{-}Cl_2)\text{-}Ir(L)_2]$. Subsequent splitting of the dimer with 2,2′-bipyridine gave the target cationic complexes. HRMS data was obtained for each of the complexes and showed the correct isotopic distribution in all cases (Fig. 3). In addition to this, ^{1}H NMR spectroscopy was particularly insightful for the determination of the coordination of the ligands to the iridium centre. This was typically noted by the upfield shift of the

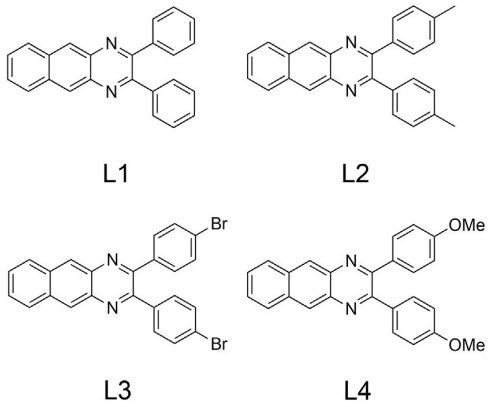

Scheme 1. The benzo[g]quinoxaline ligands synthesised in this study for Ir(III) complexation.

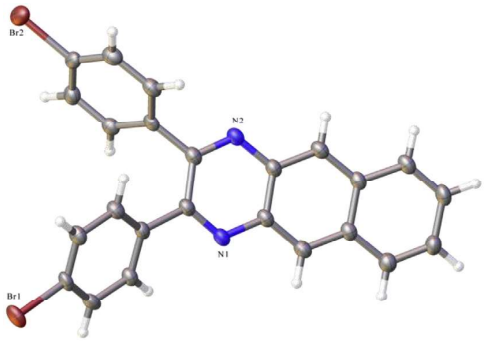

Fig. 1. X-ray crystal structure of **L3**. Ellipsoids are drawn at a 50% probability. Crystal Data: $C_{24}H_{14}Br_2N_2$, $M_r = 490.19$, monoclinic, $P2_1/n$ (No. 14), $a = 5.7963(2)$ Å, $b = 21.8021(9)$ Å, $c = 15.1661(6)$ Å, $\beta = 91.211(3)^\circ$, $\alpha = \gamma = 90^\circ$, $V = 1916.15(13)$ Å^3, $T = 100(2)$ K, $Z = 4$, $Z' = 1$, $\mu(MoK_\alpha) = 4.243$ mm^{-1}, 19907 reflections measured, 4396 unique ($R_{int} = 0.0501$) which were used in all calculations. The final wR_2 was 0.1219 (all data) and R_1 was 0.0491 ($I > 2(I)$).

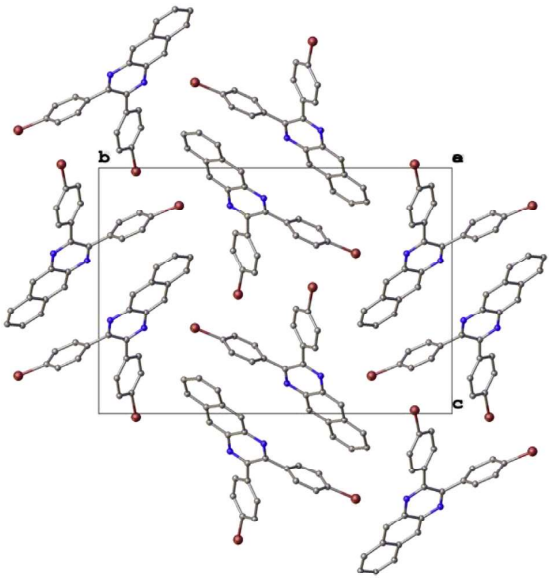

Fig. 2. Packing diagram for **L3** obtained from the X-ray crystal structure. Ellipsoids are drawn at a 50% probability.

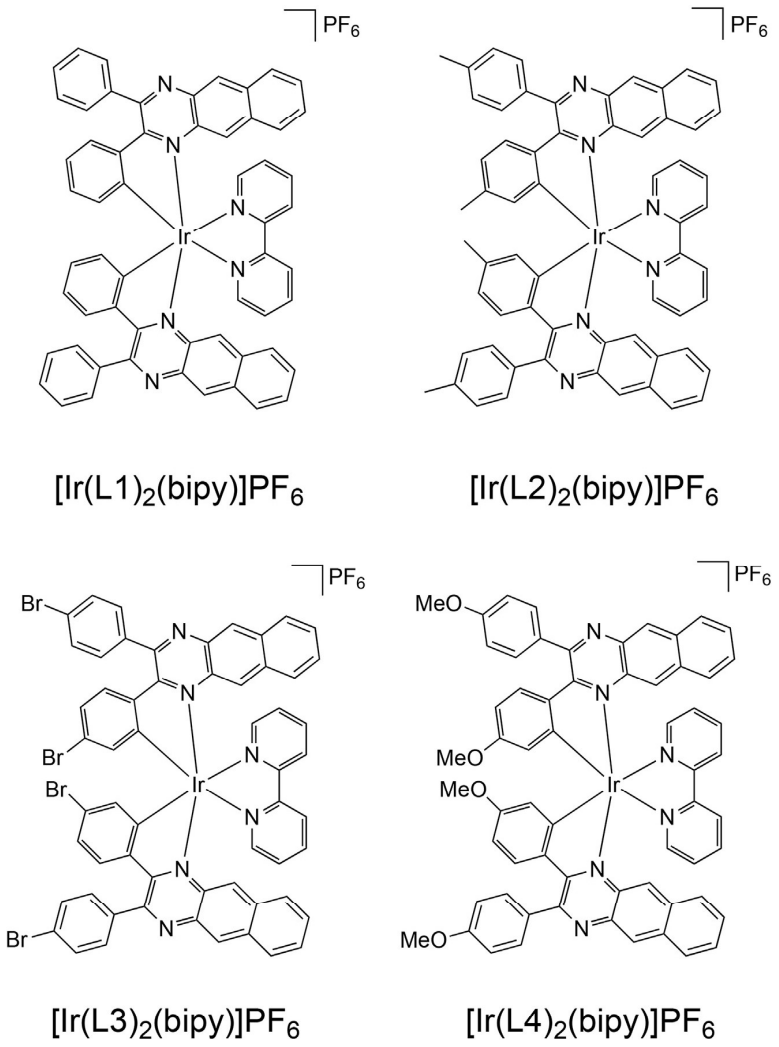

Scheme 2. The structures of the iridium(III) complexes synthesised in this study.

proton adjacent to the cyclometalating carbon atom (for example, Fig. 4). In the ^{1}H NMR spectra of [Ir(**L2**)$_2$(bipy)]PF$_6$ and [Ir(**L4**)$_2$(bipy)]PF$_6$, there were two unique methyl environments (note that they are equivalent in the free ligand) indicative of cyclometalation in the expected manner (*i.e.* the benzo[*g*]quinoxaline ligands do not act in a bridging manner). The frequency separations in these inequivalent methyl resonances was approximately 0.5 ppm.

2.2. UV-vis. and luminescence spectroscopy

The solution state absorption spectra of the ligands **L1-L4** (Fig. 5) were recorded as chloroform solutions at 1×10^{-5} M and were comparable to related literature examples that are based on the benzo[*g*]quinoxaline chromophore [11–13]. All ligands showed strong ($\varepsilon > 10^4$ M^{-1}cm^{-1}) π–π^* transitions in the UV region at 200–400 nm. A shoulder feature extended beyond 450 nm but again is attributed to low energy π–π^* transitions although weaker n–π^* transitions may also contribute in this region. The phenyl substituent (-H, -Me, -Br, -OMe) of the ligand clearly influences the positioning of these bands, with the methoxy substituted **L4** possessing the most bathochromically shifted features, which was attributed to the increased conjugation induced by the -OMe substituents. The corresponding emission spectra obtained for these ligands shows that they are all luminescent in the visible region from 400 to 550 nm showing some vibronic structure to the peak shape. Again the nature of the substituent influences the peak positioning, and in this case the benzil derivative (**L1**) possesses the longest emission wavelength. The recorded lifetimes for each ligand were found to be < 5 ns, consistent with fluorescence from a $^1\pi$–π^* emitting state.

UV-vis. spectroscopy on solutions of the complexes revealed spectra with multiple contributions across the UV and visible regions (Fig. 6; Table 1). The majority of peaks at wavelengths than 250–450 nm are attributed to different ligand-centred transitions that are perturbed upon coordination to the Ir(III) centre, as well as contributions from spin allowed metal-to-ligand charge transfer bands (^{1}MLCT).

The ancillary bipyridine ligand π–π^* absorptions are also likely to contribute ca. 270–290 nm. When compared to the ligand spectra, each of the complexes showed additional absorption bands

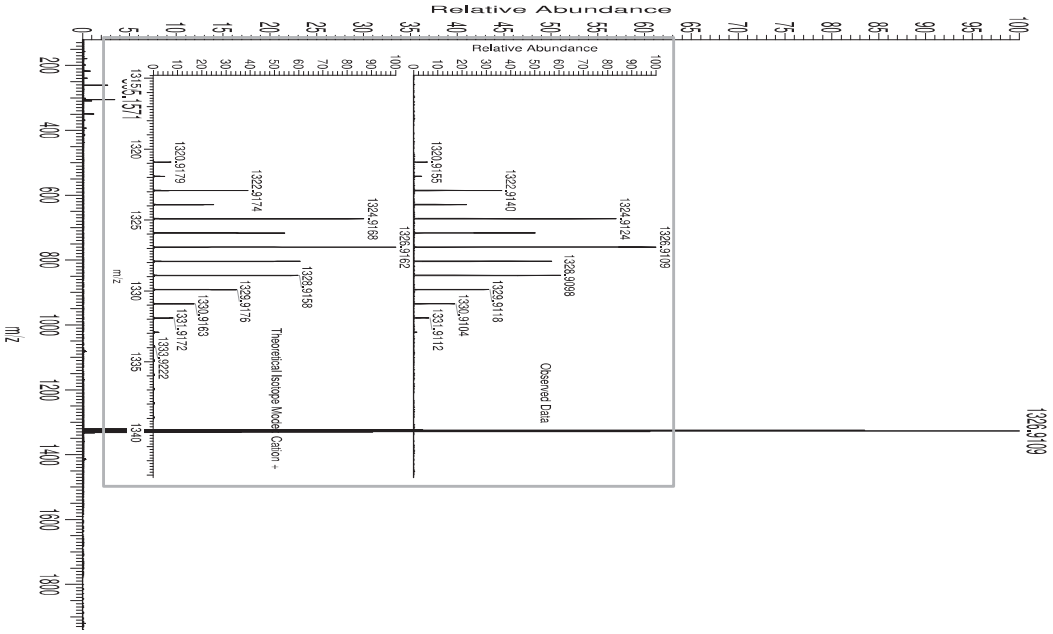

Fig. 3. Example of a high resolution mass spectrum obtained for [Ir(**L3**)$_2$(bipy)]PF$_6$ showing the cationic fragment (main) and observed *versus* theoretical isotopic distribution pattern (inset).

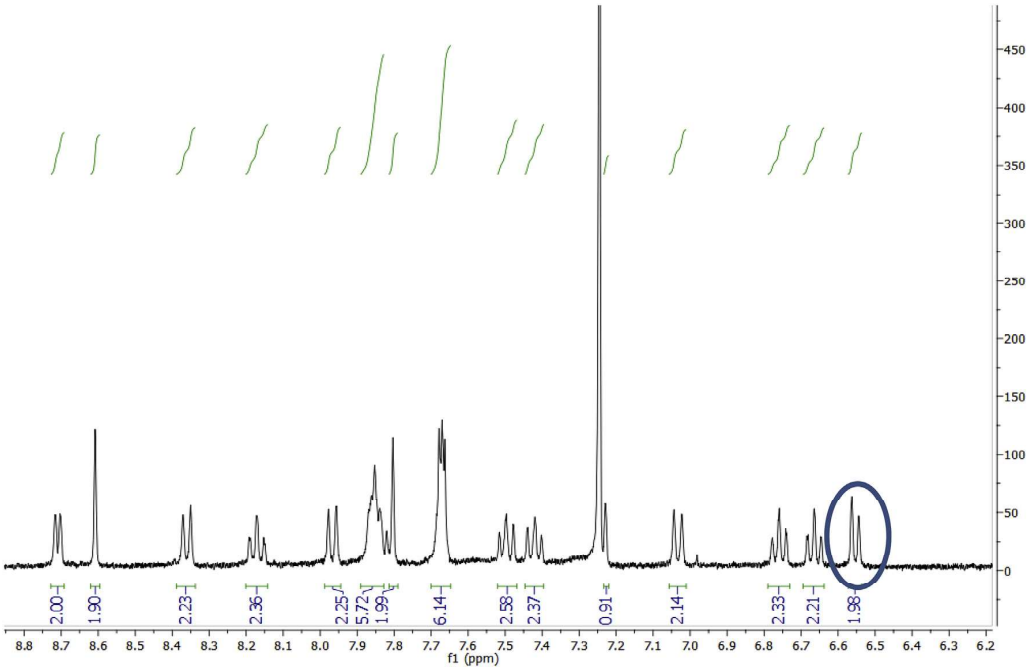

Fig. 4. ^{1}H NMR spectrum of [Ir(**L1**)$_2$(bipy)]PF$_6$ that shows the upfield shift of the ligand proton adjacent to the cyclometalating carbon atom.

across the visible region that extended >600 nm. These weaker absorption bands may comprise spin forbidden ^{3}MLCT bands [17]. These Ir(III) complexes therefore demonstrate strong bathochromic shifts in the visible region relative to related complexes based upon substituted 2-phenylquinoxaline ligands [15]. This is attributed to the lowering of the MLCT transitions due to the added conjugation of the ligand benzo[*g*]quinoxaline ligands. The subtle variation between the complexes are again indicative of the electronic character of the substituents; as with the free ligands the methoxy-substituted variant [Ir(**L4**]$_2$(bipy)]PF$_6$ possessed the lowest energy

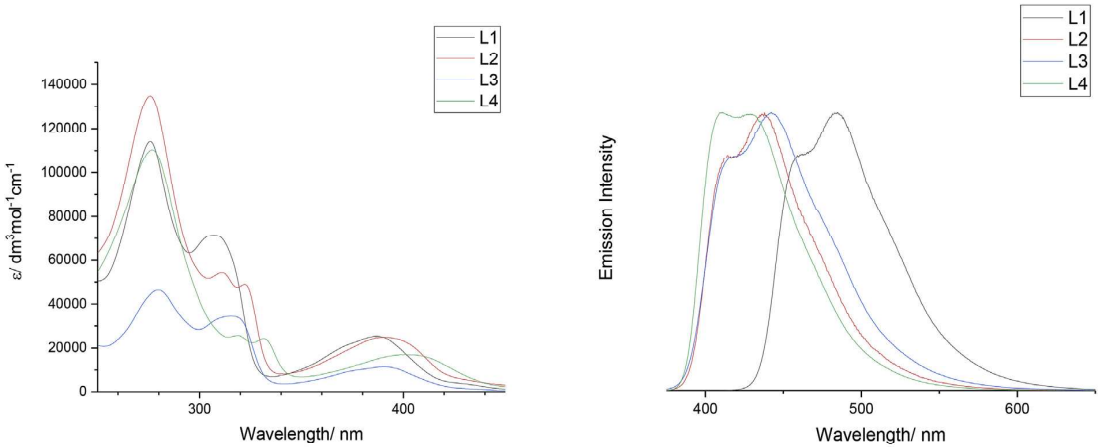

Fig. 5. UV–vis absorption (left) and emission (right) spectra of the ligands (10^{-5} M $CHCl_3$).

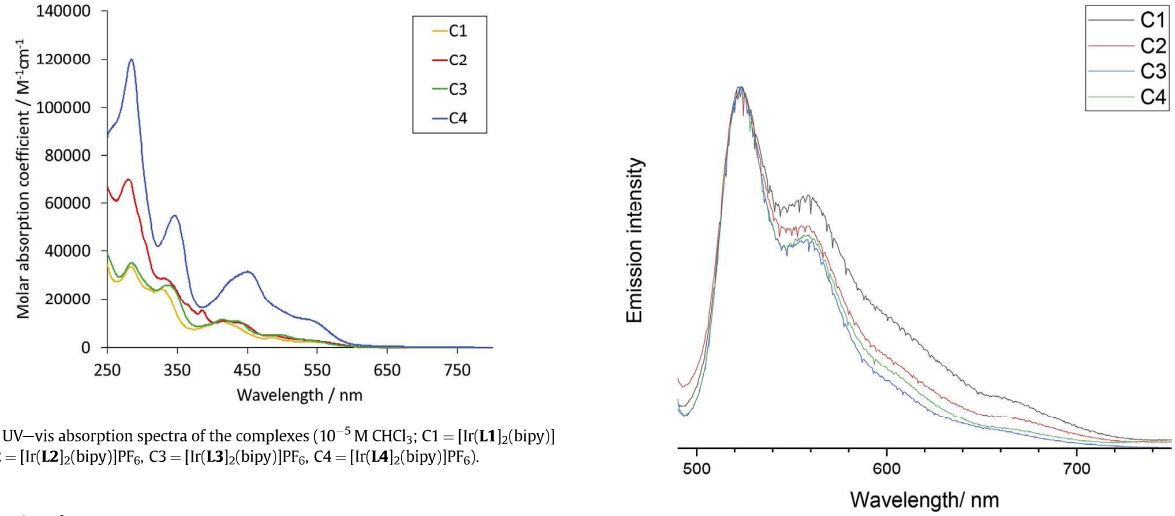

Fig. 6. UV–vis absorption spectra of the complexes (10^{-5} M $CHCl_3$; C1 = [Ir(**L1**]$_2$(bipy)]PF_6, C2 = [Ir(**L2**]$_2$(bipy)]PF_6, C3 = [Ir(**L3**]$_2$(bipy)]PF_6, C4 = [Ir(**L4**]$_2$(bipy)]PF_6).

Fig. 7. Visible emission spectra for the complexes (aerated $CHCl_3$, λ_{exc} = 405 nm; C1 = [Ir(**L1**]$_2$(bipy)]PF_6, C2 = [Ir(**L2**]$_2$(bipy)]PF_6, C3 = [Ir(**L3**]$_2$(bipy)]PF_6, C4 = [Ir(**L4**]$_2$(bipy)]PF_6).

absorption features.

The luminescence spectra for the complexes were recorded on aerated samples at room temperature (Table 1). In all cases an excitation wavelength of 470 nm was used as this corresponds to strong absorption bands in all of the complexes reported herein. The first collection of emission spectra were recorded between 490 and 750 nm and revealed a defined vibronic progression to the peak shape that was reproduced for each of the four complexes, but differentiated from the corresponding free ligands (Fig. 7). In fact these emission spectra for the complexes are virtually superimposable, with little variance in the wavelength positioning of these bands across the series. Time-resolved measurements provided the emission lifetimes for the visible emission which were all short-lived (<10 ns). Taken together the data implies that these features may be due to intraligand transitions associated with the coordinated phenyl benzo[*g*]quinoxaline units (see further discussion in computational section).

Table 1
Absorption and emission data for the ligands and complexes.[a] Recorded in aerated $CHCl_3$;[b] λ_{exc} = 405 nm;[c] λ_{exc} = 295 nm;[d] λ_{exc} = 505 nm;[e] λ_{exc} = 355 nm.

Compound	λ_{abs}/nm[a]	λ_{em}/nm[a,b] (τ/ns[c])	λ_{em}/nm[a,d] (τ/ns[e])
L1	386, 309, 276	485 (1.4)	–
L2	391, 323, 312, 276	480 (1.1)	–
L3	393, 318, 280	490 (1.8)	–
L4	402, 332, 319, 276	480 (1.1)	–
[Ir(**L1**)$_2$(bipy)]PF_6	554sh, 490, 415, 329, 286	520 (4.9)	915 (119)
[Ir(**L2**)$_2$(bipy)]PF_6	554sh, 491, 445, 420, 388, 367, 334, 283	520 (7.0)	912 (148)
[Ir(**L3**)$_2$(bipy)]PF_6	554sh, 500, 439, 415, 340, 287	520 (2.9)	928 (116)
[Ir(**L4**)$_2$(bipy)]PF_6	554sh, 455, 348, 285	520 (<1)	949 (162)

Interestingly, these observations do not correspond with the luminescence properties of closely related 2-phenylquinoxaline complexes of Ir(III), which we have previously described [15], which were shown to be phosphorescent around 620–650 nm and attributed to a ^{3}MLCT emitting state. Therefore, further luminescence studies on the complexes investigated the possibility of emission in the NIR region. Again, aerated solutions were studied at room temperature and, using an excitation wavelength of 505 nm, spectra were collected between 850 and 1300 nm.

As shown in Fig. 8, under these conditions, each of the complexes demonstrated luminescence in the NIR region peaking around 915–950 nm. The appearance of the emission peak is very broad and tails to ca. 1250 nm. This is consistent with the findings of previous work on related complex structures using different benzo[*g*]quinoxaline based ligands [12,13]. Each of the spectra includes an additional sharp emission peak centred at 1274 nm which is characteristic of the radiative decay that accompanies the spin forbidden relaxation of singlet oxygen ($^1O_2 \rightarrow {}^3O_2$). The photogeneration of singlet oxygen in solution, firstly corroborates the use of aerated solvent for the measurements, and secondly, implies the presence of an excited triplet state on a sensitizer molecule. Further, time-resolved measurements monitoring the decay kinetics of the NIR emission band revealed emission lifetimes in the range of 116–162 ns, each indicative of a triplet excited state. Critically, these lifetimes are significantly longer than those attributed to the visible emission of the complexes (measured under identical sample conditions).

2.3. Density functional theory (DFT) calculations

The geometries of all the complexes were optimised in Gaussian09 using the B3LYP functional with a combination of 6-31G* basis sets for the ligand atoms and the Stuttgart-Dresden (SDD) core potential/basis set for the iridium metal core [18]. Solvent effects were included implicitly using the self-consistent reaction field (SCRF) and polarized continuum (IEFPCM) models. Time dependent DFT (TD-DFT) calculations were performed on the stationary points to determine the first five singlet excited states for each complex, using the same basis sets and the long range corrected CAM-B3LYP functional. Phosphorescence and spin forbidden absorption bands were computed using unrestricted DFT calculations, computing parameters for the first triplet state of the complexes (T_1). Fig. 8 shows the superimposition of the calculated molecular geometries of the complexes in both singlet and triplet excited states. Whilst the geometries look broadly similar it is notable that there are differing degrees of distortion within the coordinated ligand fragments of the two excited states. The composition of the complexes' HOMOs and LUMOs are detailed in Table 2.

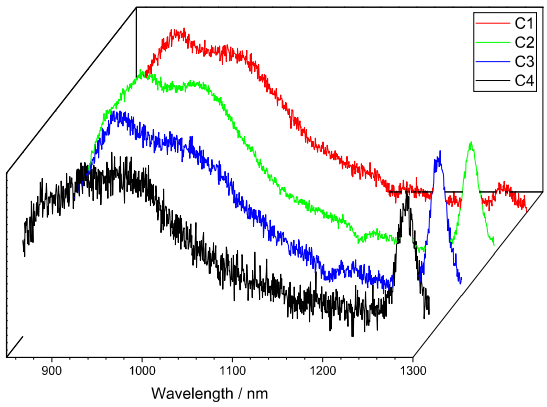

Fig. 8. Steady state near-IR emission spectra of the complexes. The peak at 1274 nm is due to the photogeneration of, and subsequent emission from, $^1O_2$. (Aerated $CHCl_3$, $\lambda_{exc} = 505$ nm; C1 = [Ir(**L1**]$_2$(bipy)]PF_6, C2 = [Ir(**L2**]$_2$(bipy)]PF_6, C3 = [Ir(**L3**]$_2$(bipy)]PF_6, C4 = [Ir(**L4**]$_2$(bipy)]PF_6).

In all cases the cyclometalated ligands are predicted to contribute strongly to both molecular orbitals, with Ir contributions of 13–26% for the HOMO. Orbital contributions to the excited states (see ESI) show that a range of transitions are predicted for each. The lowest calculated energy excited state is dominated by the HOMO → LUMO transition, which may comprise both MLCT and intra(-cyclometalated)ligand contributions (Table 2). It is noteworthy that the DFT calculations suggest that bipyridine localised orbitals primarily contribute to the upper lying LUMO+2 and LUMO+3, neither of which feature strongly as participants in contributing transitions to the predicted excited states. Ligand centred transitions, more specifically transitions localised on the benzo[*g*]quinoxaline ligands, are assigned as the dominant contributors to the visible complex emission. This is consistent with the similarity in vibronic band shapes between the free ligand emission (Fig. 2) and the complex emission band (Fig. 3). Both of these emission bands show clear vibrational progressions, with a vibrational spacing of ~1300 cm^{-1}. This vibrational frequency is consistent with quinoxalene (predominantly pyrazine) ring breathing modes, which are the most infrared active modes for these ligands. The electronic emission spectrum of the free ligand has been simulated using the Franck-Condon-Herzberg-Teller approach implemented in the Gaussian09 software package [19,20]. Both ground and excited states have been optimised using the DFT//B3LYP/6-31G(d) method, with the excited state being optimised using TD-DFT. The Franck-Condon progression has then been calculated using the vibrational frequencies from the two states, at a temperature of 300 K, and convoluted with a HWHM of 500 cm^{-1}. The computed spectrum is shown below (Fig. 9) in comparison with the experimental spectra of the free ligand **L1**, and the complex [Ir(**L1**]$_2$(bipy)]PF_6.

The spectra shown in Fig. 9 show remarkable agreement between simulation and experiment. The simulated spectrum has been deliberately slightly under convoluted to highlight the overlap of the vibronic peak positions. This agreement not only confirms the assignment of the vibronic features, but further illustrates the similarity between **L1** within the complex [Ir(**L1**]$_2$(bipy)]PF_6 and as its free ligand. The vibrational spacing is approximately consistent between the free ligand and the complex, but there is a clear change in the Franck-Condon factors associated with the progression. This is equally consistent with the assignment: the metal binding to the ligand alters the bond lengths of the pyrazine ring, slightly lengthening the C-N bonds (C=N, 1.315 Å; C-N, 1.37 Å in the free ligand, C=N, 1.347 Å; C-N, 1.39 Å in the complex) which will alter the Franck-Condon overlap between S_0 and S_1.

Further photochemical properties of the complexes have also

Table 2
Predicted MO compositions of the HOMO and LUMO of the complexes.

Compound [a]	Ir (5d)	C^N (1)	C^N (2)	bipy
		HOMO		
[Ir(**L1**)$_2$(bipy)]PF_6	26%	36%	36%	1%
[Ir(**L2**)$_2$(bipy)]PF_6	26%	37%	36%	1%
[Ir(**L3**)$_2$(bipy)]PF_6	13%	44%	42%	0%
[Ir(**L4**)$_2$(bipy)]PF_6	16%	40%	43%	1%
		LUMO		
[Ir(**L1**)$_2$(bipy)]PF_6	3%	48%	47%	1%
[Ir(**L2**)$_2$(bipy)]PF_6	3%	47%	48%	2%
[Ir(**L3**)$_2$(bipy)]PF_6	3%	49%	46%	3%
[Ir(**L4**)$_2$(bipy)]PF_6	3%	47%	49%	2%

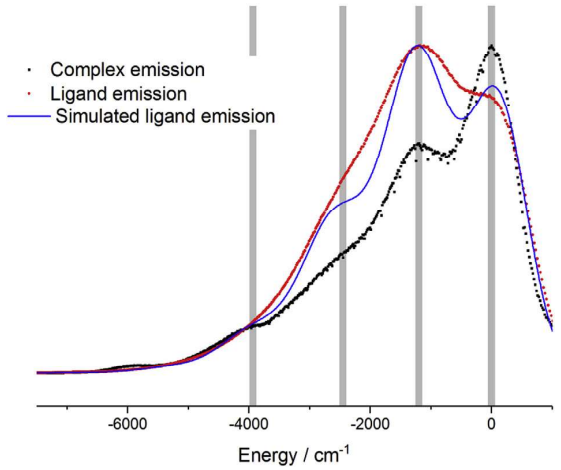

Fig. 9. Franck-Condon simulation of the **L1** A-X transition (blue), overlaid against the experimental emission spectra of the free ligand **L1** (red), and the complex **[Ir(L1]$_2$(bipy)]PF$_6$** (black). The spectra have been offset by their respective vibronic origin, and are therefore displayed as emission energy (cm^{-1}) relative to zero. The grey bars are a guide to the eye, showing different vibronic features. (For interpretation of the references to colour in this figure legend, the reader is referred to the Web version of this article.)

been computed: the wavelengths of selected calculated transitions are shown in Table 3, including those that are spin forbidden and thus relate to an excitation ($T_1 \leftarrow S_0$, at S_0 minimum energy geometry) and phosphorescence ($T_1 \rightarrow S_0$, at T_1 minimum energy geometry). The overlap between the S_1 and T_1 minimum energy geometries are highlighted in Fig. 10. The calculated data corresponds well with the experimental results and importantly predicts that the emission should occur in the NIR region around 962—1019 nm. Both the spin allowed and spin forbidden excitations correlate well with the primary features of the complexes' absorption spectra. The DFT results suggest that the variations in ligand structure induce differences in emission energy, but these subtleties were not apparent in the broadened features of the experimental data. It is also intriguing to see that such subtle changes in geometry within the triplet state, i.e. geometric relaxation after ISC, lead to dramatic changes in the $T_1 - S_0$ energy gap. Tempering or expanding upon this shift will form the basis of future work.

Table 3
Calculated vertical transitions for the complexes.

Compound	$S_1 \leftarrow S_0$/nm	$T_1 \leftarrow S_0$/nm	$T_1 \rightarrow S_0$/nm
[Ir(**L1**)$_2$(bipy)]PF$_6$	433	557	993
[Ir(**L2**)$_2$(bipy)]PF$_6$	434	602	980
[Ir(**L3**)$_2$(bipy)]PF$_6$	428	590	1019
[Ir(**L4**)$_2$(bipy)]PF$_6$	428	583	962

3. Conclusion

Extending the conjugation of cyclometalating ligands on iridium(III) can bathochromically shift luminescence from organometallic complexes into the NIR spectral region. For Ir(III), substituted benzo[*g*]quinoxaline type cyclometalting ligands are appropriate choices to achieve this and the study shows that supporting DFT calculations can reliably predict the spin forbidden transitions that dominate the lowest energy absorptions and phosphorescent emission properties of these complexes.

4. Experimental

All reactions were performed with the use of vacuum line and Schlenk techniques. Reagents were commercial grade and were used without further purification. ^{1}H and ^{13}C{^{1}H} NMR spectra were run on NMR-FT Bruker 400 or 250 spectrometers and recorded in $CDCl_3$. ^{1}H and ^{13}C-{^{1}H} NMR chemical shifts (δ) were determined relative to internal TMS and are given in ppm. Low-resolution mass spectra were obtained by the staff at Cardiff University. High-resolution mass spectra were carried out by at the EPSRC National Mass Spectrometry Service at Swansea University. UV-Vis studies were performed on a Jasco V-570 spectrophotometer as MeCN solutions (10^{-5} M). Photophysical data were obtained on a JobinYvon-Horiba Fluorolog spectrometer fitted with a JY TBX picosecond photodetection module as MeCN solutions. A Hamamatsu R5509-73 detector (cooled to −80 °C using a C9940 housing) was used for NIR luminescence measurements. For the NIR lifetimes the pulsed laser source was a Continuum Minilite Nd:YAG

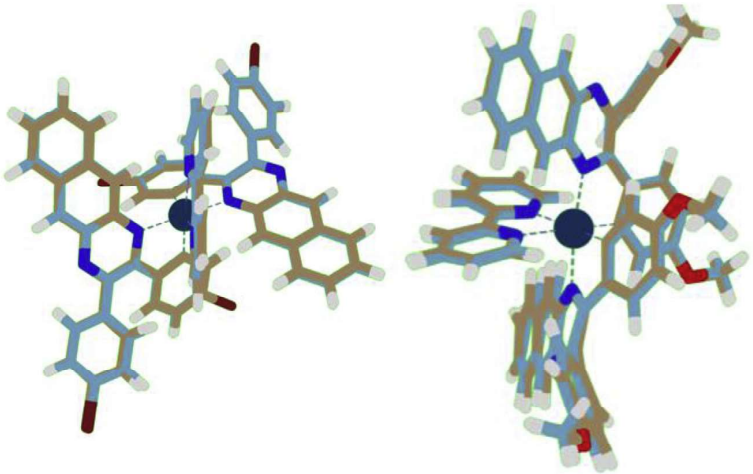

Fig. 10. A comparison of the calculated geometries of the singlet and triplet excited states for [Ir(**L3**)$_2$(bipy)]PF$_6$ (left, RMSD = 0.185 Å) and [Ir(**L4**)$_2$(bipy)]PF$_6$ (right, RMSD = 0.149 Å).

configured for 355 nm output. For all NIR emission data, a 850 nm band pass filter was used. The pulsed source was a Nano-LED configured for 295 nm output operating at 1 MHz. All luminescence lifetime profiles were obtained using the JobinYvon-Horiba FluoroHub single photon counting module and the data fits yielded the lifetime values using the provided DAS6 deconvolution software.

4.1. Data collection and processing

X-ray diffraction datasets were measured on a Rigaku AFC12 diffractometer equipped with enhanced sensitivity (HG) Saturn 724 + CCD detector mounted at the window of an FR-E + *SuperBright* rotating anode generator (Mo Kα, λ = 0.71075 Å) with VHF *Varimax* optics (70 μm focus) [21] using CrysAlisPro software [22] for data collection and reduction.

4.2. Structure analysis and refinement

The structures were solved by direct methods using Superflip [23] and refined on F_0^2 by full-matrix least-squares refinements using SHELXL [24] within the OLEX2 suite [25]. All non-hydrogen atoms were refined with anisotropic displacement parameters, and all hydrogen atoms were added at calculated positions and refined using a riding model with isotropic displacement parameters based on the equivalent isotropic displacement parameter (U_{eq}) of the parent atom.

4.3. Density functional theory

The geometries of all the complexes were optimised in Gaussian09 using the B3LYP functional with a combination of 6-31G* basis sets for the ligand atoms and the Stuttgart-Dresden (SDD) core potential/basis set for the iridium metal core [16]. Solvent effects were included implicitly using the self-consistent reaction field (SCRF) and polarized continuum (IEFPCM) models, and in all cases the solvent chosen was chloroform, characterised by an electrical permittivity of $\varepsilon = 4.7113$. Molecular orbital calculations were performed using the same basis sets and functionals, and decomposition analysis was performed on the frontier orbitals using the GaussSum software package. TD-DFT calculations were performed on the stationary points to determine the first five singlet excited states for each complex, using the same basis sets and the long range corrected CAM-B3LYP functional. Phosphorescence and spin forbidden absorption bands were computed using unrestricted DFT calculations, computing parameters for the first triplet state of the complexes (T_1). The Franck-Condon simulations were performed without implicit solvation, however it is clear from the agreement between experiment and theory that this does not significantly alter the results. Additionally, the Franck-Condon progressions are harmonic in nature. Small shifts in peak positions would be expected using anharmonic modes (the harmonic scaling factor for this functional and basis set is ca.0.962) [26], however these shifts are expected to be small relative to the peak widths. The Chimera software package was used to visualise the complexes and compare singlet and triplet geometries [27].

4.4. Synthesis

4.4.1. Synthesis of 2,3-diphenylbenzo[g]quinoxaline (*L1*)

To a stirred solution of benzil (322 mg, 1.6 mmol) in ethanol (15 mL) was added 2,3-diaminonaphthalene (250 mg, 1.6 mmol) and acetic acid (0.5 mL). The reaction mixture was heated at reflux under a nitrogen atmosphere for 24 h. The reaction mixture was cooled to room temperature and a precipitate collected by filtration to give **L1** as a brown solid (0.34 g, 64%). ^{1}H NMR (300 MHz, $CDCl_3$): δ_H 8.68 (s, 2H, CH), 8.05 (dd, $J = 3.21$ Hz, 6.39 Hz, 2H), 7.50 (m, 6H), 7.30 (m, 6H) ppm. $^{13}C\{^1H\}$ NMR (101 MHz, $CDCl_3$): δ_C 154.2, 139.2, 138.0, 134.1, 129.8, 129.0, 128.6, 128.3, 127.6, 126.8 ppm. HRMS found *m/z* 333.1387; calcd *m/z* 333.1386 for $C_{24}H_{16}N_2$. UV-vis. ($CHCl_3$) λ_{max} (ε/dm^3 mol^{-1} cm^{-1}): 386 (25200), 309 (71500), 276 (114100) nm. Selected IR (solid) $\upsilon_{max} = 1607, 1508, 1441, 1346, 1248, 1175, 1013, 976, 876, 836, 760, 741, 691, 552, 500.0, 490, 467$ cm^{-1}.

4.4.2. Synthesis of 2,3-di-p-tolylbenzo[g]quinoxaline (*L2*)

As **L1** but with 4,4′-dimethylbenzil (376 mg, 1.6 mmol) and 2,3-diaminonaphthalene (250 mg, 1.6 mmol). Product collected as a brown solid (0.41 g, 71%). ^{1}H NMR (300 MHz, $CDCl_3$) δ_H 8.73 (s, 2H), 8.12 (dd, $J = 3.2$, 6.5 Hz, 2H), 7.57 (dd, $J = 3.1$, 6.7 Hz, 2H), 7.49 (d, $J = 8.0$ Hz, 4H), 7.19 (d, $J = 8.0$ Hz, 4H), 2.41 (s, 6H) ppm. $^{13}C\{^1H\}$ NMR (101 MHz, $CDCl_3$) δ_C 154.3, 139.0, 138.0, 136.5, 134.0, 129.8, 129.0, 128.6, 127.4, 126.6, 21.4 ppm. HRMS *m/z* found 361.1699; calcd *m/z* 316.1699 for $C_{26}H_{20}N_2$. UV-vis. ($CHCl_3$) λ_{max} (ε/dm^3 mol^{-1} cm^{-1}): 391 (24800), 323 (48600), 312 (54200), 276 (134500) nm. Selected IR (solid) $\upsilon_{max} = 1607, 1508, 1445, 1346, 1247, 1174, 1109, 1013, 972, 878, 835, 819, 760, 559, 500, 490, 471, 421$ cm^{-1}.

4.4.3. Synthesis of 2,3-bis(4-bromophenyl)benzo[g]quinoxaline (*L3*)

As L1 but with 4,4′-dibromobenzil (581 mg, 1.6 mmol) and 2,3-diaminonaphthalene (250 mg, 1.6 mmol). Product collected as a light brown solid (0.56 g, 72%). ^{1}H NMR (400 MHz, $CDCl_3$) δ_H 8.66 (s, 2H), 8.05 (dd, $J = 3.2$, 6.5 Hz, 2H), 7.52 (m, 2H), 7.46 (d, $J = 8.4$ Hz, 4H), 7.38 (d, $J = 8.4$ Hz, 4H) ppm. $^{13}C\{^1H\}$ NMR (101 MHz, $CDCl_3$) δ_C 152.6, 137.9, 137.8, 134.3, 131.7, 131.4, 128.6, 127.7, 127.0, 123.9 ppm. HRMS found *m/z* 490.9569; calcd *m/z* 490.9576 for $C_{24}H_{15}Br_2N_2$. UV-vis. ($CHCl_3$) λ_{max} (ε/dm^{3}mol^{-1}cm^{-1}): 393 (11400), 318 (34300), 280 (46400) nm. Selected IR (solid) $\upsilon_{max} = 1605, 1510, 1445, 1344, 1246, 1173, 1109, 1053, 1011, 972, 880, 833, 795, 758, 745, 723, 656, 646, 623, 573, 557, 548, 532, 498, 471, 409$ cm^{-1}.

4.4.4. Synthesis of 2,3-bis(4-methoxyphenyl)benzo[g]quinoxaline (*L4*)

As **L1** but with anisil (427 mg, 1.6 mmol) and 2,3-diaminonaphthalene (250 mg, 1.6 mmol). Product collected as a light brown solid (0.50 g, 80%). ^{1}H NMR (300 MHz, $CDCl_3$) δ_H 8.61 (s, 2H, CH), 8.02 (dd, $J = 3.01$, 6.42 Hz, 2H), 7.48 (d, $J = 8.31$ Hz, 6H), 6.83 (d, $J = 8.43$, 4H), 3.78 (s, 6H) ppm. $^{13}C\{^1H\}$ (101 MHz, $CDCl_3$) δ_C 160.4, 153.8, 138.0, 133.9, 131.8, 131.3, 128.5, 127.2, 126.5, 113.8, 55.4 ppm. HRMS found *m/z* 393.1593; calcd *m/z* 392.1598 for $C_{26}H_{21}N_2O_2$. UV-vis. ($CHCl_3$) λ_{max} (ε/dm^{3}mol^{-1}cm^{-1}): 402 (16900), 332 (24200), 319 (25600), 276 (110300) nm. Selected IR (solid) $\upsilon_{max} = 1605, 1578, 1541, 1508, 1445, 1414, 1344, 1275, 1246, 1173, 1109, 1051, 1015, 976, 891, 880, 853, 833, 795, 756, 747, 656, 646, 623, 592, 573, 557, 532, 525, 496, 474, 421$ cm^{-1}.

4.5. Synthesis of complexes

Synthesis of $[Ir(C^N)_2Cl_2]_2$ $IrCl_3$. xH_2O (1 eq.) and ligand, L (2 eq.) were dissolved in 2-ethoxyethanol (10 mL) and the reaction mixture heated at reflux for 48 h. The reaction was then cooled to room temperature and water (30 mL) was added to form a dark brown precipitate. The solid was collected by filtration to yield $[(L)_2Ir(\mu\text{-}Cl_2)Ir(L)_2]$.

4.5.1. Synthesis of [Ir(*L1*)$_2$(bipy)][PF_6]

[(**L1**)$_2$Ir(μ-Cl$_2$)Ir(**L1**)$_2$] (195 mg, 0.11 mmol) and 2,2′-bipyridyl (36 mg, 0.23 mmol) were dissolved in 2-ethoxyethanol (10 mL) and heated at reflux for 24 h under a nitrogen atmosphere. The reaction mixture was then cooled to room temperature and a saturated

solution of aqueous ammonium hexafluorophosphate was added. Upon formation of a red precipitate, the mixture was filtered and the precipitate washed with water and diethyl ether. The crude solid was purified by column chromatography using DCM followed by DCM/MeOH (9:1). Product collected as first red band with DCM/MeOH and dried in vacuo to give [Ir(**L1**)$_2$(bipy)][PF$_6$] as a red solid (38 mg, 15%). ^{1}H NMR (400 MHz, CDCl$_3$) δ_H 8.65 (d, J = 5.6 Hz, 2H), 8.55 (s, 2H), 8.31 (d, J = 8.8 Hz, 2H), 8.12 (app. t, J = 8.8 Hz, 2H), 7.91 (d, J = 8.4 Hz, 2H), 7.89–7.77 (m, 6H), 7.75 (s, 2H), 7.64–7.60 (m, 6H), 7.44 (app. t, J = 8.8 Hz, 2H), 7.36 (app. t, J = 6.4 Hz, 2H), 7.17 (s, 2H), 6.98 (d, J = 8.8 Hz, 2H), 6.70 (app. t, J = 5.6 Hz, 2H), 6.61 (app. t, J = 7.2 Hz, 2H), 6.50 (d, J = 7.2 Hz, 2H) ppm. ^{13}C{^{1}H} NMR (101 MHz, CDCl$_3$) δ_C 164.5, 155.8, 154.3, 153.8, 147.9, 144.3, 139.6, 134.6, 133.7, 132.5, 131.5, 130.4, 129.4, 129.4, 128.9, 128.8, 128.2, 128.0, 127.6, 125.4, 122.0, 119.5, 114.4, 77.4, 76.7 ppm. HRMS found m/z 1011.2777; calcd m/z 1011.2786 for C$_{58}$H$_{38}$IrN$_8$. UV-vis. (CHCl$_3$) λ_{max} (ε/dm^3 mol^{-1} cm^{-1}): 554 (2100), 490 (3900), 415 (10700), 329 (24200), 286 (33200) nm. Selected IR (solid) υ_{max} = 1607, 1445, 1350, 1253, 835, 760, 738, 696, 574, 557, 500, 468 cm^{-1}.

*4.5.2. Synthesis of [Ir(**L2**)$_2$(bipy)][PF$_6$]*

As [Ir(**L1**)$_2$(bipy)][PF$_6$] but with [(**L2**)$_2$Ir(μ-Cl$_2$)Ir(**L2**)$_2$] (56 mg, 0.03 mmol) and 2,2′-bipyridyl (10 mg, 0.07 mmol). Product collected as a red solid (44 mg, 62%) ^{1}H NMR (400 MHz, CDCl$_3$) δ_H 8.67 (d, J = 6.60 Hz, 2H), 8.59 (s, 2H), 8.53 (d, J = 8.8 Hz, 2H), 8.21 (dd, J = 7.72, 8.80 Hz, 2H), 7.98 (d, J = 8.80 Hz, 2H), 7.78 (m, 8H), 7.50 (m, 6H), 7.42 (app. t, J = 7.70, 2H), 7.24 (d, J = 7.72 Hz, 2H), 7.03 (d, J = 7.72 Hz, 2H), 6.65 (d, J = 8.84 Hz, 2H), 6.43 (s, 2H), 2.57 (s, 6H), 1.94 (s, 6H) ppm. ^{13}C{^{1}H} NMR (101 MHz, CDCl$_3$) δ_C 164.8, 156.0, 148.0, 142.5, 141.7, 141.1, 140.5, 136.9, 136.3, 135.1, 134.0, 133.4, 132.3, 130.0, 129.1, 128.8, 128.5, 128.1, 128.0, 127.7, 127.5, 125.8, 123.8, 122.0, 21.8, 21.7 ppm. HRMS found m/z 1067.3406; calcd m/z 1067.3413 for C$_{62}$H$_{46}$IrN$_6$. UV-vis. (CHCl$_3$) λ_{max} (ε/dm^{3}mol^{-1} cm^{-1}): 554 (2500), 491 (4900), 445 (9700), 420 (11000), 388 (14900), 367 (16900), 334 (28300), 283 (69500) nm. Selected IR (solid) υ_{max} = 1586, 1503, 1445, 1398, 1359, 1314, 1257, 1211, 1177, 1138, 1069, 1042, 978, 833, 772, 635, 579, 556, 513, 471, 424, 407 cm^{-1}.

*4.5.3. Synthesis of [Ir(**L3**)$_2$(bipy)][PF$_6$]*

As [Ir(L1)$_2$(bipy)][PF$_6$] but with [(**L3**)$_2$Ir(μ-Cl$_2$)Ir(**L3**)$_2$] (150 mg, 0.06 mmol) and 2,2′-bipyridyl (20 mg, 0.13 mmol). Product collected as a red solid (75 mg, 61%). ^{1}H NMR (400 MHz, CDCl$_3$) δ_H 8.82 (d, J = 8.80 Hz, 2H), 8.56 (s, 2H), 8.52 (d, J = 6.40 Hz, 2H), 8.21 (app. t, J = 8.40 Hz, 2H), 7.94 (d, J = 7.20 Hz, 3H), 7.77–7.68 (m, 5H), 7.62 (s, 2H), 7.49 (app. t, J = 8.40 Hz, 3H), 7.39 (app. t, J = 6.00 Hz, 3H), 7.11 (d, J = 7.20 Hz, 3H), 6.97 (m, 5H), 6.62 (s, 2H) ppm. ^{13}C{^{1}H} NMR (101 MHz, d6-acetone) δ_C 164.5, 155.8, 153.4, 149.6, 144.1, 141.0, 138.8, 137.5, 137.4, 136.8, 134.1, 133.7, 133.6, 132.3, 131.5, 129.3, 129.1, 128.5, 128.3, 127.9, 127.5, 126.5, 126.0, 124.8, 124.2, 122.4, 78.3 ppm. LRMS found m/z 1326.90; calcd m/z 1326.92 for C$_{58}$H$_{34}$Br$_4$IrN$_6$. UV-vis. (CHCl$_3$) λ_{max} (ε/dm^3 mol^{-1} cm^{-1}): 554 (2400), 500 (5100), 439 (10700), 415 (11500), 340 (26000), 287 (34800) nm. Selected IR (solid) υ_{max} = 1607, 1512, 1445, 1348, 1248, 1174, 1109, 1013, 878, 835, 760, 559, 500 cm^{-1}.

*4.5.4. Synthesis of [Ir(**L4**)$_2$(bipy)][PF$_6$]*

As [Ir(**L1**)$_2$(bipy)][PF$_6$] but with [(**L4**)$_2$Ir(μ-Cl$_2$)Ir(**L4**)$_2$] (100 mg, 0.09 mmol) and 2,2′-bipyridyl (16 mg, 0.11 mmol). Product collected as a red solid (27 mg, 21%). ^{1}H NMR (400 MHz, CDCl$_3$) δ_H 8.63 (d, J = 4.64 Hz, 2H), 8.45 (s, 2H), 8.43 (d, J = 8.00 Hz, 2H), 8.14 (app. t, J = 9.28 Hz, 2H), 7.87 (d, J = 8.12 Hz, 2H), 7.76 (m, 6H), 7.62 (s, 2H), 7.40 (dd, J = 6.96, 8.12 Hz, 2H), 7.32 (dd, J = 5.80, 9.28 Hz, 2H), 7.27 (s, 2H), 7.24 (s, 4H), 7.11 (d, J = 8.52 Hz, 2H), 6.94 (d, J = 8.16 Hz, 2H), 5.99 (s, 2H), 3.91 (s, 6H), 3.26 (s, 6H) ppm. ^{13}C{^{1}H} NMR (101 MHz, CDCl$_3$) δ_C 164.2, 161.4, 156.0, 148.2, 141.1, 137.2, 136.7, 136.2, 134.4, 134.0, 133.1132.1, 130.5, 128.9, 128.4, 128.1, 127.5, 125.6, 121.6, 119.8, 114.7, 108.3, 55.6, 54.8 ppm. HRMS found m/z 1131.3193; calcd m/z 1131.3209 for C$_{62}$H$_{46}$IrN$_6$O$_4$. UV-vis. (CHCl$_3$) λ_{max} (ε/dm^3 mol^{-1} cm^{-1}): 554 (10000), 455 (31700), 348 (55200), 285 (120700) nm. Selected IR (solid) υ_{max} = 1580, 1503, 1447, 1400, 1358, 1246, 1224, 1173, 1134, 1020, 978, 870, 837, 810, 772, 687, 519, 471 cm^{-1}.

Acknowledgements

Cardiff University (Knowledge Economy Skills Scholarship, via the Welsh Government's European Social Fund, to K.A.P.), STG Aerospace, and EPSRC are thanked for financial support. We thank the staff of the EPSRC Mass Spectrometry National Service (Swansea University) and the UK National Crystallographic Service at the University of Southampton.

Appendix A. Supplementary data

Supplementary data to this article can be found online at https://doi.org/10.1016/j.jorganchem.2019.04.019. Information on the data underpinning the results presented here, including how to access them, can be found in the Cardiff University data catalogue at http://doi.org/10.17035/d.2019.0074136089.

References

[1] a C.-C. Hou, H.-M. Chen, J.-C. Zhang, N. Zhuo, Y.-Q. Huang, R.A. Hogg, D.T.D. Childs, J.-Q. Ning, Z.-G. Wang, F.-Q. Liu, Z.-Y. Zhang, Light Sci. Appl. 7 (2018) 17170;
b Y. Zhang, Y. Wang, J. Song, J. Qu, B. Li, W. Zhu, W.-Y. Wong, Adv. Optical Mater. 6 (2018) 1800466.
[2] X. Zhang, S. Bloch, W. Akers, S. Achilefu, Curr. Protoc. Cytom. 60 (2012), 12.27.1.
[3] a J.-C.G. Bünzli, C. Piguet, Chem. Soc. Rev. 34 (2005) 1048;
b S. Faulkner, S.J.A. Pope, B.P. Burton-Pye, Appl. Spectrosc. Rev. 40 (2005) 1;
c A.J. Amoroso, S.J.A. Pope, Chem. Soc. Rev. 44 (2015) 4723.
[4] a M.H.V. Werts, J.W. Hofstraat, F.A.J. Geurts, J.W. Verhoeven, Chem. Phys. Lett. 276 (1997) 196;
b L. Armelo, S. Quici, F. Barigelletti, G. Accorsi, G. Bottaro, M. Cavazzini, E. Tondello, Coord. Chem. Rev. 254 (2010) 487;
c A. Beeby, I.M. Clarkson, R.S. Dickens, S. Faulkner, D. Parker, L. Royle, A.S. de Sousa, J.A.G. Williams, M. Woods, J. Chem. Soc., Perkin Trans. 2 (1999) 493;
d A. Beeby, R.S. Dickins, S. Faulkner, D. Parker, J.A.G. Williams, Chem. Commun. (1997) 1401.
[5] a W. Levason, Coord. Chem. Rev. 340 (2017) 1;
b S.V. Eliseeva, J.-C.G. Bünzli, New J. Chem. 36 (2011) 1165;
c J.-C.G. Bünzli, Acc. Chem. Res. 39 (2006) 53.
[6] C. Wang, S. Otto, M. Dorn, E. Kreidt, J. Lebon, L. Srsan, P. Di Martino-Fumo, M. Gerhards, U. Resch-Genger, M. Seitz, K. Heinze, Angew. Chem. Int. Ed. 57 (2018) 1112.
[7] a S.D. Bergman, D. Gut, M. Kol, C. Sabatini, A. Barbieri, F. Barigelletti, Inorg. Chem. 44 (2005) 7943;
b B. Laramee-Milette, G.S. Hanan, Dalton Trans. 45 (2016) 12507;
c M.I.J. Polson, F. Loiseau, S. Campagna, G.S. Hanan, Chem. Commun. (2006) 1301;
d A. Damas, B. Ventura, J. Moussa, A.D. Esposti, L.-M. Chamoreau, A. Barbieri, H. Amouri, Inorg. Chem. 51 (2012) 1739.
[8] S. Silvi, E.C. Constable, C.E. Housecroft, J.E. Beves, E.L. Dunphy, M. Tomasulo, F.M. Raymo, A. Credi, Chem. Commun. (2009) 1484.
[9] a N. Su, F. Meng, P. Wang, X. Liu, M. Zhu, W. Zhu, S. Su, J. Yu, Dyes Pigments 138 (2017) 162;
b C.J. Adams, N. Fey, J.A. Weinstein, Inorg. Chem. 45 (2006) 6105;
c Y. Liu, W. Wu, J. Zhao, X. Zhang, H. Guo, Dalton Trans. 40 (2011) 9085;
d C.J. Adams, N. Fey, M. Parfitt, S.J.A. Pope, J.A. Weinstein, Dalton Trans. (2007) 4446.
[10] S. Kesarkar, W. Mroz, M. Penconi, M. Pasini, S. Destri, M. Cazzaniga, D. Ceresoli, P.R. Mussini, C. Baldoli, U. Giovanella, A. Bossi, Angew. Chem. Int. Ed. 55 (2016) 2714.
[11] P. Majumdar, X. Yuan, S. Li, B. Le Guennic, J. Ma, C. Zhang, D. Jacquemin, J. Zhao, J. Math. Chem. B 2 (2014) 2838.
[12] Z. Chen, L. Wang, C.-L. Ho, S. Chen, S. Suramitr, A. Plucksacholatarn, N. Zhu, S. Hannongbua, W.-Y. Wong, Adv. Optical Mater. 6 (2018) 1800824.
[13] H.-Y. Chen, C.-H. Yang, Y. Chi, Y.-M. Cheng, Y.-S. Yeh, P.-T. Chou, H.-Y. Hsieh, C.-S. Liu, S.-M. Peng, G.-H. Lee, Can. J. Chem. 84 (2006) 309.
[14] C. Wang, L. Lystrom, H. Yin, M. Hetu, S. Kilina, S.A. McFarland, W. Sun, Dalton

Trans. 45 (2016) 1636.
[15] a E.E. Langdon-Jones, A.J. Hallett, J.D. Routledge, D.A. Crole, B.D. Ward, J.A. Platts, S.J.A. Pope, Inorg. Chem. 52 (2013) 448;
b K.A. Phillips, T.M. Stonelake, K. Chen, Y. Hou, J. Zhao, S.J. Coles, P.N. Horton, S.J. Keane, E.C. Stokes, I.A. Fallis, A.J. Hallett, S.P. O'Kell, J.M. Beames, S.J.A. Pope, Chem. Eur J. 24 (2018) 8577.
[16] M. Nonoyama, Bull. Chem. Soc. Jpn. 47 (1974) 767.
[17] L.M. Groves, C. Schotten, J.M. Beames, J.A. Platts, S.J. Coles, P.N. Horton, D.L. Browne, S.J.A. Pope, Chem. Eur J. 23 (2017) 9407.
[18] Gaussian 09, Revision D. 01, M.J. Frisch, G.W. Trucks, H.B. Schlegel, G.E. Scuseria, M.A. Robb, J.R. Cheeseman, G. Scalmani, V. Barone, G.A. Petersson, H. Nakatsuji, X. Li, M. Caricato, A. Marenich, J. Bloino, B.G. Janesko, R. Gomperts, B. Mennucci, H.P. Hratchian, J.V. Ortiz, A.F. Izmaylov, J.L. Sonnenberg, D. Williams-Young, F. Ding, F. Lipparini, F. Egidi, J. Goings, B. Peng, A. Petrone, T. Henderson, D. Ranasinghe, V.G. Zakrzewski, J. Gao, N. Rega, G. Zheng, W. Liang, M. Hada, M. Ehara, K. Toyota, R. Fukuda, J. Hasegawa, M. Ishida, T. Nakajima, Y. Honda, O. Kitao, H. Nakai, T. Vreven, K. Throssell, J.A. Montgomery Jr., J.E. Peralta, F. Ogliaro, M. Bearpark, J.J. Heyd, E. Brothers, K.N. Kudin, V.N. Staroverov, T. Keith, R. Kobayashi, J. Normand, K. Raghavachari, A. Rendell, J.C. Burant, S.S. Iyengar, J. Tomasi, M. Cossi, J.M. Millam, M. Klene, C. Adamo, R. Cammi, J.W. Ochterski, R.L. Martin, K. Morokuma, O. Farkas, J.B. Foresman, D.J. Fox, Gaussian, Inc., Wallingford CT, 2016.
[19] V. Barone, J. Bloino, M. Biczysko, F. Santoro, J. Chem. Theory Comput. 5 (2009) 540.
[20] F. Santoro, A. Lami, R. Improta, J. Bloino, V. Barone, J. Chem. Phys. 128 (2008) 224311.
[21] S.J. Coles, P.A. Gale, Chem. Sci. 3 (2012) 683.
[22] CrysAlisPro Software System, Rigaku Oxford Diffraction, 2015.
[23] L. Palatinus, G. Chapuis, J. Appl. Crystallogr. 40 (2007) 786–790.
[24] G.M. Sheldrick, Acta Crystallogr. Sect. C Struct. Chem. 71 (2015) 3.
[25] *OLEX2*: a complete structure solution, refinement and analysis program O.V. Dolomanov, L.J. Bourhis, R.J. Gildea, J.A.K. Howard, H. Puschmann, J. Appl. Crystallogr. 42 (2009) 339–341.
[26] D. Russell, Johnson III (Eds.), NIST Computational Chemistry Comparison and Benchmark Database, NIST Standard Reference Database Number 101, Release 19, April 2018. http://cccbdb.nist.gov/.
[27] Molecular graphics and analyses performed with UCSF Chimera, developed by the Resource for Biocomputing, Visualization, and Informatics at the University of California, San Francisco, with support from NIH P41-GM103311 E.F. Pettersen, T.D. Goddard, C.C. Huang, G.S. Couch, D.M. Greenblatt, E.C. Meng, T.E. Ferrin, J. Comput. Chem. 25 (2004) 1605.